Università degli Studi di Torino
Scuola di Dottorato in Scienza ed Alta Tecnologia

Inclusive Diffractive Cross Sections in Deep Inelastic ep Scattering at HERA

Valentina Sola

Università degli Studi di Torino
Scuola di Dottorato in Scienza ed Alta Tecnologia

Indirizzo in Fisica ed Astrofisica
Ciclo XXIV

Inclusive Diffractive Cross Sections in Deep Inelastic ep Scattering at HERA

Candidata: Valentina Sola

Tutors: Michele Arneodo
Marta Ruspa

You may say I'm a dreamer
But I'm not the only one

Imagine - John Lennon

Abstract

Diffractive deep-inelastic scattering events in ep collisions at HERA are the subject of this thesis.

The cross sections for inclusive diffraction, $ep \to eXp$, measured by the H1 and ZEUS Collaborations were combined, providing a model-independent check of the data consistency and a cross calibration between the two experiments, and resulting in single data sets with improved accuracy and precision. Two sets of combined results were obtained. The cross sections measured using the proton-spectrometer data were combined, both in the range of t, the squared four-momentum transfer at the proton vertex, common to the two experiments ($0.09 < |t| < 0.55$ GeV^2) and in the extended t-range $|t| < 1$ GeV^2. The resulting cross sections cover the region $2.5 \leq Q^2 \leq 200$ GeV^2 in photon virtualities, $0.0003 \leq x_{I\!P} \leq 0.09$ in the proton fractional momentum losses and $0.0018 \leq \beta \leq 0.816$ in $\beta = x/x_{I\!P}$, where x is the Bjorken scaling variable. The cross sections obtained from data with the large rapidity gap signature were also combined in the kinematic range $2.5 \leq Q^2 \leq 1600$ GeV^2, $0.0003 \leq x_{I\!P} \leq 0.03$ and $0.0017 \leq \beta \leq 0.8$, for masses of the hadronic final state $M_X > 4$ GeV.

The inclusive diffractive reduced cross section $\sigma_r^{D(3)}$ was measured with data collected by the ZEUS detector, at two different centre-of-mass energies, 318 and 225 GeV. The diffractive data were selected with the large rapidity gap method in the kinematic region $20 < Q^2 < 130$ GeV^2, $0.05 < \beta < 0.85$ and $0.00063 < x_{I\!P} < 0.01$. The measurement covers an unexplored range of y ($y \gtrsim 0.55$), the inelasticity of the interaction.

Contents

Introduction **v**

1 Inclusive Diffraction at HERA **1**
1.1 Neutral-Current Deep Inelastic *ep* Scattering . . . 1
1.1.1 Kinematics of Deep Inelastic *ep* Scattering . . . 1
1.1.2 The *ep* Cross Section and the Structure Functions . . . 3
1.1.3 The Quark-Parton Model . . . 4
1.1.4 Scaling Violations of F_2 and QCD . . . 5
1.1.5 The Longitudinal Structure Function F_L . . . 7
1.1.6 DGLAP Evolution Equations and the Q^2-x Plane . . . 9
1.1.7 QCD Hard Scattering Factorisation and PDFs . . . 11
1.2 Hadronic Diffraction . . . 12
1.2.1 The Analogy with Optical Diffraction . . . 13
1.2.2 Regge Formalism and the Pomeron . . . 14
1.2.3 Hard Diffraction . . . 18
1.3 Diffraction in Deep Inelastic *ep* Scattering . . . 19
1.3.1 Hadronic Behaviour of the Photon . . . 20
1.3.2 Kinematics in Diffractive DIS . . . 21
1.3.3 The Diffractive DIS Cross Section . . . 22
1.3.4 Theoretical Models . . . 26
1.3.4.1 Partonic Structure of the Pomeron . . . 26
1.3.4.2 Colour Dipole Models . . . 30

2 The ZEUS detector at HERA **33**
2.1 The HERA Accelerator . . . 33
2.2 The ZEUS Detector . . . 35
2.2.1 The Micro Vertex Detector (MVD) . . . 38
2.2.2 The Central Tracking Detector (CTD) . . . 39
2.2.3 The Calorimeter (CAL) . . . 40

2.2.4 The Small-angle Rear Tracking Detector (SRTD) . . . 43
2.2.5 The Hadron-Electron Separator (HES) . . . 44
2.2.6 The Luminosity Measurement . . . 44
2.2.7 The Leading Proton Spectrometer (LPS) . . . 45
2.2.8 The Forward Plug Calorimeter (FPC) . . . 46
2.2.9 Trigger and Data Acquisition (DAQ) . . . 47

3 Methods of Selecting Diffraction at HERA 49
3.1 Proton Spectrometer Method (PS) . . . 50
3.2 Large Rapidity Gap Method (LRG) . . . 51
3.3 M_X Method . . . 52
3.4 Comparison between Selection Methods . . . 53

4 Combined Measurement of the Inclusive Diffractive Cross Sections at HERA 55
4.1 Introduction . . . 55
4.2 Combination Method . . . 56
4.3 Combination of Proton Spectrometer Cross Sections . . . 58
4.3.1 Combined Data Sets . . . 58
4.3.2 Binning Scheme and Correlated Systematic Sources . . . 58
4.3.3 Normalisation and t-slope . . . 60
4.3.4 Combined Proton Spectrometer Cross Section in the Visible t-range . . . 64
4.3.4.1 Consistency between Data Sets and Pull Distributions . . . 64
4.3.4.2 Procedural Uncertainties . . . 67
4.3.4.3 Combined Cross Section . . . 68
4.3.5 Combined Proton Spectrometer Cross Section in the Extended t-range . 74
4.3.6 Discussion . . . 79
4.4 Combination of LRG Cross Sections . . . 80
4.4.1 Combined Data Sets . . . 80
4.4.2 Binning Scheme and Correlated Systematic Sources . . . 80
4.4.3 Normalisation . . . 81
4.4.4 Combined LRG Cross Section . . . 82
4.4.5 Discussion . . . 89

5 Measurement of the Inclusive Diffractive Cross Section at high-y with the ZEUS Detector at HERA 91
5.1 Data Set . . . 91
5.2 Event Simulation . . . 92
5.2.1 Diffractive Event Simulation: SATRAP . . . 93
5.2.2 Inclusive DIS Event Simulation: DJANGOH . . . 95

5.2.3 Photoproduction Event Simulation: PYTHIA . . . 95
5.2.4 Hard Diffractive Photoproduction Event Simulation: RAPGAP . . . 96
5.2.5 Simulation of the ZEUS Detector . . . 96
5.3 Event Reconstruction . . . 96
5.3.1 Diffractive DIS Event Reconstruction . . . 97
5.3.2 Track and Vertex Reconstruction . . . 98
5.3.3 Reconstruction of the Scattered Electron . . . 99
5.3.3.1 Electron Finder . . . 99
5.3.3.2 Electron Energy . . . 99
5.3.3.3 Electron Position . . . 100
5.3.4 Reconstruction of the Hadronic Final State . . . 100
5.3.5 Reconstruction of the DIS Kinematic Variables . . . 103
5.3.6 Reconstruction of the Diffractive Kinematic Variables . . . 105
5.4 Event Selection and Background Discussion . . . 108
5.4.1 Aim of the Selection . . . 108
5.4.2 Trigger Selection . . . 108
5.4.3 Offline Selection . . . 109
5.4.3.1 DIS Selection . . . 109
5.4.3.2 Diffractive Selection . . . 112
5.4.4 Reweighting of the Monte Carlo . . . 113
5.4.5 Comparison between Data and Monte Carlo . . . 113
5.4.6 Background Discussion . . . 120
5.4.6.1 The Photoproduction Background . . . 120
5.4.6.2 The Double Dissociative Background . . . 120
5.5 Detector Studies . . . 122
5.5.1 Energy Flow Studies . . . 122
5.5.1.1 Energy Flow and W . . . 122
5.5.1.2 Energy in the Calorimeter . . . 123
5.5.1.3 Energy Flow and η_{MAX} . . . 123
5.5.1.4 Energy Flow and Event Topology . . . 128
5.5.2 Non-Vertex Track Studies . . . 130
5.5.3 Efficiency Studies . . . 134
5.5.3.1 Trigger Efficiency . . . 134
5.5.3.2 Vertex Efficiency . . . 136
5.6 Results . . . 137
5.6.1 Bin Selection . . . 137
5.6.1.1 Resolution of the Kinematic Variables . . . 137
5.6.1.2 Acceptance and Purity . . . 138

5.6.2 Cross Section and Uncertainties . . . 145
5.6.2.1 Cross Section Extraction . . . 145
5.6.2.2 Statistical Uncertainties . . . 145
5.6.2.3 Systematic Uncertainties . . . 146
5.6.3 Diffractive DIS Cross Section Measurement . . . 156
5.6.3.1 Comparison with Previous Measurements . . . 158
5.6.3.2 Comparison with Predictions . . . 158

6 Summary **163**

A Intercalibration of the CMS Electromagnetic Calorimeter with the Azimuthal Symmetry Method **165**
A.1 The CMS Electromagnetic Calorimeter . . . 165
A.2 The CMS ECAL Calibration Strategy . . . 166
A.3 Calibration with the ϕ-Symmetry Method . . . 167
A.3.1 The Method . . . 167
A.3.2 ϕ-Symmetry Online Calibration Stream . . . 167
A.3.3 Effect of Azimuthal Detector Non-Uniformity . . . 168
A.3.4 Supermodule Relative Scale . . . 169
A.3.5 Crystal-by-Crystal Calibration . . . 170
A.4 In-Situ Inter-Calibration from 2010 Data . . . 171
A.5 The ϕ-Symmetry Calibration with 2011 Data . . . 172

Bibliography **173**

Introduction

High-energy diffraction in particle physics has attracted much interest in the last two decades following the observation of hard diffraction in $p\bar{p}$ collisions at the SPS and the Tevatron, as well as in deep inelastic ep scattering at HERA and more recently in pp collisions at the LHC.

The term *diffraction* was introduced in high-energy physics in the 50's and is used in strict analogy with the familiar optical phenomenon that occurs when a beam of light impinges on an obstacle or a slit whose dimensions are comparable to its wavelenght. To the extent that the propagation and the interaction of hadrons are nothing but the absorption of their wave functions caused by the many inelastic channels open at high energy, the use of the optical terminology seems indeed appropriate.

In-depth studies of diffraction have been performed in hadron-hadron interactions. As a general definition, diffractive processes occur when no quantum numbers are exchanged between the high-energy colliding particles, and consequently the final states have the same quantum numbers as the incident particles. Historically, hadronic diffraction was studied as a soft phenomenon. The main novelty of the last 20 years is the discovery and investigation of diffractive processes in the presence of a hard scale.

A successful method to study hard diffractive interactions is deep inelastic electron-proton scattering (DIS), in which the interaction between the electron and the proton is mediated by a virtual photon (neutral current DIS). The latter may fluctuate into a quark-antiquark ($q\bar{q}$) pair or into a quark-antiquark-gluon ($q\bar{q}g$) state with the same quantum numbers as the photon. The photon effectively acquires hadronic properties, and hence the capability of interacting diffractively with the proton. The partonic fluctuations of the photon can have different sizes, since the transverse dimension of the $q\bar{q}$ or $q\bar{q}g$ states is related to the inverse of the photon virtuality, Q^2. The advantage of using virtual photons is therefore that the scale of the interaction can be varied by changing Q^2. In diffractive interactions the photon probe allows thus to resolve the partonic content of the proton for the events in which the proton emerges intact from the interaction, carrying a large fraction of its initial energy. Universal diffractive parton distribution functions can be extracted from one process and used to predict the cross sections of other diffractive processes.

The experimental signature of diffractive exchange in ep (or hadron-hadron) interactions is the presence of a leading proton (i.e. a scattered proton carrying a large fraction of the initial proton beam energy) and of a large rapidity gap in the hadronic final state, that is a large angular region where no outgoing particles are detected. Because of the lack of colour exchange, hadron radiation between the dissociated photon system and the remnant of the proton is strongly suppressed, while in non-diffractive DIS the colour transfer between the struck quark and the proton remnant fills the rapidity interval between them with hadrons. A significant rate of such large rapidity gap events in DIS ($\sim 10\%$) was observed by the HERA experiments, opening a new domain of studies on diffraction. A large amount of high-quality diffractive data have been collected and analysed by the H1 and ZEUS Collaborations in the past 20 years and much progress has been made towards the understanding of diffractive processes in terms of perturbative QCD, the theory of strong interactions.

This thesis presents the first combination of the diffractive cross section measurements from the H1 and ZEUS Collaborations. Because of the variety of the selection methods, the complementary features of the data and the statistical limitation of some samples, combining the H1 and ZEUS data provides the most precise and kinematically extended data sets on diffraction in DIS. Two sets of samples were combined: one where diffractive events were selected by tagging the scattered proton, and one in which the selection was based on the presence of a large rapidity gap between the hadronic system and the proton. The combination provides a model-independent check of the data consistency; moreover it allows a reduction of the correlated systematic uncertainties, resulting in improved accuracy.

This thesis presents also a new measurement of the inclusive diffractive DIS ep cross section with data collected by the ZEUS experiment during the years 2006/07, when HERA collided positrons of 27.5 GeV with protons at two different beam energies, 920 and 460 GeV, yielding collisions at centre-of-mass energies of 318 and 225 GeV, respectively. The corresponding integrated luminosities of the data sets are 44.5 pb^{-1} and 13.9 pb^{-1}. This is the first measurement of inclusive diffraction with the ZEUS data after the luminosity upgrade of the HERA collider. The event reconstruction and selection were optimised for large values of the inelasticity of the interaction, y, and specifically the region $y \gtrsim 0.55$ became accessible for the first time at HERA.

The thesis is organised as follows:

- The first Chapter gives a brief overview of deep inelastic scattering. Hadronic diffraction and its phenomenology are also introduced. Then, hard diffraction is presented within the context of DIS; the variables and the kinematics relevant to the present analyses are described. Finally, some of the theoretical models for diffractive deep inelastic scattering are reviewed.

- The second Chapter gives a description of the HERA collider and the ZEUS apparatus. Components of the ZEUS detector essential for the analyses presented here are illustrated in detail.
- In the third Chapter the experimental signatures of the inclusive diffractive events in DIS and the selection methods used at HERA are presented. An overview of the recent diffractive results from the H1 and ZEUS Collaborations is also given, followed by a brief comparison of the available measurements.
- The fourth Chapter presents the combination of the H1 and ZEUS diffractive cross sections. First, the method used to combine the cross sections is described. The latest H1 and ZEUS measurements from proton spectrometers are introduced and the results of the combination are presented for two different ranges of t, the squared four-momentum transfer at the proton vertex: the range covered by both spectrometers, $0.09 < |t| < 0.55$ GeV^2, and the extended range $|t| < 1$ GeV^2. Finally, the combination of the H1 and ZEUS cross sections from large-rapidity gap data is also shown.
- The fifth Chapter is devoted to the measurement of the inclusive diffractive cross section in the high-y region. The ZEUS offline software and the Monte Carlo event simulation are described. Then, the reconstruction of the event and of the kinematic variables is presented. The event selection is described, followed by a discussion of the background that could affect the measurement. Finally, the results are shown, together with the acceptance and systematics studies.

The thesis contains an Appendix devoted to the results obtained on the calibration of the Electromagnetic Calorimeter of the CMS experiment at the LHC. The presented method exploits the azimuthal symmetry of minimum bias events to provide a fast and precise calibration of the calorimeter.

The material presented in Chapters 4 and 5, as well as that of Appendix A is my original contribution to this thesis. Part of the material in Chapter 4 has been presented at the EPS 2011 Conference [1] and is about to be published in Physics Letters B; part of Appendix A has been published in [2].

Chapter 1

Inclusive Diffraction at HERA

1.1 Neutral-Current Deep Inelastic ep Scattering

The process in which the constituents of the proton (quarks and gluons) are probed by means of leptons is known as deep inelastic scattering (DIS). The interaction is "inelastic" when a quark is knocked out of the proton and the proton is broken up. It is called "deep" when the proton is probed with a gauge boson with small wavelength, thereby resolving small distances.

In electron-proton (ep) neutral-current (NC) deep inelastic scattering, a neutral boson, i.e. a photon or a Z^0, is exchanged between the electron and the quark, whereas in charged-current interactions a charged W-boson is exchanged, with a neutrino in the final state.
For the kinematic coverage of the data discussed in this thesis, only photon exchange is relevant.

1.1.1 Kinematics of Deep Inelastic ep Scattering

A diagram of a deep inelastic scattering event, $e(k) + p(P) \rightarrow e(k') + X$, is shown in Fig. 1.1.

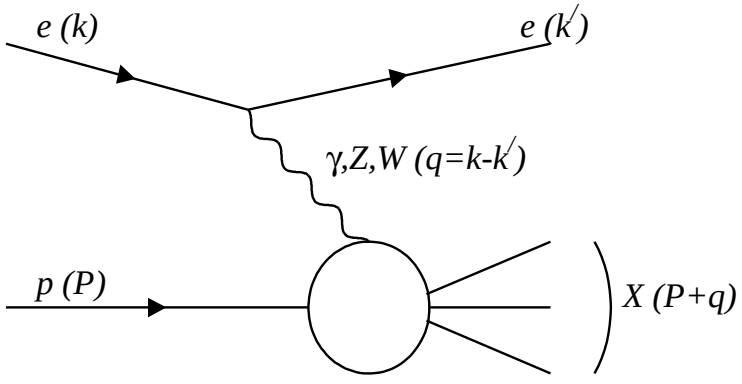

Figure 1.1: *Schematic diagram of deep inelastic electron-proton scattering.*

The incident electron with four-momentum k scatters off a proton carrying four-momentum P. A virtual photon, γ^*, with four-momentum q is exchanged in the interaction. Because of lepton number conservation, the scattered electron has to be present in the final state, with four-momentum k'. In addition, the hadronic system X is produced, with four-momentum denoted by P'.

The kinematics of deep inelastic ep scattering can be described by the following Lorentz-invariant variables[1]:

- $s \;=\; (k+P)^2 \;=\; m_p^2 + 2P\cdot k \;\simeq\; 4E_eE_p$
  the centre-of-mass energy squared of the electron-proton system, where m_p is the mass of the proton and the electron mass is neglected;
- $Q^2 \;=\; -q^2 \;=\; -(k-k')^2$
  the negative four-momentum squared of the virtual photon (γ^*);
- $x \;=\; \frac{Q^2}{2P\cdot q}$
  the fraction of the proton momentum carried by the struck quark (dimensionless Bjorken scaling variable);
- $y \;=\; \frac{P\cdot q}{P\cdot k}$
  the fraction of energy lost by the electron in the proton rest frame (inelasticity);
- $W^2 \;=\; (P+q)^2 \;=\; m_p^2 + \frac{Q^2}{x}(1-x)$
  the invariant mass squared of the photon-proton system.

However, for a given centre-of-mass energy $\sqrt{s}$, only two of these variables are independent. Neglecting the masses of the electron and the proton, Q^2, x and y are related to s through the relation:

$$Q^2 \;=\; sxy\;. \tag{1.1}$$

The photon virtuality Q^2 gives the scale of the interaction: the wavelength λ of the photon gives the smallest distance that the probe can resolve, $\lambda \;\approx\; \hbar c/|q|$. Sizes as small as $\sim 10^{-18}$ m can be resolved with photons of $Q^2 \sim 10^4$ GeV^2, allowed in the HERA kinematics. The kinematic variables described above have a limited range of allowed values:

$$\begin{gathered} 0 \;<\; Q^2 \;<\; s \\ 0 \;<\; x \;<\; 1 \\ 0 \;<\; y \;<\; 1 \\ m_p \;<\; W \;<\; \sqrt{s} \end{gathered}$$

[1]Natural units, which correspond to setting $\hbar = c = 1$, will be used throughout this thesis. Here $\hbar$ indicates the reduced Planck constant and c is the speed of light in the vacuum.

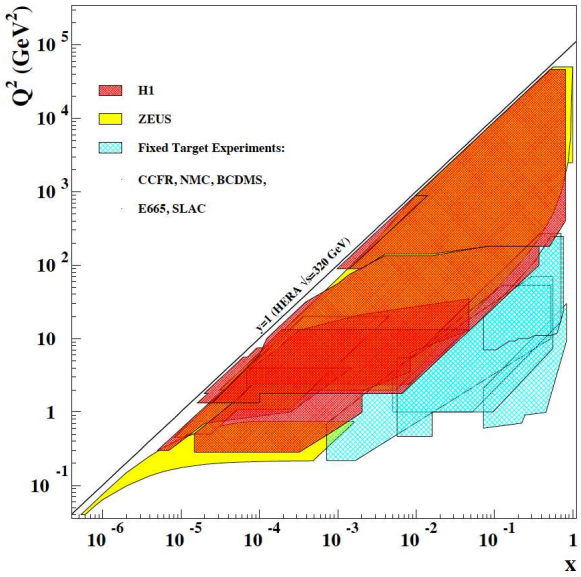

Figure 1.2: *Kinematic coverage of the H1 and ZEUS experiments at HERA in the Q^2-x plane, compared to that of fixed-target experiments. A straight line for $y = 1$ is also shown.*

At HERA, electrons (or positrons[2]) of 27.5 GeV collided with protons of 920 GeV, resulting in a centre-of-mass energy of $\sqrt{s} = 318$ GeV, providing the coverage in the Q^2-x plane illustrated in Fig. 1.2.

In *ep* interactions two kinematic regions can be distinguished:

- the *deep inelastic scattering* (*DIS*) regime, which is defined by the following conditions:

$$Q^2 \gg m_p^2 \ , \ W^2 > m_p^2$$

- the *photoproduction* regime (*PHP*), in which the exchanged photon is real or quasi-real (small values of Q^2).

1.1.2 The *ep* Cross Section and the Structure Functions

The cross section for unpolarized *ep* scattering originates from the contribution of a leptonic and a hadronic part, $\sigma \sim L_{\mu\nu} W^{\mu\nu}$, where the tensor $L_{\mu\nu}$ corresponds to the leptonic vertex, while the tensor $W^{\mu\nu}$ describes the transition from the initial nucleon to all possible final states X at the hadronic vertex.

[2]In the following, the term electron will be used to indicate both electrons and positrons.

Using current conservation, the hadronic tensor can be expressed by means of three independent structure functions, and the cross section reads:

$$\frac{d^2\sigma_{ep}}{dxdQ^2} = \frac{2\pi\alpha^2}{xQ^4}\left[2xy^2F_1\left(x,Q^2\right) + 2\left(1-y\right)F_2\left(x,Q^2\right) - \left(2y+y^2\right)xF_3\left(x,Q^2\right)\right] \ , \tag{1.2}$$

where α is the fine-structure "constant"[3], $\alpha = e^2/4\pi\hbar c \approx 1/137$.
The structure functions F_1 and F_2 contain the information about the inner structure of the target proton. Moreover, the structure function F_1 is proportional to the transverse component of the cross section, σ_T, which is due to the interaction with a transversely polarized γ^* (i.e. with helicity ± 1), whereas the difference between F_1 and F_2 is related to the longitudinal part of the cross section, σ_L, where a longitudinally polarized (virtual) photon is absorbed (helicity 0). In more detail, these relations can be expressed as:

$$F_1 = \frac{Q^2}{8x\pi^2\alpha}\sigma_T \ , \ F_2 = \frac{Q^2}{8x\pi^2\alpha}(\sigma_T + \sigma_L) \ . \tag{1.3}$$

The structure function F_3 contains the parity violating part of the cross section. Since the electro-magnetic coupling conserves parity, this term can be neglected at low Q^2, where photon exchange dominates the cross section. This approximation is hence always valid in the kinematic domain of the present work.

Omitting the parity violating contribution, Eq. (1.2) can be written as:

$$\frac{d^2\sigma_{ep}}{dxdQ^2} = \frac{2\pi\alpha^2}{xQ^4}\left[\left(1+(1-y)^2\right)F_2\left(x,Q^2\right) - y^2\left(F_2\left(x,Q^2\right) - 2xF_1\left(x,Q^2\right)\right)\right] \ . \tag{1.4}$$

1.1.3 The Quark-Parton Model

The first DIS measurements, performed at SLAC [3] and DESY [4] at the end of the 60's, showed that the structure functions F_1 and F_2 were to a first approximation independent of Q^2 and that they were functions of the variable x only. This feature, predicted by Bjorken [5], is called *scale invariance*.

Feynman interpreted this scaling property as evidence of the fact that the proton is composed of free (non-interacting), point-like constituents, called *partons* [6]. The parton model predicts that in the infinite-momentum frame, where the interaction between partons as well as their transverse momenta can be neglected, the proton may be depicted as a beam of partons, each carrying a momentum fraction x. In this model inelastic lepton-proton scattering is interpreted in terms of an elastic lepton-parton interaction. Based on the above assumptions, the total *ep* cross section may be expressed as the incoherent sum of elastic electron-parton

[3] In fact, the fine-structure "constant" is not constant, but depends on Q^2 due to vertex corrections: $\alpha(Q^2) = \alpha(\mu^2)[1 + (\alpha(\mu^2)/3\pi)\log Q^2/\mu^2 + ...]$.

scattering cross sections:

$$\frac{d^2\sigma_{ep}}{dxdQ^2} = \sum_i e_i^2 f_i(x) \left(\frac{d\sigma}{dQ^2}\right)_i \ , \tag{1.5}$$

where e_i is the electric charge of parton i, $f_i(x)$ is the parton distribution function (PDF), which gives the probability to find a parton with momentum fraction between x and $x+dx$ inside the proton, and $(d\sigma/dQ^2)_i$ represents the cross section for elastic scattering on a single parton i. The functions $f_i(x)$, have to satisfy the momentum sum rule, stating that the sum of the momenta of all partons must add up to the momentum of the proton:

$$\sum_i \int_0^1 x f_i\left(x\right) dx = 1 \ . \tag{1.6}$$

From the comparison between Eqs. (1.4) and (1.5), one derives:

$$F_2(x) = \sum_i e_i^2 x f_i(x) \tag{1.7}$$

and

$$F_2(x) = 2xF_1(x) \ , \tag{1.8}$$

where the latter equation is known as the Callan-Gross relation [7] and is a direct consequence of the assumption of spin-1/2 free partons in the nucleon.

The deep inelastic *ep* differential cross section in the parton model thus becomes:

$$\frac{d^2\sigma_{ep\to eX}}{dxdQ^2} = \frac{2\pi\alpha^2}{xQ^4}\left[1+\left(1-y\right)^2\right] F_2\left(x\right) \ . \tag{1.9}$$

The success of the parton model in explaining the observed scaling phenomenon, as well as the confirmation of the Callan-Gross relation from measurements at SLAC, led to the identification of the partons with the spin-1/2 *quarks* that Gell-Mann [8] and Zweig [9] introduced independently in hadron spectroscopy.

1.1.4 Scaling Violations of F_2 and QCD

At the beginning of the 70's evidence appeared against the "naive" quark-parton model:

- more accurate measurements showed variations of the structure function F_2 with Q^2: the scaling hypothesis does not hold for small (large) values of x, where the structure function F_2 was observed to increase (decrease) with Q^2 (*scaling violations*, see Fig. 1.3, where results from the HERA experiments together with fixed target experiments are shown);

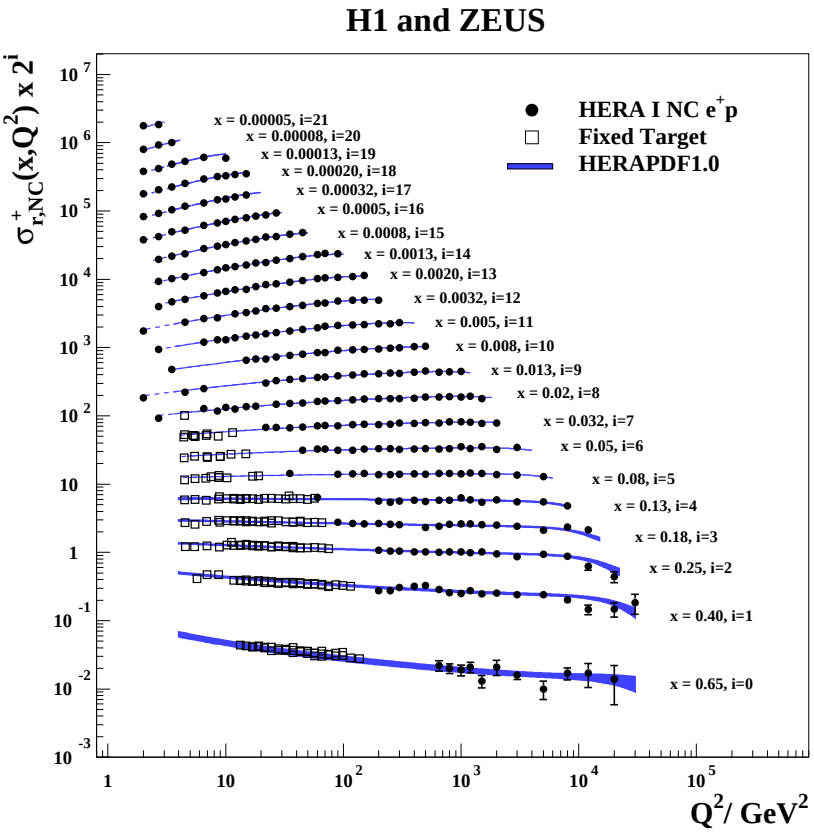

Figure 1.3: *The reduced cross section σ_r as a function of Q^2 for different values of x (in the kinematic region covered by the measurements, $\sigma_r \sim F_2$). A compilation of results from HERA and fixed-target experiments is shown, compared to predictions from a NLO QCD fit to the HERA data [14].*

- as already discussed, if the proton consisted only of charged quarks, their momenta would be expected to add up to the proton momentum, $\Sigma_i \int x f_i(x) dx = 1$. However, experimentally a value of ~ 0.5 was found [10], which means that only half of the proton momentum is carried by charged quarks and the remaining part has to be carried by neutral partons (later identified as *gluons*);
- moreover, the fact that quarks are confined in hadrons implies the presence of strong binding forces between them, which cannot be understood within Quantum Electrodynamics (QED).

The explanation of all these issues was brought by Quantum Chromodynamics (QCD). QCD describes the interactions of quarks and gluons, the mediators of the strong interaction, which

couple through the colour charge. QCD is analogous to QED, which describes the interaction mediated by photons between charged particles, coupled through the electric charge. However, QCD is a non-Abelian gauge theory [11], with the consequence that gluons carry colour charge and can interact among themselves.

The strong coupling "constant" α_s, which varies with Q^2, in leading-order perturbation theory is written as [15]:

$$\alpha_s(Q^2) = \frac{12\pi}{(33 - 2n_f)\ln(Q^2/\Lambda^2)} \ ,$$

where n_f is the number of quark flavours and Λ is the QCD scale parameter that determines the energy scale at which α_s becomes so large that perturbation theory breaks down. At large energy scales, α_s decreases logarithmically and this behaviour is known as *asymptotic freedom*. Within the framework of QCD the quark-parton model appears only in the asymptotic limit $Q^2 \to \infty$.

When QCD is invoked, the quark-parton model is modified, since the partons in the proton (the quarks and gluons) can split up. In the quark-parton model the proton is static, whereas in QCD the proton becomes a dynamic system. According to QCD, structure functions have a Q^2 dependence, resulting in scaling violations. This fact can be interpreted as follows: the higher the scale, the better the resolution with which the proton is probed (see Fig. 1.4). At low values of Q^2 only the valence quarks with relatively large x values can be resolved. In the high Q^2 region gluon radiation leads to an increase of the number of quarks with small fraction x of the proton momentum, and accordingly to a depletion of the high x region. In fact, at low x a rapid increase of F_2 with increasing Q^2 is observed, while at large x values F_2 decreases (see Fig. 1.3). The proton structure function F_2 and its scaling violations have been measured extensively from the HERA experiments, H1 and ZEUS [12, 13]. The combination of inclusive ep cross sections measured by the H1 and ZEUS Collaborations from all the data recorded in the first period of HERA operation resulted in the most precise extraction of the scaling violation of the structure function F_2 over a wide kinematic region [14].

1.1.5 The Longitudinal Structure Function F_L

In the quark-parton model the longitudinal part of the cross section is suppressed, since the interaction between a quark and a longitudinally polarised (virtual) photon does not conserve helicity. This is best seen in the Breit frame, the frame in which the quark is "reflected" by the interaction with the photon. In this frame the quark conserves its spin in the interaction, while reverses its direction. Extending the quark-parton model by adding gluons, helicity conservation can be retained in the interaction with a longitudinal photon (see Fig. 1.5). This leads to a violation of the Callan-Gross equation:

$$F_L(x) = F_2(x) - 2xF_1(x) \ . \tag{1.10}$$

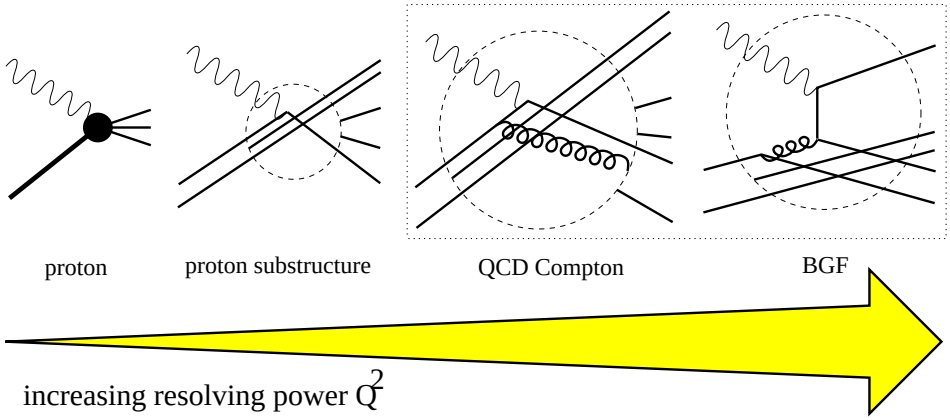

Figure 1.4: *Schematic diagram to illustrate the increase of the γ^* resolving power with Q^2.*

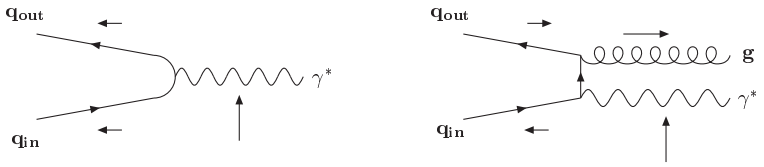

Figure 1.5: *An incoming quark in the Breit frame interacts with a longitudinally polarised photon, and subsequently flips its helicity, which is not allowed (left). Helicity conservation is preserved by adding a gluon (right). The arrows represent the spin orientation.*

The difference between F_2 and F_1 due to the longitudinal part of the cross section brings to the definition of the longitudinal structure function, F_L. From the positivity requirement of the cross sections for longitudinally (σ_L) and transversely (σ_T) polarised photons, $\sigma_L \geq 0$ and $\sigma_T \geq 0$, and from the relations between these cross sections and the structure functions F_1 and F_2 (see Eq. (1.3)), it follows that $F_2 \geq 2xF_1$ and therefore $0 \leq F_L \leq F_2$.

The unpolarised NC ep cross section in terms of F_2 and F_L then becomes:

$$\frac{d^2\sigma_{ep\to eX}}{dxdQ^2} = \frac{2\pi\alpha^2}{xQ^4} Y_+ \left[F_2\left(x, Q^2\right) - \frac{y^2}{Y_+} F_L\left(x, Q^2\right) \right] \tag{1.11}$$

where $Y_+ = 1 + (1-y)^2$. Due to the factor y^2, the structure function F_L gives a negligible contribution to the cross section at low values of y ($y \lesssim 0.5$), but becomes relevant for larger values of y.

From its nature, F_L has direct sensitivity to the gluon emission inside the proton. In the

QCD framework, F_L at leading order is given by [22, 23]:

$$F_L(x,Q^2) = \frac{\alpha_s}{4\pi} x \int_x^1 \frac{dz}{z^3} \left[\frac{16}{3} F_2(z,Q^2) + 8 \sum_q e_q^2 (1 - \frac{x}{z}) z g(z,Q^2) \right] . \tag{1.12}$$

and therefore the F_L extraction provides information on the gluon distribution inside the proton.

A direct measurement of the longitudinal structure function requires several set of DIS cross sections at fixed x and Q^2, but at different y, which from Eq. (1.1) means different s. This can be better seen once Eq. (1.11) is written in terms of the reduced cross section σ_r:

$$\sigma_r(x,Q^2;y) = \left(\frac{xQ^4}{2\pi\alpha^2 Y_+} \right) \frac{d^2\sigma_{ep}}{dxdQ^2} = F_2(x,Q^2) - \frac{y^2}{Y_+} F_L(x,Q^2) , \tag{1.13}$$

The direct measurement of F_L has been achieved at HERA by changing the proton beam energies while keeping that of the lepton beam fixed. Both the H1 and ZEUS Collaborations obtained independent results of F_L [24, 25] and a combination of the measurements from the two experiments brought to a precise and unique extraction of the longitudinal proton structure function from HERA [26].

1.1.6 DGLAP Evolution Equations and the Q^2-x Plane

The evolution with Q^2 of the structure functions, or more precisely of the quark densities, $q_i(x,Q^2)$, and of the gluon density, $g(x,Q^2)$, can be described by the Dokshitzer-Gribov-Lipatov-Altarelli-Parisi (DGLAP) coupled evolution equations [16], that consider the splitting probability of a quark into a quark and a gluon, and the annihilation probability of a gluon in a $q\bar{q}$ pair:

$$\frac{dq(x,Q^2)}{dlnQ^2} = \frac{\alpha_s}{2\pi} \int_x^1 \frac{dy}{y} \left[q(y,Q^2) P_{qq}\left(\frac{x}{y}\right) + g(y,Q^2) P_{qg}\left(\frac{x}{y}\right) \right] , \tag{1.14}$$

$$\frac{dg(x,Q^2)}{dlnQ^2} = \frac{\alpha_s}{2\pi} \int_x^1 \frac{dy}{y} \left[\sum_q q(y,Q^2) P_{gq}\left(\frac{x}{y}\right) + g(y,Q^2) P_{gg}\left(\frac{x}{y}\right) \right] , \tag{1.15}$$

where P_{qq}, P_{qg}, P_{gq} and P_{gg} are the splitting functions, whose meaning is graphically shown in Fig. 1.6.

The DGLAP equations neglect higher order contributions of the form $\alpha_s \ln 1/x$. At finite order, these terms might give non-negligible contributions at low values of x, where the evolution is dominated by the gluon cascade. The evolution in terms of $\ln 1/x$ is know as BFKL equation [17] and predicts a strong increase in the gluon density at small x, which is somehow balanced by means of recombination processes between partons. Efforts are being made to combine the DGLAP and BFKL approaches.

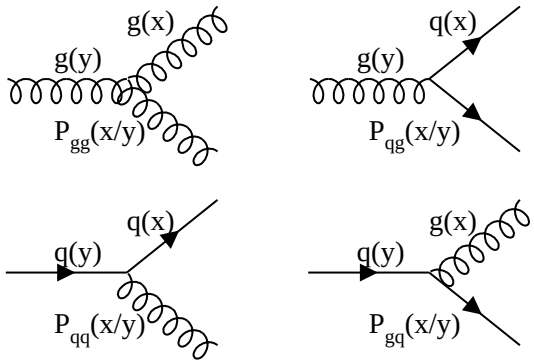

Figure 1.6: *Elementary vertexes in QCD and associated splitting functions.*

At extremely small values of x the steep rise of structure functions predicted by BFKL must stop, in order not to violate unitarity. At $x \to 0$ the probability of interactions between partons (gluons, in particular) becomes so large that they begin to recombine with each other bringing to saturation effects, thus requiring the introduction of non-perturbative corrections. The GLR equations [18] introduce a shadowing correction which slows the increase of F_2 for decreasing x.

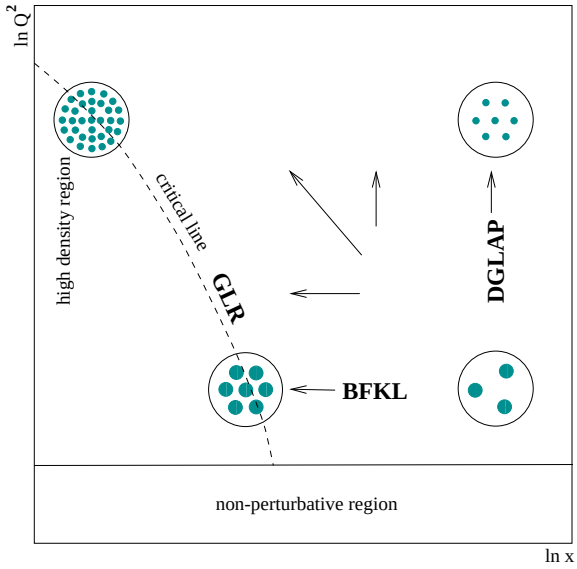

Figure 1.7: *Validity range for different evolution equations.*

On the other hand, for very low values of Q^2 ($Q^2 \lesssim 1$ GeV), the value of $\alpha_s(Q^2)$ becomes large and perturbative QCD cannot be applied. Phenomenological models, such as Regge theory [19] (see Sect. 1.2.2), are used to describe the interactions between particles.

The validity region in the Q^2-x plane for different approaches is summarized in Fig. 1.7.

1.1.7 QCD Hard Scattering Factorisation and PDFs

The basic idea behind the factorisation theorem of QCD [20] is that physical processes at very different scales do not interfere with each other, i.e. they factorize. It has been proven that in perturbation theory factorisation holds to all orders [21]. According to factorisation, the cross section for *ep* scattering can be written as the convolution of two terms: the perturbative calculable hard scattering Born cross section, $\hat{\sigma_{ei}}$, for the short-distance interaction, times the non-perturbative (and not calculable by perturbation theory) parton densities, f_i, describing the long-distance interaction with the proton structure:

$$\sigma_{ep}(x, Q^2) = \sum_i \sigma_{ei}(x, Q^2, \mu_F) \otimes f_i(x, \mu_F) \ , \tag{1.16}$$

where the sum runs over all the contributing partons i. Here, μ_F is the *factorisation scale* and represents the scale at which the perturbatively calculable hard scattering cross section is separated from the non-perturbative parton densities. A parton emitted from the incoming quark or gluon at a scale larger than μ_F is considered part of the hard interaction, while a parton emitted at a smaller scale than μ_F is considered part of the proton. The latter is absorbed into the parton density functions. Such functions are non-perturbative objects and contain the information about the structure of the proton. They are assumed to be universally valid, i.e. they do not depend on the hard process under study and need to be extracted from experimental data.

From a next-to-leading order (NLO) QCD analysis based on the combined HERA *ep* cross sections, a set of HERA parton distribution functions was obtained [14]. Predictions from HERA PDFs compared to the experimental data are shown in Fig. 1.3.

1.2 Hadronic Diffraction

The first authors to give a definition of *hadronic diffraction* were Good and Walker [27] who, in 1960, wrote: *"...a phenomenon is predicted in which a high energy particle beam undergoing diffraction scattering from a nucleus will acquire components corresponding to various products of the virtual dissociation of the incident particle... These diffraction-produced systems would have a characteristic extremely narrow distribution in transverse momentum and would have the same quantum numbers of the initial particle..."*. Figure 1.8 shows the different types of

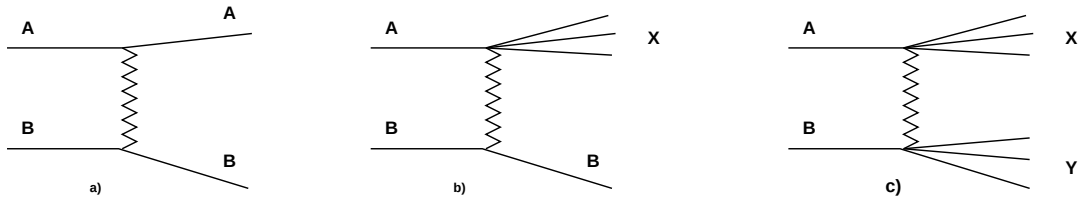

Figure 1.8: *(a) Elastic hadron-hadron scattering, (b) Single dissociation, (c) Double dissociation.*

diffractive processes in the collision of two hadrons:

1. *elastic scattering*, when exactly the same particles emerge from the collision;
2. *single diffraction*, when the energy transfer in the collision remains small, but one hadron dissociates into a multi-particle final state, preserving the quantum numbers of the initial hadron;
3. *double diffraction*, when both hadrons dissociate preserving the quantum numbers of the initial hadrons.

The remaining configurations correspond to inelastic interactions.

In the general case of the diffractive reaction $a + b \to X + Y$ no quantum numbers are exchanged. In QCD this means that no colour charge is exchanged and consistently there is no colour field between X and Y. As a consequence, these two final state systems are well separated in phase space. This is true especially for elastic or single dissociation events, where at least one of the incident particles experiences only a very small energy loss. Diffractive events are therefore characterised by a large rapidity gap (LRG) $\Delta\eta$ between the quasi-elastically scattered particle and the rest of the final state. For a particle of energy E and longitudinal momentum p_L, rapidity is defined by:

$$\mathcal{Y} = \frac{1}{2} \ln \frac{E + p_L}{E - p_L} \ , \tag{1.17}$$

which for particles with small masses is very well approximated by the pseudorapidity variable:

$$\eta = -\ln \left(\tan \frac{\theta}{2} \right) \ , \tag{1.18}$$

where θ is the polar angle measured with respect to the direction of the incident particles.

A complete and quantitative discussion on the subject can be found in [30].

1.2.1 The Analogy with Optical Diffraction

The process $a + b \to X + Y$ can be described by two independent Mandelstam variables:

$$\begin{aligned} s &= (p_a + p_b)^2 = 4(p^2 + m^2) \ , \\ t &= (p_a - p_X)^2 = (p_b - p_Y)^2 = -2p^2(1 - \cos\theta) \ , \end{aligned} \tag{1.19}$$

where p is the four-momentum in the centre-of-mass system, θ is the scattering angle, and it is assumed that particles a and b have identical mass m.

Diffractive processes are characterised by a pronounced forward peak in the differential cross section $d\sigma/dt$, which is exponentially suppressed. The small t region is parametrised according to:

$$\begin{aligned} \frac{d\sigma}{dt} &= \left(\frac{d\sigma}{dt}\right)_{t=0} \cdot e^{bt} \\ &\simeq \left(\frac{d\sigma}{dt}\right)_{t=0} \cdot \left(1 - b(p\theta)^2\right) \ , \end{aligned} \tag{1.20}$$

where b is the slope of the forward peak. The t dependence of the cross section is reminiscent of the behaviour of the optical phenomenon that occurs when a beam of light meets an obstacle or crosses a hole whose dimensions are of the same order of magnitude as its wavelenght. In optics the intensity of diffracted light at small scattering angles, θ, and large photon wave numbers, k, is given by:

$$I = I_0 \left(1 - \frac{R^2}{4}(k\theta)^2\right) \ , \tag{1.21}$$

where R is the radius of the obstacle, and $kR \simeq \sin\theta/\theta$. The comparison of Eqs. (1.20) and (1.21) gives the relation between the t-slope b and the interaction radius R:

$$b = \frac{R^2}{4} \ . \tag{1.22}$$

When we look at the plot of the t differential pp cross section (Fig. 1.9) the analogy to the optical case becomes even more explicit. The forward peak is followed by a minimum and a secondary maximum in the $|t| > 1$ GeV^2 region. It can be observed that the slope b increases slowly with s. This effect is known as shrinkage of the diffractive peak and can be interpreted as an increase of the interaction radius, since $R_{int} \sim \sqrt{ln\ s}$ for $s \to \infty$.

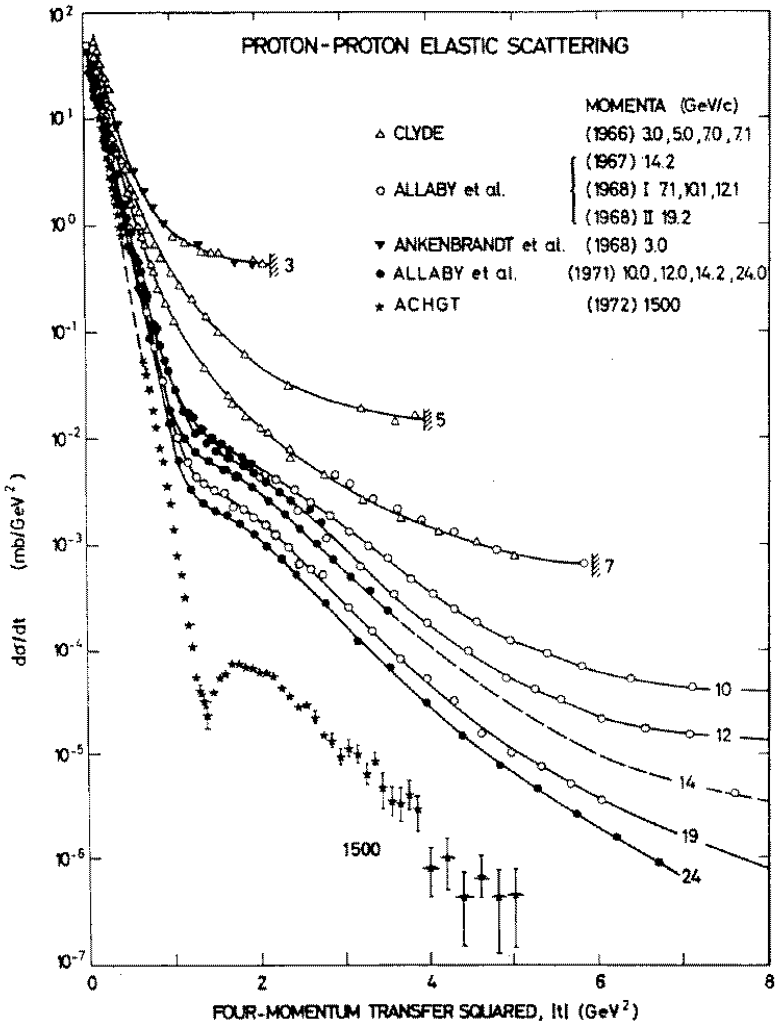

Figure 1.9: *The differential pp elastic scattering cross section $d\sigma/dt$ for different values of the centre-of-mass energy squared s [28].*

1.2.2 Regge Formalism and the Pomeron

Soft hadron-hadron interactions are well described by Regge phenomenology [29], which is based on the formalism of the analytical continuation of the scattering amplitude into the angular momentum plane. It successfully describes the energy dependence of the total hadron-hadron cross section and many properties of elastic and diffractive scattering. A review of Regge theory can be found in [19].

Regge theory belongs to the class of the so-called t-channel models. These models describe hadronic processes in terms of the t-channel exchange of "something". In the simplest version of the t-channel models, this "something" is a (virtual) *particle*. This picture, however, becomes

inapplicable at high energies, where the amplitude for the exchange of a single resonance is real and hence does not contribute to the cross section, which is proportional to the imaginary part of the scattering amplitude. Regge theory overcomes this drawback, by assuming that the strong interaction is not due to the exchange of particles with a definite spin, but rather to the exchange of a *Regge trajectory*, i.e. of a whole family of resonances with the same quantum numbers, but different spin. The large s-limit of a hadronic process is determined by the exchange of one or more Regge trajectories in the t-channel. Adopting a particle physics language, Regge trajectories are often called *reggeons* (*IR*).

All exchanged particles form linear trajectories in the J-m^2 plane, where J is the spin and m is the mass of the particle. The Chew-Frautschi plot [31] in Fig. 1.10 shows a few exemplary Regge trajectories. The continuation of a trajectory to negative values of m^2 leads to a parametrisation in terms of the square of the four momentum transfer, t:

$$\alpha(t) = \alpha_0 + \alpha' t \ , \tag{1.23}$$

where α_0 is the intercept and α' is the slope of the trajectory. The lightest particle on a trajectory gives the name to the trajectory. For most of the trajectories the slope is close to 1 GeV^2. The intercept of Regge trajectories for known particles is within the range 0-0.5 (for example: $\alpha_\pi \approx 0$, $\alpha_\rho \approx 0.5$).

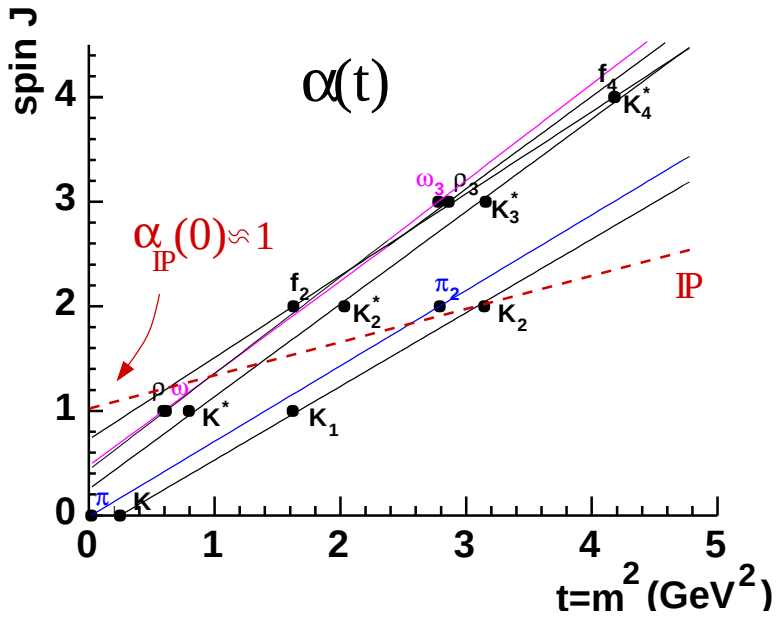

Figure 1.10: *Spin versus mass squared for different mesons. Straight lines are the result of a linear fit and correspond to Regge trajectories.*

In the high energy limit, $s \to \infty$, and at fixed t the scattering amplitude for each Regge trajectory can be written as

$$A(s,t) \overset{s\to\infty}{\longrightarrow} \beta(t) \left(\frac{s}{s_0}\right)^{\alpha(t)} , \tag{1.24}$$

where $s_0 \simeq 1$ GeV^2 is the hadronic mass scale. Then the cross section of the elastic scattering process $ab \to ab$ can be expressed as:

$$\frac{d\sigma}{dt} \propto \frac{1}{s^2}|A(s,t)|^2 \propto F(\beta(t)) \left(\frac{s}{s_0}\right)^{2\alpha(t)-2} , \tag{1.25}$$

where in this case $\alpha(t)$ is the leading trajectory exchanged in elastic scattering, that is the trajectory with the largest real part, whose contribution to the exponent of s is therefore dominant. The s-dependence of the slope b comes from the comparison to Eq. (1.20):

$$b = b_0 + 2\alpha' \ln\left(\frac{s}{s_0}\right) , \tag{1.26}$$

which quantifies the shrinkage of the diffractive peak.

Using the optical theorem, which relates the total cross section to the elastic scattering amplitude, the energy dependence of total hadron-hadron cross sections is given by

$$\sigma_{tot} \sim \frac{1}{s}\mathrm{Im}[A(s,t=0)] \propto \left(\frac{s}{s_0}\right)^{\alpha_0-1} . \tag{1.27}$$

Different processes will, in general, receive contribution from different trajectories. The contributions to a given reaction depend on the quantum numbers that this reaction exhibits in the crossed channel. The total cross sections for different hadron-hadron interactions, together with those for γp and $\gamma\gamma$ interactions (see Sect. 1.3.1), are plotted as a function of $\sqrt{s}$ in Fig. 1.11. At high energies, a similar energy dependence for these processes can be seen. The fall-off at low energies in Fig. 1.11 can be explained by the exchange of Regge trajectories corresponding to known particles. The slowly increasing cross section at high energies requires a Regge trajectory with $\alpha_0 \gtrsim 1$, while all known trajectories interpolating existing particles or resonances have an intercept $\alpha_0 \lesssim 0.5$. In order to describe the data in the Regge framework, the existence of a new trajectory has to be postulated. After I.Ya. Pomeranchuk, the so-called *pomeron (IP) trajectory* was introduced [31, 33] with $\alpha_0 \approx 1$ (see Fig. 1.10). The pomeron trajectory does not correspond to any known particle and has the quantum numbers of the vacuum. Thus, the pomeron is the dominant trajectory in the elastic and diffractive processes at high energies.

Total hadron-hadron cross sections are successfully described by the sum of reggeon and pomeron contributions. Donnachie and Landshoff [34] fitted all available hadronic data to a parametrisation of the form

$$\sigma_{tot} = As^{\alpha_{I\!R}-1} + Bs^{\alpha_{I\!P}-1} . \tag{1.28}$$

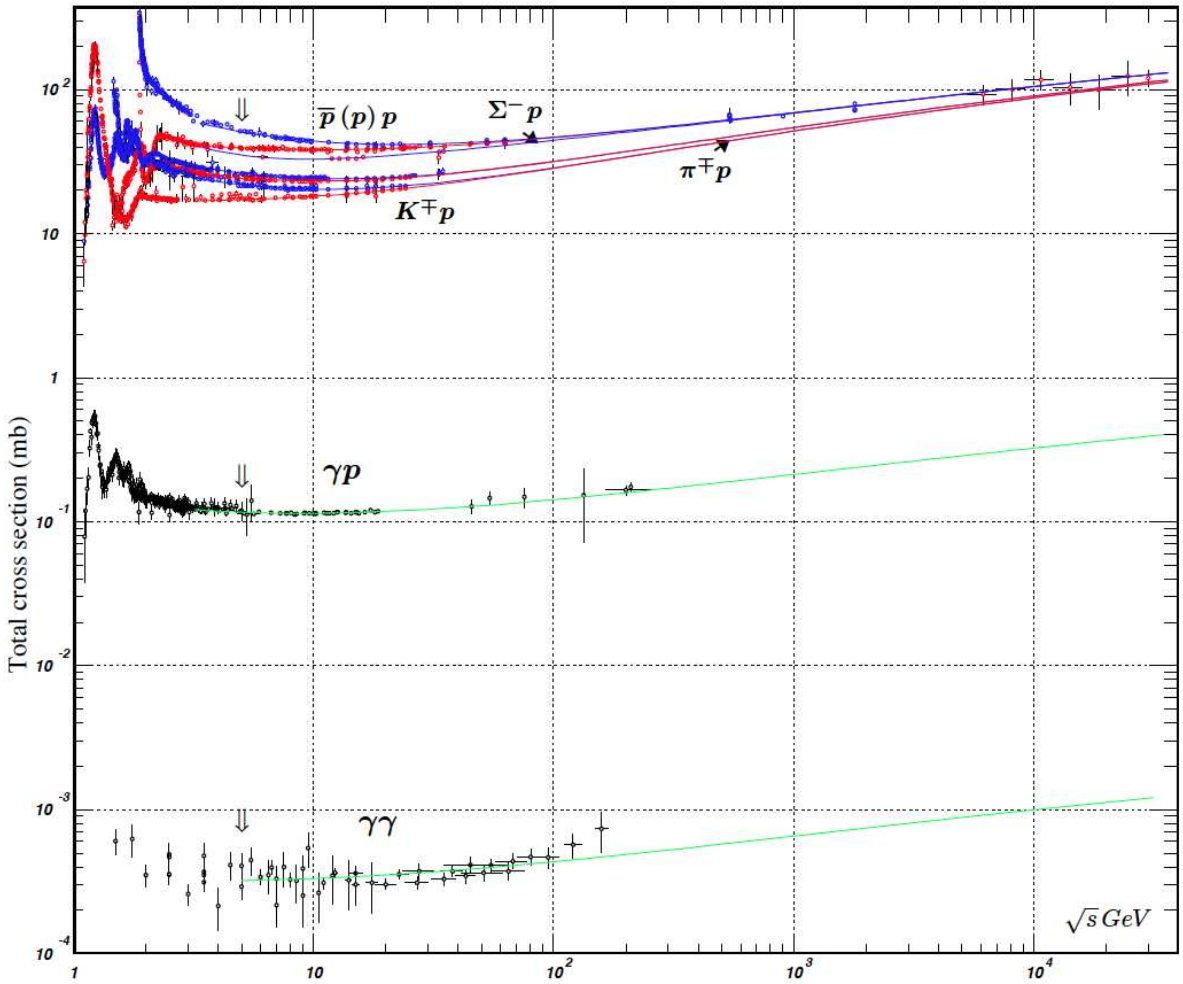

Figure 1.11: *The total cross sections for hadron-hadron, γp, and $\gamma\gamma$ scattering as a function of $\sqrt{s}$ [32].*

The parameters A and B depend on the process whereas $\alpha_{I\!R}$ and $\alpha_{I\!P}$ were fitted globally. The first term in Eq. (1.28) corresponds to the reggeon exchange, responsible for the decrease of the cross section at low energies, while the second one represents the pomeron contribution which dominates at high energies. The results of the fits are: $\alpha_{I\!R} \approx 0.55$, $\alpha_{I\!P} \approx 1.1$.
The following parametrisation of the pomeron trajectory was obtained [35]:

$$\alpha(t) = 1.096 + 0.25t \ , \tag{1.29}$$

where t is expressed in GeV^2. This trajectory, which describes the weak energy dependence of the total cross section, is also known as *soft pomeron*.

1.2.3 Hard Diffraction

Regge theory gives a description of diffraction within a non-perturbative, phenomenological approach, suitable for processes dominated by peripheral, long-range interactions, with small transverse momenta. Regge formalism, however, provides no insight into the microscopic structure of the diffractive exchange. When it was realized that QCD was more than a simple candidate to the theory of hadronic interactions, the problem arose to interpret the pomeron in terms of the QCD degrees of freedom, quarks and gluons. Low and Nussinov [36, 37] proposed to picture pomeron exchange as a *two-gluon exchange*. Two is the minimal number of gluons needed to reproduce the vacuum quantum numbers. This general picture represents the Born approximation of the pomeron in QCD. In a more complete description, the QCD pomeron emerges as a gluon ladder in a colour-singlet configuration [38]. The properties of this ladder depend on the energy and scales involved, implying its non-universal character. The sum at all orders of the gluon ladder diagrams results in a pomeron much more complicated than a single Regge trajectory, called *hard* or *BFKL pomeron* [39].

In 1985, Ingelman and Schlein [40] suggested to investigate diffractive production of high-p_T jets as a way to probe the partonic structure of the pomeron. The first observation of a hard scale in diffractive processes was given by the UA8 Collaboration in $p\bar{p}$ collisions at the S$p\bar{p}$S collider [41]. In a sub-sample of diffractive events, jets with a high transverse energy were found (see Fig. 1.12). However, only with subsequent data from ep collisions at HERA, $p\bar{p}$ collisions at Tevatron and the recent pp interactions at the LHC a clearer understanding of diffraction in terms of QCD has been achieved.

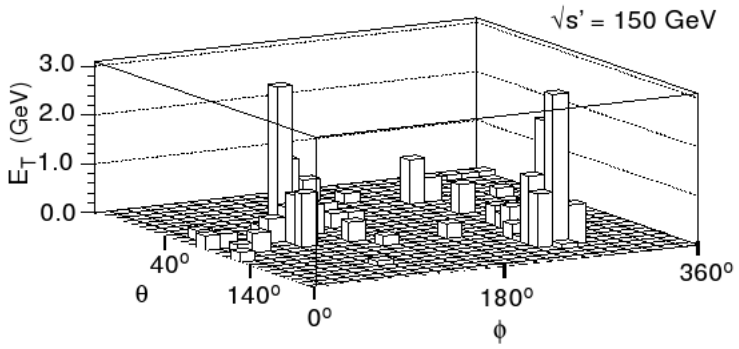

Figure 1.12: *Raw energy display from the UA8 experiment. The energy distribution in the calorimeter (θ vs. ϕ projection) for an event with a detected dijet system in coincidence with a leading proton is shown. Each jet has* $E_T^{jet} > 8$ GeV.

1.3 Diffraction in Deep Inelastic *ep* Scattering

The final state of a standard *ep* DIS event consists of the scattered electron, the current jet, originating from the parton struck by the virtual photon, and the proton debris. The gap in rapidity, $\Delta\eta$, between the struck parton and the proton remnant is exponentially suppressed due to parton radiation in the resulting QCD colour field (see Fig 1.13a), so that [30]:

$$\frac{dN}{d\Delta\eta} \sim e^{-\Delta\eta}\ (non{-}diffractive\ DIS)\ . \tag{1.30}$$

However, soon after the HERA experiments started, a different type of hadronic final state was observed. Events in which only the scattered electron and particles in the direction of the struck parton were detected, without any evidence of the proton remnant in the detector (see Fig 1.13b) and therefore with a large gap in the rapidity distribution of particles in the forward (i.e. the proton) direction. The $\Delta\eta$ distribution for such events was of the type:

$$\frac{dN}{d\Delta\eta} \sim const\ (diffractive\ DIS)\ . \tag{1.31}$$

This signature was attributed to a diffractive exchange between the photon and the proton, since a colour singlet exchange strongly suppresses the parton radiation between the current jet and the proton remnant, which escapes into the beampipe carrying a large fraction of its incoming momentum.

The appearance of such large rapidity-gap events in NC DIS was reported by the ZEUS [42] and H1 [43] Collaborations based on the first data detected at HERA. It was a surprise that the rate

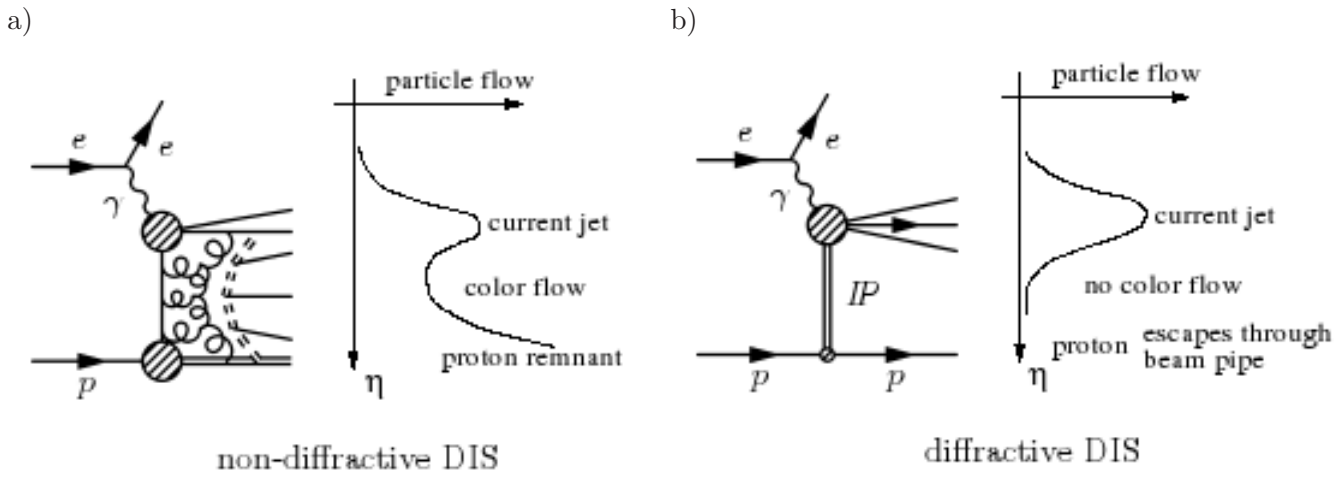

Figure 1.13: *Event topologies and particle flow diagrams for a non-diffractive deep inelastic scattering event (a) and for a diffractive DIS event (b).*

of these events was as much as 10% of the total, even at high Q^2. In diffractive deep inelastic scattering (DDIS) the photon virtuality Q^2 provides a variable hard scale. DIS offers therefore a unique, well-controlled environment in which to study the QCD properties of diffraction.

1.3.1 Hadronic Behaviour of the Photon

Diffraction is a typical hadronic process while *ep* scattering at HERA is an electro-weak reaction, where the electron radiates a virtual photon, which then interacts with the proton. To understand how diffractive events can occur at HERA, it is useful to look at *ep* scattering in a frame where the virtual photon moves very fast (for instance in the proton rest frame, where the γ^* has a momentum of up to about 50 TeV at HERA). The virtual photon can fluctuate into a quark-antiquark pair, whose quantum numbers are the same as those of the photon. Because of its large Lorentz boost, this virtual pair has a lifetime much longer than a typical strong interaction time. In other words, the photon fluctuates into a pair long before the collision, and it is the pair which interacts with the proton. This pair is a small colour dipole (see Sect. 1.3.4.2). Since the interaction between the pair and the proton is mediated by the strong interaction, diffractive events are possible. Therefore, the scattering of a virtual photon and a proton can be treated within the formalism of hadron-hadron collisions [44].

By analogy to the hadron-hadron case, the $\gamma^* p$ diffractive scattering can be classified into four processes, depending on the final state (see Fig. 1.14): the photon can fluctuate into a vector meson (ρ, ω, ϕ, ...) with the quantum numbers of the photon, where the proton either

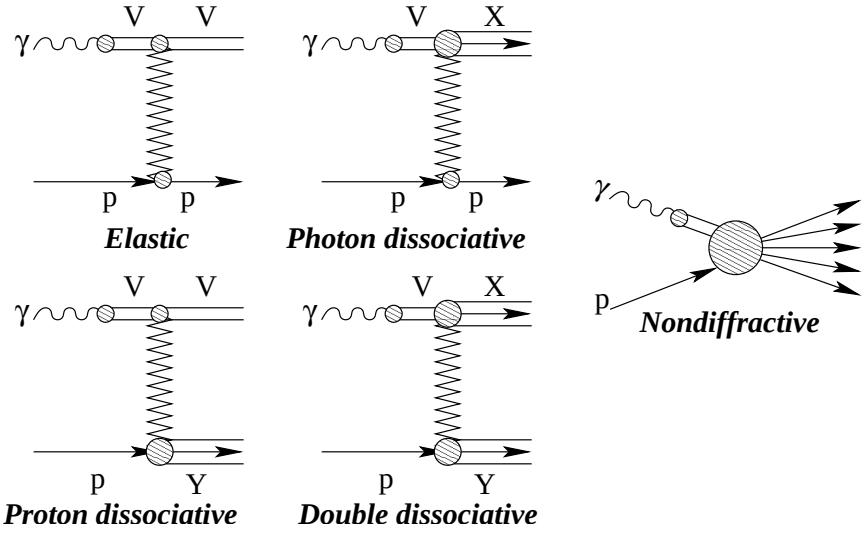

Figure 1.14: *Diagrams illustrating the classification of diffractive processes in $\gamma^* p$ scattering. For comparison a diagram for a non-diffractive process is also shown.*

stays intact (*elastic vector meson production*) or dissociates into a system Y (*proton-dissociative vector meson production*). The photon can also dissociate into a high-mass system X. In this case if the proton remains intact the process is called *single diffractive dissociation* (SD) while if it dissociates into a Y system the process is called *double diffractive dissociation* (DD).

1.3.2 Kinematics in Diffractive DIS

The description of the diffractive DIS process (Fig. 1.15)

$$e(k) + p(P) \to e'(k') + p'(P') + X \tag{1.32}$$

requires additional variables besides the conventional DIS variables introduced in Sect. 1.1.1.

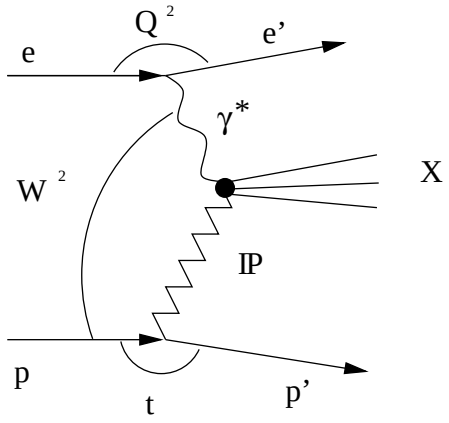

Figure 1.15: *Diagram of a diffractive DIS event where the virtual photon dissociates.*

The four momentum transfer squared at the proton vertex is defined as:

$$t = (P - P')^2 \ , \tag{1.33}$$

where P and P' are the four-momenta of the incoming and outgoing proton, respectively.

It is convenient to define and use two invariant quantities:

$$x_{I\!P} = \frac{(P - P') \cdot q}{p \cdot q} = \frac{M_X^2 + Q^2 - t}{W^2 + Q^2 - m_p^2} \ , \tag{1.34}$$

$$\beta = \frac{Q^2}{2(P - P') \cdot q} = \frac{x}{x_{I\!P}} = \frac{Q^2}{M_X^2 + Q^2 - t} \ . \tag{1.35}$$

In a model with a pomeron exchanged in the t-channel, $x_{I\!P}$ is the fraction of the proton momentum carried by the pomeron, while β corresponds to the momentum fraction of the struck

quark within the pomeron. The variables $x_{I\!P}$ and β are related to the Bjorken scaling variable x through:

$$x = \beta x_{I\!P} \ . \tag{1.36}$$

By virtue of their definitions, $x_{I\!P}$ and β have a limited range of allowed values between 0 and 1. M_X denotes the mass of the hadronic system X, which results from the virtual photon dissociation. It may happen that the proton does not remain intact, but dissociates into an hadronic system Y, with mass M_Y.

1.3.3 The Diffractive DIS Cross Section

The diffractive cross section can be expressed in terms of the diffractive four-fold structure functions, which are defined by analogy to the inclusive structure functions of the proton, Eq. (1.11):

$$\frac{d^4\sigma_{ep}^{diff}}{d\beta dQ^2 dx_{I\!P} dt} = \frac{2\pi\alpha^2}{\beta Q^4} Y_+ \left[F_2^{D(4)}(\beta, Q^2, x_{I\!P}, t) - \frac{y^2}{Y_+} F_L^{D(4)}(\beta, Q^2, x_{I\!P}, t) \right] \ , \tag{1.37}$$

where, again, $Y_+ = (1 + (1-y)^2)$ and $F_2^{D(4)}$ ($F_L^{D(4)}$) can be interpreted as the proton structure function F_2 (F_L) when a fast proton is present in the final state.

It is also worthwhile to introduce the three-fold structure function $F_2^{D(3)}$, where an integration over t of the previous equation is performed:

$$\frac{d^3\sigma_{ep}^{diff}}{d\beta dQ^2 dx_{I\!P}} = \int \frac{d^4\sigma_{ep}^{diff}}{d\beta dQ^2 dx_{I\!P} dt} dt = \frac{2\pi\alpha^2}{\beta Q^4} Y_+ \left[F_2^{D(3)}(\beta, Q^2, x_{I\!P}) - \frac{y^2}{Y_+} F_L^{D(3)}(\beta, Q^2, x_{I\!P}) \right] \ . \tag{1.38}$$

The results of diffractive measurements are often presented in terms of the NC diffractive reduced cross section $\sigma_r^{D(3)}$:

$$\sigma_r^{D(3)}(\beta, Q^2, x_{I\!P}) = F_2^{D(3)}(\beta, Q^2, x_{I\!P}) - \frac{y^2}{Y_+} F_L^{D(3)}(\beta, Q^2, x_{I\!P}) \ , \tag{1.39}$$

such that $\sigma_r^{D(3)} \simeq F_2^{D(3)}$ in a wide range of the experimentally accessible kinematic region, in particular for $y \lesssim 0.5$.

The diffractive structure function F_2^D has been measured extensively by the H1 and ZEUS Collaborations at HERA [45–53]. Figure 1.16 shows a comparison between ZEUS data [51] collected during the first HERA running period and H1 data [49] from the whole HERA data taking period. In Figs. 1.17 and 1.18 the dependence of the diffractive cross section as a function of $x_{I\!P}$ and β, respectively, is also shown.

As in the inclusive case (see Sect. 1.1.5), measuring $\sigma_r^{D(3)}$ at fixed β, Q^2, $x_{I\!P}$ and different values of y, i.e. different centre-of-mass energies $\sqrt{s}$, makes possible the direct extraction of the longitudinal diffractive structure function, F_L^D. A first direct measurement of F_L^D has been

recently published by the H1 Collaboration [54]. It is shown in Fig. 1.19 as a function of β, at fixed Q^2 and $x_{I\!P}$ values.

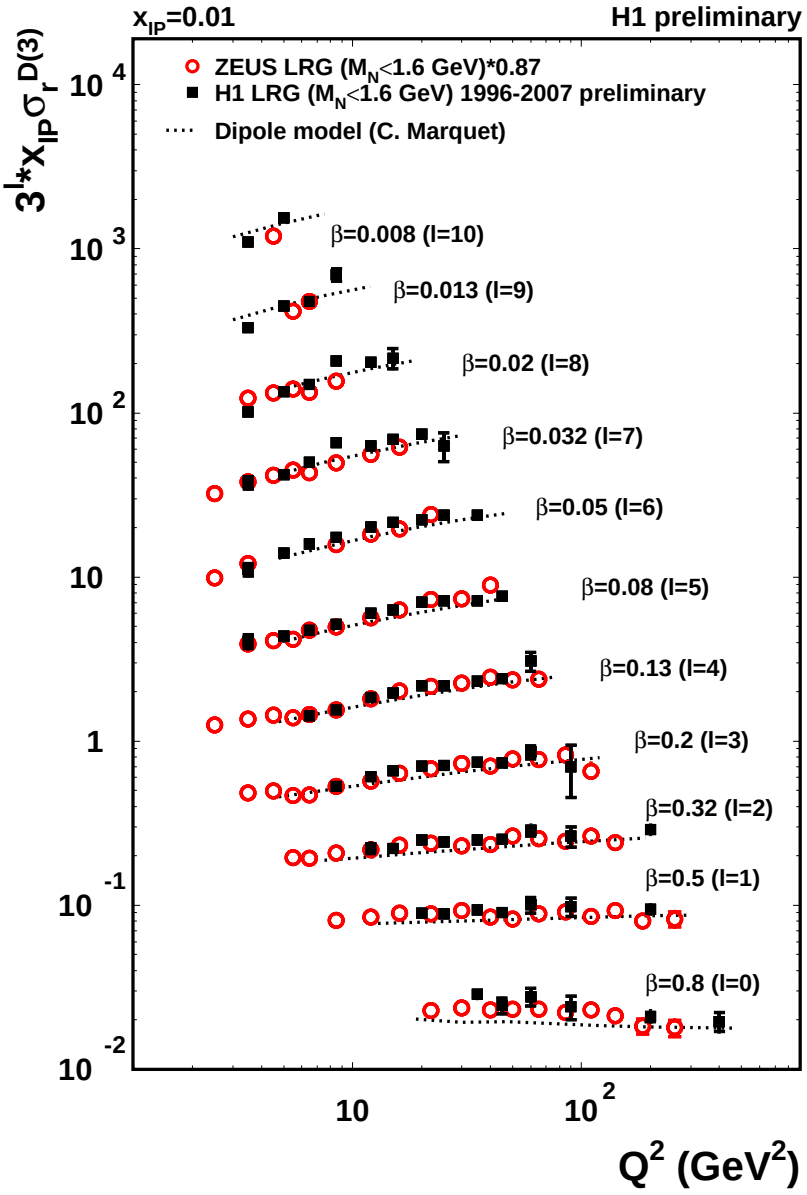

Figure 1.16: *The Q^2 dependence of the diffractive reduced cross section, multiplied by $x_{I\!P}$, for fixed β and at $x_{I\!P} = 0.01$. The H1 data [49] are compared to the ZEUS results [51].*

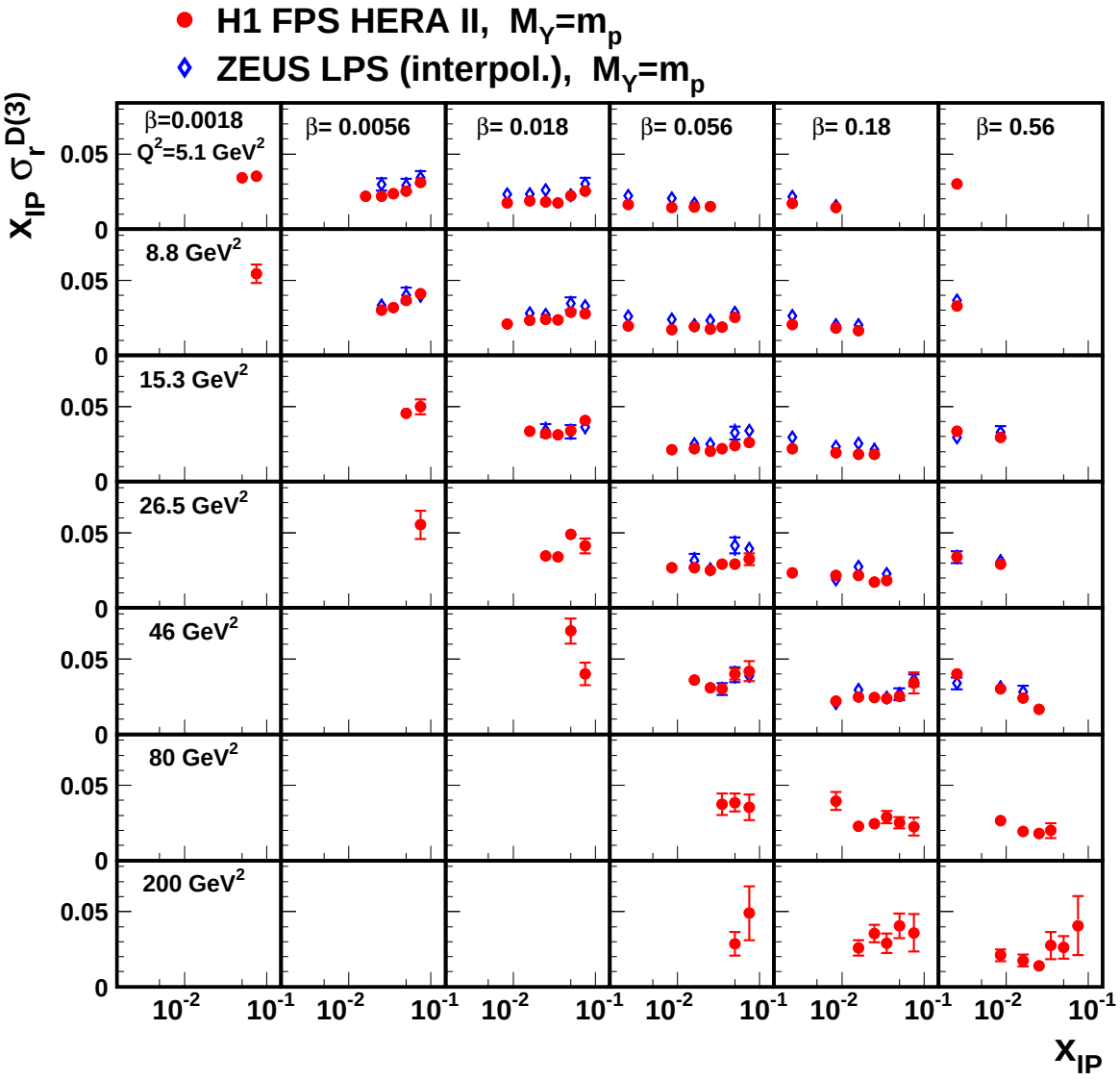

Figure 1.17: *The diffractive reduced cross section $x_{I\!P}\sigma_r^{D(3)}$ as a function of $x_{I\!P}$ for different values of β and Q^2. H1 data [46] are compared to the ZEUS results [51] and to dipole model predictions [55].*

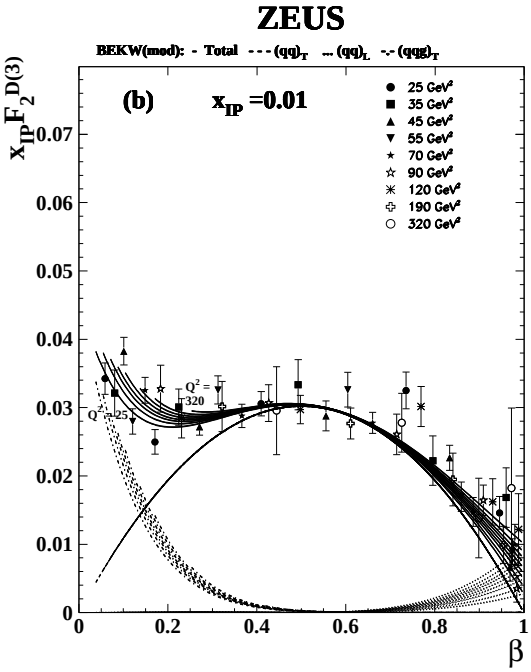

Figure 1.18: *The β dependence of the ZEUS diffractive reduced cross section [53], multiplied by $x_{I\!P}$, for different Q^2 values and at $x_{I\!P} = 0.01$ (in the kinematic region covered by the measurement, $\sigma_r^D \sim F_2^D$).*

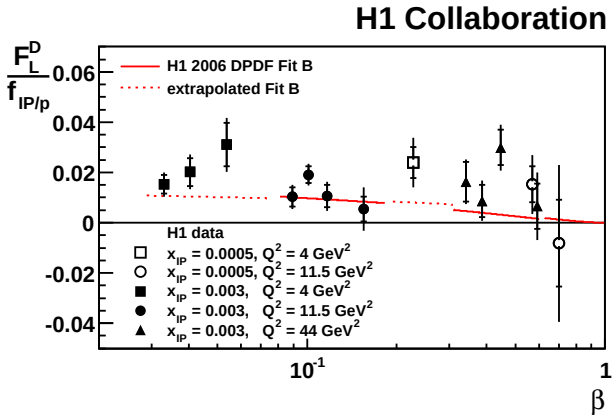

Figure 1.19: *The diffractive longitudinal structure function F_L^D measured by H1 [54], divided by a parametrisation of the $x_{I\!P}$ dependence of the reduced cross section $f_{I\!P/p}$ [48], as a function of β at the indicated values of Q^2 and $x_{I\!P}$.*

1.3.4 Theoretical Models

Several models have been proposed to explain diffractive interactions at high Q^2 in ep scattering. There are essentially two main approaches:

1. In the Breit reference frame: pomeron with a partonic structure (quark and gluon densities).
2. In the rest frame of the proton: pomeron described as a two-gluon exchange.

In the following a brief description of the main aspects of these models is given.

1.3.4.1 Partonic Structure of the Pomeron

QCD Factorisation It has been proven in perturbative QCD [56, 57] that, similarly to what happens in inclusive DIS, a factorisation theorem holds for the diffractive cross section. This can thus be written in terms of diffractive parton distribution functions (DPDFs) convoluted with the hard scattering cross sections:

$$\sigma_{ep}^{diff}(x, Q^2, x_{I\!P}, t) = \sum_i f_i^D(x, Q^2, x_{I\!P}, t) \otimes \sigma_{ei}(x, Q^2) \tag{1.40}$$

The DPDFs $f_i^D(x, Q^2, x_{I\!P}, t)$ represent the probability to find, in a proton, a parton of type i carrying a momentum fraction x, under the condition that the proton remains intact, except for a small momentum transfer quantified by $x_{I\!P}$ and t. The partonic cross sections $\sigma_{ei}(x, Q^2)$ are the same as for inclusive DIS. Thus, the only difference between DIS and DDIS resides in the parton distributions.

It is important to notice that it has been demonstrated by Collins [56] that factorisation is violated in hadron-hadron diffractive scattering. Therefore, in order to use the diffractive parton densities extracted from DDIS to make predictions for diffractive processes at hadron colliders, other effects need to be considered, such as the survival probability of a rapidity gap [58].

Regge Factorisation The Regge factorisation hypotesis makes the extra assumption that the diffractive PDFs do not depend (other than in normalisation) on $x_{I\!P}$ and t. This leads to a formalism where the diffractive parton densities can be separated into two terms, which represent the pomeron flux and the hard scattering of the photon with the pomeron. The first one involves the $x_{I\!P}$ and t variables, the latter is described by β and Q^2 only. The Regge factorisation scheme is illustrated in Fig. 1.20 and can be formulated as:

$$f_i^D(x, Q^2, x_{I\!P}, t) = f_{I\!P/p}(x_{I\!P}, t) \cdot f_{i/I\!P}(\beta = x/x_{I\!P}, Q^2) \ , \tag{1.41}$$

where $f_{I\!P/p}$ is the pomeron flux from the proton and $f_{i/I\!P}$ represent the pomeron PDFs, i.e. the probability of finding a parton i with momentum fraction β at a given Q^2 in the pomeron. The

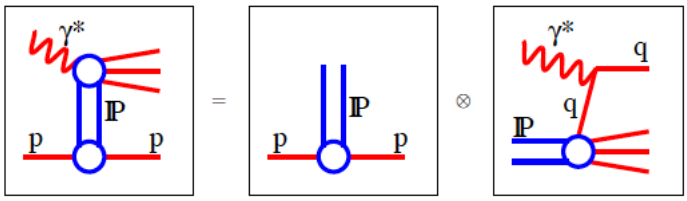

Figure 1.20: *Sketch of Regge factorisation. The diffractive exchange interaction is factorised into two parts: a soft scale flux component, and a hard scale scattering process.*

pomeron flux gives the probability that a pomeron with specific values $x_{I\!P}$ and t is emitted by to the proton, and has the form:

$$f_{I\!P/p} = \frac{1}{16\pi^2}|g_{I\!P}(t)|^2 x_{I\!P}^{1-2\alpha_{I\!P}(t)} \tag{1.42}$$

where $g_{I\!P}(t)$ is the pomeron coupling to the proton.

The scales for the processes described by the two terms are different. At the proton vertex, the relevant scale is t, which is small in the diffractive interactions. Any dynamics occurring here will appear frozen when viewed from the hard scattering vertex, where the relevant scale is Q^2. Therefore, thanks to Regge factorisation, the perturbative scale of the process is decoupled from the $x_{I\!P}$ behaviour, that is genuinely non-perturbative and can only be described by a phenomenological parametrisation. Indeed, it must be stressed that since the pomeron is *not* a particle, the separation of the flux from the pomeron cross section is quite arbitrary, and the normalisation of the pomeron flux is ambiguous.

Experimentally, the Regge, or proton-vertex, factorisation holds to a good approximation, as shown in Fig. 1.17. The $x_{I\!P}$ dependence of the diffractive cross section multiplied by $x_{I\!P}$ is roughly flat for all β and Q^2 values, implying that the reduced cross section approximately follows a $\sigma_r^{D(3)} \propto 1/x_{I\!P}$ dependence. The variations in the $x_{I\!P}$ dependence as β changes are expected from the interplay between the leading pomeron and a sub-leading trajectory exchange (i.e. a reggeon).

Diffractive PDFs In analogy with the inclusive DIS case, the diffractive structure functions are related to the diffractive parton distribution functions (DPDFs), and their dependence on the scale Q^2 is given by the DGLAP evolution equations, see Eqs. (1.15). Thus, an experimental determination of these DPDFs can give an insight into the partonic structure of a proton undergoing a diffractive interaction. In Fig. 1.16 the Q^2 dependence of the diffractive reduced cross sections measured by the H1 and ZEUS experiments is shown. The cross section increases with Q^2 for all β values, except the highest (up to 0.5). This is reminiscent of the scaling violations of F_2 in the inclusive case, except that F_2 rises with Q^2 only for $x \lesssim 0.2$ and the

scaling violations become negative at higher x (see Fig. 1.3). In the proton, negative scaling violations reflect the presence of valence quarks which radiate gluons, while positive scaling violations are due to the increase of the sea quark and gluon densities as the proton is probed with higher resolution. The F_2^D data thus suggest that the partons resolved in diffractive events are predominantly gluons. The direct measurement of the longitudinal diffractive structure function, shown in Fig. 1.19, provides an independent tool to verify the understanding of the underlying dynamics of diffraction up to NLO in QCD, and to test the DPDFs, notably the gluon density.

The diffractive parton distribution functions have been extracted from QCD fits to diffractive DIS data at HERA following the formalism introduced so far, and assuming both QCD and Regge factorisation. Diffractive quark and gluon densities extracted from the ZEUS DDIS data [59] are shown in Fig. 1.21. The ZEUS DPDF SJ parametrisation have been obtained from a NLO DGLAP QCD fit to the ZEUS inclusive diffractive data [51] and diffractive DIS dijet data [60], as dijet processes are particularly sensitive to the density of gluons in the diffractive exchange. The quark densities are well constrained by the inclusive data; the inclusion of the dijet data, allowed within the QCD factorisation framework, provides an additional constraint on the gluons, resulting in a determination of both the quark and gluon density with good accuracy. The comparison with ZEUS DPDF C fit, based on inclusive diffractive data

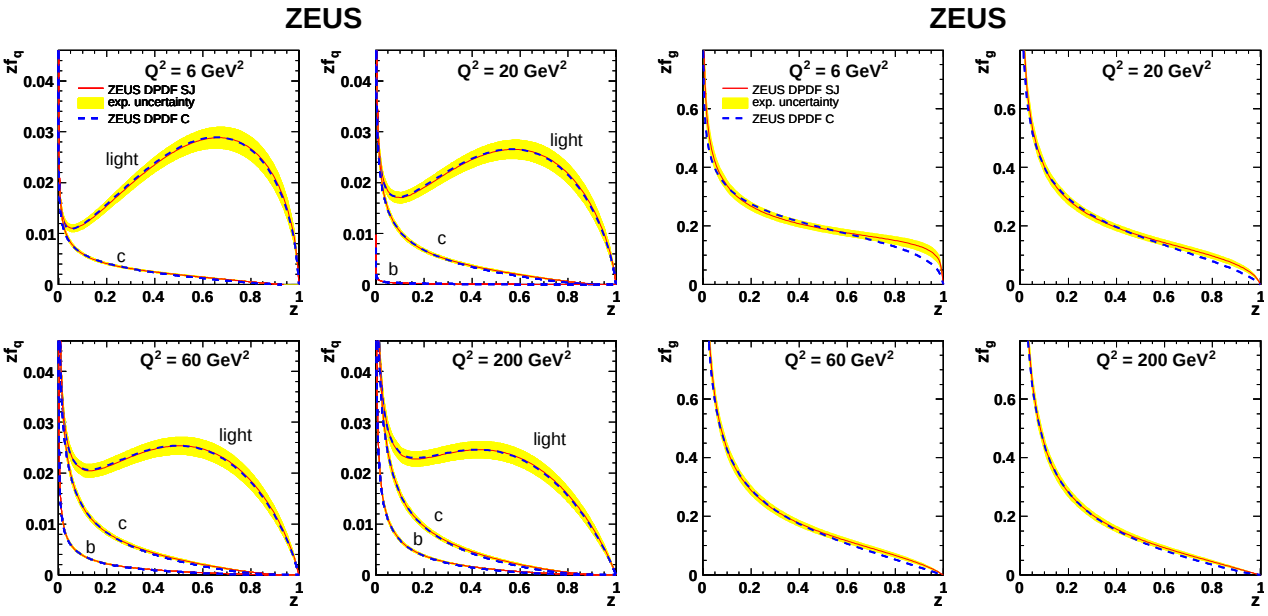

Figure 1.21: *ZEUS singlet (left) and gluon (right) densities [59] as a function of the momentum fraction, z, for four different values of Q^2. The shaded error bands represent the experimental uncertainty.*

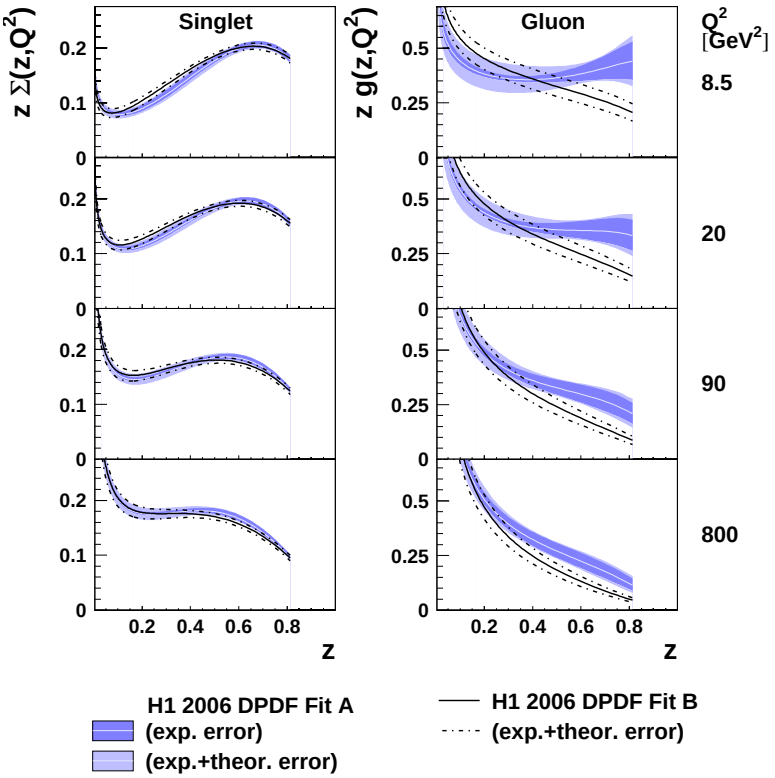

Figure 1.22: *H1 singlet (left) and gluon (right) densities [48] as a function of the momentum fraction, z, for four different values of Q^2. The shaded error bands represent the experimental+theoretical uncertainty.*

only and obtained from a different input parametrisation of the gluon density, shows a good consistency in the whole phase space. Two different diffractive PDF parametrisations from a NLO DGLAP QCD fit to the H1 inclusive diffractive data [48] are also shown in Fig. 1.22, based on different assumption on the input free parameters which determine the quark singlet and gluon distributions. The H1 2006 DPDF Fit B better reproduces diffractive DIS dijet results. The main difference between the H1 and ZEUS DPDFs extraction, other than the different input data sets, is the treatment of the heavy quark contributions. In Fig. 1.23, a comparison between predictions from ZEUS DPDF SJ and H1 2006 DPDF Fit B, is shown compared to the ZEUS reduced diffractive cross section as a function of Q^2 for fixed β and $x_{I\!P}$. At higher β and where the predictions are extrapolated the agreement worsens. These features reflect the degree of consistency between the H1 and ZEUS data, visible for e.g. from Fig. 1.16, and suggest the need to extract a common set of HERA diffractive PDFs, once a combined set of HERA diffractive cross sections will be released.

The interpretation of the diffractive parton densities as the probability of finding, inside

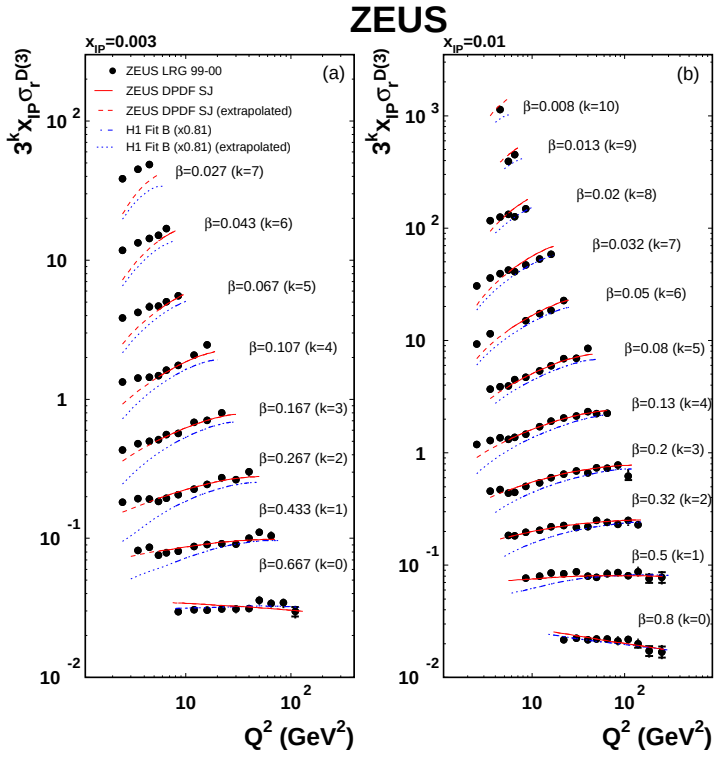

Figure 1.23: *The fit ZEUS DPDF SJ [59] (continuous line) and H1 Fit B [48] (dashed dotted lines) compared to the ZEUS data [51] at (a) $x_{I\!P} = 0.003$ and (b) $x_{I\!P} = 0.01$ as a function of Q^2 for different β values. The dashed (dotted) lines represent the DGLAP extrapolation beyond the ZEUS (H1) fitted region.*

the pomeron, a parton with momentum fraction β, makes sense only as far as it is possible to specify unambiguously the probability of finding a pomeron in the proton (i.e. the pomeron flux), and assume the pomeron to be a real particle. Since this is not the case, the whole picture must be taken as a purely phenomenological one. A more rigorous approach would be based on the direct extraction of the 4-fold differential partonic distribution functions $f_i^D(x, Q^2, x_{I\!P}, t)$, but this procedure is limited by the low statistics of $\sigma_r^{D(4)}$ data. However, the precise results of the QCD based fit to $f_i^D(x/x_{I\!P}, Q^2)$ and the good description of diffractive DIS data allow the usage of the Regge assumption on the DPDFs extraction.

1.3.4.2 Colour Dipole Models

A complementary approach to describe diffractive DIS is offered by the colour dipole models. Seen in the proton rest frame, the photon fluctuates into different hadronic states, the

leading contributions being a $q\bar{q}$ pair and a $q\bar{q}$g system. The modelling of the interaction between the proton and the $q\bar{q}$ fluctuation of the photon was first proposed by Nikolaev and Zakharov [61]. In [62] this concept was extended to more complicated hadronic states. The wave function of the photon can be thus expressed as:

$$|\gamma>=|\gamma>_{bare}+|q\bar{q}>+|q\bar{q}g>+.... \tag{1.43}$$

According to this model, the diffractive cross section is proportional to the transverse size ρ of the fluctuation and to the gluon distribution G in the proton [63]:

$$\sigma \propto \alpha_s^2 \rho^2 x G(x, q_{eff}^2), \tag{1.44}$$

where ρ is inversely proportional to the effective scale of the $\gamma^* p$ interaction, q_{eff}^2, namely a linear combination of Q^2, the mass squared of the produced quarks and t. The fact that the cross section decreases at small values of ρ reflects the fact that the effective colour charge of a $q\bar{q}$ pair is small due to screening of one parton by the other. This phenomenon, described by (1.44), is known as *colour transparency*.

The advantage with respect to diffraction in hadron-hadron collisions is that by varying q_{eff}^2 one modifies the dimension of the incoming hadronic system: when the size is small enough, the coupling constant of the strong interaction becomes small and we enter the pQCD regime. The interaction with the proton proceeds at leading order through the exchange of two gluons (i.e. a pomeron), as shown in Fig. 1.24. Many models have been proposed, which differ in the way the two-gluon exchange is handled in QCD.

Common to this approach is the prediction of a dominant contribution of the longitudinal photons in the high β region, while the transverse polarized photons dominate the intermediate and low β region, as shown in Fig. 1.18, where the low β region (i.e. high M_X) is populated by the $q\bar{q}g$ configurations of the photon.

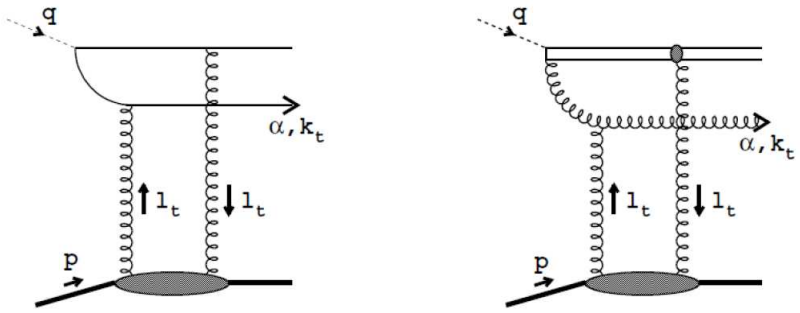

Figure 1.24: *Diagram describing the fluctuation $\gamma^* \to q\bar{q}$ (left) or $q\bar{q}g$ (right) and subsequent interaction with the proton through two gluon exchange.*

The saturation model developed by Golec-Biernat and Wüsthoff [64] is related to the color dipole models. It considers saturation effects occurring when the photon wavelenght $1/Q$ reaches the size of the proton at small Q^2. A second kind of saturation appears in the low x region where the parton density is very high and the recombination effects limit a further growth of the density. A simple ansatz for the dipole-proton cross section $\hat{\sigma}$ is made:

$$\hat{\sigma} = \sigma_0\{1 - exp[-r^2/(4R_0^2(x))]\} \ , \tag{1.45}$$

where r denotes the transverse $q\bar{q}$ separation, $R_0(x)$ is a x dependent saturation scale, $R_0^2(x) = (x/x_0)^\lambda$ in GeV^{-2}, and σ_0, x_0 and λ are free parameters that need to be determined from fits to total $\gamma^* p$ cross section.

Chapter 2

The ZEUS detector at HERA

2.1 The HERA Accelerator

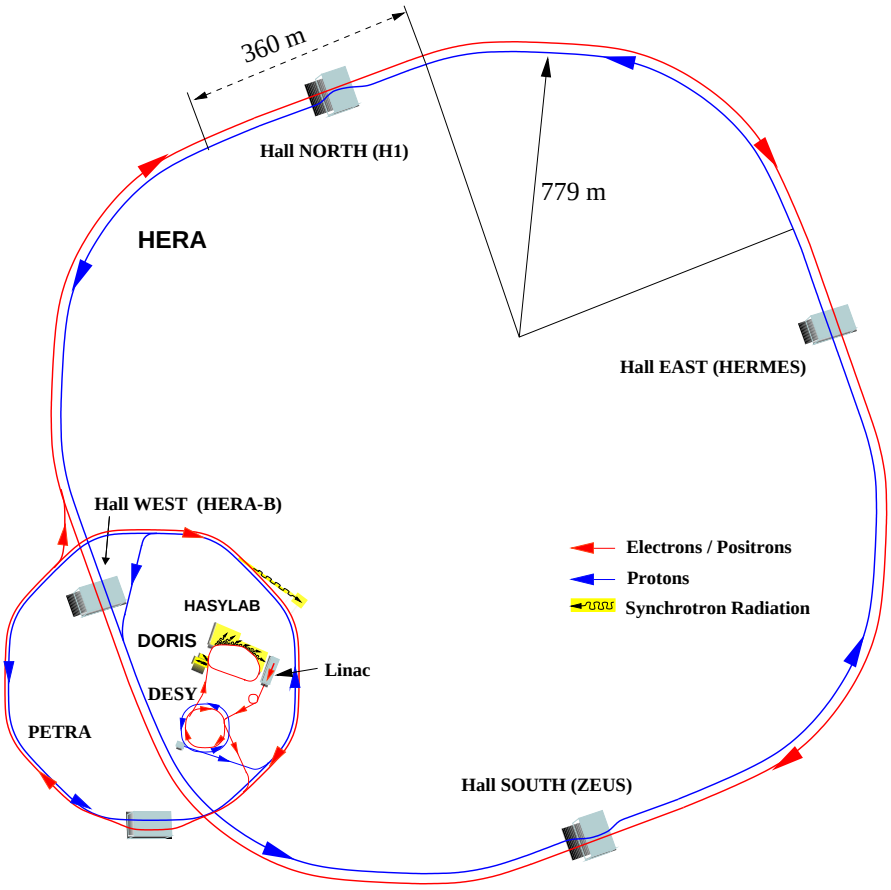

Figure 2.1: *Schematic view of the HERA accelerator and its injectors.*

HERA [65] was the only accelerator in the world which collided electrons (or positrons) with protons. It was located at the Deustches Elektronen Synchroton (DESY) laboratory in Hamburg, Germany. HERA started to be built in 1984 and operated from 1992 to 2007. The HERA tunnel was situated 15-30 meters underground and had a circumference of 6.3 km. Two storage rings, one for electrons and one for protons, were situated inside the tunnel. In the electron ring, normal-conducting cavities were used in order to accelerate the beam, whereas super-conducting cavities were used for the proton beamline. The two beams were brought to collision every 96 ns in two points along the circumference where the experiments ZEUS [66] and H1 [67] were placed (Fig. 2.1).

Two more experiments used the beams provided by HERA, HERMES and HERA-B, which were fixed-target experiments. HERMES used the electron beam to study the spin structure of the nucleon by scattering longitudinally polarized electrons off polarized gas jet targets of hydrogen, deuterium or helium. HERA-B was designed to measure $\mathcal{CP}$-violation in the $B^0\overline{B^0}$-system. The B-mesons were produced by collisions of beam halo protons with a wire target. HERA-B stopped data taking in 2000.

In the first period of operation, namely from 1992 to 1997, HERA accelerated electrons and protons to 27.5 and 820 GeV, respectively, resulting in a centre-of-mass energy $\sqrt{s} = 310$ GeV. In 1998, the proton beam energy was increased to 920 GeV, reaching the design goal $\sqrt{s} = 318$ GeV.

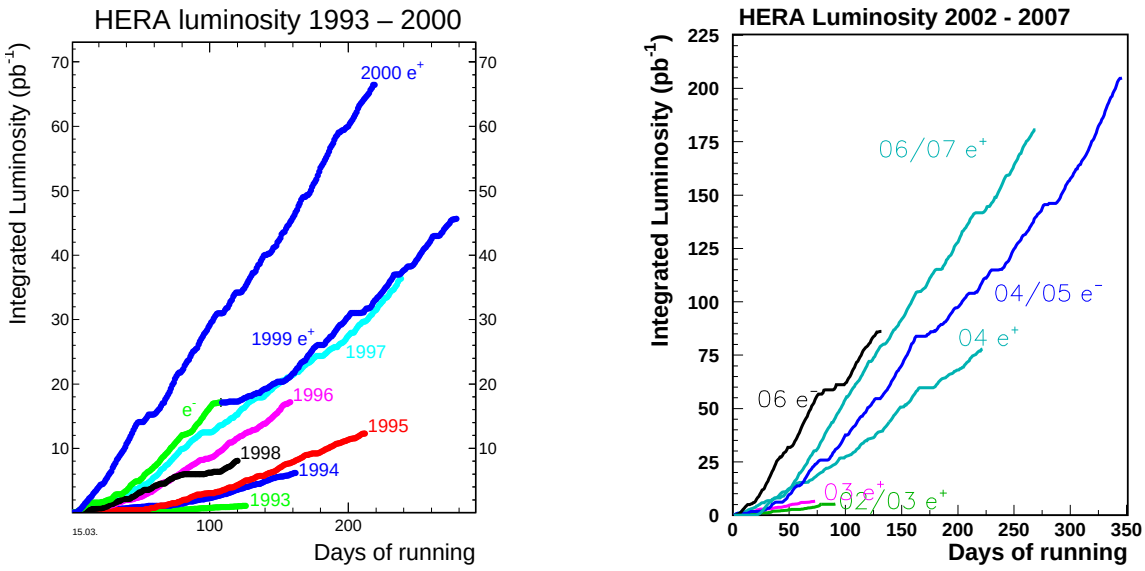

Figure 2.2: *The integrated luminosity delivered by HERA during the HERA I (left) and HERA II (right) running periods.*

At the end of 2000, HERA was shut-down for an upgrade [68]. The aims of the upgrade were to increase the specific luminosity of the machine by a factor of 5, and to incorporate the spin rotators to deliver longitudinally polarized lepton beams at the interaction points of the H1 and ZEUS experiments. HERA operations restarted in October 2002. Because of the shut down, two data taking periods are commonly distinguished at HERA, namely *HERA I* and *HERA II* for the data collected before and after the break, respectively.

During the last year of data taking, the HERA operation was devoted to the direct measurement of the longitudinal proton structure function and the γp total cross section. For this purpose, special runs were recorded by the H1 and ZEUS experiments, and the proton beam energy was lowered. In the period from March to May 2007 protons were accelerated to 460 GeV, and in June 2007 to 575 GeV, while keeping $E_e = 27.5$ GeV, for resulting centre-of-mass energies of 225 and 252 GeV, respectively.

The integrated luminosity delivered by HERA, for the different running periods, is shown in Fig. 2.2 [69].

2.2 The ZEUS Detector

The ZEUS detector was a general-purpose magnetic detector with an almost hermetic coverage designed to study electron-proton scattering at HERA. ZEUS had a size of $12 \times 11 \times 20$ m^3 and a weight of 3600 tons. It was built and operated by a collaboration of more than 400 physicists from 51 institutes in 12 different countries.

The ZEUS coordinate system is shown in Fig. 2.3. It is a right-handed orthogonal system with the origin at the nominal interaction point (IP), the z-axis pointing in the proton beam direction (defining the forward direction), the y-axis pointing upwards and the x-axis pointing horizontally toward the centre of HERA. The polar angle θ of the proton (electron) beam,

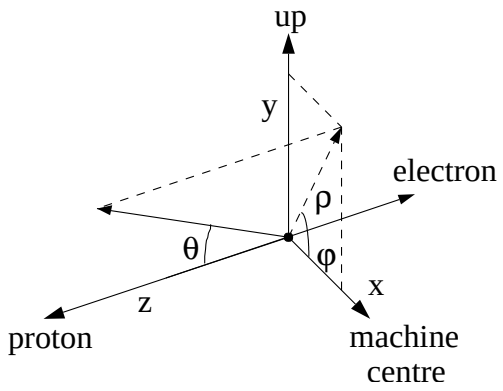

Figure 2.3: *The ZEUS coordinate system.*

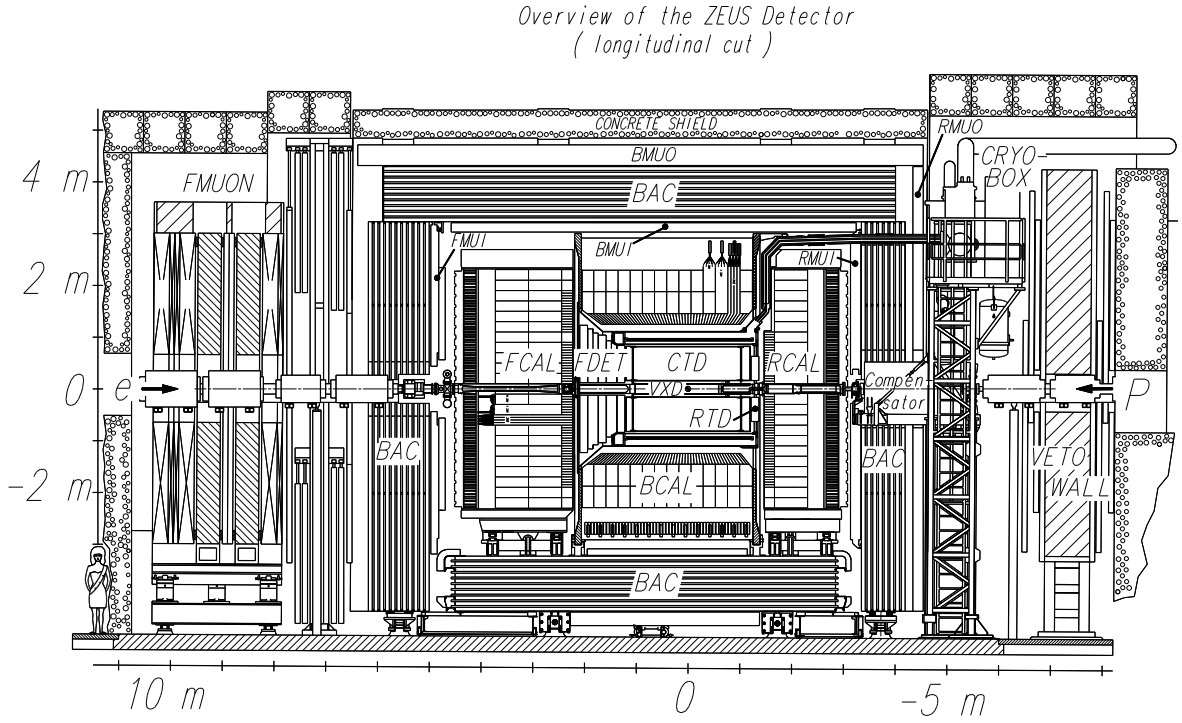

Figure 2.4: *Cross section of the ZEUS detector along the beam axis.*

measured with respect to the z-axis, is 0° (180°). The azimuthal angle ϕ is measured with respect to the x-axis.

Figures 2.4 and 2.5 show the cross sections of the ZEUS detector along and perpendicularly to the beam axis, respectively. The design of the detector was not symmetric with respect to the nominal interaction point ($z = 0$). The difference in energy of the electron and proton beams resulted in a large boost of the centre-of-mass system in the direction of the proton beam and in a large forward-backward asymmetry of the particle production. Therefore, the forward part of the detector was more instrumented than the rear one. Various components were installed to measure final state hadrons and leptons, and to characterize observed final state in terms of particle energy, direction and time. A brief overview is given below, followed by a more detailed description of the components relevant for this work. For a complete description refer to [70].

In the ZEUS detector the interaction point was surrounded by the tracking system. The innermost detector was a silicon-strip micro vertex detector (MVD, see Section 2.2.1), installed during the shutdown of 2001. The central tracking detector (CTD, see Section 2.2.2), a cylindrical wire drift chamber, enclosed the MVD. The CTD was surrounded by a super-conducting solenoid, providing a field of 1.43 T for the determination of the charge and momentum of the charged particles. In the forward and rear directions additional tracking information was

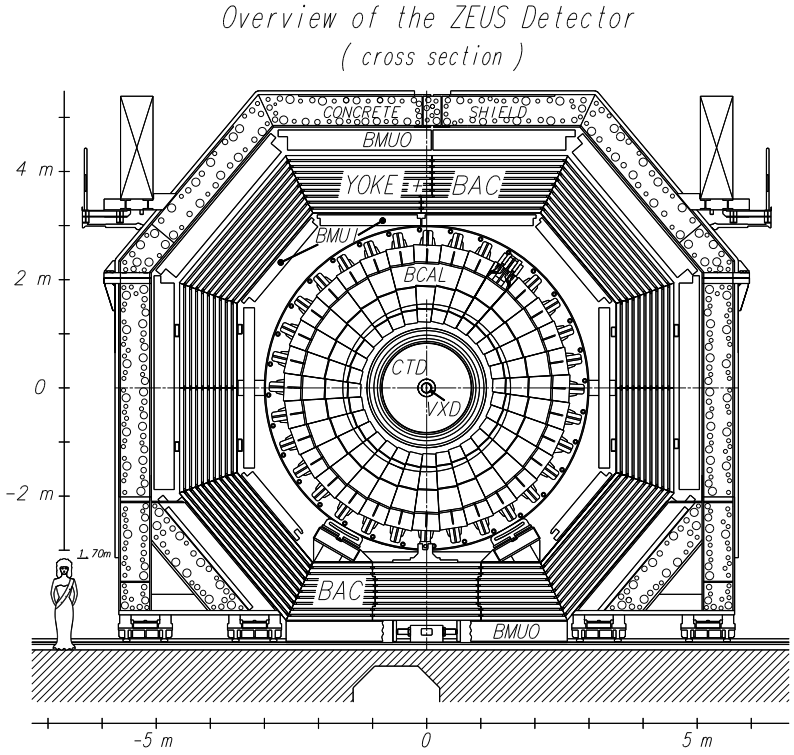

Figure 2.5: *Cross section of the ZEUS detector perpendicular to the beam axis.*

provided by the FTD/STT (labeled as FDET in Fig. 2.4) and RTD chambers, respectively. The FTD consisted of three sets of planar drift chambers. The STT, which consisted of two modules built of straw-tube layers, filled the gaps between the three chambers of the FTD. The RTD was made of one planar drift chamber with three layers.

A compensating high resolution uranium calorimeter (CAL, see Section 2.2.3) surrounded the tracking system. It was divided into forward (FCAL), barrel (BCAL) and rear (RCAL) sections. Attached to the front face of the RCAL was the small angle rear tracking detector (SRTD, see Section 2.2.4). Presampler detectors (FPRES, BPRES, RPRES) were mounted on the front of the calorimeter. These detectors were used to estimate the energy loss of the particles due to their interactions with the inactive material located in front of the calorimeter. The hadron-electron separator (HES, see Section 2.2.5) was installed at a depth of 3 radiation lengths, X_0, inside the forward and the rear sections of the calorimeter. The CAL was surrounded by an iron yoke, which provided a return path for the magnetic field flux and served as absorber for the backing calorimeter (BAC). The BAC measured the energy leakage from the main calorimeter and acted as a tracking calorimeter for muons. The muon detector systems were placed inside (FMUI, BMUI, RMUI) and outside (FMUON, BMUON, RMUON) the iron yoke.

The VETO wall was a iron-scintillator detector located in the rear part and was used to

reject background from proton beam-gas interactions. The timing information provided by the VETO wall together with that given by the C5 counter, placed close to the rear end of the calorimeter, was also used to reject proton beam-gas events.

The luminosity measurement was performed with the luminosity monitor (LUMI) and the spectrometer (SPEC) systems (see Section 2.2.6), placed along the beampipe in the rear direction, together with the 6m Tagger.

The Leading Proton Spectrometer (LPS) and the Forward Plug Calorimeter (FPC), mainly used for diffractive analyses, were placed along the forward beamline. They operated during the HERA I running period and were then dismantled.

2.2.1 The Micro Vertex Detector (MVD)

The silicon-strip micro vertex detector (MVD) [71] was installed during the shutdown of 2001. Its aim was the improvement of the global precision of the existing tracking system, allowing also to identify events with secondary vertexes coming from the decay of long-lived states, such as hadrons with charm or bottom quarks and τ leptons.

The MVD was divided into two parts, the barrel (BMVD) and foward (FMVD) detectors. The BMVD was located around the interaction point and had a length of 64 cm. The FMDV was located next to the barrel region and extended to $z = 72.9$ cm in the forward direction. A schematic view of the MVD is shown in Fig. 2.6.

The BMVD consisted of single-sided silicon sensors with dimensions of 64×64 mm^2 and thickness of 320 μm. Each sensor had 512 readout strips with a pitch of 120 μm. The hit position could be measured very precisely by comparing the charge collected in two adjacent readout strips. The hit resolution at normal incidence is $\sigma \sim 23$ μm [72]. The sensors were arranged in double-sided modules which were mounted in three concentric layers around the interaction point. The inner layer was not complete due to the elliptical shape of the beampipe.

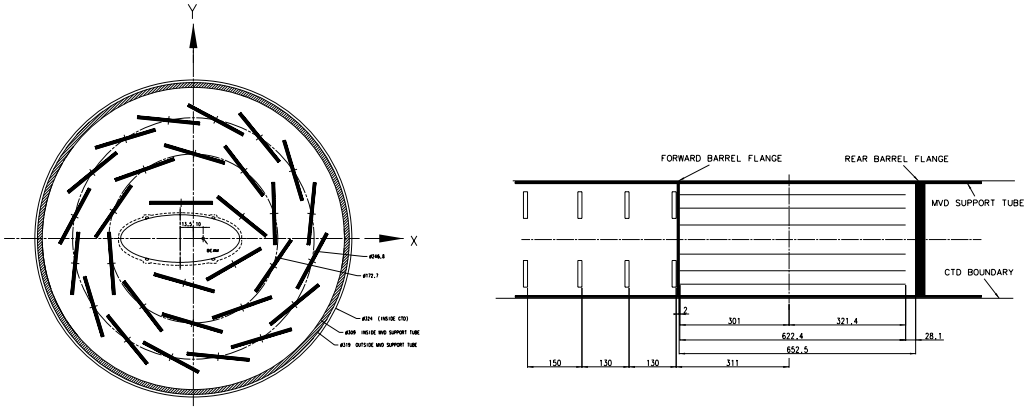

Figure 2.6: *Layout of the MVD in the xy-view (left) and along the beam direction (right).*

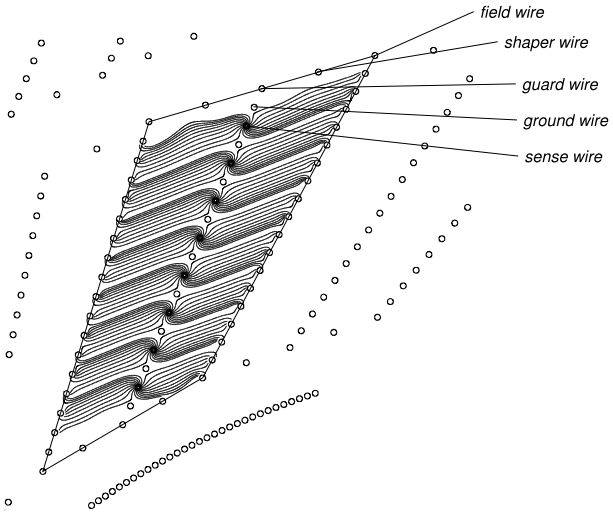

Figure 2.7: *Layout of a drift cell in the CTD.*

The forward section consisted of four wheels made of two layers of 14 silicon sensors, with a trapezoidal shape. In each of the wheels, the two layers were parallel but the strips were tilted by $180°/14$ in opposite directions.

2.2.2 The Central Tracking Detector (CTD)

The CTD [73] was a cylindrical drift chamber which measured the momentum of charged particles and the energy loss dE/dx, used for particle identification. Its active volume ranged from $z = -100$ cm to $z = 104$ cm. The inner and outer radius were 18.2 cm and 79.4 cm, respectively, with polar coverage of $15° < \theta < 164°$ and complete azimuthal angular coverage. The CTD was filled with a mixture of argon, ethane and carbon dioxide.

The CTD consisted of cells made up of 8 sense wires (see Fig. 2.7). The wires collected the signals produced by the charged particles which, passing through the gas, ionized the gas molecules along their trajectories producing electrons and positive ions which drifted towards the wires.

The cells were arranged in 9 super-layers (SL). The wires of the odd-numbered SLs were parallel to the beam axis, whereas for the even-numbered SLs they were inclined by a "stereo" angle of $\sim \pm 5°$ (see Fig. 2.8). This allowed the determination of the z position of the hit with an accuracy of ~ 2 mm. In addition, SLs 1, 2 and 3 were equipped with a z-by-timing system, used mainly for trigger purposes, which determined the z-position from the arrival times at both ends of the CTD.

The transverse momentum resolution [74] for tracks fitted to the interaction vertex and with $p_T > 150$ MeV, was given by

$$\frac{\sigma(p_{\mathrm{T}})}{p_{\mathrm{T}}} = 0.0058 \cdot p_T \oplus 0.0065 \oplus 0.0014/p_{\mathrm{T}} \ , \tag{2.1}$$

where p_T is in GeV and where the symbol $\oplus$ indicates sum in quadrature. The first term results from the position resolution, whereas the second and third are due to multiple scattering before and inside the CTD, respectively. The resolution of the combined CTD+MVD tracking [75] was given by

$$\frac{\sigma(p_{\mathrm{T}})}{p_{\mathrm{T}}} = 0.0026 \cdot p_T \oplus 0.0104 \oplus 0.0019/p_{\mathrm{T}} \ . \tag{2.2}$$

2.2.3 The Calorimeter (CAL)

The ZEUS calorimeter [76–79] was a high resolution uranium-scintillator calorimeter. The calorimeters are devices which measure the particle energy from the shower produced by the interaction of the particle with the detector mass.

The CAL was a sampling calorimeter consisting of alternating layers of depleted uranium[1] as absorber medium and organic scintillator as active material. The thickness of the layers was 3.3 mm and 2.6 mm for the uranium and the scintillating material, respectively. These values were optimized to obtain the same response to electromagnetic and hadronic particles

[1] 98.1% U^{238}, 1.7% Nb, 0.2% U^{235}.

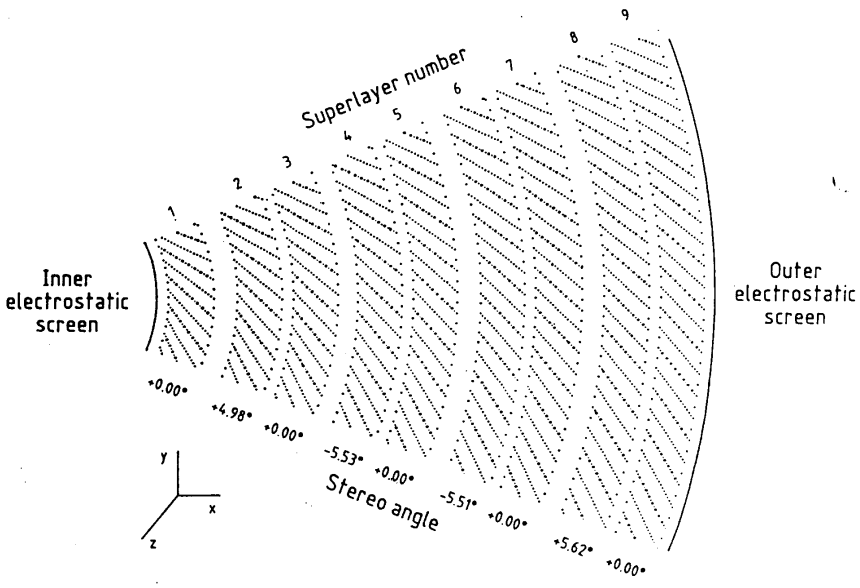

Figure 2.8: *A xy-cross section of one octant of the CTD. The dots indicate sense wires.*

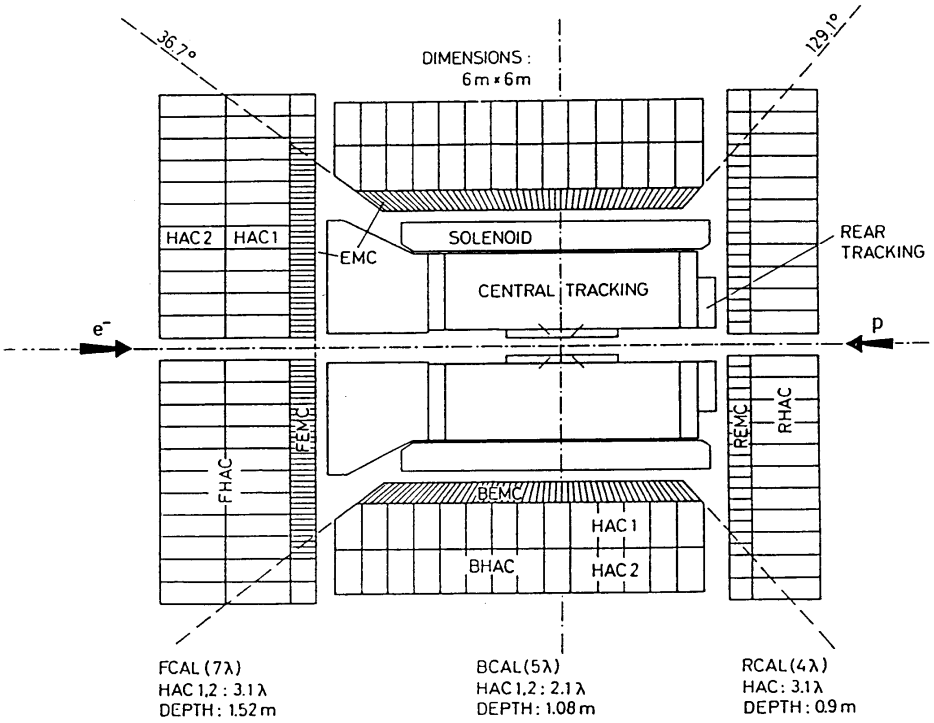

Figure 2.9: *Schematic view of the CAL.*

of equal energy. This property, called compensation, was achieved with a factor of $e/h = 1.00 \pm 0.05$.

The energy resolutions of the CAL, as measured under test beam conditions, were

$$\frac{\sigma_e}{E} = \frac{18\,\%}{\sqrt{E}} \oplus 2\,\% \tag{2.3}$$

for electrons and

$$\frac{\sigma_{\mathrm{had}}}{E} = \frac{35\,\%}{\sqrt{E}} \oplus 1\,\% \tag{2.4}$$

for hadrons, with E in GeV. The symbol $\oplus$ indicates sum in quadrature.

The calorimeter consisted of three parts: FCAL, BCAL and RCAL, with different polar-angle coverage, as shown in Fig. 2.9. The sections had different thickness: since the final state particles were boosted to the forward (proton) direction, the FCAL part was the thickest one, with a total absorption length $\lambda = 7.14$, followed by the BCAL with $\lambda = 4.92$ and the RCAL with $\lambda = 3.99$. All the sections were divided in modules (see Fig. 2.10). The FCAL and RCAL had 23 modules each, whereas the BCAL consisted of 32 calorimeter modules. Each of these modules was subdivided into towers of 20×20 cm^2, which were segmented longitudinally into an electromagnetic (EMC) and two (only one for the RCAL) hadronic (HAC) sections. The

EMC sections were further transversely divided into four cells (only two for the RCAL). The basic properties of the different regions of the CAL are summarized in Table 2.1.

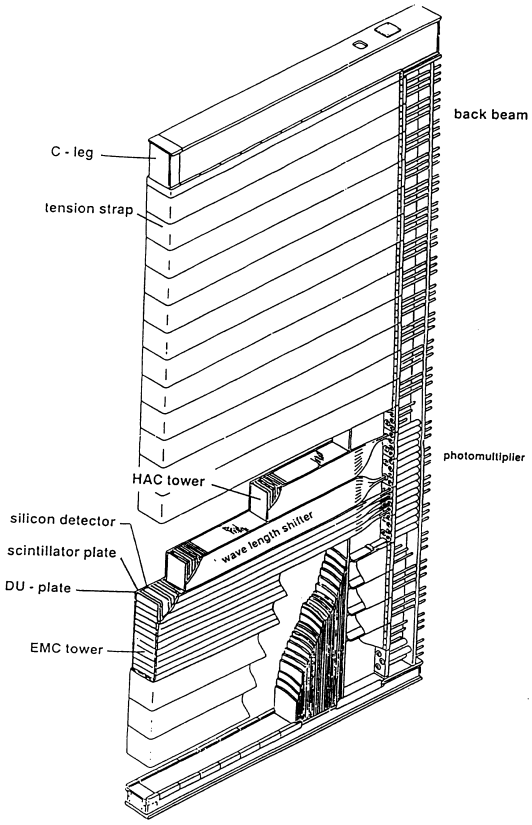

Figure 2.10: *Layout of a CAL module.*

Each cell was read out on the two opposite sides by photomultiplier tubes (PMTs) that received the scintillator light via wavelength shifters. Using this kind of readout, the energy measurement becomes independent of the impact position within the cell, since the signals of the two PMTs are summed up. Also, the comparison between the two signals allows the determination of the horizontal impact position. The excellent time resolution of the CAL - of the order of $1 \div 2$ ns - allowed the rejection of background events.

The energy calibration of the CAL was performed using test beam measurements with various types of particles of different energies. Continuous monitoring of the calibration was done using the signal from the radioactive decay of the ^{238}U (half-life $4.5 \cdot 10^9$ years). The PMTs and the readout electronics were additionally calibrated using LED, LASER and test pulses.

	FCAL	BCAL	RCAL
θ-range	$2.5° - 39.9°$	$36.7° - 129.1°$	$128.1° - 178.4°$
EMC rad. length X_0	25.9	22.7	25.9
total abs. length λ	7.14	4.92	3.99
EMC cell dimensions	$20 \times 5\ cm^2$	$20 \times 5\ cm^2$	$20 \times 10\ cm^2$
HAC cell dimensions	$20 \times 20\ cm^2$	$20 \times 20\ cm^2$	$20 \times 20\ cm^2$

Table 2.1: *Basic properties of the three regions of the CAL.*

2.2.4 The Small-angle Rear Tracking Detector (SRTD)

The SRTD [80] was designed to improve the energy and position measurement of the electrons and charged particles around the beampipe in the RCAL region. It was attached to the front face of the RCAL and covered an area of 68×68 cm^2 (excluding the beampipe hole). The detector consisted of two planes of scintillator strips, each with four quadrants of 24 cm $\times$ 44 cm. The strips were arranged along the x direction in one of the planes and along the y direction in the other (see Fig. 2.11). The total number of strips was 272; each had a width of 1 cm.

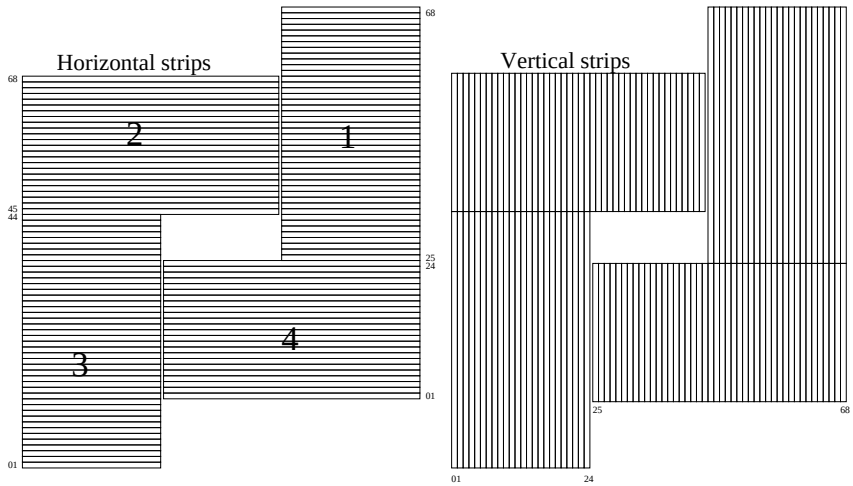

Figure 2.11: *Orientation and numbering scheme of the strips of the two SRTD planes.*

Electrons which lost energy through showers in the inactive material in front of the CAL deposited more energy in the SRTD than the non-showering electrons. These energy deposits can be used to correct for these energy losses, improving the electron energy measurement. For the position measurements, the SRTD provided a resolution of 3 mm.

2.2.5 The Hadron-Electron Separator (HES)

The HES detector [81] consisted of a layer of 3×3 cm^2 silicon diodes, located in the RCAL (RHES) and FCAL (FHES) at a longitudinal depth of 3.3 radiation lengths, which corresponds to the approximate position of the electromagnetic shower maximum in the CAL. The fact that the hadronic interaction length is 20 times larger than the electromagnetic radiation length allowed the separation between hadrons and electrons, since the signals produced by hadrons in the HES were smaller. The HES provided a spatial resolution of $\sim$ 9 mm for a single hit. In case of more hits, clusters were formed and the resolution in the particle position improved up to 5 mm.

2.2.6 The Luminosity Measurement

The event rate $\mathcal{R}$ for a process of cross section σ is related to the luminosity $\mathcal{L}$ by

$$\mathcal{R} = \mathcal{L} \cdot \sigma \, . \tag{2.5}$$

Therefore, an accurate measurement of the luminosity is crucial in order to extract any cross section. The values of the luminosity can be calculated either from the beam parameters or using a well known process and applying Eq. (2.5).

In ZEUS, $\mathcal{L}$ was determined using the *bremsstrahlung* events produced by the Bethe-Heitler process, $ep \to e\gamma p$. The main reason to choose this process was that it has a large and theoretically well known cross section. In addition, the Bethe-Heitler process has a clean experimental signature: the coincidence of an electron and a photon at small angles with respect to the lepton beam direction, with energies that add up to the initial electron energy.

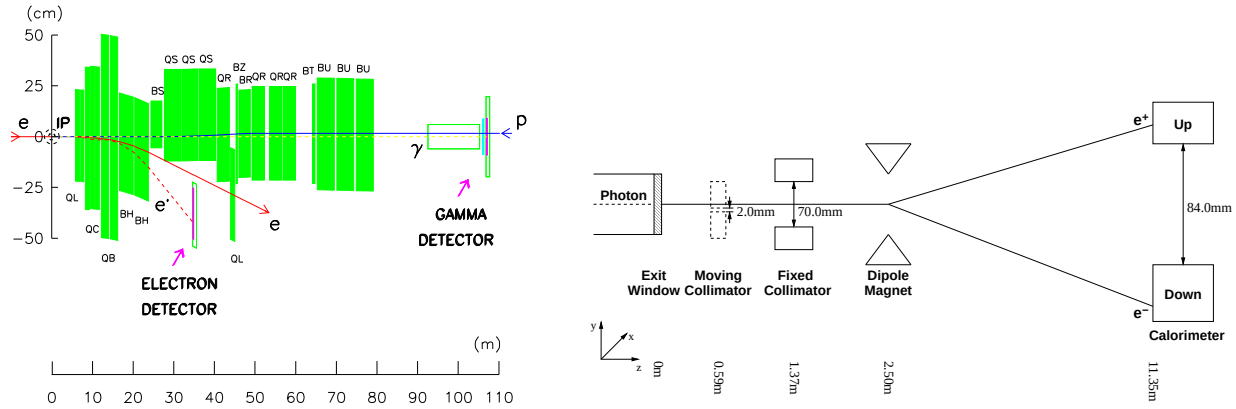

Figure 2.12: *Schematic views of the LUMI (left) and the SPEC (right).*

The luminosity measurement was performed with two systems: the Luminosity Monitor (LUMI) and the Spectrometer (SPEC). The LUMI was used since the beginning of the data taking, in 1992, whereas the SPEC was designed for the new higher-lumi scenario after the HERA upgrade in 2001, in which the increased synchrotron radiation and the higher probability of bremsstrahlung photons per bunch crossing posed new challenges.

The LUMI [82] system counted the rate of bremsstrahlung photons. The detector was located upstream of the interaction point along the direction of the lepton beam (see Fig. 2.12). The bremsstrahlung photons left the beampipe through a Cu-Be window of 0.0095 X_0 thickness which was situated at $z = -92.5$ m, and they were detected by a lead-scintillator sampling calorimeter at $z = -107$ m, with an energy resolution of $\sigma(E)/E = 23\%/\sqrt{E}$. The measurement of the photon rate is corrected for the background originating from the bremsstrahlung of leptons interacting with the residual gas in the beampipe. The largest uncertainty comes from the acceptance of the photon calorimeter.

Unlike the LUMI system, in the SPEC [83] the bremsstrahlung photons were not directly measured, but were detected through their pair conversion, $\gamma \to e^+ e^-$, in the material of the exit window. The window of the SPEC was located 92 m from the nominal interaction point. Approximately 10% of the photons converted into a pair. This fraction of converted photons was uniform over the surface of the window. The converted pairs, after traversing the collimators, were separated vertically by a magnetic dipole. Finally, the electrons and positrons were detected by a segmented tungsten-scintillator sampling calorimeter. A schematic layout of the SPEC is shown in Fig. 2.12.

2.2.7 The Leading Proton Spectrometer (LPS)

The LPS [84] detected positively charged particles scattered at very small angles and carrying a substantial fraction, ${x_L}^2$, of the incoming proton momentum; these particles remained in the beampipe and their trajectories were measured by a system of silicon microstrip detectors that could be inserted very close (typically a few mm) to the proton beam by means of movable Roman Pots. The detectors were grouped in six stations, S1 to S6, placed along the beam line in the direction of the proton beam, between 23.8 m and 90.0 m from the interaction point (see Fig. 2.13). The particle deflection induced by the magnets of the proton beam line allowed a momentum analysis of the scattered proton. The resolution was about 0.5% on the longitudinal momentum fraction and about 5 MeV on the transverse momentum. The effective transverse-momentum resolution was dominated by the intrinsic transverse-momentum spread of the proton beam at the interaction point, which was about 45 MeV in the horizontal plane and about 100 MeV in the vertical plane. The LPS acceptance was approximately 2% and x_L independent for $x_L \gtrsim 0.98$; it increased smoothly to about 10% as x_L decreased to 0.9.

[2] x_L is the fractional longitudinal momentum of the scattered proton, and is defined as $x_L = |p'_z|/p_z \simeq 1 - x_{I\!P}$.

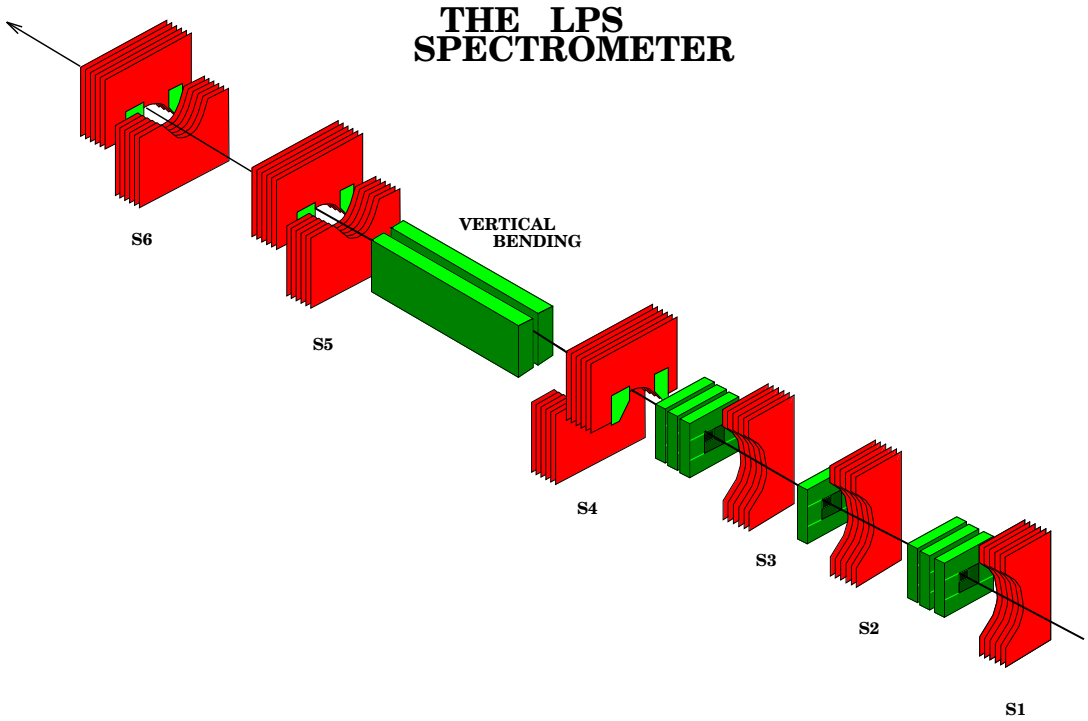

Figure 2.13: *Layout of the LPS detectors along the outgoing proton direction. Longitudinal distances between elements are not drawn to scale.*

The six stations formed two independent spectrometers: S1-S3 used the horizontal bending magnets, and S4-S6 took advantage of the vertical bending. The two LPS spectrometers had only a small region of overlap in acceptance: S1-S3 detected mainly low-momentum protons and S4-S6 high momentum protons, including the $x_L \sim 1$ region.

2.2.8 The Forward Plug Calorimeter (FPC)

In 1998 the FPC [85] was installed into the FCAL beam hole. It was used to measure the energy of particles in the pseudorapidity range $\eta \sim 4-5$. It was a lead-scintillator sandwich calorimeter read out by wavelenght-shifter fibers and photomultipliers. The FPC had outer dimensions of $19.2 \times 19.2 \times 108$ cm^3 and had a central hole with radius 3.15 cm to accommodate the beampipe. In the FPC, 15 mm thick lead plates alternated with 2.6 mm thick scintillator layers. The FPC was subdivided longitudinally into an elecromagnetic (10 layers) and a hadronic section (50 layers) representing a total of 5.4 nuclear absorption lengths. The energy resolution for electrons, as measured in a test beam, was $\sigma(E)/E = (0.41 \pm 0.02)/\sqrt{E} \oplus 0.062 \pm 0.002$, with E in GeV. When installed in the FCAL, the energy resolution for pions was $\sigma(E)/E = (0.65 \pm 0.02)/\sqrt{E} \oplus 0.006 \pm 0.001$, with E in GeV, and the e/h ratio was close to unity.

2.2.9 Trigger and Data Acquisition (DAQ)

The HERA accelerator had a bunch crossing rate of 10.4 MHz. The rate of interesting ep events is several orders of magnitude smaller (e.g. for NC DIS events, with $Q^2 > 100$ GeV^2, the rate[3] is about 0.1 Hz).

In order to select interesting events, ZEUS had a three-level, pipe-lined trigger system [70, 86], which achieved the necessary rate reduction. A schematic view of the trigger system is shown in Fig. 2.14.

The First Level Trigger (FLT) was a hardware trigger which reduced the output rate below 1 kHz. The components of the ZEUS detector had their own FLT electronics and produced their own trigger decision based on raw quantities. These decisions were made within ~ 2 μs after a bunch crossing and then were sent to the Global First Level Trigger (GFLT). Within ~ 5 μs, the GFLT decided whether the event should be passed onto the next trigger level.

The Second Level Trigger (SLT) was based on a transputer network. It was designed to reduce the rate to $50 - 100$ Hz. The different components of the SLT sent the information to the Global Second Level Trigger (GSLT). The time for the GSLT to take a decision was longer than for the FLT, hence the algorithms were more complex and allowed a first reconstruction which made possible a trigger decision based on event topologies. If the event was accepted, the complete information was sent to the Event Builder (EVB), which organized the data in the final format.

The Third Level Trigger (TLT) was a software trigger running on a computer farm. At this stage, the events could be fully reconstructed using algorithms very similar to the ones in the offline code. The events were accepted and classified using different physics-based filters. The final output rate at the TLT was ~ 5 Hz. In the last step, events were written to tape at the DESY computer center, ready for the offline reconstruction and analysis.

[3] For an instantaneous luminosity of $2 \cdot 10^{31} \mathrm{cm}^{-2}\mathrm{s}^{-1}$.

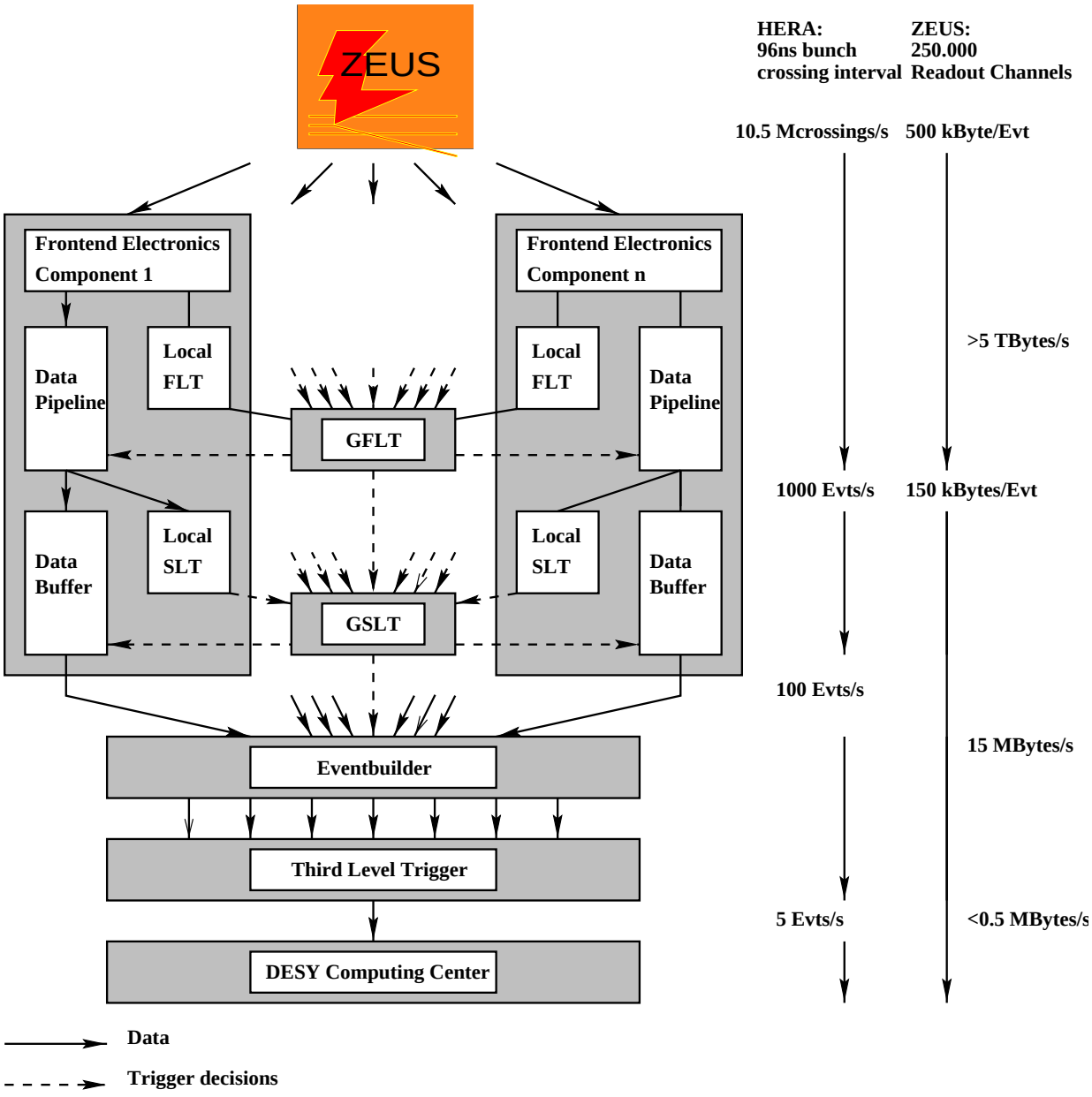

Figure 2.14: *The ZEUS trigger and data acquisition system.*

Chapter 3

Methods of Selecting Diffraction at HERA

Different methods were adopted to select diffractive events at HERA. Each method exploited a specific experimental signature of diffraction, and can be considered complementary to the others.

An example of a diffractive event as seen in the ZEUS detector is shown in Fig. 3.1.

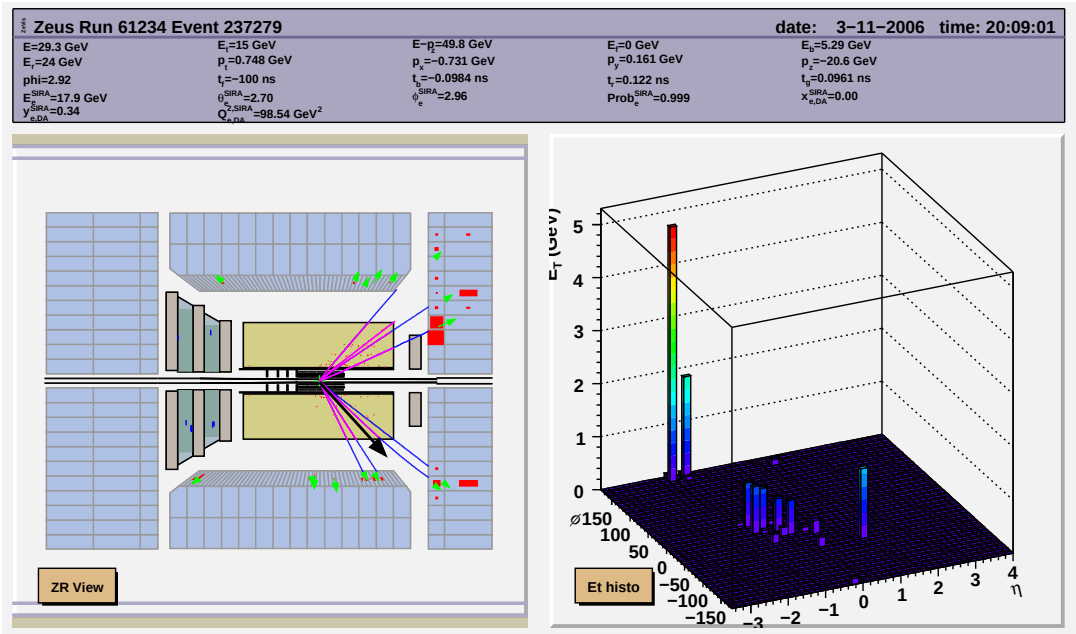

Figure 3.1: *A diffractive DIS event in the ZEUS detector (left) and its E_T projection on the (η, ϕ) plane (right). Note the absence of signals in the forward direction (which points to the left, as defined in Sect. 2.3), corresponding to high η values.*

3.1 Proton Spectrometer Method (PS)

In principle, the cleanest way to identify diffractive events is to directly detect the final-state proton (*leading proton*), which carries a large fraction, x_L, of the initial proton momentum. Diffractive events thus appear as a peak at $x_L \sim 1$, the diffractive peak, which at HERA covered the region $x_L \gtrsim 0.98$ (see Fig 3.2). At $x_L \lesssim 0.9$ the continuum due to double dissociation, reggeon exchange and inclusive DIS dominates the x_L spectrum.

For diffractive events, the absolute value of the four-momentum-transfer squared, $|t|$, is typically smaller than 1 GeV^2. Since the leading protons have small transverse momenta and tend to stay very close to the beam line, their detection required the use of Roman Pots, movable stations that allowed inserting high precision proton detectors down to few millimeters from the beam. The proton spectrometer technique was widely exploited at HERA with a total of three such spectrometers operational: the H1 Forward Proton Spectrometer (FPS) [45, 46], the H1 Very Forward Proton Spectrometer (VFPS) [47] and the ZEUS Leading Proton Spectrometer (LPS) [50, 51].

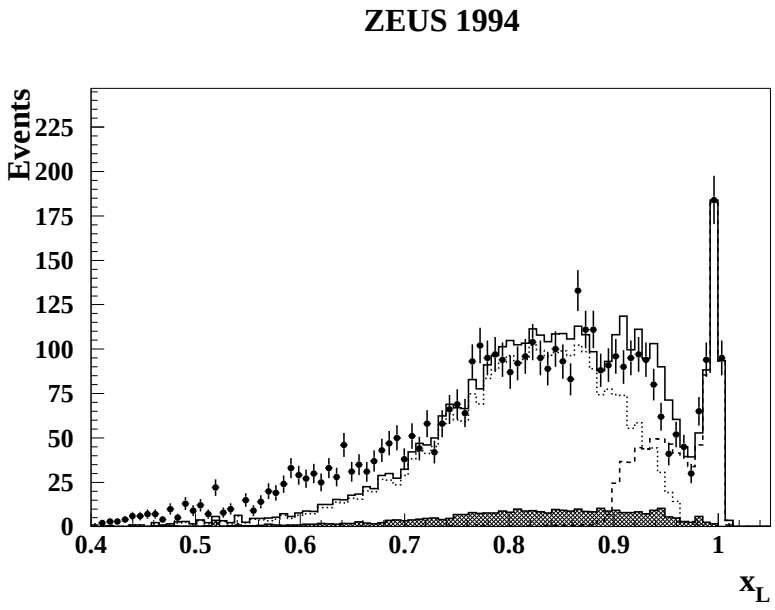

Figure 3.2: *The measured x_L spectrum of protons (dots) with the diffractive peak at $x_L \sim 1$. The diffractive signal modelled by a Monte Carlo program is represented by the dashed line. The dotted line is the pion-exchange contribution. The shaded area corresponds to proton dissociation [87].*

3.2 Large Rapidity Gap Method (LRG)

The presence of a large rapidity gap between the struck parton and the proton remnant, discussed in Sect. 1.3, was also exploited to select diffractive events [48, 49, 51] at HERA. According to Eqs. (1.30) and (1.31), diffractive and non-diffractive events exhibit a different behaviour as a function of $\Delta\eta$, the rapidity gap between the proton remnant and the struck parton. Using the definition of rapidity, $\mathcal{Y}$, and pseudorapidity, η, given in Eqs. (1.17) and (1.18), it is possible to quantify the LRG size between the proton and the diffractive system X as a function of the kinematics:

$$\Delta\eta = \eta_p - \eta_X \sim ln\frac{W^2}{M_X^2} \sim ln\frac{1}{x_{I\!P}} \ . \tag{3.1}$$

Since the diffractive cross section increases with decreasing $x_{I\!P}$, most of the events have small $x_{I\!P}$ and therefore a large separation in rapidity between the outgoing proton and any other hadronic activity in the event.

The LRG method consists of applying a cut on the pseudorapidity, η_{MAX}, of the most forward energy deposit in the detector, assuming that the proton escapes inside the beam-pipe in the forward direction. In Fig. 3.3 a typical η_{MAX} distribution is shown. It is clear from the plot that the low η_{MAX} region, corresponding to larger $\Delta\eta$ values, is dominated by diffractive events. Experimentally, rapidity gap widths in the forward direction of the order of 2.5-3 units are required. Therefore, the cut on η_{MAX} limits the pseudorapidity interval that can be covered

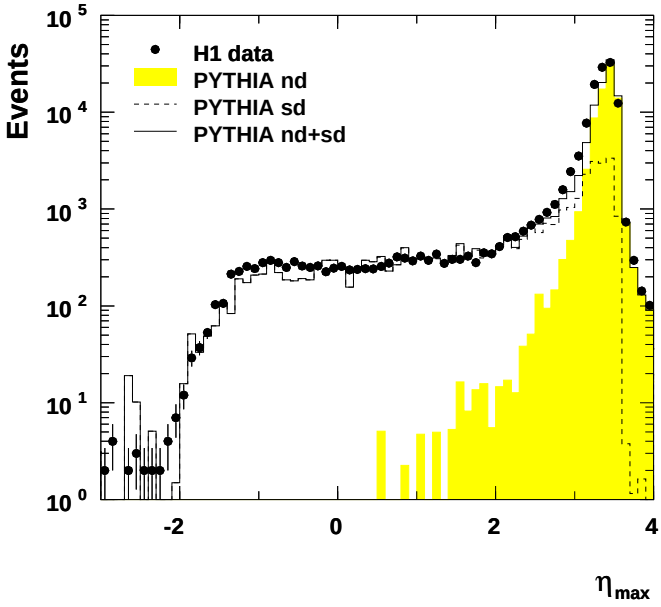

Figure 3.3: *Maximum pseudorapidity η_{MAX} distribution of H1 data compared to a diffractive (dashed line) and a non-diffractive (shaded area) Monte Carlo model, and their sum [88].*

by the X system, so that diffractive events with large M_X are kinematically excluded by this method.

3.3 M_X Method

A further method was adopted to select diffractive events at HERA [52, 53]: it exploits the difference in shape of the M_X distribution for diffractive and non-diffractive events. This method is closely related to the LRG method, since from Eq. (3.1), if the size of the LRG is large, the ratio M_X/W must be small. The diffractive signal is defined as the excess contribution in the lnM_X^2 distribution above the exponential fall-off of the non-diffractive peak (see Fig. 3.4).

This method will not be used in the present work.

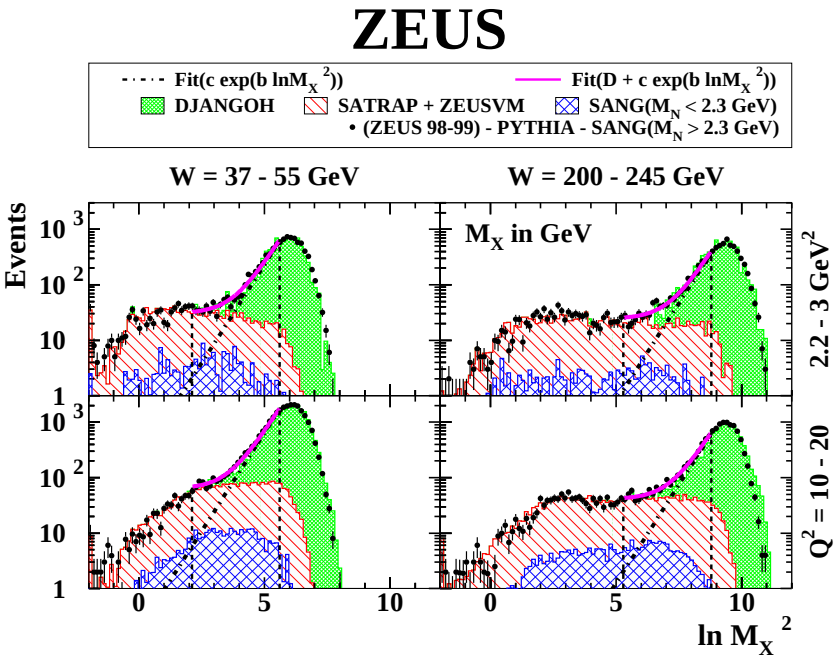

Figure 3.4: *Distributions of lnM_X^2 (M_X in unit of GeV) for different (W, Q^2) bins. The points with error bars show the data. The shaded areas show the non-diffractive contribution. The diffractive contribution from $ep \to eXp$ ($ep \to eXY$, $M_Y < 2.3$ GeV) are shown as hatched (cross-hatched) areas [52].*

3.4 Comparison between Selection Methods

The methods described differ substantially in their dominant sources of systematic uncertainties.

The FPS and LPS data have little or no background from non-diffractive DIS or from double-dissociative events, $ep \to eXY$ (see Fig. 1.14), in which the proton also dissociates into a low-mass state, Y, separated from X by a rapidity gap. The spectrometers allow a direct measurement of the variables t and $x_{I\!P}$, and give also access to values of $x_{I\!P} \gtrsim 0.05$ and high M_X. However, the proton-tag method has the drawback of small acceptance, and, consequently, low statistics, and it is not possible to reject the background due to reggeon exchange, which becomes relevant at high $x_{I\!P}$.

In the LRG method, events with high M_X are not accessible since the rapidity gap becomes more and more forward (and eventually becomes confined to the beam-pipe). The need to contain the system X in the central detector limits the kinematic coverage to $x_{I\!P} \lesssim 0.05$. In addition, the measured cross section includes a contribution from double-dissociative events. This happens when the Y system escapes entirely into the forward beam-pipe. Therefore, the contribution from proton-dissociative events depends on the geometrical coverage of the detector in the forward direction. While these limitations add to the systematic uncertainties of the method, the statistical precision of the results is good due to the high acceptance of the central detector. Although the acceptance is not limited in t, no measurement of t is possible because of the poor resolution on the transverse momentum of the system X.

The M_X method is equivalent to the LRG one for $M_X \to 0$, but differences are to be expected at larger M_X, where the LRG method measures the full cross section from all sources at a given (β, Q^2, $x_{I\!P}$) point, whereas the M_X method involves the subtraction of the "non-diffractive" component.

Comparing the results from the three different methods is a powerful test of the control over the systematics of the measurements. A complete and detailed comparison between all the inclusive diffractive results from HERA I data can be found in [89]. The ZEUS LRG data in [51] are compared to the diffractive cross sections from the H1 LRG and ZEUS LPS and M_X samples. A more recent comparison between H1 and ZEUS LRG results is given in [49]. The most recent, high statistics, H1 FPS measurement in [46] is compared to the H1 LRG and ZEUS LPS data. A compilation of all the H1 inclusive diffractive cross sections is given in [47].

At low $x_{I\!P}$, namely $x_{I\!P} \lesssim 0.02$, where the contribution from proton dissociation in the PS samples becomes negligible, the ratio of results obtained by the LRG and M_X methods to those from the proton-tagging method can also be used to quantify the proton dissociation contributions in the former samples. Figures 3.5 and 3.6 show the ratios of cross sections extracted from the PS and LRG data as obtained by the H1 and ZEUS experiments, respectively. There is no evidence for any dependence on any of the kinematic variables, as expected in the framework of the proton-vertex factorization (see Sect. 1.3.4.1). This translates into the assumption

that double dissociative events only affect the normalization of the LRG results, without any effect on the shape of the cross section. Therefore, at low $x_{I\!P}$, the measurements from Proton Spectrometer data fix the absolute normalisation of the ep diffractive reduced cross section.

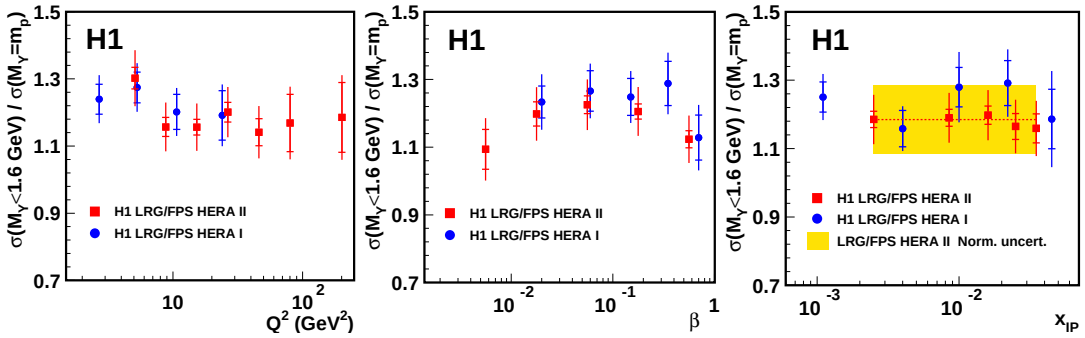

Figure 3.5: *The ratio of the H1 LRG measurement (corrected to $M_Y < 1.6$ GeV) to the H1 FPS measurement ($M_Y = m_p$), after the integration over the variables not shown in each case. The dashed line represents a fit to the data assuming no dependence on any of the variables [46].*

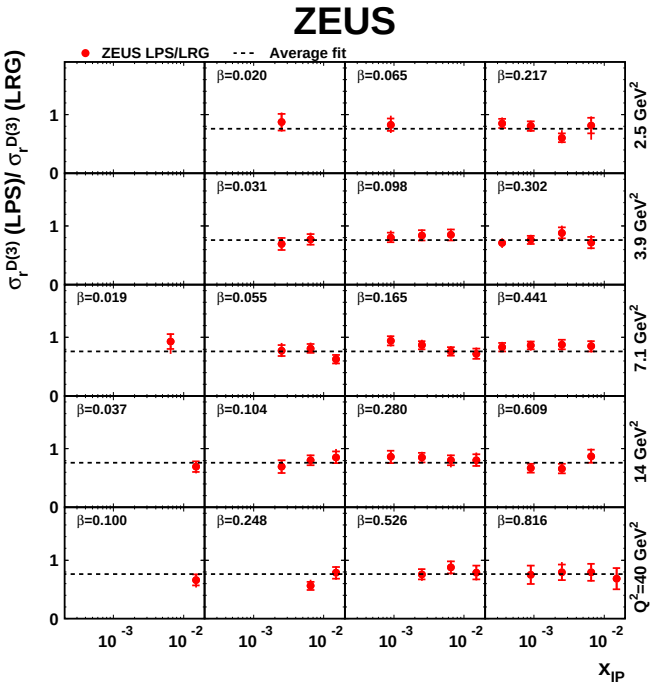

Figure 3.6: *The ratio of the ZEUS LPS measurement ($M_Y = m_p$) to the ZEUS LRG measurement. The dashed lines represent the average value of this ratio [51].*

Chapter 4

Combined Measurement of the Inclusive Diffractive Cross Sections at HERA

4.1 Introduction

During the 15 years of HERA data taking, a huge amount of high quality diffractive DIS data were recorded by the experiments. Various measurements of the diffractive reduced cross section were performed by the H1 and ZEUS Collaborations. After the shut-down of the collider, an effort has been made to combine the results of the two experiments.

One of the aims of this work is to combine the diffractive results published by the H1 and ZEUS Collaborations. The combination of the diffractive cross sections has several advantages. In principle, the combination procedure offers a model-independent tool to test the consistency between different experiments. Furthermore, a unique diffractive data set is easier to handle from outside the Collaborations, since some technical details of the measurements, as correlated uncertainties between experiments, are not completely documented. Moreover, a true experience of the detectors and their experimental challenges is only possible within the Collaborations. The ultimate, long-term, goal of the combination is to obtain a unique set of diffractive reduced cross sections, which will be used as input for a NLO QCD fit to extract precise HERA diffractive PDFs.

The combination of the diffractive reduced cross sections was performed by means of a dedicated program developed within the H1 and ZEUS Collaborations [90]. For the purpose of this analysis, the source code was adapted to the diffractive case, to take into account the 3-dimensional dependence of the diffractive DIS reduced cross section, $\sigma_r^{D(3)}$.

4.2 Combination Method

The combination of the data sets is based on a χ^2 minimisation method described in [90, 91] and already used for previous HERA combined results [14]. The averaging procedure is based on the assumption that the H1 and ZEUS experiments are measuring the same cross section at the same kinematic point. The correlated systematic uncertainties are included in the minimisation so that the two experiments effectively calibrate each other. This allows a model independent check of the data consistency and a significant reduction of the correlated systematic uncertainty.

For a single data set the χ^2 function is defined as:

$$\chi^2_{exp}(\boldsymbol{m},\boldsymbol{a}) = \sum_i \frac{\left[m^i - \sum_j \frac{\partial \mu^i}{\partial \alpha_j}(a_j - \alpha_j) - \mu^i\right]^2}{\Delta_i^2} + \sum_j \frac{(a_j - \alpha_j)^2}{\Delta^2_{\alpha_j}} \ . \tag{4.1}$$

Here μ^i is the measured cross section value at a point i (i.e. $\mu^i = \sigma_r^{D(3),i}(\beta, Q^2, x_{I\!P})$) with combined statistical and uncorrelated systematic uncertainty $\Delta_i = (\Delta^2_{i,stat} + \Delta^2_{i,uncor})^{1/2}$, α_j is the value measured for a correlated systematic error source j with an uncertainty Δ_{α_j}, while $\partial\mu^i/\partial\alpha_j$ quantifies the sensitivity of the measurement μ^i to the systematic source j. The vector $\boldsymbol{m}$ of physical quantities m^i contains the predicted values of the combined cross section for each point i and the vector $\boldsymbol{a}$ of quantities a_j quotes the set of correlated systematic uncertainties of the combined cross section. The second term in the expression for χ^2_{exp} defines the sum of the predicted shifts of the systematic uncertainties. The χ^2 function defined in Eq. (4.1) by construction has a minimum $\chi^2_{exp} = 0$ for $m^i = \mu^i$ and $\alpha_j = 0$.

Upon introducing the variables $b_j = (a_j - \alpha_j)/\Delta_{\alpha_j}$ and $\Gamma^i_j = (\partial\mu^i/\partial\alpha_j)\Delta_{\alpha_j}$, Eq. (4.1) can be written as:

$$\chi^2_{exp}(\boldsymbol{m},\boldsymbol{b}) = \sum_i \frac{\left[m^i - \sum_j \Gamma^i_j b_j - \mu^i\right]^2}{\Delta_i^2} + \sum_j b_j^2 \ . \tag{4.2}$$

The formalism introduced is suitable for measurements in which the uncertainties are absolute, i.e. do not depend on the central value of the measurement (additive errors). However, for the H1 and ZEUS cross section data, the correlated and uncorrelated systematic errors are to a good approximation proportional to the central values (multiplicative errors), while the statistical errors scale with the square roots of the expected number of events. Therefore, the combination of the data sets obtained with Eq. (4.2) leads to a small bias to lower cross-section values since the measurements with lower central values have smaller absolute uncertainties. To take this effect into account, the χ^2 definition is modified to:

$$\chi^2_{exp}(\boldsymbol{m},\boldsymbol{b}) = \sum_i \frac{\left[m^i - \sum_j \gamma^i_j m^i b_j - \mu^i\right]^2}{\delta^2_{i,stat}\mu^i \left(m^i - \sum_j \gamma^i_j m^i b_j\right) + \left(\delta_{i,uncor} m^i\right)^2} + \sum_j b_j^2 \ . \tag{4.3}$$

Here $\gamma_j^i = \Gamma_j^i/\mu^i$, $\delta_{i,uncor} = \Delta_{i,uncor}/\mu^i$ and $\delta_{i,stat} = \Delta_{i,stat}/\mu^i$ are relative correlated systematic, uncorrelated systematic and statistical uncertainties, respectively. In contrast to Eq. (4.2), the χ^2 function of Eq. (4.3) is not a simple quadratic form with respect to m^i and b_j. The combined values are obtained with an iterative averaging procedure: first Eq. (4.2) is used to get an initial approximation for $\mu^{i,ave}$ and $b_{j,ave}$ which are used to recalculate the errors as $\Gamma_j^i = \gamma_j^i \mu^{i,ave}$ and $\Delta_i^2 = \delta_{i,stat}^2 \mu^i (\mu^{i,ave} - \sum_j \gamma_j^i \mu^{i,ave} b_{j,ave}) + (\delta_{i,uncor} \mu^{i,ave})^2$. Then the determination of $\mu^{i,ave}$ is repeated. Convergence is usually reached after two iterations.

If several analyses provide measurements at the same (β, Q^2, $x_{I\!P}$) values, they can be combined by using the formula above, generalised for the case of multiple data sets. Then a total χ^2 function, χ^2_{tot}, is built from the sum of the χ^2_{exp} functions for each data set e according to:

$$\chi^2_{tot}(\boldsymbol{m}, \boldsymbol{b}) = \sum_e \chi^2_{exp,e} = \sum_e \sum_i^{N_M} \frac{\left[m^i - \sum_j^{N_S} \gamma_{j,e}^i m^i b_j - \mu_e^i \right]^2}{\delta_{i,stat\ e}^2 \mu_e^i \left(m^i - \sum_j \gamma_{j,e}^i m^i b_j \right) + \left(\delta_{i,uncor\ e} m^i \right)^2} + \sum_j^{N_S} b_j^2 \ , \quad (4.4)$$

where the summation over i (j) runs over all N_M measured points (all N_S systematic error sources) of all data sets considered. The symbol $w_{i,e}$ is equal to unity if the data set e contributes a measurement at the point i, otherwise it is zero. Similarly, the symbol $\gamma_{j,e}^i$ equals zero if the measurement i from the data set e is insensitive to the systematic source j. The predictions m^i are given under the assumption that there is a single true value of the cross section corresponding to each data point i. This definition of χ^2_{tot} assumes that the data sets are statistically uncorrelated. The systematic error sources b_j, however, may be either uncorrelated (separate sources) or correlated across data sets (different data sets sharing a common source).

The value of χ^2_{min} corresponds to the minimum of Eq. (4.4). The ratio χ^2_{min}/n_{dof} is a measure of the consistency of the data sets. The number of degrees of freedom, n_{dof}, is calculated as the difference between the total number of measurements and the number of averaged points, N_M. Although this system of equations has a large dimension, it has a simple structure, allowing a fast and precise solution. If none of the correlated sources is present, this minimisation is equivalent to taking a standard weighted average of the structure function measurements.

Possible tensions between data sets can be investigated by means of pull distributions. For the measurement at the point i of the data set e, the pull is defined as:

$$p^{i,e} = \frac{\mu^{i,e} - \mu^{i,ave}(1 - \sum_j \gamma_j^{i,e} b_{j,ave})}{\sqrt{\Delta_{i,e}^2 - \Delta_{i,ave}^2}} \ , \quad (4.5)$$

where $\Delta_{i,e}^2$ ($\Delta_{i,ave}^2$) is the quadratic sum of the statistical and uncorrelated systematic uncertainty for the measurement e (average). The pull value is $p^{i,e} \neq 0$ under the condition that measurements from more than one data set average at the same point i. This means that if

only one input data set e contributes to the point i, the value of the combined cross section in that point is $\mu^{i,ave} = \mu^{i,e}/(1 - \sum_j \gamma_j^{i,e} b_{j,ave})$.

The definition of pull for the correlated systematic sources in given by:

$$p_s = \frac{b_{j,ave}}{\sqrt{1 - \Delta^2_{b_j,ave}}} \,, \tag{4.6}$$

where $\Delta^2_{b_j,ave}$ is the uncertainty of the source j after the averaging.

4.3 Combination of Proton Spectrometer Cross Sections

4.3.1 Combined Data Sets

For the combination of the diffractive reduced cross sections from Proton Spectrometer data, the most precise, high-statistics samples from the H1 [46] and ZEUS [51] experiments were used. For a detailed discussion on the diffractive measurements based on proton-tagging see sect. 3.1.

The H1 FPS data correspond to an integrated luminosity of 156.6 pb^{-1}, collected during the HERA II running period. The data sample covers the range $0.1 < |t| < 0.7$ GeV^2, $x_{I\!P} < 0.1$ and $4 < Q^2 < 700$ GeV^2. The y coverage is $0.03 < y < 0.7$ for $Q^2 < 110$ GeV^2 and $0.03 < y < 0.8$ for $Q^2 > 120$ GeV^2.

The ZEUS LPS sample was collected in the years 1999 and 2000 and corresponds to an integrated luminosity of 32.6 pb^{-1}. The kinematic region covered by the data is $0.09 < |t| < 0.55$ GeV^2, $0.0002 < x_{I\!P} < 0.1$ and $2.5 < Q^2 < 120$ GeV^2. The W range lies between 40 and 240 GeV. No measurements were possible during the HERA II running period, since the LPS was dismantled during the HERA upgrade.

Both data sets were collected when the HERA collider operated at electron and proton beam energies of $E_e = 27.5$ GeV and $E_p = 920$ GeV, respectively, corresponding to an ep centre-of-mass energy of $\sqrt{s} = 318$ GeV.

The H1 data taken with the VFPS [47], still under analysis, cover a different kinematic region and therefore are expected to have little influence in the range of this combined FPS+LPS measurement.

4.3.2 Binning Scheme and Correlated Systematic Sources

The averaging procedure is based on the assumption that there is a single true value of the cross section for a given data point. Therefore, cross-section values from different data sets are needed at the same (β, Q^2, $x_{I\!P}$) point in order to be combined. The original binning scheme of the H1 and ZEUS measurements is very different: the H1 cross section is measured at fixed β, while in the ZEUS case, measurements are extracted at fixed M_X; also, the Q^2 and $x_{I\!P}$ central

Description	Name	Symbol
H1 hadronic energy scale	Eh scale, H1	$\delta_{had,H1}$
H1 electromagnetic energy scale	Ee scale, H1	$\delta_{ele,H1}$
H1 electron angle	theta e, H1	$\delta_{\theta,H1}$
H1 β reweighting	beta, H1	$\delta_{\beta,H1}$
H1 $x_{I\!P}$ reweighting	xIP, H1	$\delta_{x_{I\!P},H1}$
H1 t reweighting	t, H1	$\delta_{t,H1}$
H1 Q^2 reweighting	Q2, H1	$\delta_{Q^2,H1}$
H1 leading proton energy	EpFPS, H1	$\delta_{E_p,H1}$
H1 horizontal projection of the leading proton transverse momentum	PxFPS, H1	$\delta_{p_x,H1}$
H1 vertical projection of the leading proton transverse momentum	PyFPS, H1	$\delta_{p_y,H1}$
H1 event vertex reconstruction	vtx, H1	$\delta_{vtx,H1}$
H1 background subtraction (DD, PHP and proton beam halo)	bgn, H1	$\delta_{bgn,H1}$
H1 bin centre corrections	bcc, H1	$\delta_{bcc,H1}$
H1 global normalisation	norm, H1	$\delta_{norm,H1}$
ZEUS hadronic energy scale	Eh scale, ZEUS	$\delta_{had,Z}$
ZEUS electromagnetic energy scale	Ee scale, ZEUS	$\delta_{ele,Z}$
ZEUS $x_{I\!P}$ reweighting	xIP, ZEUS	$\delta_{x_{I\!P},Z}$
ZEUS t reweighting	t, ZEUS	$\delta_{t,Z}$
ZEUS DD background subtraction	bgn, ZEUS	$\delta_{bgn,Z}$
ZEUS global normalisation	norm, ZEUS	$\delta_{norm,Z}$

Table 4.1: *Correlated sources of systematic uncertainties from the H1 and ZEUS Proton Spectrometer measurements [46, 51].*

values differ. Therefore, prior to be combined, the ZEUS points were interpolated to the H1 binning scheme using the NLO QCD fit ZEUS SJ [59] (see Sect. 1.3.4.1). Most of the swimming factors have a moderate value, $< 10\%$, while few points undergo a significant swim, up to $\sim 40\%$.

For the combination procedure, 20 independent sources of correlated systematic uncertainties, including global normalisations, were considered. In the H1 case, all the systematic sources documented in [46] have been treated as point-to-point correlated, since no explicit prescriptions are given. In the ZEUS case, the total systematic uncertainties given in [51] have been separated between correlated and uncorrelated sources following the prescriptions in [59] and

have been symmetrised before performing the averaging[1].

The list of correlated systematic sources is given in Table 4.1. All the systematic uncertainties were treated as independent between H1 and ZEUS.

4.3.3 Normalisation and t-slope

As already mentioned in Sect 3.4, the Proton Spectrometer results play a key role in diffraction, since they fix the absolute normalisation of the diffractive DIS reduced cross section. However there is a difference in the normalisation, covered by the experimental uncertainties, between the H1 and ZEUS proton-tagged measurements. The ratio of the H1 FPS to ZEUS LPS data, over the measured kinematic range is [46]:

$$\frac{\text{H1 FPS}}{\text{ZEUS LPS}} = 0.85 \pm 0.01(stat) \pm 0.03(sys)^{+0.09}_{-0.12}(norm) \ , \tag{4.7}$$

which is consistent with unity taking into account the normalisation uncertainties of 6% and $^{+11}_{-7}$% for the H1 FPS and ZEUS LPS data, respectively. The possible sources of this 15% difference in normalisation between the H1 and ZEUS measurements were carefully investigated, prior to combining the results. It was found that a large portion of the 15% normalisation difference is due to the difference of the t-slope parameter b, introduced in Eq. (1.20), measured by the two experiments. Since the Proton Spectrometers have a limited acceptance in t, the reduced cross section $\sigma_r^{D(3)}(\beta, Q^2, x_{I\!P})$, defined as the integral of $\sigma_r^{D(4)}(\beta, Q^2, x_{I\!P}, t)$ over the extended t-range $|t| < 1$ GeV2,is obtained by extrapolating the proton-tagged data from the visible to the extended t-range, using the value of the t-slope at each $(\beta, Q^2, x_{I\!P})$ point.

The differences between the H1 and ZEUS experiments in the integration over t of the visible cross section are summarised as follow:

H1 FPS [46] :

At low $x_{I\!P}$, the data are compatible with a constant t-slope parameter, $b \simeq 6$ GeV^{-2}. A weak decrease of the b-parameter value from 6 GeV^{-2} to less than 5 GeV^{-2} is observed towards larger values of $x_{I\!P} \gtrsim 0.05$, attributed to the Reggeon exchange contribution. No significant Q^2 or β dependence is observed. The integration over t of the reduced cross section from the visible range $0.1 < |t| < 0.7$ GeV^2 to $|t_{min}|^{\,2} < |t| < 1$ GeV^2 is performed algebraically. The extrapolation factor amounts to a value of ~ 1.8 with an uncertainty of 4%, included in the global normalisation uncertainty, and depends weakly on $x_{I\!P}$.

ZEUS LPS [51] :

The value of the t-slope parameter is $b = 7.0 \pm 0.3$ GeV^{-2} in the region $0.0002 < x_{I\!P} < 0.01$ and $b = 6.9 \pm 0.3$ GeV^{-2} in the high $x_{I\!P}$ region, $0.01 < x_{I\!P} < 0.1$. The value of the t-slope in

[1] The result of the average is insensitive to the details of the symmetrisation procedure.

[2] $|t_{min}|$ is the minimum kinematically accessible value of $|t|$ and is defined as $|t_{min}| = -\frac{x_{I\!P}^2 m_p^2}{1-x_{I\!P}}$.

different bins of Q^2, M_X and $x_{I\!P}$ shows no dependence on the kinematics. The integration over t of the reduced cross section from the visible range $0.09 < |t| < 0.55$ GeV^2 to the extended t-range ($|t| < 1$ GeV^2) is hidden in the acceptance corrections estimated through the Monte Carlo, assuming a constant value of $b = 7.0$ GeV^{-2}. The extrapolation factor is of the order of 2 and introduces a normalisation uncertainty of +9%.

To correct for the differences in normalisation introduced with the integration over t, the H1 FPS measurement was restricted to the visible t-range common to the two experiments, namely $0.09 < |t| < 0.55$ GeV^2. In this kinematic region the normalisation uncertainties become 4.5% and 7% for the H1 FPS and ZEUS LPS data, respectively, and the difference in normalisation reduces to:

$$\frac{\text{H1 FPS}}{\text{ZEUS LPS}} = 0.91 \pm 0.01(stat) \pm 0.03(sys) \pm 0.08(norm) \ . \tag{4.8}$$

The combination of the H1 FPS and ZEUS LPS data was performed both in the visible and in the extended t-ranges. In both cases the normalisation of the input measurements was left free to vary in the averaging procedure, without any external assumption.

A comparison of the H1 and ZEUS input cross sections in the visible t-range is shown in Figs. 4.1 and 4.2 as a function of $x_{I\!P}$ and Q^2, respectively [1]. The same comparison in the extended t-range is shown in Fig. 1.17.

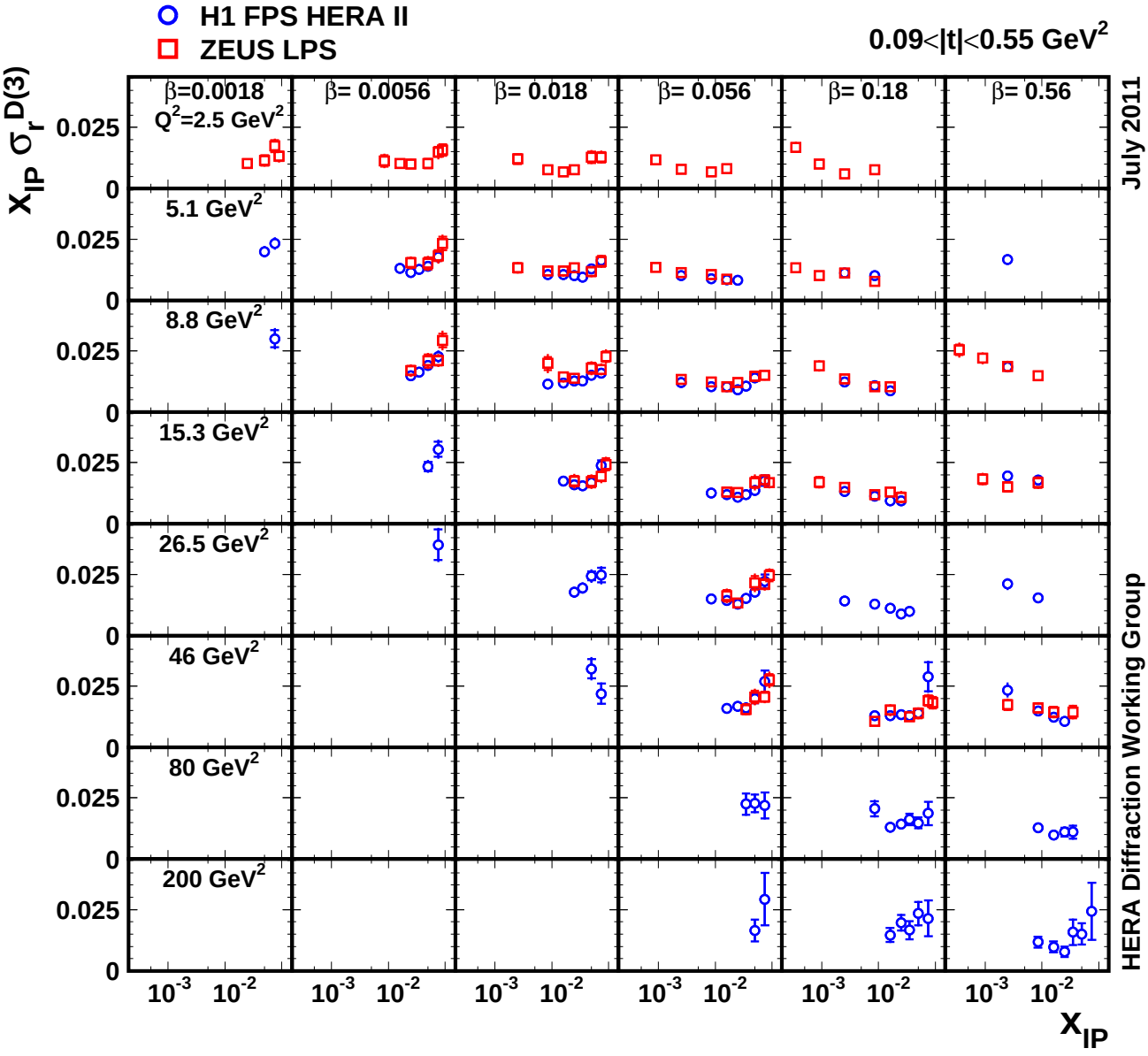

Figure 4.1: *The H1 FPS and ZEUS LPS reduced diffractive cross sections* $x_{I\!P}\sigma_r^{D(3)}(\beta, Q^2, x_{I\!P})$ *as a function of* $x_{I\!P}$ *for different values of* β *and* Q^2.

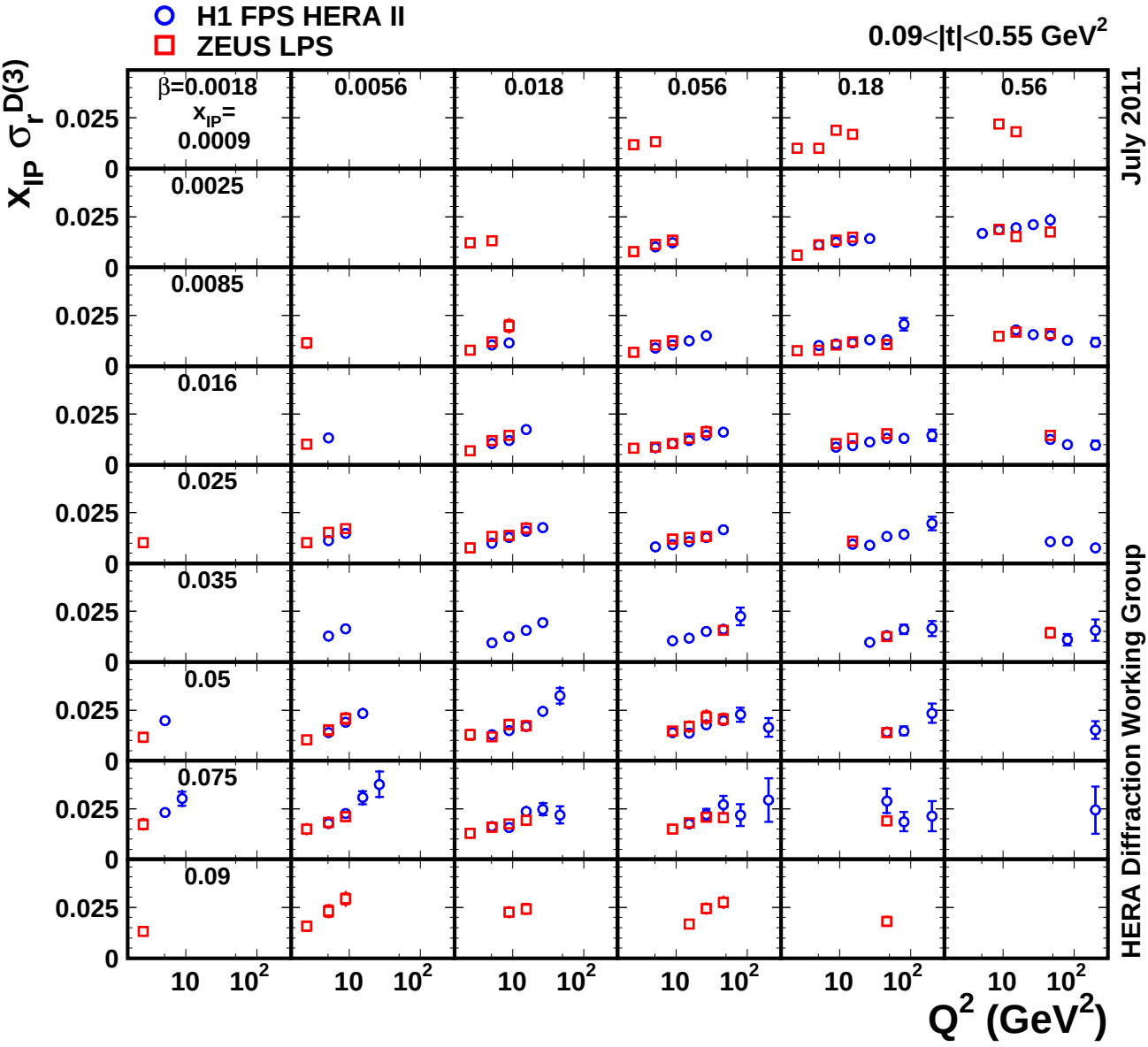

Figure 4.2: *The H1 FPS and ZEUS LPS reduced diffractive cross sections $x_{I\!P}\sigma_r^{D(3)}(\beta, Q^2, x_{I\!P})$ as a function of Q^2 for different values of β and $x_{I\!P}$.*

4.3.4 Combined Proton Spectrometer Cross Section in the Visible t-range

The results discussed in this Section are available in [1] and have been presented in [92].

4.3.4.1 Consistency between Data Sets and Pull Distributions

In the minimisation procedure, 227 data points are combined to 169 cross section measurements. The data show good consistency, with $\chi^2/n_{dof} = 52/58$. For a standard weighted average the resulting χ^2/n_{dof} is 38/58.

The distributions of pulls, $p^{i,e}$, exhibit no tensions between the two input data sets across the kinematic plane, as shown in Fig. 4.3. Since there are only two input data sets, the pull distributions for the H1 and ZEUS data are symmetric.

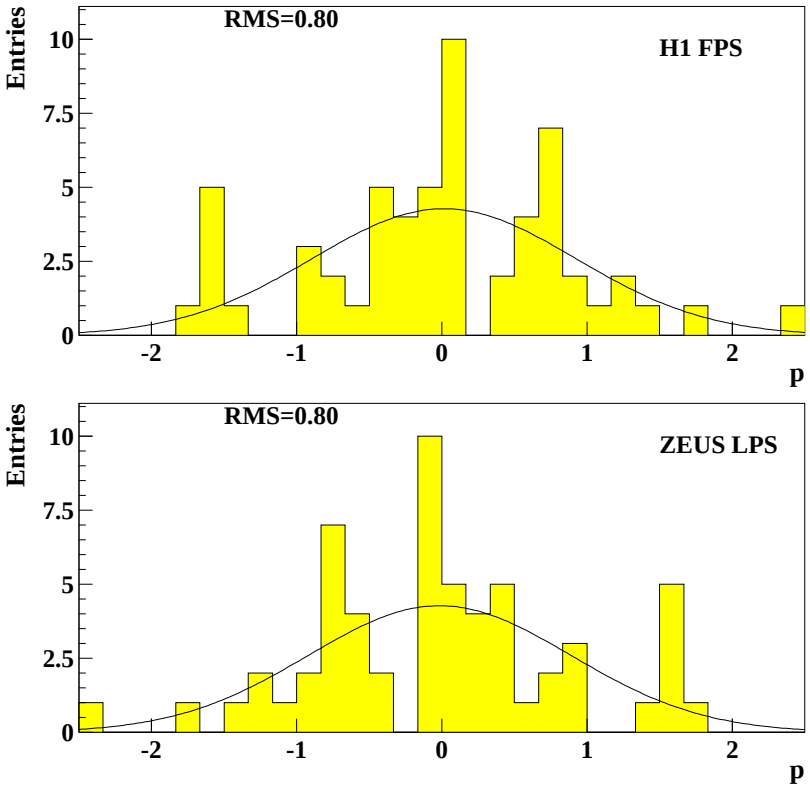

Figure 4.3: *Distributions of pulls p in the visible t-range. There are no entries outside the histogram range. RMS gives the root mean square of the distributions. The curves show the result of a Gaussian fit to the distributions.*

Correlated source	b	γb (%)
Eh scale, H1	-1.62	63.6
Ee scale, H1	0.93	89.5
theta e, H1	0.53	74.4
beta, H1	0.11	93.1
xIP, H1	0.09	98.8
t, H1	1.08	83.1
Q2, H1	0.22	98.4
EpFPS, H1	0.42	51.1
PxFPS, H1	0.66	80.1
PyFPS, H1	-0.43	90.8
vtx, H1	-0.14	98.1
bgn, H1	0.27	92.3
bcc, H1	-0.42	91.1
norm, H1	0.10	90.6
Eh scale, ZEUS	0.12	60.2
Ee scale, ZEUS	0.17	68.3
xIP, ZEUS	-0.24	99.0
t, ZEUS	-0.39	89.4
bgn, ZEUS	0.15	96.0
norm, ZEUS	-0.16	75.4

Table 4.2: *For each source of correlated uncertainty, the shifts resulting from the combination (b), in σ units, and the reduction in percent of the original uncertainty (γb) are given (visible t-range).*

None of the 20 sources of correlated systematic uncertainties shifts by more than 2σ of the nominal value in the averaging procedure, and only the shift related to the H1 hadronic energy scale exceeds 1σ. The distribution of pulls for the correlated systematic sources, p_s, is given in Fig. 4.4. The shifts of the correlated systematic uncertainties are summarised in Table 4.2.

The influence of several correlated systematic uncertainties is reduced significantly for the combined result. Notably, the contribution of the H1 uncertainty in the leading proton energy is reduced by a factor of 2. Since H1 and ZEUS use different reconstruction methods, similar systematic sources influence the measured cross section differently as a function of the kinematics. Therefore, requiring the cross sections to agree at all (β, Q^2, $x_{I\!P}$) points constrains the

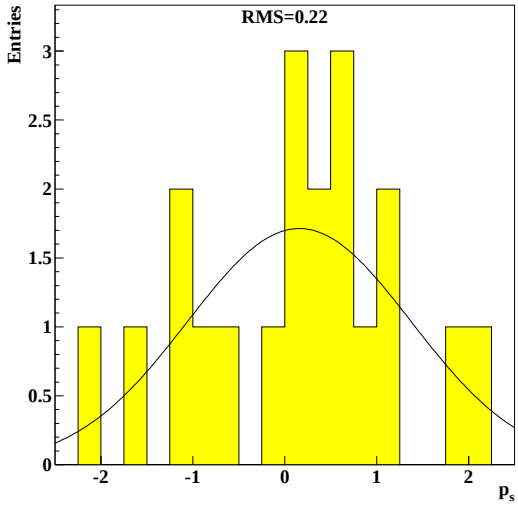

Figure 4.4: *Distribution of pulls, p_s, for correlated systematic uncertainties in the visible t-range. There are no entries outside the histogram range. RMS gives the root mean square of the distribution. The curve shows the result of a Gaussian fit to the distribution.*

the systematics efficiently. In addition, for certain regions of the phase space, one of the two experiments has superior precision compared to the other. For these regions, the less precise measurement is fitted to the more precise one, with a simultaneous reduction of the correlated systematic uncertainty. This reduction propagates to the other average points, including those which are based only on the measurement from the less precise experiment. Thanks to this cross calibration effect, the combined measurement shows an average improvement in accuracy and precision of about 20% with respect to the original H1 data, though they have a statistics 5 times larger than the ZEUS sample.

Some studies have been performed on the systematic source related to the H1 hadronic energy scale to understand the origin of the large shift by 1.6σ. A possible explanation is the H1 reconstruction strategy of the diffractive variables, which uses different reconstruction methods according to the kinematic region considered [46]. In fact, the $x_{I\!P}$ variable is always reconstructed directly from the leading proton energy information measured in the Forward Proton Spectrometer, while β is reconstructed as $\beta = x/x_{I\!P}$, from Eq. (1.36), exploiting the FPS information, in the range $x_{I\!P} > 0.012$, and from the hadronic final state information reconstructed in the central detector for $x_{I\!P} < 0.012$. Therefore, the contribution of this systematic error source becomes relevant only at lowest $x_{I\!P}$ values. A possible solution is to treat the H1 hadronic energy scale as a point-to-point uncorrelated error source, as no explicit prescriptions are given on its nature and the choice to consider it as correlated has been purely arbitrary. Other H1

systematic sources could be treated as uncorrelated, namely the sources related to the event vertex reconstruction efficiency, the bin centre corrections and the background subtraction. This alternative treatment of H1 systematic errors has been studied as a procedural uncertainty, as described in the next Section.

4.3.4.2 Procedural Uncertainties

A series of uncertainties which may affect the combined measurement due to the combination procedure were studied. All the following effects are considered and treated as correlated procedural errors; for each data point, the ratio of the alternative to the nominal average is extracted and summed in quadrature to the total uncertainty.

The χ^2 function given by Eq. (4.3) treats all systematic uncertainties as multiplicative, i.e. proportional to the expected central values. To study the sensitivity of the average result to this assumption, an alternative averaging is performed, for which only normalisation uncertainties are taken as multiplicative while all other uncertainties are treated as additive. The difference between this average and the nominal average result is of the order of 4%.

The H1 and ZEUS experiments use similar methods for detector calibration, apply similar reweighting to the Monte Carlo for the acceptance corrections and employ similar Monte Carlo simulation models for radiative corrections, for the hadronic final state simulation and for the proton-dissociation background subtraction. Such similarities may lead to correlations between measurements. Four sources of similar systematic uncertainties of the two experiments were identified. These are related to the electromagnetic energy scale of the calorimeter of the main detector, the proton dissociation background and the $x_{I\!P}$ and t reweighting. Then 2^4 different averages are calculated assuming each of the 4 pairs to be correlated or uncorrelated and all the alternative averages are compared to the nominal average for which all sources are assumed to be uncorrelated. The differences between these averages is around 1% with no particular dependence on the kinematics.

In the nominal average the systematic error sources of the H1 FPS measurement [46] are all considered as point-to-point correlated. An alternative average is performed considering the hadronic energy scale, the event vertex reconstruction, the bin centre corrections and the background subtraction as uncorrelated errors. The difference with the nominal case is on average below 1%, increasing up to 10% for the lowest $x_{I\!P}$ bin, where it is driven by the hadronic energy scale.

The bias introduced by interpolating the ZEUS data to the H1 binning scheme has been studied by using swimming factors obtained from the NLO QCD fit H1 'Fit B' [48]. The estimated overall effect is of the order of 1%.

4.3.4.3 Combined Cross Section

In Figs. 4.5 and 4.6, the combined data are compared to the H1 FPS and ZEUS LPS original data as a function of $x_{I\!P}$ and Q^2, respectively. The combined result extends the kinematic coverage with respect to the separate H1 and ZEUS measurements and the resulting cross section covers the region $2.5 \leq Q^2 \leq 200$ GeV^2, $0.0018 \leq \beta \leq 0.816$ and $0.0003 \leq x_{I\!P} \leq 0.09$, for $0.09 < |t| < 0.55$ GeV^2. The combination is driven by the H1 results, which are statistically more powerful.

Fig. 4.7 show a zoomed plot of the combined cross section as a function of Q^2 at $x_{I\!P} = 0.016$, for different values of β. The reduction of the total uncertainty of the HERA measurement compared to the input cross sections is visible. The rate of the growth of the reduced cross section with Q^2 depends on β - a clear illustration of the scaling violations in diffractive DIS.

Figs. 4.8 and 4.9 show the first HERA combined diffractive reduced cross section based on Proton Spectrometer data in the t-range common to both the H1 and the ZEUS spectrometers. The result shows an improvement in accuracy and precision in a wider kinematic coverage with respect to the H1 and ZEUS measurements, separately.

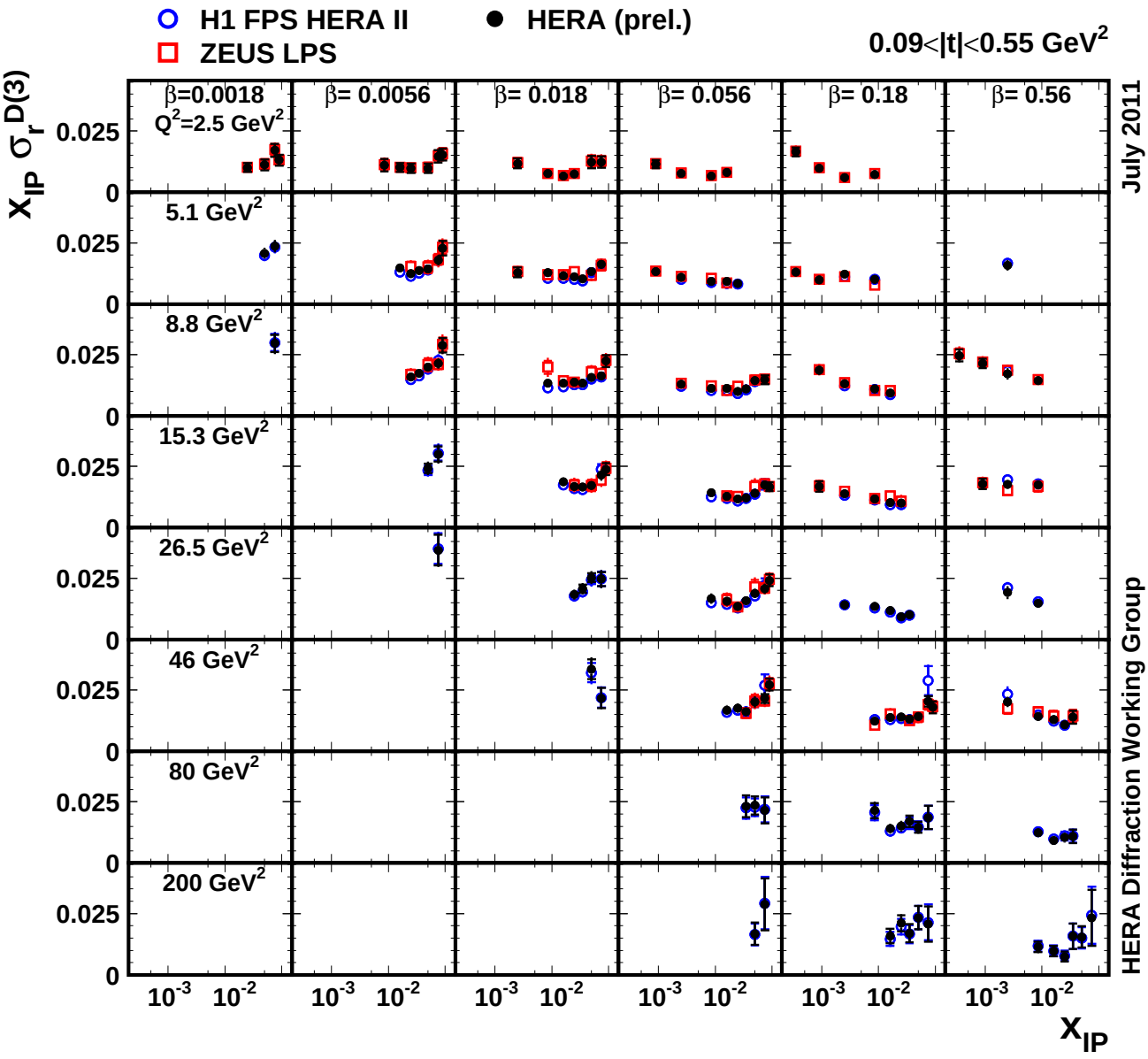

Figure 4.5: *HERA combined diffractive reduced cross section* $x_{I\!P}\sigma_r^{D(3)}(\beta, Q^2, x_{I\!P})$ *in the visible t-range as a function of* $x_{I\!P}$ *for different values of* β *and* Q^2*, compared to the separate H1 FPS [46] and ZEUS LPS [51] data.*

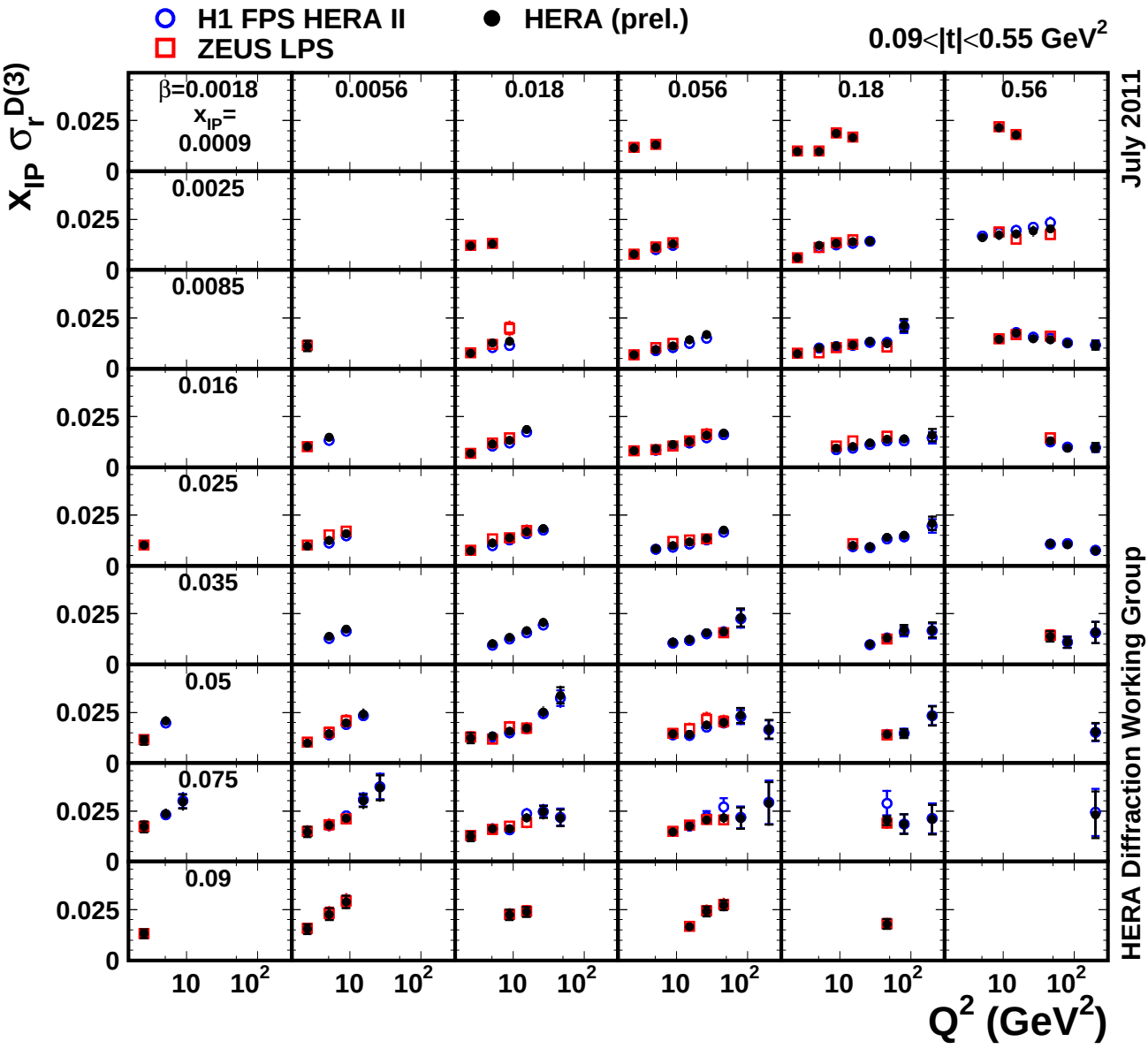

Figure 4.6: *HERA combined diffractive reduced cross section* $x_{I\!P}\sigma_r^{D(3)}(\beta, Q^2, x_{I\!P})$ *in the visible t-range as a function of* Q^2 *for different values of* β *and* $x_{I\!P}$*, compared to the separate H1 FPS [46] and ZEUS LPS [51] data.*

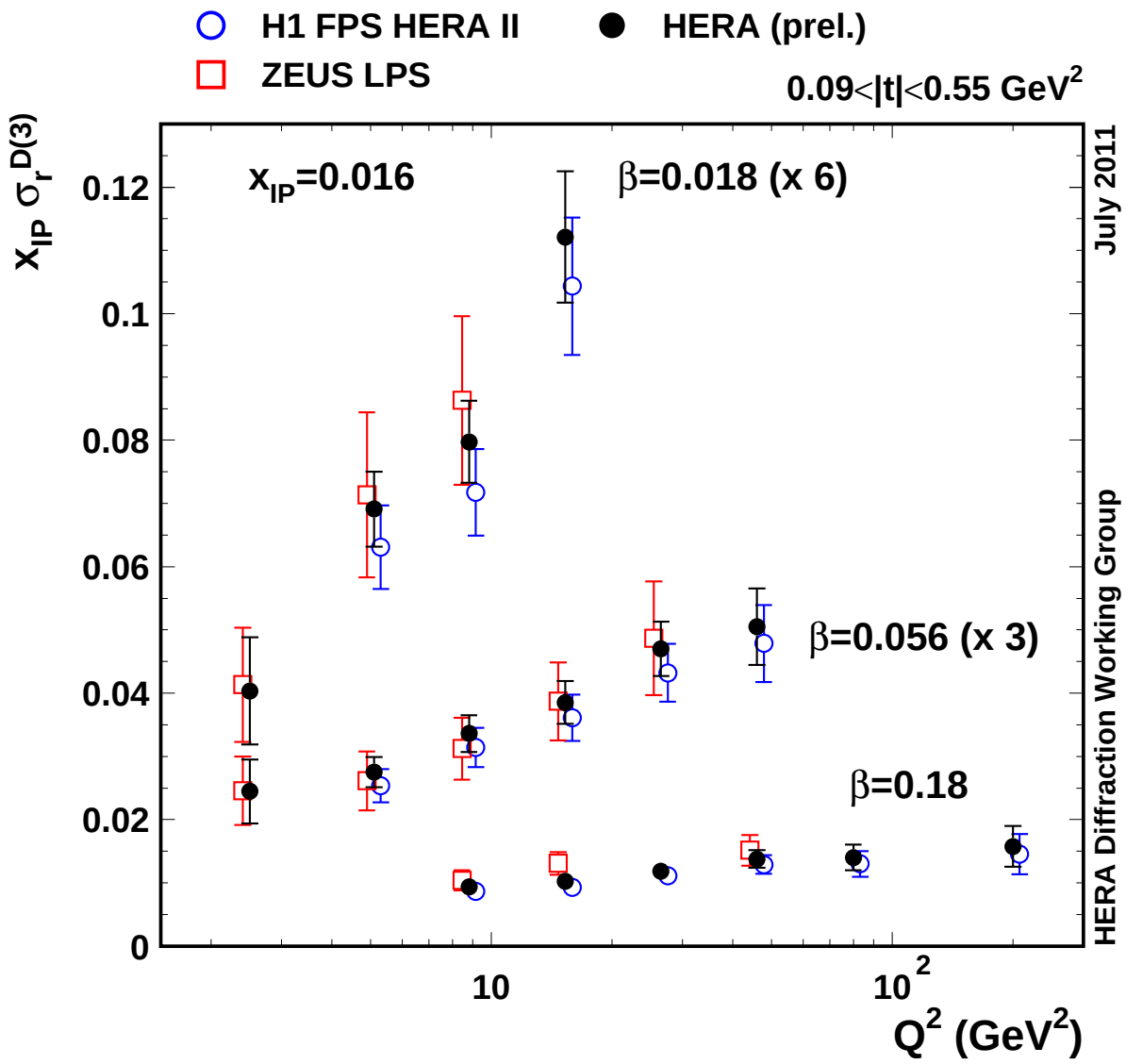

Figure 4.7: *HERA combined diffractive reduced cross section* $x_{I\!P}\sigma_r^{D(3)}(\beta, Q^2, x_{I\!P})$ *in the visible t-range as a function of* Q^2 *for three different* β *bins, at* $x_{I\!P} = 0.016$*, compared to the separate H1 FPS [46] and ZEUS LPS [51] data. The individual measurements are slightly displaced horizontally for better visibility.*

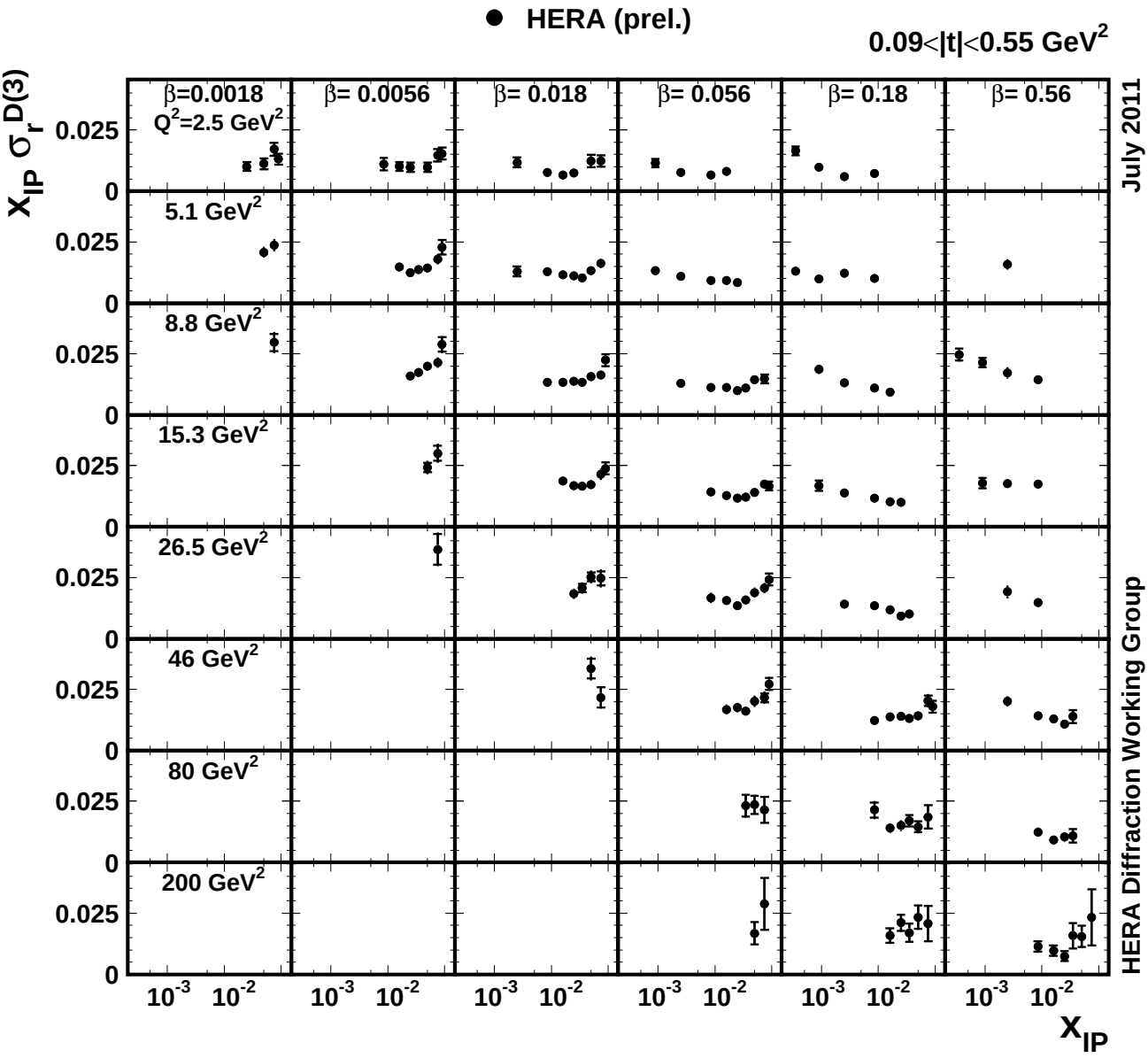

Figure 4.8: *HERA combined diffractive reduced cross section* $x_{I\!P}\sigma_r^{D(3)}(\beta, Q^2, x_{I\!P})$ *in the visible t-range as a function of* $x_{I\!P}$ *for different values of* β *and* Q^2.

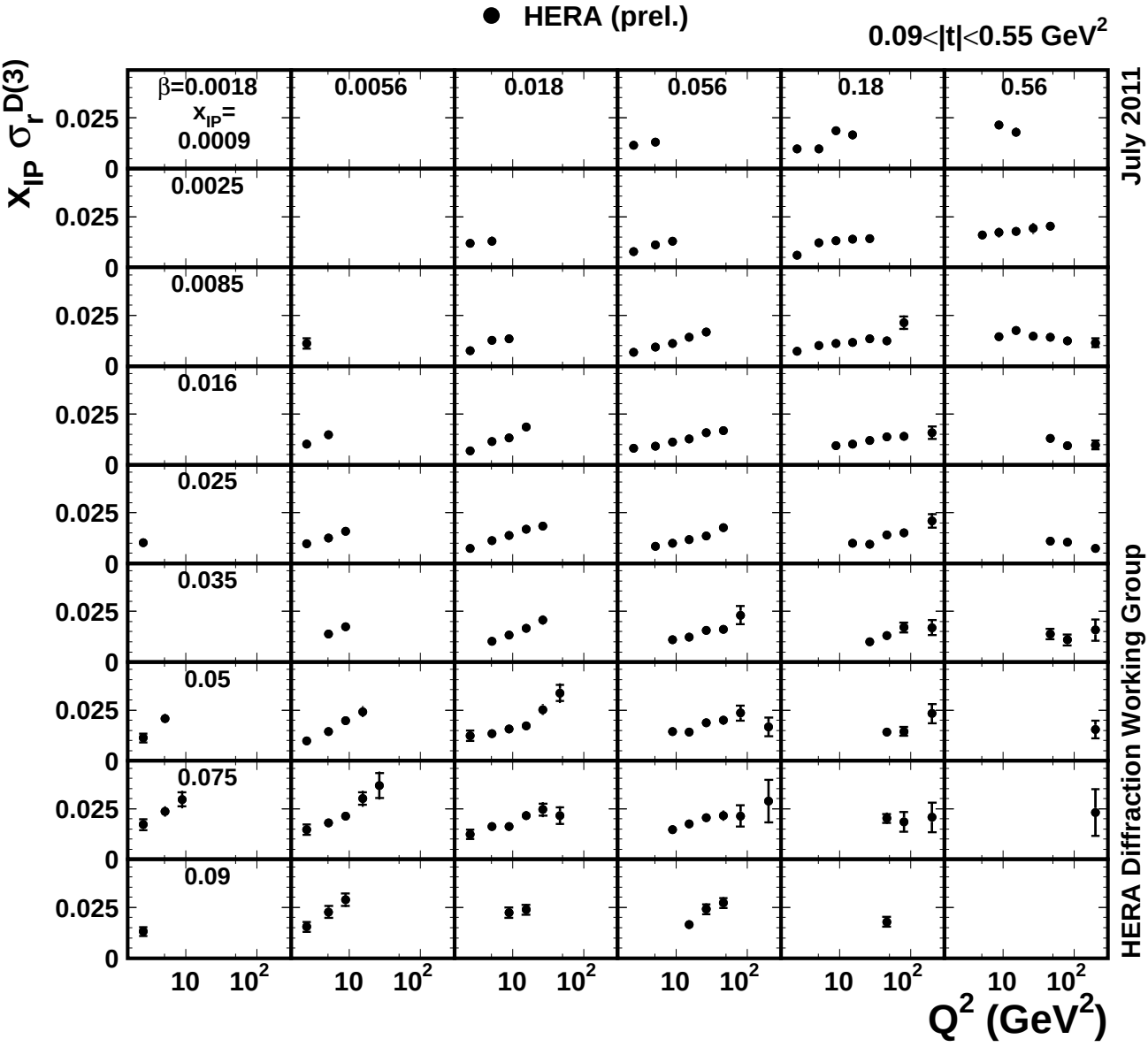

Figure 4.9: *HERA combined diffractive reduced cross section $x_{I\!P}\sigma_r^{D(3)}(\beta, Q^2, x_{I\!P})$ in the visible t-range as a function of Q^2 for different values of β and $x_{I\!P}$.*

Correlated source	b	γb (%)
Eh scale, H1	-1.72	63.8
Ee scale, H1	0.91	89.7
theta e, H1	0.55	75.1
beta, H1	0.23	93.1
xIP, H1	0.01	98.8
t, H1	0.70	82.9
Q2, H1	0.18	98.3
EpFPS, H1	0.31	50.4
PxFPS, H1	0.20	82.7
PyFPS, H1	-0.32	90.8
vtx, H1	-0.02	98.3
bgn, H1	-0.32	92.6
bcc, H1	0.06	91.4
norm, H1	0.68	88.7
Eh scale, ZEUS	-0.06	60.9
Ee scale, ZEUS	0.36	68.9
xIP, ZEUS	-0.08	99.1
t, ZEUS	-0.16	90.9
bgn, ZEUS	0.37	95.9
norm, ZEUS	-1.01	70.5

Table 4.3: *For each source of correlated uncertainty, the shifts resulting from the combination (b), in σ units, and the reduction in percent of the original uncertainty (γb) are given (extended t-range).*

4.3.5 Combined Proton Spectrometer Cross Section in the Extended t-range

The combination of the H1 and ZEUS cross sections in the extended t-range, follows the same procedure already discussed in Sect. 4.3.4 and summarised here.

The original 227 data points are combined to 169 cross section measurements. Also in this case good consistency is observed between the input H1 FPS and ZEUS LPS data, with $\chi^2/n_{dof} = 48/58$. The result from a standard weighted average is $\chi^2/n_{dof} = 51/58$.

The pull distributions for the combined points, $p^{i,e}$, and for the correlated systematics, p_s, are shown in Figs. 4.10 and 4.11, respectively. The shifts of the correlated systematic uncertainties

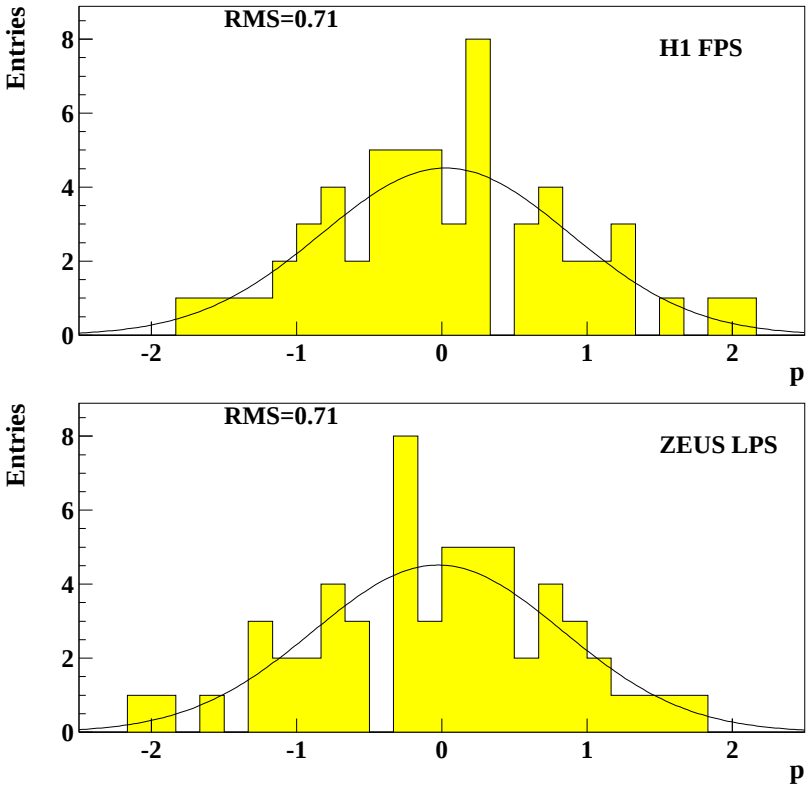

Figure 4.10: *Distributions of pulls p in the extended t-range. There are no entries outside the histogram range. RMS gives the root mean square of the distributions. The curves show the result of a Gaussian fit to the distributions.*

are summarised in Table 4.3.

Also in the extended t-range the influence of the correlated systematic uncertainties is reduced significantly by the combination and no particular tensions are observed between systematics. Only the H1 hadronic energy scale shift exceeds 1σ and reaches 1.7σ.

The evaluation of the procedural uncertainties and their values are the same discussed in Sect. 4.3.4.

The combined cross section compared to the published H1 FPS and ZEUS LPS measurements is shown as a function of $x_{I\!P}$ and Q^2 in Figs. 4.12 and 4.13, respectively.

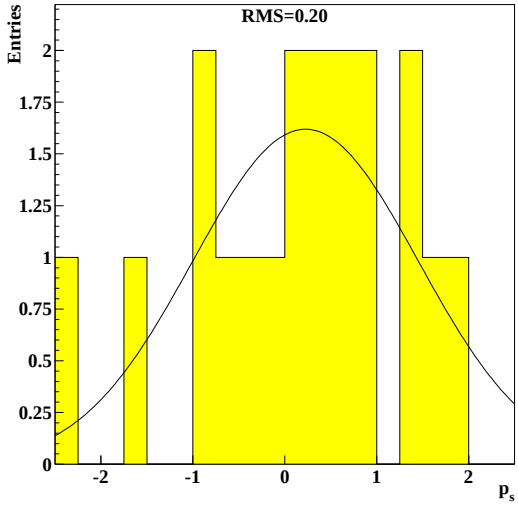

Figure 4.11: *Distribution of pulls p_s for correlated systematic uncertainties in the extended t-range. There are no entries outside the histogram range. RMS gives the root mean square of the distribution. The curve shows the result of a Gaussian fit to the distribution.*

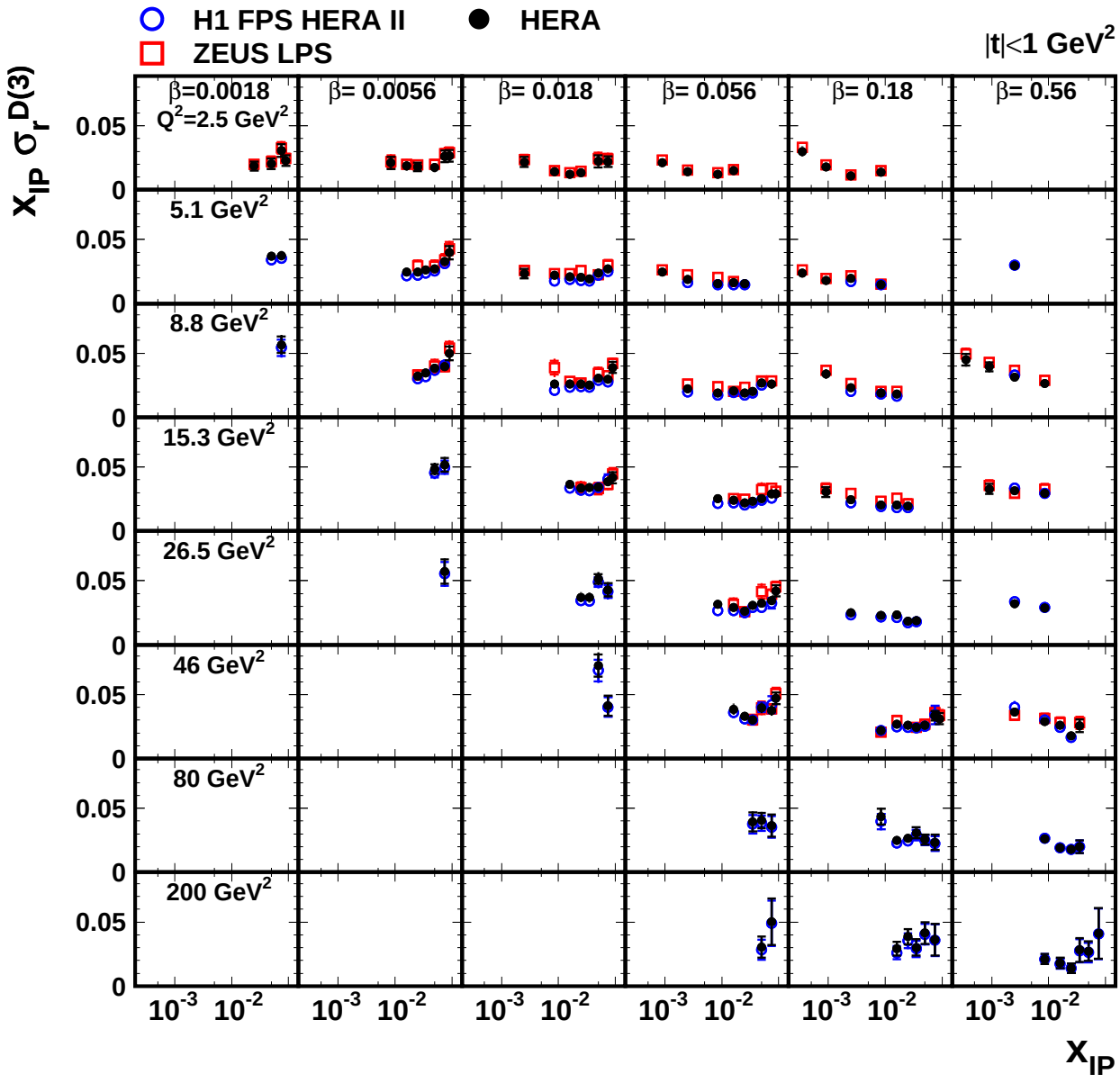

Figure 4.12: *HERA combined diffractive reduced cross section $x_{I\!P}\sigma_r^{D(3)}(\beta, Q^2, x_{I\!P})$ in the extended t-range as a function of $x_{I\!P}$ for different values of β and Q^2, compared to the separate H1 FPS [46] and ZEUS LPS [51] data.*

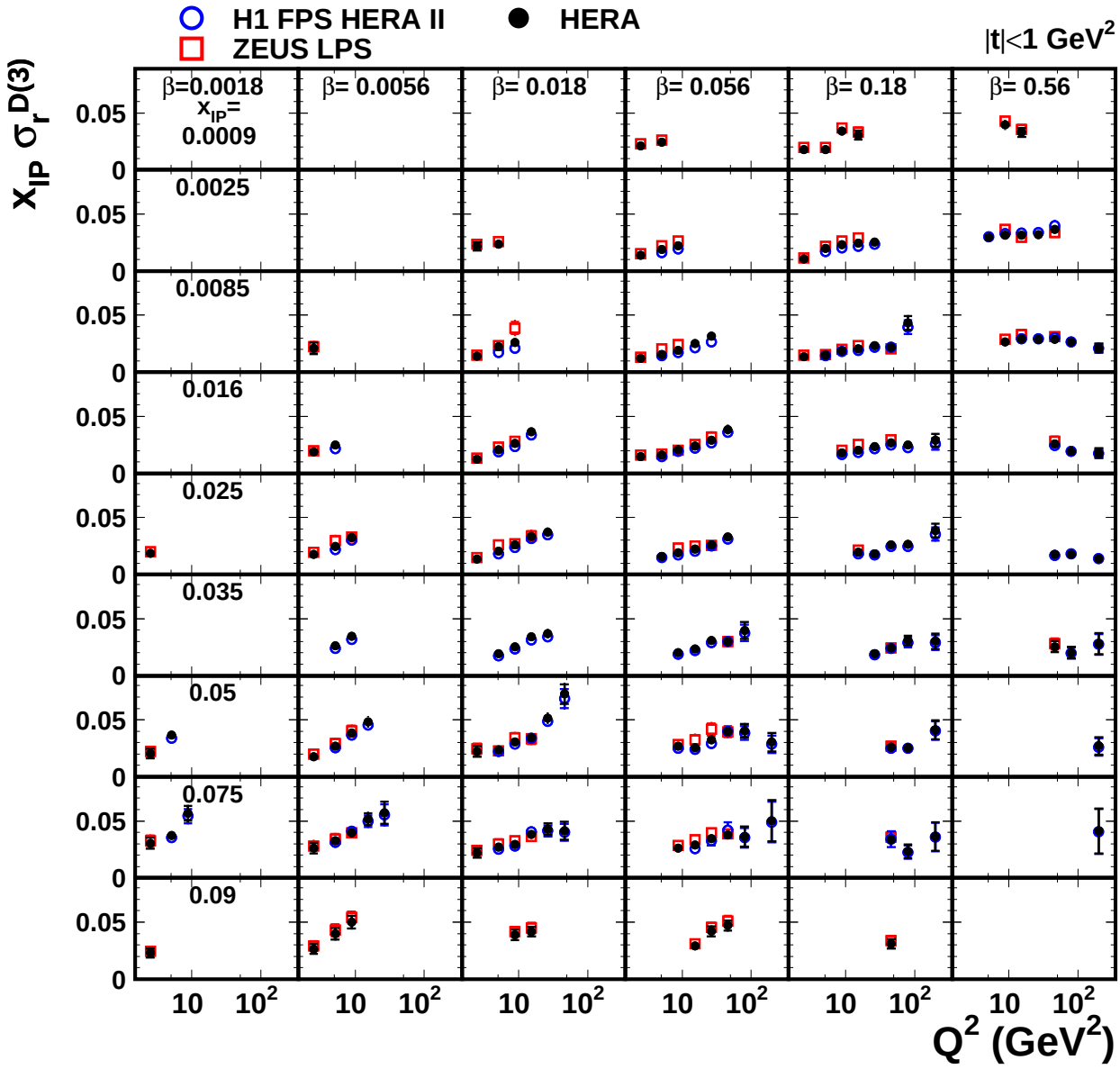

Figure 4.13: *HERA combined diffractive reduced cross section $x_{I\!P}\sigma_r^{D(3)}(\beta, Q^2, x_{I\!P})$ in the extended t-range as a function of Q^2 for different values of β and $x_{I\!P}$, compared to the separate H1 FPS [46] and ZEUS LPS [51] data.*

4.3.6 Discussion

The first combination of the HERA diffractive reduced cross sections $\sigma_r^{D(3)}$ from Proton Spectrometer data was carried out, both in the visible t-range common to FPS and LPS [1] and in the extended t-range. The combined result extends the kinematic coverage with respect to the separate H1 and ZEUS measurements and the resulting cross sections cover the region $2.5 \leq Q^2 \leq 200$ GeV^2, $0.0018 \leq \beta \leq 0.816$ and $0.0003 \leq x_{I\!P} \leq 0.09$. Thanks to the cross calibration between the two experiments, the combined measurement shows an average improvement in precision of about 20% with respect to the original H1 data, prior to including the contribution of the procedural uncertainties.

Some work is still needed towards a final result. The current proposal is to use the H1 systematic uncertainties related to the hadronic energy scale, the vertex reconstruction, the bin centre corrections and the background subtraction as uncorrelated sources. Moreover, a study on the 4% uncertainty arising from the comparison between a multiplicative rather than an additive treatment of the correlated uncertainties is needed. This 4% discrepancy suggests that probably a source of multiplicative nature has been treated as additive in the checks. Furthermore, two other data sets can be used as input for the combination: the H1 FPS HERA I data [45] and the ZEUS LPS 1997 data [50]. Though the statistics of these measurements is poorer than that of the present analysis, adding new samples can improve the cross calibration between different data sets and increase the degrees of freedom in the χ^2 minimisation.

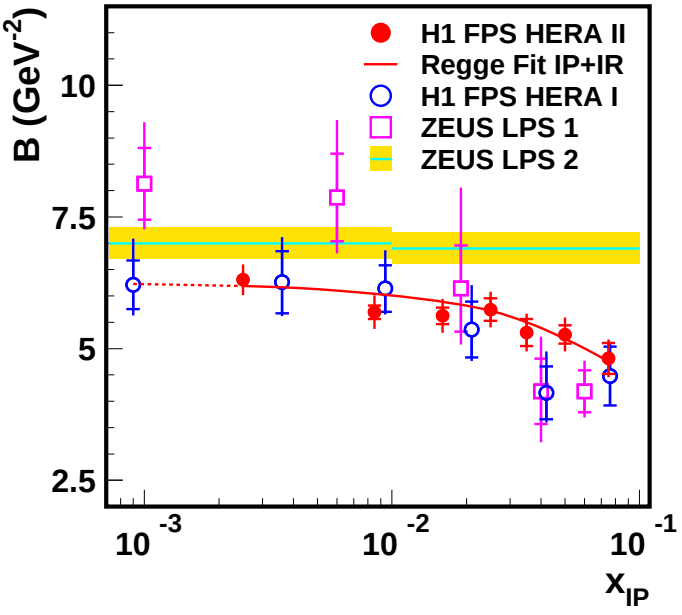

Figure 4.14: *A compilation of the t-slope parameter b from different H1 and ZEUS measurements.*

It is important to notice that the integration over t of the combined result would provide the absolute normalisation of the diffractive DIS reduced cross section. For this purpose, the value of the t-slope b is needed. Figure 4.14 summarises results of the t-slope measured by the H1 and ZEUS experiments [45, 46, 50, 51], as a function of $x_{I\!P}$. Efforts are being made by the Collaborations to extract a common b measurement from the Proton Spectrometer data.

For the time being, the HERA diffractive cross section in the extended t-range fixes the absolute normalisation of the DIS diffractive cross section.

4.4 Combination of LRG Cross Sections

4.4.1 Combined Data Sets

For the combination of the diffractive reduced cross sections from the Large Rapidity Gap data, the last published LRG results from H1 [48] and ZEUS [51] were used.

For the H1 LRG results different event samples were used for different Q^2 ranges of the measurement. For the interval $3 < Q^2 < 13.5$ GeV^2, a 'minimum bias' sample corresponding to an integrated luminosity of 2.0 pb^{-1} was used. For intermediate photon virtualities, $13.5 < Q^2 < 105$ GeV^2, data taken throughout 1997 were used, corresponding to an integrated luminosity of 10.6 pb^{-1}. The kinematic range $Q^2 > 133$ GeV^2 is covered by a sample corresponding to 61.6 pb^{-1}, taken in the years 1999 and 2000. The cross section is measured in the kinematic range $3.5 \leq Q^2 \leq 1600$ GeV^2, $0.0003 \leq x_{I\!P} \leq 0.1$ and $0.0017 \leq \beta \leq 0.8$. The y coverage is $0.04 < y < 0.63$ for $Q^2 < 890$ GeV^2 and $0.04 < y < 0.9$ for $Q^2 > 890$ GeV^2.

The ZEUS LRG sample was collected in the years 1999 and 2000, and corresponds to a luminosity of 62.4 pb^{-1}. The kinematic region covered by the data is $2 < Q^2 < 305$ GeV^2, $2 < M_X < 25$ GeV and $0.0002 < x_{I\!P} < 0.02$. The W range lies between 40 and 240 GeV.

For all samples, HERA collided positrons with protons, the positron beam energy being always $E_e = 27.5$ GeV. The proton beam energy was $E_p = 820$ GeV in 1997 and $E_p = 920$ GeV in 1999 and 2000, leading to ep centre-of-mass energies of $\sqrt{s} = 300$ GeV and $\sqrt{s} = 318$ GeV, respectively.

New H1 LRG measurements from 1999, 2000 and HERA I data [49] are still under analysis and not included in the present combination.

4.4.2 Binning Scheme and Correlated Systematic Sources

To be compared with the H1 results, the ZEUS LRG cross sections in [51] were extracted at the H1 β and $x_{I\!P}$ values, but at different Q^2 values. To account for the different Q^2 binning, the H1 data were interpolated to the ZEUS Q^2 values by applying small correction factors obtained with the 'H1 Fit B' parametrisation [48]. The value of swimming factors is small, between 2% and 5%.

Description	Name	Symbol
H1 hadronic energy scale of the Liquid Argon calorimeter	Eh LAr scale, H1	$\delta_{lar,H1}$
H1 hadronic energy scale of the Spaghetti calorimeter	Eh SpaCal scale, H1	$\delta_{spa,H1}$
H1 plug energy scale	Eh Plug scale, H1	$\delta_{Plug,H1}$
H1 electromagnetic energy scale	Ee scale, H1	$\delta_{ele,H1}$
H1 electron angle	theta e, H1	$\delta_{\theta,H1}$
H1 calorimeter noise treatment	noise, H1	$\delta_{noise,H1}$
H1 background subtraction	bgn, H1	$\delta_{bgn,H1}$
H1 β reweighting	beta, H1	$\delta_{\beta,H1}$
H1 $x_{I\!P}$ reweighting	xIP, H1	$\delta_{x_{I\!P},H1}$
H1 Q^2 reweighting	Q2, H1	$\delta_{Q^2,H1}$
ZEUS hadronic energy scale	Eh scale, ZEUS	$\delta_{had,Z}$
ZEUS electromagnetic energy scale	Ee scale, ZEUS	$\delta_{ele,Z}$
ZEUS energy threshold on LRG cut	Ecut, ZEUS	$\delta_{cut,Z}$
ZEUS $x_{I\!P}$ reweighting	xIP, ZEUS	$\delta_{x_{I\!P},Z}$

Table 4.4: *Correlated sources of systematic uncertainties from H1 [48] and ZEUS [51] LRG measurements.*

No corrections were applied to extrapolate the 1997 data to $\sqrt{s} = 318$ GeV. From Eq. (1.39), the diffractive reduced cross section depends weakly on the energy via the term containing the inelasticity y. For the y region covered by the 1997 input data, the effect is negligible compared to the experimental precision and therefore not considered.

In the combination procedure, 14 independent sources of correlated systematic uncertainties were considered. For the H1 data, the point-to-point correlated sources listed in [48] were used. In the ZEUS case, the total systematic uncertainties given in [51] were separated between correlated and uncorrelated sources following the prescriptions in [59] and were symmetrised before performing the fit. Global normalisation uncertainties of the H1 and ZEUS results were not included.

The list of correlated systematic sources is given in Table 4.4. All the systematic uncertainties were treated as independent between H1 and ZEUS.

4.4.3 Normalisation

As mentioned in Sect. 3.4, LRG results are affected by the presence of the double dissociative background (DD), which changes the normalisation of the measured cross sections, but not the

shape. The contribution of the DD background depends on the geometrical acceptance of the detector in the forward direction and therefore is different between H1 and ZEUS.

The studies on the proton dissociation contribution and relative normalisation of the H1 and ZEUS LRG measurements can be summarised as follows:

H1 LRG [48] :

The published H1 LRG results are corrected to $M_Y < 1.6$ GeV. A comparison with the HERA I FPS measurement [45] gives a ratio of the cross sections for $M_Y < 1.6$ GeV and $M_Y = m_p$ of $1.23 \pm 0.03(stat) \pm 0.16(sys)$, which is consistent with a Monte Carlo prediction of $1.15^{+0.15}_{-0.08}$.

ZEUS LRG [51] :

The contribution of double dissociative background for ZEUS LRG results is estimated, both through a comparison with ZEUS LPS results and a Monte Carlo study, to be $25 \pm 1(stat) \pm 3(sys)\%$. A factor of 0.91 ± 0.07, evaluated with a Monte Carlo study, provides the correction of the ZEUS data to the H1 M_Y range, $M_Y < 1.6$ GeV. Despite the correction to the H1 M_Y range, the ZEUS data are higher than the H1 data by 13% on average, as estimated with a global fit to data with $Q^2 > 6$ GeV^2. This normalisation discrepancy is consistent with the 8% uncertainty on the proton-dissociation correction of 0.91 ± 0.07 combined with the 7% relative normalisation uncertainty between the two data sets ($\pm$7% for H1 and $\pm$2.25% for ZEUS).

Several averages have been performed, with different normalisation of the input data sets. It has been observed that the fit results are independent of the input global normalisation and that the resulting shape of the combined cross section is also not affected. Hence the decision was made to scale the ZEUS results by a factor 0.91×0.87, thus fixing the normalisation to that of the H1 measurement.

The final result can be corrected to $M_Y = m_p$ by using the information from the Proton Spectrometer cross sections. The 7% relative normalisation uncertainty between H1 and ZEUS data sets can be considered as the global normalisation uncertainty of the combined HERA LRG measurement.

4.4.4 Combined LRG Cross Section

The results discussed in this Section have been presented in [93] and follow previous attempts to combine HERA LRG diffractive cross sections [89].

In the minimisation procedure, 494 individual measurements were averaged to 341 points. The fit reveals some inconsistency between the data sets, with $\chi^2/n_{dof} = 366/153$. To improve the quality of the combination a region where the disagreement between the H1 and ZEUS measurements is significant was identified and excluded: a cut on the mass of the hadronic final

state X, M_X, was applied to reject the region where the reconstruction of the kinematic variables is affected by the contribution of detector noise and where vector meson production dominates. Only measured points with $M_X > 4$ GeV were hereafter included in the combination[3]. After such selection, the combined points reduce to 268 and the consistency between the two experiments results improves, with $\chi^2/n_{dof} = 146/113$. For a standard weighted average the χ^2/n_{dof} is 140/113.

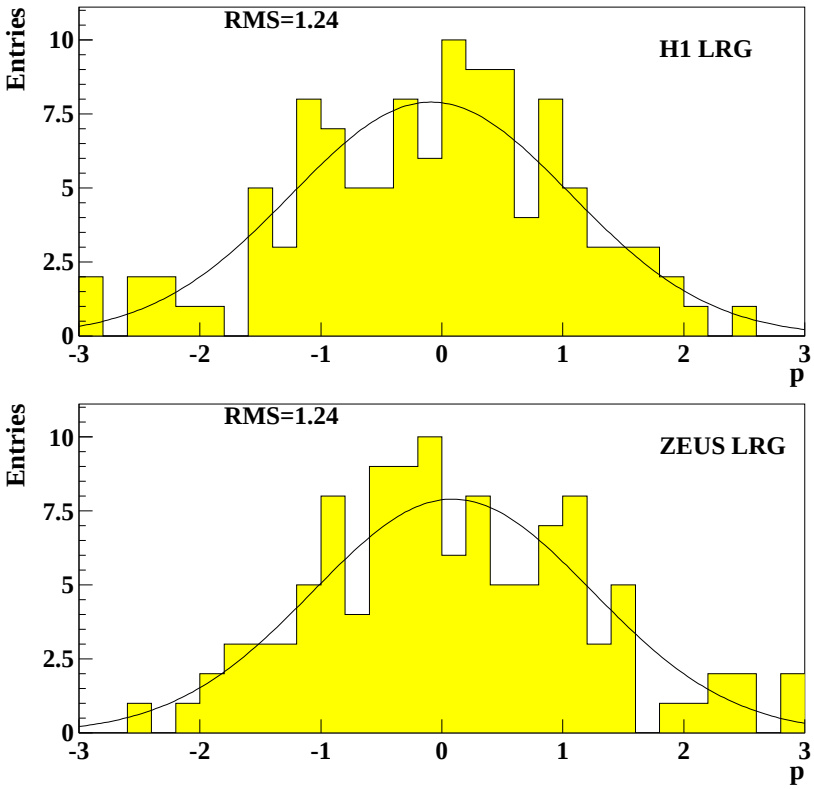

Figure 4.15: *Distributions of pulls p of the input H1 [48] and ZEUS [51] LRG data sets. There are no entries outside the histogram range. RMS gives the root mean square of the distributions. The curves show the result of a Gaussian fit to the distributions.*

The distributions of pulls, $p^{i,e}$, for the input data sets are shown in Fig. 4.15. The value of $RMS = 1.24$ reveals a weak tension between the H1 and ZEUS data. A careful study of the pulls as a function of the kinematics shows that the tensions are equally distributed across the

[3]Since $\beta = Q^2/(M_X^2 + Q^2)$, cutting on the M_X variable corresponds implicitly to cutting on Q^2 and β.

phase space and it is not possible to isolate a region where the disagreement concentrates.

Correlated source	b	γb (%)
Eh LAr scale, H1	0.73	81.5
Eh SpaCal scale, H1	0.34	75.8
Eh Plug scale, H1	-0.17	92.5
Ee scale, H1	1.86	52.3
theta e, H1	-0.06	70.9
noise, H1	-0.71	47.9
bgn, H1	0.06	61.1
beta, H1	-0.23	88.2
xIP, H1	-0.47	91.2
Q2, H1	0.52	95.2
Eh scale, ZEUS	-0.75	71.5
Ee scale, ZEUS	0.66	64.5
Ecut, ZEUS	-0.50	96.9
xIP, ZEUS	0.59	77.8

Table 4.5: *For each source of correlated uncertainty, the shifts resulting from the combination (b), in σ units, and the reduction in percent of the original uncertainty (γb) are given (LRG data).*

The distribution of pulls for the 14 correlated systematic uncertainties, p_s, is shown in Fig. 4.16 and the shifts are summarised in Table 4.5. All systematic errors shift by less than 1σ from the nominal value in the averaging procedure, with the exception of the H1 electromagnetic energy scale, which shifts by 1.8σ. Several correlated systematic uncertainties are reduced significantly; notably, the contribution of the H1 calorimeter noise is reduced by more than a factor of 2.

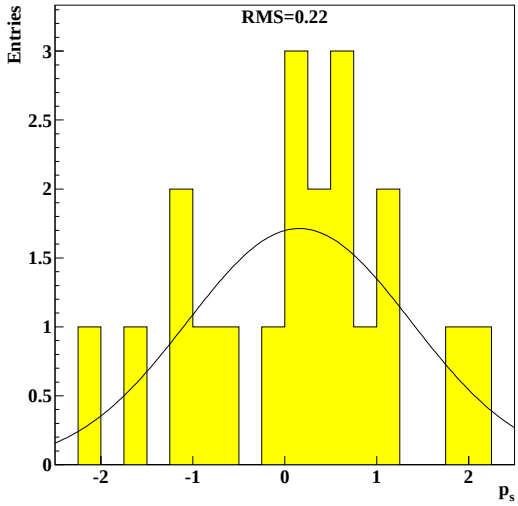

Figure 4.16: *Distribution of pulls p_s for correlated systematic uncertainties from LRG data fit. There are no entries outside the histogram range. RMS gives the root mean square of the distribution calculated as $\bar{p^2}$. The curve shows the result of binned log-likelihood Gaussian fit to the distribution.*

Figures from 4.17 to 4.19 show the combined HERA LRG data compared to the input H1 and ZEUS measurements, as a function of Q^2 for different values of β and $x_{I\!P}$. The combined measurement is driven by the ZEUS results, statistically more powerful, and it shows an average 17% improvement in accuracy and precision with respect to the input ZEUS data. Thanks to the reduction of several systematic uncertainties, the fitting procedure allows to gain $\sim 9\%$ in precision with respect to the standard weighted average. The kinematic region covered by the HERA LRG combined cross section is $2.5 \leq Q^2 \leq 1600$ GeV^2, $0.0017 \leq \beta \leq 0.8$ and $0.0003 \leq x_{I\!P} \leq 0.03$, for $M_X > 4$ GeV.

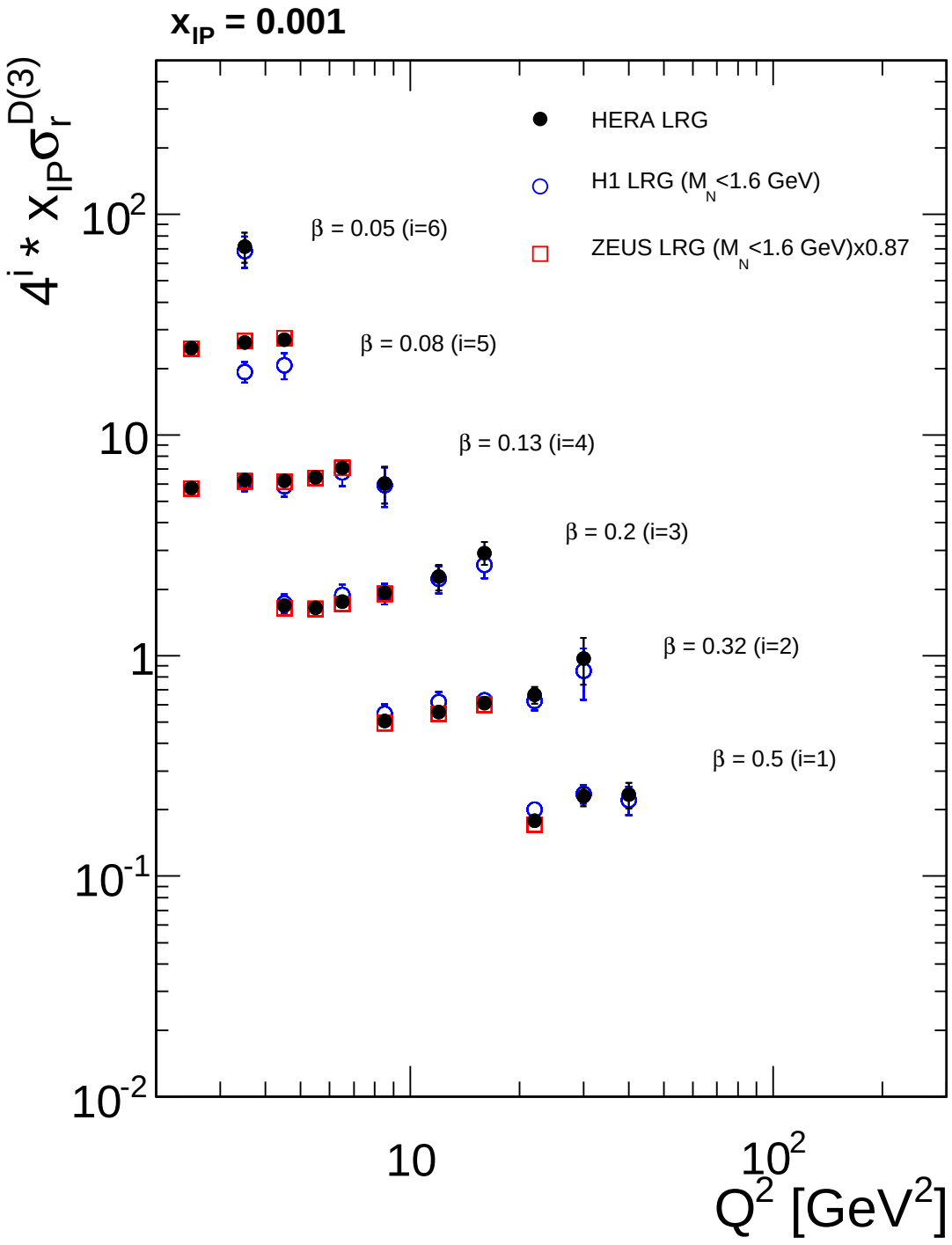

Figure 4.17: *HERA LRG combined diffractive reduced cross section* $x_{I\!P}\sigma_r^{D(3)}(\beta, Q^2, x_{I\!P})$ *as a function of* Q^2 *for different values of* β *, at* $x_{I\!P} = 0.001$*. Data are multiplied by a factor of* 4^i *for visibility, with* i *as indicated.*

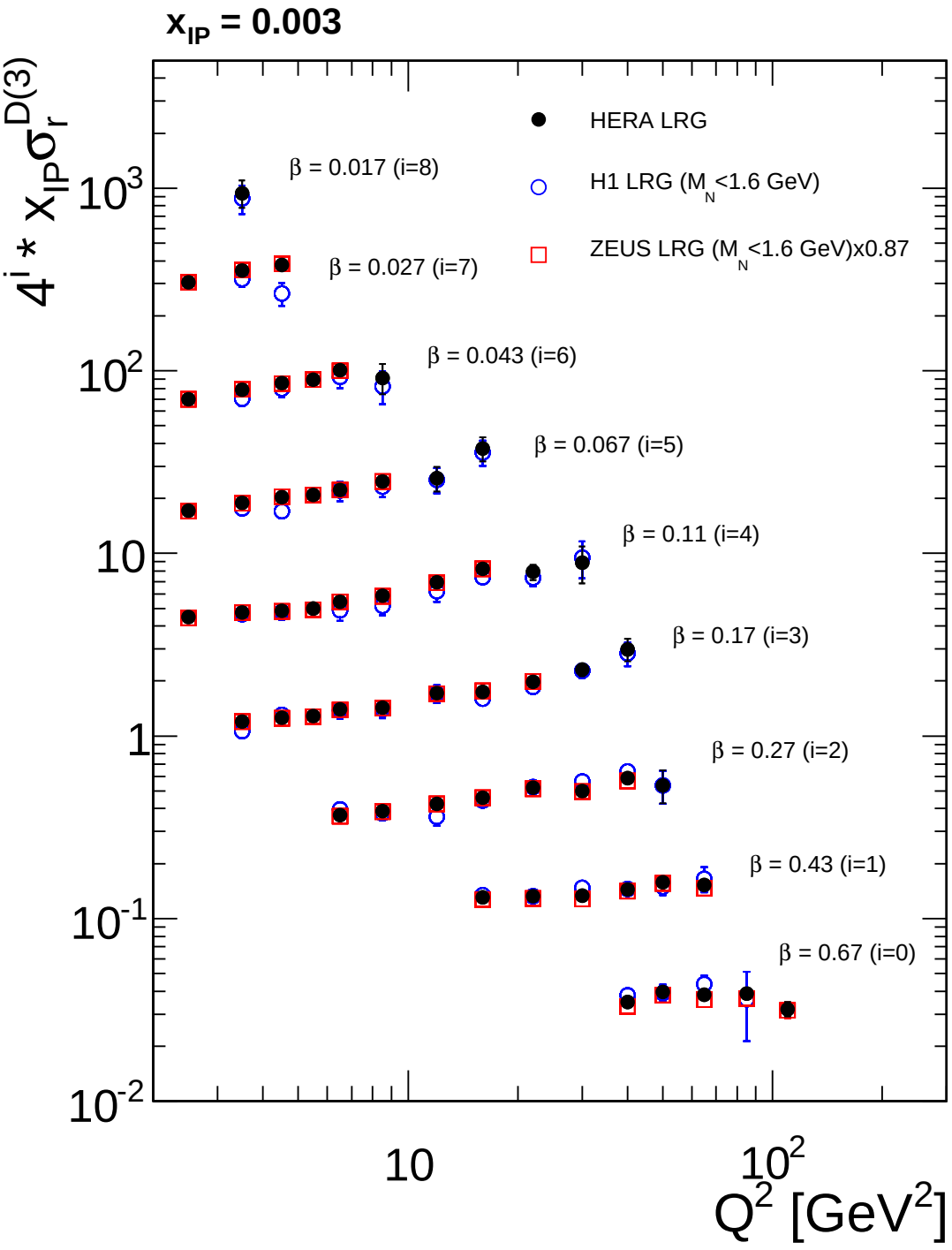

Figure 4.18: *HERA LRG combined diffractive reduced cross section* $x_{I\!P}\sigma_r^{D(3)}(\beta, Q^2, x_{I\!P})$ *as a function of* Q^2 *for different values of* β *, at* $x_{I\!P} = 0.003$*. Data are multiplied by a factor of* 4^i *for visibility, with* i *as indicated.*

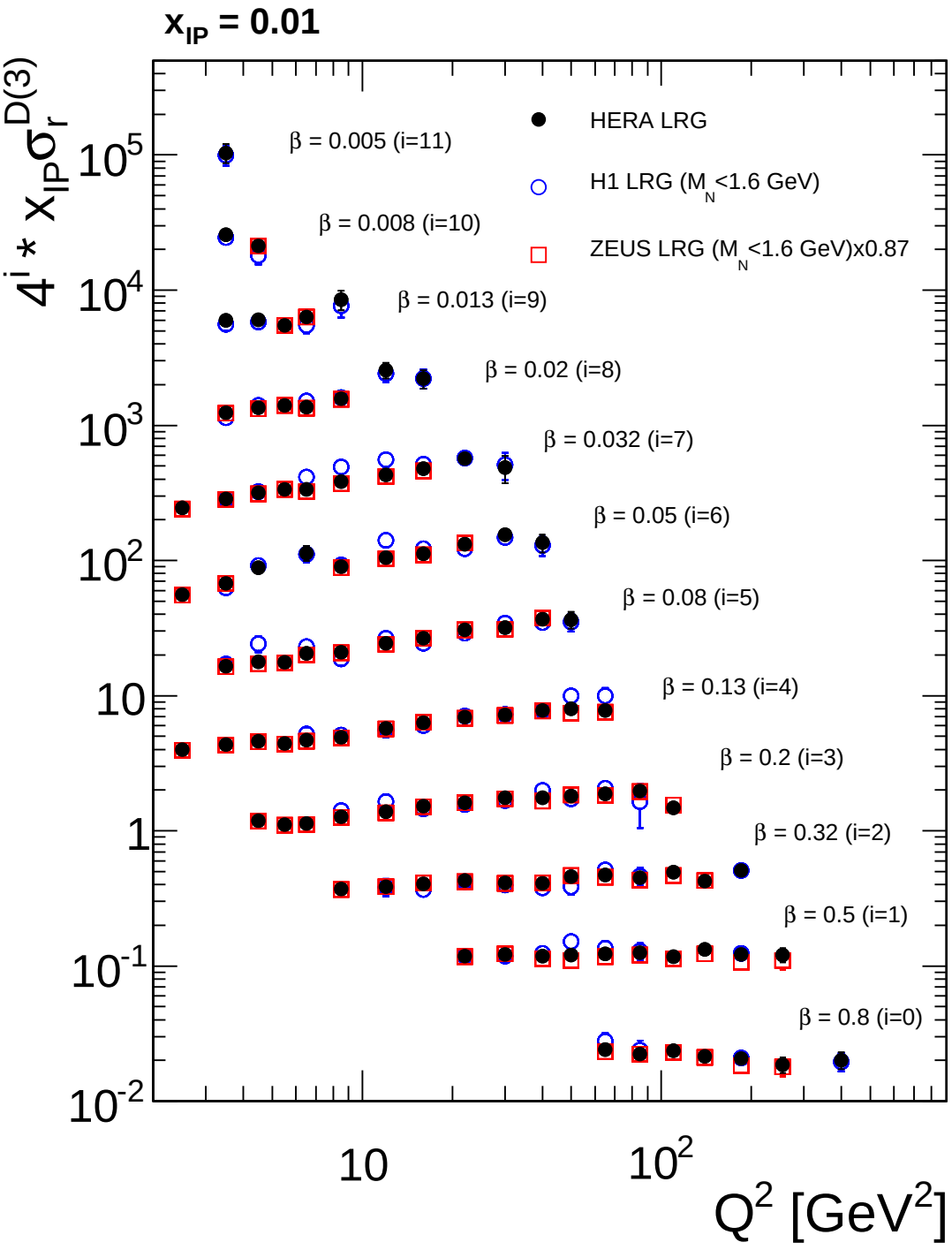

Figure 4.19: *HERA LRG combined diffractive reduced cross section* $x_{I\!P}\sigma_r^{D(3)}(\beta, Q^2, x_{I\!P})$ *as a function of* Q^2 *for different values of* β *, at* $x_{I\!P} = 0.01$*. Data are multiplied by a factor of* 4^i *for visibility, with* i *as indicated.*

4.4.5 Discussion

The kinematic region covered by the HERA combined LRG cross section is $2.5 \leq Q^2 \leq 1600$ GeV^2, $0.0017 \leq \beta \leq 0.8$ and $0.0003 \leq x_{I\!P} \leq 0.03$, for $M_X > 4$ GeV. The combined measurement is driven by the ZEUS results, statistically more powerful, and it shows an average 17% improvement in accuracy and precision with respect to the input ZEUS data. Thanks to the reduction of several systematic uncertainties, the fitting procedure allows a gain in accuracy of the order of 9% compared to a standard weighted average. The combination of the H1 and ZEUS LRG data gives precise results over a wide kinematic range, but at the same time it shows some inconsistency between the input data sets. Possible solutions have been investigated and can be used to improve the agreement of the H1 and ZEUS results.

A first possibility is to normalise the H1 and ZEUS measurements at fixed β and $x_{I\!P}$ values, instead of applying the 13% global normalisation correction factor. This procedure allows a detailed investigation on the shape differences as a function of Q^2 and can show tensions in the scaling violation measurements of H1 and ZEUS.

Another, more rigorous, possibility is to combine the H1 and ZEUS data with a treatment of the uncorrelated uncertainties similar to the procedure used by the Particle Data Group [32] for combining several results from different experiments. The basic assumption is that inconsistencies between different measurements originate from an underestimation of the uncorrelated errors. Increasing the statistical and uncorrelated uncertainties of all input data points by a factor $\sqrt{\chi^2/n_{dof}}$ forces algebraically the resulting χ^2/n_{dof} to be 1, though it worsens the final global precision. An alternative solution is to fix a threshold on the pull value of the input data points, identifying those points which contribute most to the disagreement. Only for those 'outliers', the statistical and uncorrelated errors is increased by a factor proportional to the pull value. This method preserves the global gain in precision of the final result, affecting only few localised points. However, it is not statistically motivated, since the χ^2 fluctuates from point to point and there are no rigorous motivations to penalise just some points. An elegant and more rigorous alternative can be to extract a factor as a function of the kinematics. It is possible, for example, to extract a χ^2 for all the points at the same β and $x_{I\!P}$, and then to multiply the statistical and uncorrelated uncertainties of the data points by $\sqrt{\chi^2/n_{dof}(\beta, x_{I\!P})}$.

New LRG results will be released soon by the H1 Collaboration [49]. The new data sets can be added to the combination to further improve the accuracy and precision of the HERA LRG results.

Chapter 5

Measurement of the Inclusive Diffractive Cross Section at high-y with the ZEUS Detector at HERA

The aim of this analysis is the measurement of the inclusive diffractive DIS ep cross section with data collected by the ZEUS experiment during the years 2006/07. This is the first inclusive diffractive measurement with the ZEUS data after the luminosity upgrade of the HERA collider, when detector components crucial for previous diffractive analyses, such as the Leading Proton Spectrometer and the Forward Plug Calorimeter (see Sects. 2.2.7 and 2.2.8), were dismantled, thus reducing the geometrical acceptance of the ZEUS detector in the forward direction (the direction of the outgoing proton, see Sect. 2.2) by more than one unit in pseudorapidity. Since for the present analysis diffractive events were selected with the Large Rapidity Gap method (see Sect. 3.2), a reduction of the detector coverage reflected in the reduction of the accessible phase space for most of the kinematic variables and in an increase of the contribution of the double dissociative background. On the other hand, data collected in the 2006/07 period allow the measurement of the diffractive reduced ep cross section in the high y region, accessible for the first time at HERA. The fact that this analysis represents the first inclusive diffractive measurement after the HERA upgrade and the aim to reach high y values, made the extraction of the inclusive diffractive ep cross section challenging.

5.1 Data Set

During the last year of running, the HERA collider delivered special run periods to make possible the direct measurement of the longitudinal proton structure function, F_L. For this purpose, protons were accelerated at three different energies, E_p = 920, 460 and 575 GeV,

while positrons[1] were accelerated at $E_e = 27.5$ GeV. The corresponding centre-of-mass energies were $\sqrt{s} = 318$, 225 and 252 GeV and the different running periods are known as High Energy Run (HER), Low Energy Run (LER) and Medium Energy Run (MER), respectively. Crucial for the direct F_L extraction is the possibility to access the high y region at relatively small Q^2 ($Q^2 \lesssim 100$ GeV^2). To reach this goal, dedicated triggers (see Sect. 2.2.9) were developed for each specific running period.

The diffractive analysis presented here is based on the same 2006/07 e^+p HER and LER data sets used for the ZEUS F_L measurements [25, 94]. Only runs where the luminosity was > 0.9 nb^{-1} and the essential detector components (the CTD, the calorimeter and the luminosity monitors) were working properly, were considered. The resulting integrated luminosity of the data sets was 44.5 pb^{-1} and 13.9 pb^{-1} for the HER and LER samples, respectively. Due to its low statistics (7.1 pb^{-1}), the MER sample could not be used for a diffractive cross section measurement.

5.2 Event Simulation

With an ideal detector, events can be measured, and their yields divided by the luminosity to obtain the desired cross section. In practice, the measurement is affected by detector effects. For instance, scattered electrons can escape through the beam hole, or can be absorbed in inactive material located between the interaction point and the calorimeter. An accurate detector simulation is therefore needed to estimate the acceptance, efficiency and resolution of the detector and to correct for these effects.

In order to decide whether an observed discrepancy between data and event simulation is caused by a faulty detector simulation or by a physics event, all the known physics processes need to be simulated properly.

Monte Carlo (MC) models are used. The simulation consists of two steps:

1. **Event generation**, where the theoretical knowledge about the physics process is implemented. The kinematics of the reaction is simulated and the four-momenta of all particles produced in the interaction are provided.

2. **Simulation of the detector** and trigger-system response to the particles generated in the first step.

The output of the simulation and the real data are in the same format. Therefore both samples can be fed into the same physics analysis programs.

Four MC programs were used:

- SATRAP [95] for the diffractive sample;

[1]The term electron will be used in the following instead of positron.

Process	Generator	E_p [GeV]	Q^2 [GeV^2]	σ [nb]	Events
Diffractive DIS	SATRAP	920	$Q^2 > 10$	10.97	6M
$ep \to eXp$		460		7.95	3M
		920	$Q^2 > 4$	29.84	4M
		460		22.91	2M
Inclusive DIS	DJANGOH	920	$Q^2 > 4$	319.44	10M
$ep \to eX$		460		263.02	10M
Photoproduction	PYTHIA	920	$Q^2 < 1.5$	2072.18	20M
		460	$y > 0.5$	1970.17	20M
Hard Diffractive	RAPGAP	920	$Q^2 < 4$	2.15	1M
Photoproduction			$y > 0.5$		

Table 5.1: *Summary of the Monte Carlo samples used in the measurement of the inclusive diffractive DIS ep cross section.*

- DJANGOH 1.6 [96] for the inclusive DIS background;
- PYTHIA 6.416 [97, 98] for the photoproduction background;
- RAPGAP 3.01/26 [99] for the hard-diffractive photoproduction background.

A summary of the MC samples used for the analysis is given in Table 5.1.

5.2.1 Diffractive Event Simulation: SATRAP

Diffractive events, $ep \to eXp$ (see Fig 5.1), were simulated with the SATRAP event generator, interfaced to RAPGAP 2.08. SATRAP is based on the saturation model by Golec-Biernat and Wüsthoff [64], introduced in Sect. 1.3.4.2. In the saturation model the photon splits into a $q\bar{q}$ pair, which is described by the $\gamma q\bar{q}$ wave function. The $q\bar{q}$ system interacts with the proton with a cross section $\hat{\sigma}_{q\bar{q}}$ which is assumed to be of the form $\hat{\sigma} = \sigma_0\{1 - exp[-r^2/(4R_0^2(x))]\}$, where r is the transverse distance between the quark and the antiquark, $R_0(x)$ defines the saturation radius which is given by $R_0^2 = (x/x_0)^\lambda$, and σ_0, x_0 and λ are free parameters. Fluctuations of the incoming photon into $q\bar{q}g$ states are also taken into account and $\hat{\sigma}_{q\bar{q}} = \hat{\sigma}_{q\bar{q}g}$ is assumed. The cross section for the scattering of $q\bar{q}$ and $q\bar{q}g$ states originating from transverse and longitudinal photons can be calculated. The free parameters are determined from fits to HERA inclusive DIS cross sections (i.e. $F_2(x, Q^2)$ data) yielding $\sigma_0 = 23$ mb, $\lambda = 0.29$ and $x_0 = 0.0003$. For the t dependence of the diffractive cross section the form $d\sigma/dt \propto exp(Bt)/B$ with $B = 6$ GeV^{-2} is assumed.

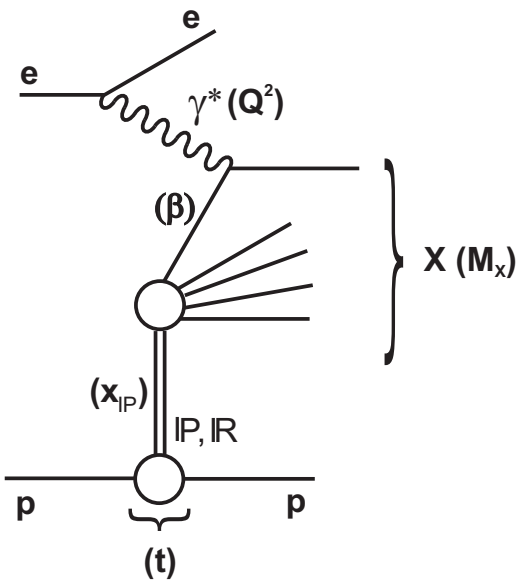

Figure 5.1: *Schematic illustration of a NC diffractive DIS process $ep \to eXp$. The diffractive variables defined in Sect. 1.3.2 are also indicated.*

Through Rapgap, Satrap is interfaced to Heracles 4.6 [100], which includes leading-order QED radiative corrections to the Born-level cross section (see Fig. 5.2). Radiative corrections coming from the hadron lines are smaller than the leptonic ones and are absorbed in the parton distribution functions. QED radiative effects not only change the Born level cross section, but also introduce new types of events since additional photons can emerge, affecting the relationship between the kinematics at the hadronic vertex and the quantities measured on the electron side.

The QCD cascade is simulated using Ariadne 4.03 [101]: the struck quark radiates gluons

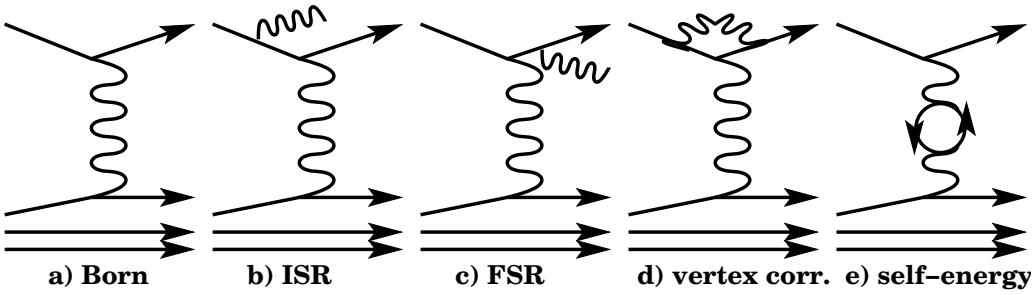

Figure 5.2: *Feynman diagrams of the Born level and the LO QED corrections to NC DIS scattering implemented in* Heracles.

which can emit softer gluons or split into $q\bar{q}$ pairs. In the final step the coloured partons produced in the QCD cascade have to form colourless hadrons; this process cannot be described by perturbation theory because the coupling constant, α_s, becomes large at scales of the order of the mass of hadrons. Therefore the hadronisation has to be described by phenomenological models. In the case of this analysis, the Lund string fragmentation model [102], as implemented in the JETSET 7.404 [97] program, was applied.

5.2.2 Inclusive DIS Event Simulation: DJANGOH

Non-diffractive DIS events ($e^+p \to e^+X$) were simulated with the DJANGOH event generator, using the CTEQ5D PDF parametrisation [103] of the parton distribution functions. DJANGOH is also interfaced to HERACLES 4.6 for the radiative corrections, and to ARIADNE 4.12 [101] and JETSET 7.4 [97] for parton showering and hadronisation.

A graphical scheme of the DIS event generation procedure is shown in Fig. 5.3.

5.2.3 Photoproduction Event Simulation: PYTHIA

Photoproduction (PHP) can represent a serious source of background to any process in DIS, as the ep cross section peaks at $Q^2 = 0$. It is impossible to reject all PHP events because some of them are indistinguishable from the DIS ones. This happens when some calorimetric activity is wrongly identified as the scattered electron, while the electron has escaped through the beam hole (for example, a pion can be misidentified as an electron). To estimate the photoproduction background left after the event selection, the PYTHIA MC was used.

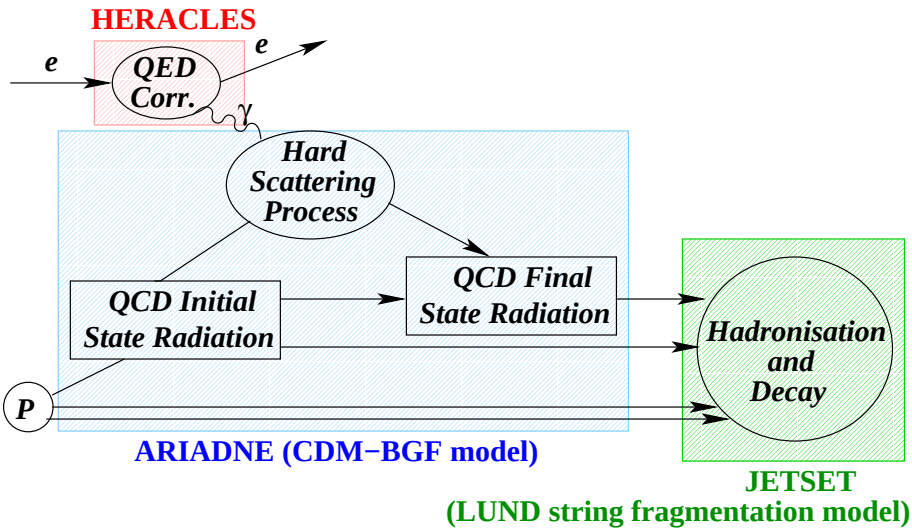

Figure 5.3: *Schematic diagram of an inclusive DIS Monte Carlo generator.*

The PHP Monte Carlo sample consists of several processes with different production mechanisms:

- diffractive PHP processes: $\gamma p \to Vp$, $\gamma p \to Xp$, $\gamma p \to VY$ and $\gamma p \to XY$, where V is one of the light vector mesons ρ, ω or ϕ, and X (Y) is the photon (proton) dissociative system;
- soft non-diffractive processes;
- hard (perturbative) non-diffractive PHP, where a hard scale other than Q^2 is present.

The relative contribution of each subprocess has been determined from fits to earlier ZEUS results.

5.2.4 Hard Diffractive Photoproduction Event Simulation: Rapgap

The diffractive PHP events simulated with the Pythia MC include only soft processes. To include hard diffractive processes, with high p_T-jet production in PHP, the Rapgap 3.01/26 MC was used.

5.2.5 Simulation of the ZEUS Detector

All Monte Carlo generators used for physics analyses of ZEUS are interfaced to a package named Amadeus [104], which provides generated output files in a format compatible with the ZEUS simulation software. After the generation, the hadron-level system must undergo a full detector simulation in order to be compared to the experimental data. The interaction of the particles with the material of the detector components is simulated with the "Monte Carlo For ZEUS Analysis, Reconstruction and Trigger" (Mozart), which uses the Geant 3 package [105]. The ZEUS online trigger for each event is simulated with the Complete Trigger simulation, Zgana Analysis Routine (Czar). All these steps are managed by the ZEUS Monte Carlo Facility, named Funnel [107].

5.3 Event Reconstruction

The Monte Carlo events as well as the raw data from the ZEUS detector are reconstructed offline via the ZEUS PHYsics Reconstruction (Zephyr) package, which includes all calibration and correction factors and provides the higher level data structure. The event is then stored on tape and made available for the offline analysis. Finally, Orange (Overlying Routine for Analysis Ntuple GEneration) [108] is the analysis shell which takes as input the event information from Zephyr and provides the reconstruction of the kinematic variables and their storage in Paw [109] and Root [110] format, from which the user analysis starts.

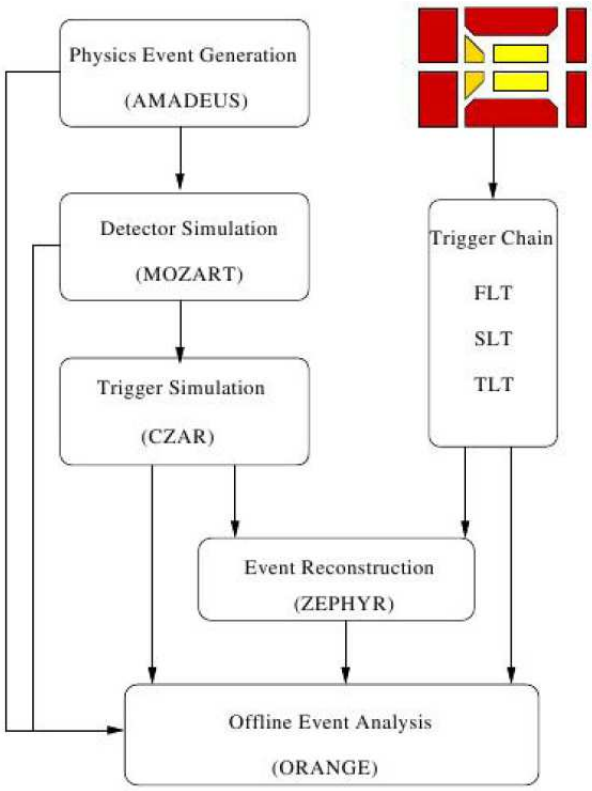

Figure 5.4: *Data flow of real data and Monte Carlo events in the ZEUS experiment.*

The complete data flow diagram for both real data and Monte Carlo events is shown in Fig. 5.4.

5.3.1 Diffractive DIS Event Reconstruction

The purpose of the present analysis is the measurement of the diffractive DIS cross section.

The characteristic signature of a deep inelastic neutral current ep interaction is the presence of the scattered electron. The identification of the electron inside the detector, as well as a precise reconstruction of the electron energy and position, represent the main task of a DIS analysis. A good electron reconstruction is fundamental to distinguish between DIS and background events, mainly due to photoproduction, where high energetic photons and pions can be misidentified as an electron in the calorimeter.

A diffractive event is characterised by the absence of particles between the outgoing proton, which remains inside the beampipe with a small fractional energy loss, and the rest of the hadronic final state inside the detector. Therefore, to identify and reconstruct properly diffractive events, a good understanding of the hadronic system is also needed.

The reconstruction of the DIS kinematic variables in the present analysis is closely related to that used in the published and the new, ongoing, ZEUS F_L analyses [25, 94].

5.3.2 Track and Vertex Reconstruction

It is important for the event reconstruction to have a good measurement of the interaction vertex and of all the tracks originating from it. The CTD and MVD were the main tracking devices (see Sects. 2.2.2 and 2.2.1) of ZEUS. Their information is used to obtain tracks, which are the reconstructed trajectories of charged particles. The main quantities reconstructed for a track are the momentum, the charge and the energy loss.

The track reconstruction is performed by the VCTRACK [111] package. The basic steps to measure a track are the pattern recognition and the track fit. In the pattern recognition, measured hits are assigned to a track candidate. During the fit phase, the hits belonging to a track candidate are fitted to obtain the trajectory. The tracks are fitted using a five-parameter helix model. Three modes are available for the reconstruction:

CTD-only : only CTD information is used. The search for the track candidates starts with a group of hits (segments), from the outermost superlayer to the innermost. After this the fit is performed;

Regular : joint information from CTD and MVD is used. MVD hits are combined in segments and compared with CTD segments. If they are compatible, a track candidate is formed. MVD segments which are not compatible with CTD ones are also kept as MVD stand-alone tracks;

ZTT : this mode uses the CTD+MVD tracks as input for a re-fitting procedure based on Kalman filter techniques [75] and estimates the trajectory by taking into account the uncertainty on the hit positions, as decribed in [112]. Also, appropriate corrections for the ionisation energy loss and multiple scattering are applied to the track parameters.

The ZTT mode has been chosen for this analysis. Reconstructed ZTT tracks are used to find the vertex of the interaction. Tracks intersecting the beam-line are fitted until a vertex position is found (*primary vertex*). The tracks are then refitted to the vertex and are denoted as 'vertex tracks'. Tracks originating from the decay of relatively long-lived particles are also fitted, allowing the identification of *secondary vertices*. Tracks which cannot be associated to any vertex are denoted as 'non-vertex tracks'. An accurate determination of the event vertex, especially of its z-component (z_{vtx}), is crucial, because the reconstruction of angles, and consequently of kinematic variables, depends on this quantity.

5.3.3 Reconstruction of the Scattered Electron

A complete and detailed description of the electron reconstruction used in this analysis can be found in [94].

5.3.3.1 Electron Finder

The experimental signature of an electron in the ZEUS detector is a deposit of energy in the electromagnetic calorimeter (see Sect. 2.2.3), with little energy leaking into the hadronic part. The determination of the shower profile, i.e. its width and depth, allows the discrimination between energy deposits originating from an electron and those from hadronic sources. However, other particles like energetic photons or π^0 decaying into two photons deposit energy in the calorimeter via electromagnetic showers which mimic the scattered electron at low energies. Moreover, in the high-y region, the electron is not well isolated from the hadrons in the final state.

An electron finder based on a neural network, named SINISTRA [113], is used. SINISTRA inspects the energy clusters in the whole calorimeter and returns the probability of each cluster to be an electron. If the cluster lies in the CTD acceptance, the additional requirement of having a track associated to the electron is also used. SINISTRA has the highest efficiency for events with a scattered electron in the RCAL, as in the case of this analysis (see Sect. 5.4.3.1).

5.3.3.2 Electron Energy

A precise measurement of the electron energy is necessary in order to determine x and Q^2 (see Sect. 5.3.5). Moreover, in order to make possible a measurement in an enlarged y region (up to 0.825), low values of E'_e need to be accessed (down to 5 GeV), as illustrated by Eq. (5.3).

The ZEUS calorimeter was able to provide an accurate measurement of the electron energy[2]. However, measurements of individual electrons could of course deviate from the average response. This deviation was caused typically by variations in the scintillator response, non-uniformities of the detector, i.e. cracks, cell-by-cell miscalibrations, and inactive material in front of the detector. Different methods have been developed to study these variations, making use of data samples in which the scattered electron energy could be determined by other means:

- **Double angle** (DA) sample (for $E'_e > 15$ GeV):
  the double angle method [114] predicts the electron energy from the angular information of the scattered electron and the hadrons (see Sect. 5.3.5);
- **Kinematic peak** (KP) sample (for $E'_e \sim 27.5$ GeV):
  the kinematic peak is the region where the energy of the scattered electron is equal to the incoming beam energy; these events can be selected by requiring a low hadronic activity ($y < 0.02$).

[2]Each cell is individually calibrated using the measured depleted-uranium activity (DU noise).

In the RCAL, a cell-by-cell scale factor is extracted with a combination of DA and KP methods. For each cell, the ratio $E_{measured}/E_{expected}$ is fitted with a Gaussian distribution. The resulting scale factor is given by an average of the mean values of the Gaussian fits from DA and KP distributions. Non-uniformities in the RCAL are corrected by using the DA predicted energies and dividing the calorimeter in five different regions. For each region the ratio of the DA and measured energies is plotted as a function of x_{CAL} and y_{CAL} for data and MC separately, and then fitted with Gaussian distributions. The final corrections are the product of the x_{CAL} and y_{CAL} dependent factors. The correction for the inactive material in front of the calorimeter is applied directly by the SINISTRA algorithm. The ratio of corrected electron energy to the KP energy shows that the MC distribution is narrower than that of the data. To account for this effect a small smearing ($< 3\%$) is applied to the MC energy.

The electromagnetic energy scale is known to within 1% for the whole energy range of interest for this analysis.

5.3.3.3 Electron Position

For events in which the electron is in the tracking acceptance region, its position can be calculated from the track information, but in the kinematic range of the present analysis not all the electrons have a matched track. Hence, the SRTD and the HES (see Sects. 2.2.4 and 2.2.5) are used in this analysis for the electron position reconstruction, as they have finer granularity and therefore give better position resolution than the CAL.

The fine granularity of the 1 cm wide strips of the SRTD allows to measure the electron impact position with a resolution of ~ 3.5 mm [115]. The SRTD is aligned with respect to the HES [116]. When the SRTD position is not available, the HES information is used. Each cluster in the Rear HES is the result of the signals in 9 diodes (3×3) coming from the combination of the highest energy diode with the eight neighbouring ones. The position resolution of the HES is ~ 4 mm [116].

Both the SRTD and the HES are aligned to the CTD, which fixes the 'absolute' coordinate system. For the data used in this analysis, shifts had to be applied to SRTD [116] and HES [117].

5.3.4 Reconstruction of the Hadronic Final State

The hadronic final state system consists of neutral and charged particles. Most of them were detected in the uranium-scintillator calorimeter; charged ones were also measured by the tracking detectors. When possible, the CAL and CTD information was used together. The output from the cell clustering and track matching algorithm is a set of objects known as Energy Flow Objects (EFOs[3] [115, 118, 119]). The procedure to obtain EFOs is described in detail in the following. The particles which reached the ZEUS calorimeter showered and deposited their

[3]Historically known also as ZUFOs (ZEUS Unidentified Flow Objects) in the ZEUS nomenclature.

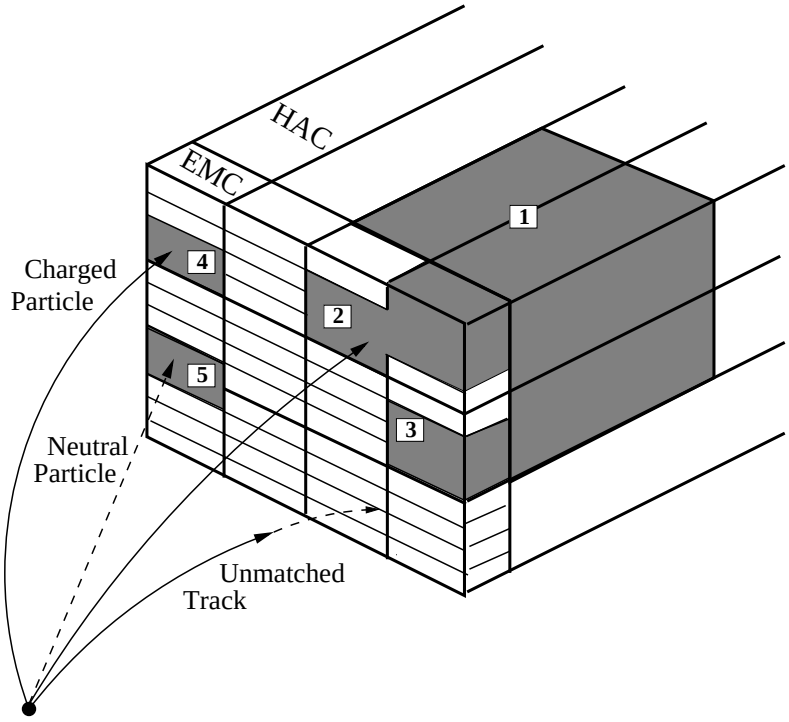

Figure 5.5: *The principle of combining neighbouring calorimeter cells into cell islands. There are four EMC islands and one HAC island in the picture. The matching of CTD tracks to the calorimeter objects is also shown.*

energy in several adjacent cells. The electric signals coming from the calorimeter-cell photomultipliers (PMTs) are converted into energies according to calibration constants determined from calorimeter-module test beam measurements. The signals are corrected for energy absorption by the inactive material in front of the CAL and for noisy cells, i.e. cells with not-properly working PMTs. A cell is tagged as noisy if no neighbouring cell has a signal and the cell signal amplitude is less than 80 MeV for cells in the electromagnetic section and 140 MeV for cells in the hadronic section. A clustering algorithm merges cells, which in an ideal case belong to the shower of a single particle. Afterwards clusters are matched to the corresponding charged tracks; in this case, the particle energy and momentum are taken from the track since the tracking system yields a better measurement than the calorimeter. As a first step, adjacent cells in the electromagnetic and hadronic sections of the calorimeter are grouped into *cell islands* (see Fig. 5.5). The cells are merged only if their signal is above the noise threshold and if they are contiguous. Then the information from the two sections of the calorimeter is combined, so that the resulting cell islands which belong to a shower of a single particle or a jet of particles are joined into 3-dimensional objects, the so called *cone islands* (see Fig. 5.6). The

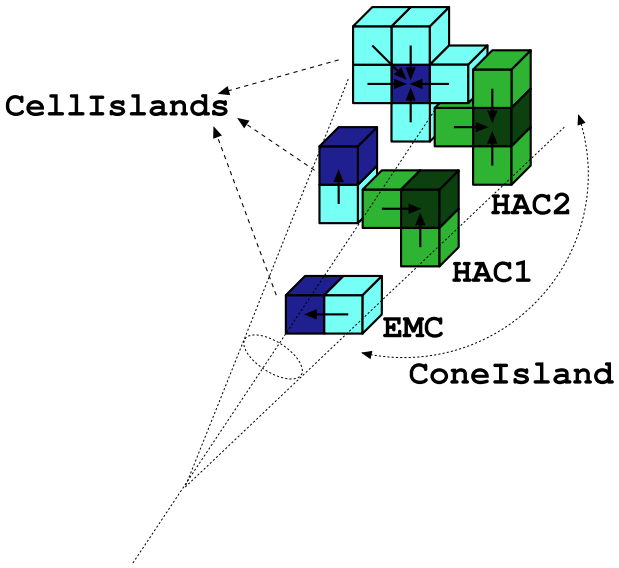

Figure 5.6: *Combining EMC and HAC cell islands into cone islands.*

position of the cone is measured as the weighted mean of the cell positions, taking into account the exponential fall-off of the shower energy distribution. The final stage is matching the 'good tracks' found by the tracking system to the cone islands (see Fig. 5.5).
A good track must satisfy the following conditions:

- the track should go through at least 4 superlayers of the CTD;
- the transverse momentum should be in the range $0.1 < p_t < 20$ GeV; for tracks that passed more than 7 superlayers the maximum p_t is increased to 25 GeV;
- the track should come from the primary vertex.

The tracks satisfying the above criteria are extrapolated to the inner surface of the calorimeter. A good track matches an island if its distance of closest approach to the cone island position is less than 20 cm or less than the maximum radius of the island. This operation produces groups of matched tracks and islands. They are used to determine the energy of the final state particles as follows:

- for a good track without any matched calorimeter island, the particle energy is determined from the track momentum, assuming that the particle was a pion;
- calorimeter objects not associated to a track are counted as due to neutral particles and the calorimeter information is used;

- calorimeter objects associated to more than 3 tracks are counted with their calorimeter energy.

There are several advantages in using combined information from the tracking and the calorimeter. First, it is possible to maximise the resolution for a given value of energy. Furthermore, it is possible to measure precisely low-energy charged-particles which did not reach the calorimeter, or which lost a large amount of their energy in the inactive material in front of the calorimeter.

Having built the EFOs, the total four-momentum of the hadronic final state is reconstructed as:

$$\begin{aligned} E_h &= \sum_{i=1}^{\#EFOs} E_i, \\ p_{j,h} &= \sum_{i=1}^{\#EFOs} p_{ji}, \end{aligned} \tag{5.1}$$

where $j = x, y, z$ and the sums run over all EFOs, excluding the one associated to the scattered electron.

The hadronic energy scale is known to within 2% for the data sets considered in this analysis [94].

5.3.5 Reconstruction of the DIS Kinematic Variables

Different methods provide the reconstruction of the kinematic variables for a DIS event. They use information coming from the scattered electron, from the hadronic system or from a combination of the two. The resolution of the measurement in a given kinematic region varies depending on the chosen method.

In this analysis, the electron method was used to reconstruct Q^2, y and x, in view of measuring the cross section in the high y region, where the precision of this method is known to be better compared to the other methods.

The electron method [114] uses the energy of the scattered electron, E'_e, and its scattering angle, θ_e, for the calculation of the kinematic variables:

$$Q^2_{EL} = 2E_e E'_e(1 + \cos\theta_e) \ , \tag{5.2}$$

$$y_{EL} = 1 - \frac{E'_e}{2E_e}(1 - \cos\theta_e) \ , \tag{5.3}$$

$$x_{EL} = \frac{Q^2}{sy} \ . \tag{5.4}$$

Moreover, from the E'_e and θ_e information the longitudinal and transverse momentum components of the scattered electron are derived:

$$p_{z,e} = E'_e \cos\theta_e \ , \tag{5.5}$$

$$p_{T,e} = E'_e \sin\theta_e \ . \tag{5.6}$$

This method gives good results at high y, where E'_e is significantly different from the electron beam energy E_e, but at low y ($y \lesssim 0.1$) the resolution becomes poor. In addition, this method is affected by QED radiation.

The kinematic reconstruction method based on the hadronic system information was developed by Jacquet and Blondel [120]. It is based on the assumption that the total transverse momentum carried by the hadrons which escape detection through the beam hole in the proton direction, as well as the energy carried by the particles escaping through the beam hole in the electron direction, can be neglected. This method is based on the quantities:

$$\delta_h = \sum_{i=1}^{\#EFOs} E_i(1-\cos\theta_i) = E_h - p_{z,h} \tag{5.7}$$

and

$$p^2_{T,h} = \left(\sum_{i=1}^{\#EFOs} p_{x,i}\right)^2 + \left(\sum_{i=1}^{\#EFOs} p_{y,i}\right)^2 = p^2_{x,h} + p^2_{y,h} \ , \tag{5.8}$$

where the sums run over all EFOs except the one corresponding to the scattered electron.

In the Jacquet-Blondel method, y is obtained as:

$$y_{JB} = \frac{\delta_h}{2E_e} \ . \tag{5.9}$$

At low y ($y \lesssim 0.04$), y_{JB} has a superior resolution compared to y_{EL}.

A relevant variable related to the hadronic final state is the angle γ_h, which in the naive quark parton model is interpreted as the polar angle of the struck quark. The angle γ_h is measured as the ratio of the measured quantities δ_h and $p_{T,h}$:

$$\cos\gamma_h = \frac{p^2_{T,h} - \delta^2_h}{p^2_{T,h} + \delta^2_h} \ . \tag{5.10}$$

The double angle method [114] takes into account both the scattered electron and the hadronic final state system and makes use of their polar angle information only. The measurement of the angles is less affected by detector effects than the energy measurements. This method is to a good approximation independent of the energy scales of the detector. However, it is sensitive to QED radiation.

According to this method, the kinematic variables Q^2 and x are calculated as:

$$Q^2_{DA} = 4E_e^2 \frac{sin\gamma_h(1+cos\theta_e)}{sin\theta_e + sin\gamma_h - sin(\theta_e+\gamma_h)} \ , \tag{5.11}$$

$$x_{DA} = \frac{E_e}{E_p} \frac{sin\theta_e + sin\gamma_h + sin(\theta_e+\gamma_h)}{sin\theta_e + sin\gamma_h - sin(\theta_e+\gamma_h)} \ . \tag{5.12}$$

From its definition (see Sect. 1.1.1), the invariant mass squared of the photon-proton system is obtained as:

$$W^2 = m_p^2 + \frac{Q^2}{x}(1-x) \ . \tag{5.13}$$

For this analysis W is reconstructed by using a combination of the electron and double angle methods, the so-called weighted method [114]:

$$W_w = (1-f)\cdot W_{EL} + f \cdot W_{DA} \ , \tag{5.14}$$

where $f = min(1, (E'_e/25)^2)$ and E'_e is given in GeV. This procedure improves the kinematic reconstruction, especially in the region close to the kinematic phase space limits.

A quantity commonly used at HERA to distinguish between DIS and PHP regime is:

$$\delta_{TOT} \equiv E - p_z = \sum_i E_i - p_{z,i} \ , \tag{5.15}$$

where the sum runs over all the detected particles, including the scattered electron. Since E_{TOT} and $p_{z,TOT}$ are conserved, also δ_{TOT} has to be conserved. Before the interaction $\delta_{TOT} = \Sigma_{e,p}(E - p_z) = (920 - 920) + (27.5 + 27.5) = 55$ GeV $= 2E_e$. If the scattered electron escapes into the beampipe, as in γp interactions at $Q^2 \simeq 0$, δ_{TOT} is smaller than $2E_e$.

5.3.6 Reconstruction of the Diffractive Kinematic Variables

One of the most important variables for this analysis is the maximum pseudorapidity of the event, η_{MAX}, since the diffractive selection is performed by means of the Large Rapidity Gap method (see Sect. 3.2). For each EFO the pseudorapidity is evaluated as $\eta = -\ln(\tan\theta/2)$, from Eq. (1.18). The variable η_{MAX} is reconstructed as the pseudorapidity of the most forward EFO with energy above 400 MeV in the CAL. This requirement ensures that calorimeter noisy cells are not counted as particles.

Another fundamental variable for a diffractive analysis is the invariant mass of the hadronic final state, M_X, which is given by:

$$M_X^2 = E_h^2 - p_{x,h}^2 - p_{y,h}^2 - p_{z,h}^2 \ . \tag{5.16}$$

For the present analysis, two different methods to reconstruct M_X were adopted, one based on EFOs and the other on the scattered electron information, respectively. A brief description of the two methods is given:

$M_{X,EFO}$ **:** the hadronic energy and momentum components to be inserted in Eq. 5.16 were obtained as the sum of all the EFOs with a rapidity $\eta < \eta_{MAX}$, provided the EFO related to the scattered electron was excluded. All the low energy EFOs with $\eta > \eta_{MAX}$ were not considered in the mass reconstruction. This requirement ensured that noisy cells, particularly frequent in the forward part of the calorimeter, do not affect the mass of the event.

$M_{X,EL}$ **:** from the definition of the invariant mass it is possible to rewrite M_X as a combination of electron and hadronic variables:

$$\begin{aligned} M^2_{X,EL} &= E^2_h - p^2_{x,h} - p^2_{y,h} - p^2_{z,h} \\ &= E^2_h - p^2_{z,h} - p^2_{T,h} \\ &= (E_h - p_{z,h})(E_h + p_{z,h}) - p^2_{T,e} \\ &= (55 - (E_e - p_{z,e}))(E_h + p_{z,h}) - p^2_{T,e} \ , \end{aligned} \tag{5.17}$$

assuming $p_{T,h} = p_{T,e}$ and $(E_e - p_{z,e}) + (E_h - p_{z,h}) = 55$, from Eq. (5.15) (all quantities are expressed in GeV).

The relative difference between the reconstructed and the generated M_X values $(M_{X,rec} - M_{X,gen})/M_{X,gen}$ was determined for both methods as a function of $M_{X,gen}$. The mean value of the distribution gives the systematic shift from generated to measured values, while the width of the distribution estimates the resolution of the measured M_X. In Fig. 5.7 the shift and the resolution of $M_{X,EFO}$ and $M_{X,EL}$ are shown as a function of the generated M_X. The mass reconstructed through the hadronic method suffers from a visible shift with respect to the generated value, and therefore a correction function needs to be applied. The correction factor has the form:

$$f(M_{X,EFO}) = 0.8806 + 0.0017 M_{X,EFO} \ ,$$

and the reconstructed mass was corrected to the generated value via $M_{X,EFO}/f(M_{X,EFO})$ applied both to data and to MC. On the other hand, the mass from the electron method shows only a small shift with respect to the true value and no correction is needed. Both methods exhibit a poor resolution in the region $M_{X,gen} < 4$ GeV, but $M_{X,EL}$ shows a better resolution for $M_{X,gen} \gtrsim 10$ GeV. Both methods were used for the cross section extraction, giving compatible results (see Sect. 5.6.2.3). The electron method was chosen as nominal since it is less sensitive to changes in the hadronic energy scale.

The variables $x_{I\!P}$ and β were obtained from Eqs. (1.34) and (1.35), using the reconstructed values of Q^2, W, M_X and neglecting t, since $|t| \ll Q^2$ and M^2_X.

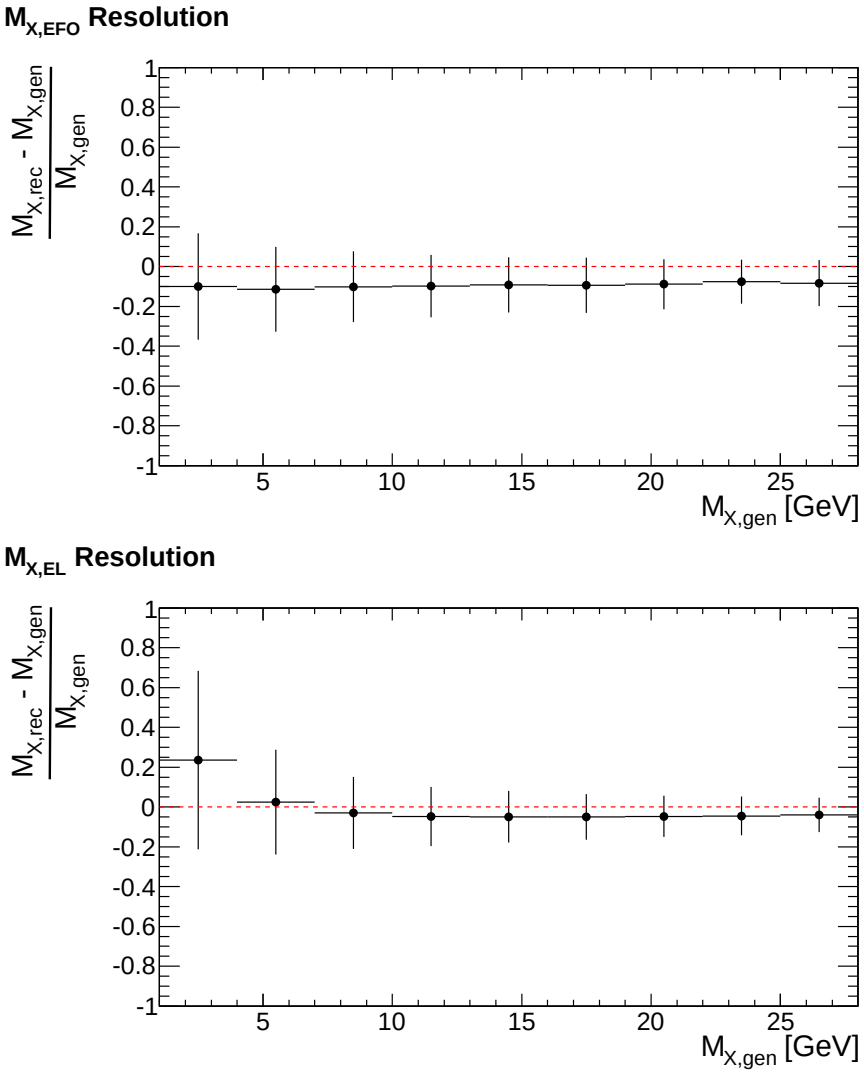

Figure 5.7: *Relative difference between the generated and reconstructed value of M_X as a function of the generated value, for M_X reconstructed from EFOs (upper plot) or from the electron variables (lower plot).*

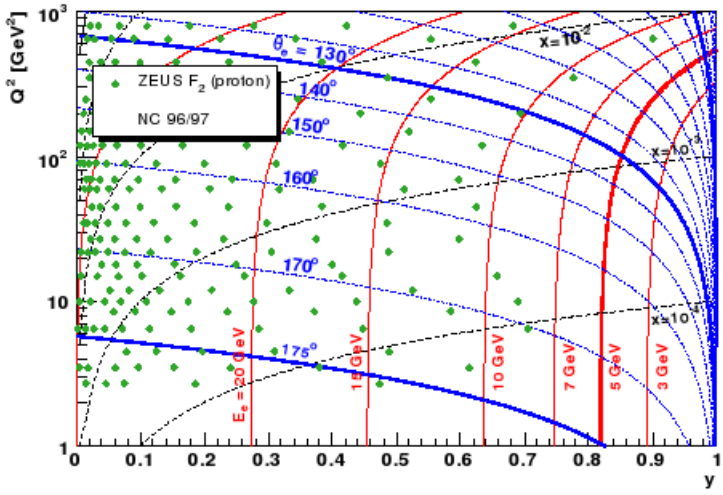

Figure 5.8: *The kinematic plane (Q^2, y). Contours of constant E'_e and θ_e are indicated, as of constant Bjorken-x. The RCAL fiducial region lies between $\theta_e = 130°$ and $\theta_e = 175°$. The solid points indicate the values of (Q^2, y) where ZEUS has previously performed structure function measurements [13].*

5.4 Event Selection and Background Discussion

5.4.1 Aim of the Selection

The purpose of the present analysis is to extend the measurement of the *ep* diffractive cross section to high-y (up to 0.825) for medium Q^2 values (between 20 and 130 GeV^2). From Eq. (5.3), one can see that in order to reach high y values, scattered electrons with small energies need to be measured. The main background to DIS events in this kinematic region is photoproduction (PHP).

As a first step, a DIS sample was selected, in a region where the scattered electron is well reconstructed and the backgrounds are reduced as much as possible.

Then, single-diffractive events (SD), where only the γ^* dissociates, were selected from the DIS sample, in a region where the hadronic final state can be properly reconstructed. Whitin the diffractive sample, events in which not only the virtual photon, but also the proton dissociate (the so-called double diffractive events, DD) represent a relevant background, which must be estimated and subtracted.

5.4.2 Trigger Selection

Considering the bandwidth of the data transfer and the computing resources, it was impossible to store the data coming from all collisions. In order to reject events that did not have the signature of the desired signal, data passed a three-stage trigger selection before being stored

on tape (see Sect. 2.2.9). After the HERA luminosity upgrade the ZEUS trigger selection for DIS events mainly concentrated in the high Q^2 region. For the 2006/07 running period specific trigger algorithms were implemented to take data in the high y, medium Q^2 kinematic region. This implies selecting events with a relatively low energy electron in the rear calorimeter (see Fig. 5.8 where the kinematic plane (Q^2, y) is shown).

The online trigger selection applied to collect both the HER and LER data sets used in this analysis was based on a slot of the First Level Trigger, the FLT30 slot. The logic of FLT30 is summarised as follows:

$$\text{FLT30} = \text{RIsoE } \textit{and } (E_{REMC,nom} > 2\text{GeV } \textit{or } E_{REMC,th} > 15\text{GeV}) \ , \tag{5.18}$$

where RIsoE corresponds to the requirement of finding an electromagnetic cluster (EMC) with energy above 2 GeV in the RCAL which could be considered as an isolated electron, $E_{REMC,nom}$ is the sum of all EMC energy deposits in the RCAL with energy above 464 MeV and $E_{REMC,th}$ is the same sum with no threshold on the energy cluster.

Only the FLT30 trigger slot was used for the sample selection, since it was the only high y, medium Q^2 slot without the requirement of a 'Good Track' in the CTD. All the trigger slots with the 'Good Track' requirement were ignored for this analysis. Because the trigger efficiency of the CTD lowered during the 2006/07 data taking period and this could introduce a bias.

5.4.3 Offline Selection

5.4.3.1 DIS Selection

The DIS selection limited the analysis to a region where the electron could be well identified and the non-DIS background was under control.

- $\mathbf{|z_{vtx}| < 30\ cm}$
  This cut excludes events which do not originate from ep collisions, like events coming from beam-gas interactions, and selects a region in which the vertex is well reconstructed and the agreement between data and Monte Carlo distributions is good.
  Events without a reconstructed vertex were rejected.

- $\mathbf{E'_e > 5\ GeV,\ \ P_{SI} > max(0.8, 0.95 - 1.5 \cdot e^{-\frac{E'_e}{2.5}})}$
  Cuts on the energy, E'_e, and on the probability of electron identification by the SINISTRA electron finder (see Section 5.3.3.1), P_{SI}, were applied to achieve high purity and efficiency in the scattered electron identification [116]. Within the electron candidates found by SINISTRA, that with the highest probability was selected.

- $\mathbf{42 < E - p_z < 65\ GeV}$
  The lower limit rejects background coming from photoproduction events, where the electron escapes through the beampipe, reducing the value of $E - p_z$. The upper limit is used

to reduce overlay events in which DIS events and beam-gas events occur in the same bunch crossing.

- **Track requirement**
  The purpose of this requirement is to reduce the photoproduction background, which is large in the high y region, by requiring the presence of a track between the vertex and the electron candidate. In the kinematic region considered, most of the electrons were outside the CTD and MVD acceptance required for well reconstructed tracks. However, information from single hits in the tracking detectors was used, without performing the full tracking reconstruction. This was obtained by means of the UVF tool [116]. The idea is to build a "road" between the reconstructed vertex and the position in the calorimeter where the electron was found, and then estimate the number of strips of the MVD and wires of the CTD with hits inside this road. The selection was made on the fraction of hits effectively associated to the particle with respect to all those the particle should have caused with its passage through the detectors. The event was accepted if the MVD fraction was greater than 0.45 and the CTD fraction was above 0.6.

- $\mathbf{R_{CTD} > 20}$ **cm**
  This requirement on the radius of the scattered electron "impact point" on the surface of the CTD, R_{CTD}, almost overlaps with the track one, as the CTD inner radius was 18.2 cm, and selects a region in which events can be well reconstructed. This cut also influences the kinematic region of the analysis because it corresponds to an angular selection, since for $R_{CTD} = 20$ cm, $\theta_e \simeq 170°$ (see Fig. 5.8).

- $\mathbf{y_{JB} > 0.05}$
  This cut limits the event migration from the low y region.

- $\mathbf{p_{T,h}/p_{T,e} > 0.3}$
  A minimal $p_{T,h}/p_{T,e}$ requirement rejects beam-gas, cosmic and halo muon events, due to the asymmetric energy flow of those events.

- **Bunch crossing requirement**
  This requirement on the ep bunch crossing condition helps in further rejecting beam-gas, cosmic and halo muon events.

- **QED Compton cut**
  Compton scattering ($ep \to e\gamma p$) is the radiation of a hard photon from the initial or scattered electron and represents a source of background since such an event could fake a DIS event with a low hadronic mass, if both the electron and the photon were detected in the calorimeter. These events were easily identified and rejected by their characteristic topology with only two electromagnetic clusters in the detector, balanced in transverse momentum.

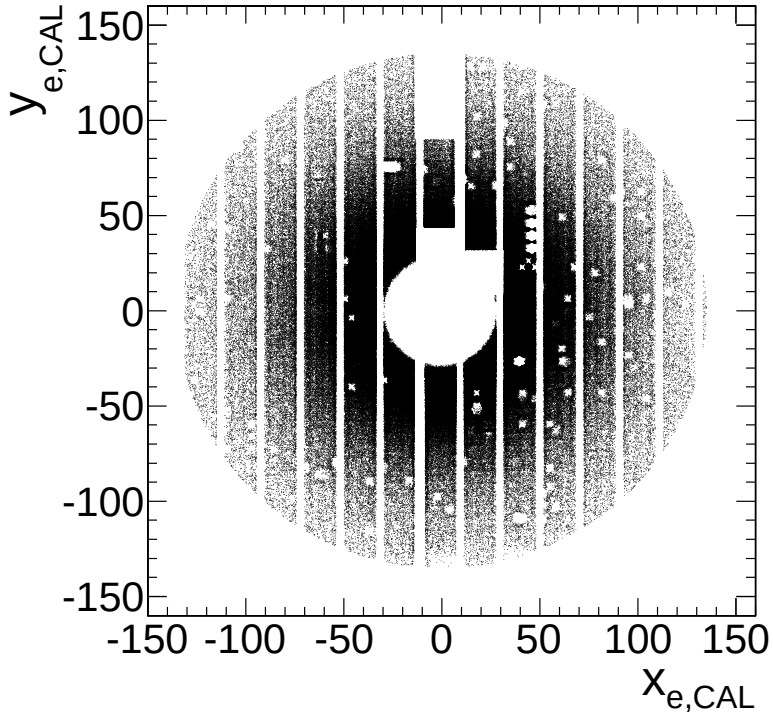

Figure 5.9: *The electron position after the DIS selection for the HER data sample.*

- **Fiducial geometry cut**
  To ensure an accurate scattered electron measurement, as well as its reliable identification by the electron finder, a set of geometrical cuts on the electron position was applied. The removed areas correspond to problematic regions of the calorimeter, like for example the crack region between the two calorimeter halves, regions near module edges or problematic cells [94]. Events with the electron outside the RCAL acceptance were rejected.
  The position of the electron in the RCAL after the DIS selection is shown in Fig. 5.9.

After the DIS selection, the events were 891748 and 218562 for the HER and LER sample, respectively. The requirement of an electron with $R_{CTD} > 20$ cm and inside the RCAL acceptance limits the kinematic region of the measurement to $20 < Q^2 < 130$ GeV^2. The lower limit on $E'_e > 5$ GeV implies $y < 0.825$.

5.4.3.2 Diffractive Selection

The diffractive sample was selected from the inclusive DIS one by using the Large Rapidity Gap technique (see Sect. 3.2). Further requirements were applied to the diffractive sample to limit the measurement to a kinematic region where the hadronic final state could be well identified and reconstructed:

- $\eta_{\mathbf{MAX}} < \mathbf{2.2}$
  To ensure the absence of activity between the photon dissociative system, X, and the proton escaping through the beam-hole, a rapidity gap of the order of $\Delta\eta = \eta_p - \eta_X \sim 2$ was required[4]. The value $\eta_{MAX} < 2.2$ is close to the value already used for previous ZEUS diffractive measurement [121] based on HERA I data when the FPC was not installed (see Sect. 2.2.8), and hence with a forward instrumentation similar to that of the present measurement.

- $\mathbf{M_X > 4\ GeV}$
  This requirement limited the measurement to a region where the mass of the hadronic final state could be reconstructed with good resolution (see Sect. 5.3.6) and was not affected by noise and backgrounds induced by the detector. It also rejected the low-mass region where vector meson production dominates.

- $\mathbf{M_X < 25\ GeV}$
  This requirement limited the measurement to a region with reasonable statistics and where the trigger efficiency of the data was well reproduced by the Monte Carlo simulation (see Sect. 5.5.3.1).

- **Less than 10 non-vertex tracks with DCA $>$ 10 cm**
  After the HERA luminosity upgrade the background induced by the machine increased. Events were observed with lots of tracks not fitted to the event vertex and with a distance of closest approach (DCA) to the primary vertex of the order of few centimeters. All these tracks could leave energy deposits in the calorimeter and bias the reconstruction of the hadronic system. Moreover, the amount of non-vertex tracks in the data was not well reproduced by the Monte Carlo simulation. Therefore, a cut on non-vertex tracks was applied: events with more than 10 non-vertex tracks with DCA $>$ 10 cm were rejected. The fraction of events rejected both in data and in MC was estimated and taken into account for the cross section extraction (see Sect. 5.5.2).

After the diffractive selection, the final number of events was 28233 and 6899 for the HER and LER samples, respectively. The resulting kinematic region for the diffractive DIS ep cross section measurement was $0.05 < \beta < 0.85$ and $0.00063 < x_{I\!P} < 0.01$.

[4]For the data taking period considered by this analysis, the forward coverage of the ZEUS detector reached $\eta \sim 4$, .

5.4.4 Reweighting of the Monte Carlo

The Monte Carlo samples had to be reweighted to better reproduce the data.

The reweighting of the DJANGOH and PYTHIA samples is the same as that used for the inclusive DIS analysis and is carefully discussed in [94].

The reweighting of the diffractive events simulated with SATRAP was applied differently for the HER and the LER samples as a function of the generated variables. The samples needed to be reweighted especially in the high y region, where the dependence of the cross section is known only through predictions extrapolated from previous data. To each event of the HER and LER MC samples the factor $f(W_{gen}) \times f(\beta_{gen})$ was applied, where the contribution of $f(W_{gen})$ changes according to the Q^2_{gen} value.
For the HER MC sample the weighting factors are defined as:

$$f(W_{gen}) = \left(\frac{182}{W_{gen}}\right)^{0.15} \quad \text{for } Q^2_{gen} = 20 - 27 \text{ GeV}^2 \,, \tag{5.19}$$

$$f(W_{gen}) = \left(\frac{182}{W_{gen}}\right)^{0.35} \quad \text{for } Q^2_{gen} = 27 - 44 \text{ GeV}^2 \,, \tag{5.20}$$

$$f(W_{gen}) = \left(\frac{182}{W_{gen}}\right)^{0.50} \quad \text{for } Q^2_{gen} = 44 - 130 \text{ GeV}^2 \,, \tag{5.21}$$

$$f(\beta_{gen}) = 0.93 + \frac{0.1}{\beta_{gen}} \,. \tag{5.22}$$

For the LER MC sample the weighting factors are defined as:

$$f(W_{gen}) = \left(\frac{135}{W_{gen}}\right)^{0.05} \quad \text{for } Q^2_{gen} = 20 - 27 \text{ GeV}^2 \,, \tag{5.23}$$

$$f(W_{gen}) = \left(\frac{135}{W_{gen}}\right)^{0.25} \quad \text{for } Q^2_{gen} = 27 - 44 \text{ GeV}^2 \,, \tag{5.24}$$

$$f(W_{gen}) = \left(\frac{135}{W_{gen}}\right)^{0.40} \quad \text{for } Q^2_{gen} = 44 - 130 \text{ GeV}^2 \,, \tag{5.25}$$

$$f(\beta_{gen}) = \left(\frac{0.3}{\beta_{gen}}\right)^{0.1} \,. \tag{5.26}$$

5.4.5 Comparison between Data and Monte Carlo

After the reconstruction and the correction procedures described in Sect. 5.3 and after the event selection and MC reweighting, data and Monte Carlo can be compared. The main distributions are presented below. As a general rule, dots represent data, with MC histograms superimposed. DJANGOH and PYTHIA MC distributions are normalised to the luminosity of the data samples, while SATRAP MC distributions are normalised to the number of data events.

The η_{MAX} distribution is shown in Fig. 5.10, where the contribution of non-diffractive DIS (DJANGOH), photoproduction (PYTHIA) and single-diffraction (SATRAP), which are then summed up, are compared to the HER and LER data. This variable drives the diffractive selection.

In the diffractive region, up to η_{MAX} =2.2 for this analysis (shown as a vertical dashed line), the agreement is good. The worse agreement in the high η_{MAX} region, $\eta_{MAX} \gtrsim 4$, is due to the fact that it is a region outside the geometrical acceptance of the ZEUS detector and the reconstruction algorithm is only able to estimate the centre of the remnant cone inside the beampipe, using information from the calorimeter clusters around the hole.

It is important to notice that the photoproduction background in the diffractive region is very small (only a few events survive the $\eta_{MAX} < 2.2$ cut), while the DIS non-diffractive contribution is less than 5%. Both contributions are therefore not considered in the following.

The distributions for several variables after the diffractive selection are shown in Figs. 5.11-5.14, for the HER and LER data sets. Only the single-diffractive contribution simulated with SATRAP is compared to the data samples. Good agreement between data and MC is observed over a wide kinematic range for most of the observed variables. A small shift is visible at low M_X values, which reflects on the $x_{I\!P}$ distribution. However, it is important to notice that high y values, up to 0.825, are reached in the region $20 < Q^2 < 130$ GeV^2 without any PHP background contamination.

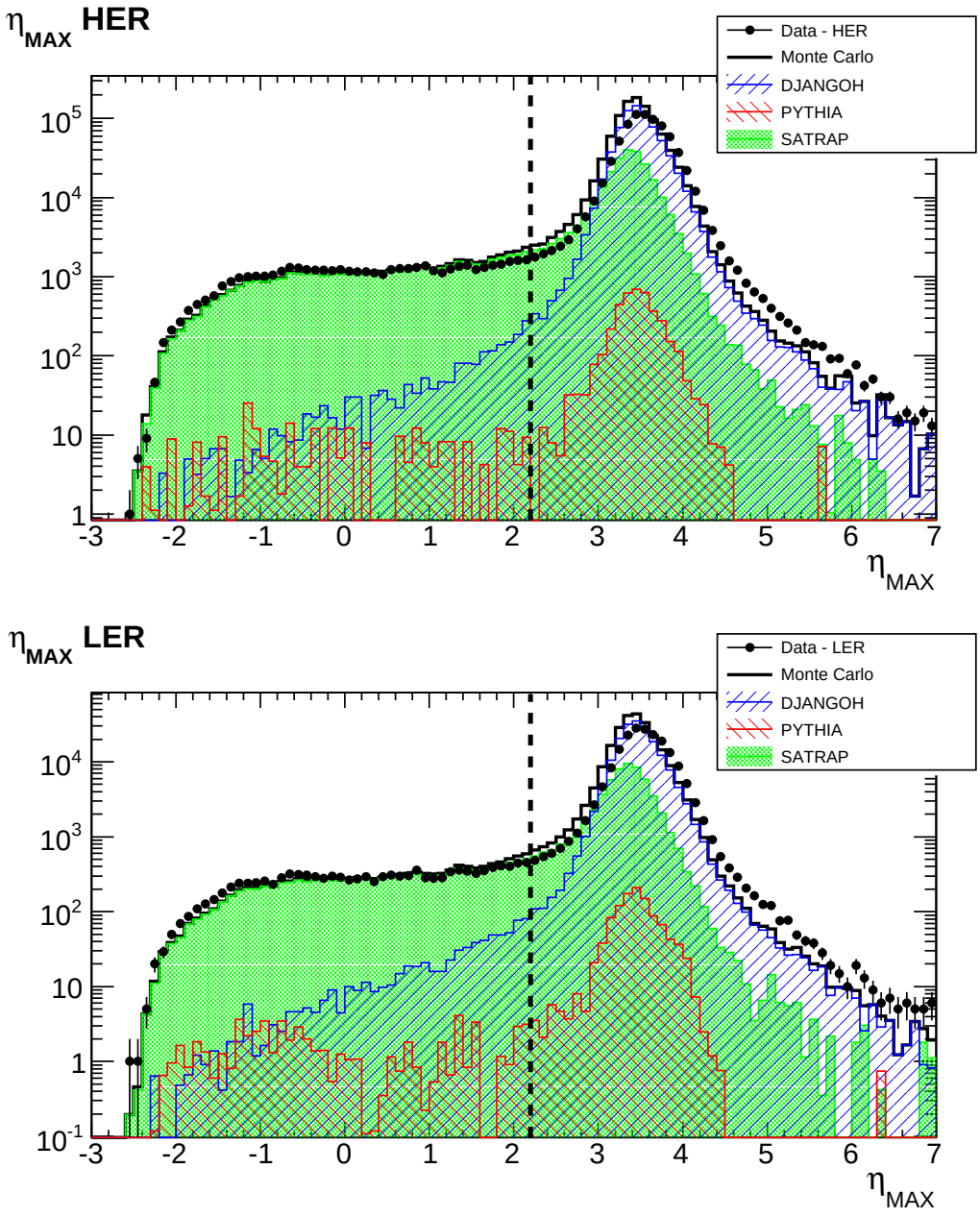

Figure 5.10: *The η_{MAX} distributions for the DIS HER (up) and LER (down) inclusive data samples. The histograms represent the sum of the Monte Carlo contribution: non-diffractive DIS (*DJANGOH*) is the blue histogram, photoproduction (*PYTHIA*) is the red one and diffractive events (*SATRAP*) are shown in green.*

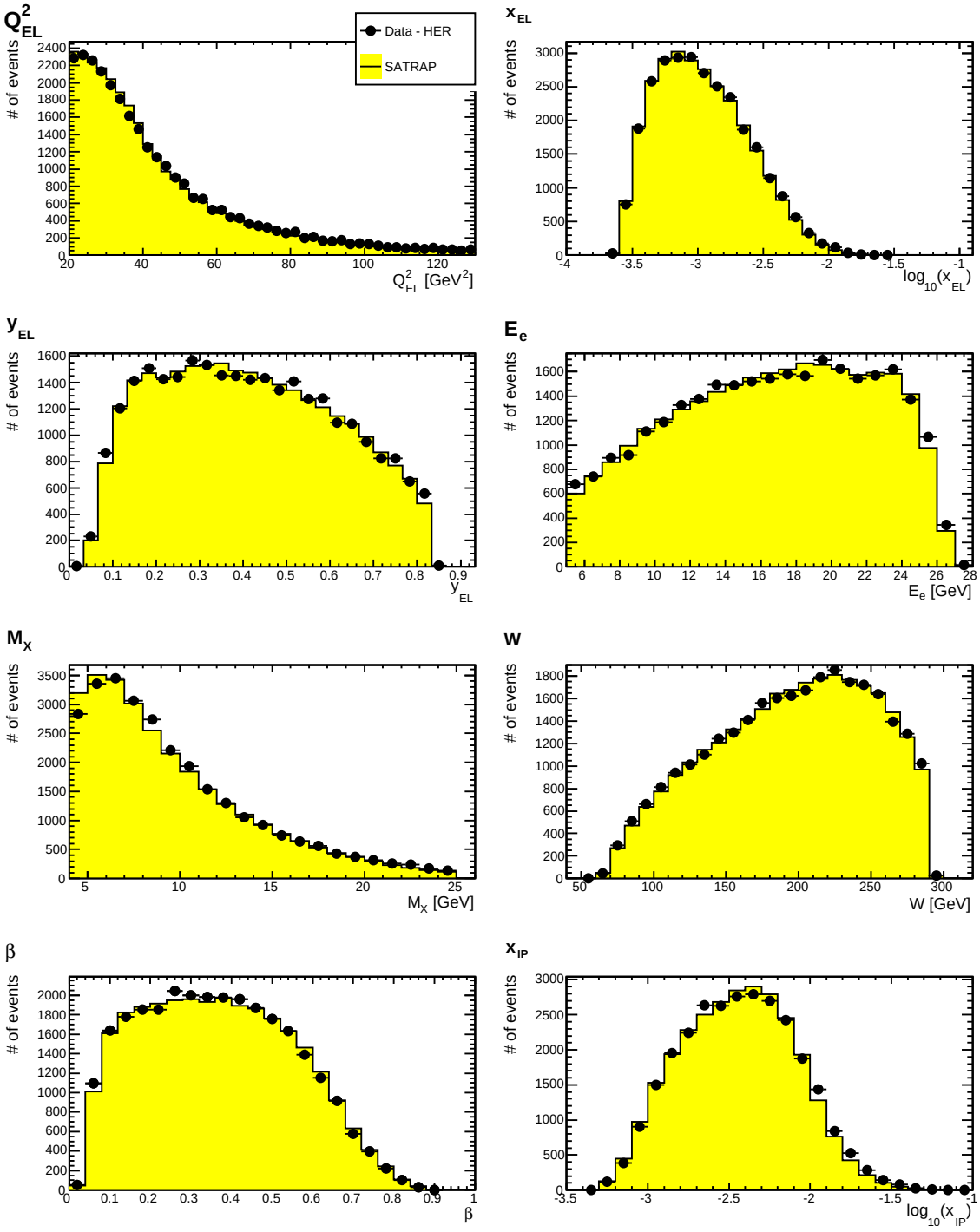

Figure 5.11: *Comparison between the HER data set (black dots) ant the* SATRAP *diffractive MC (yellow histograms), after the DIS and diffractive selections. The variables Q^2_{EL}, x_{EL}, y_{EL} and E'_e (upper part), and M_X, W, β and $x_{I\!P}$ (lower part) are shown.*

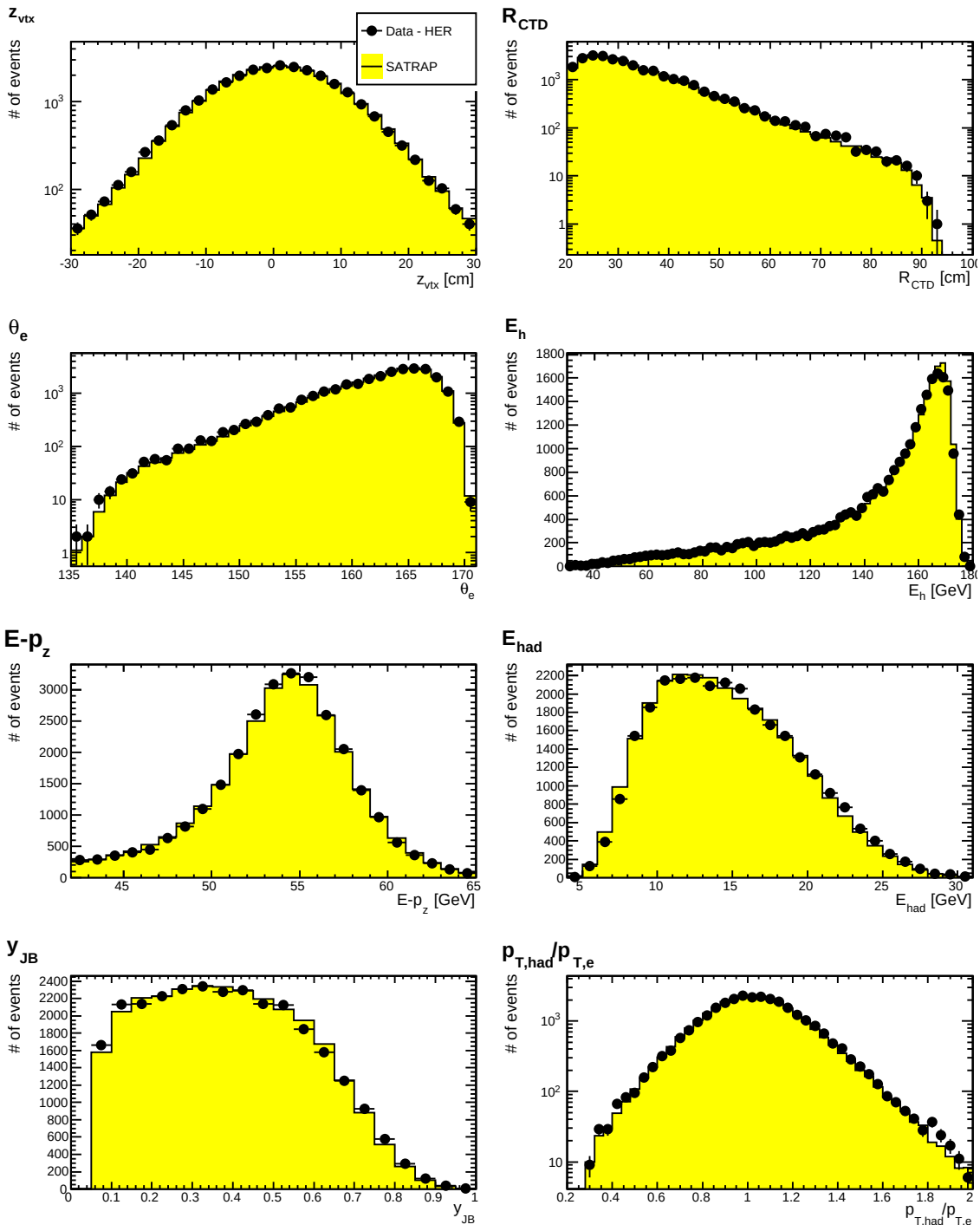

Figure 5.12: *Comparison between the HER data set (black dots) ant the* SATRAP *diffractive MC (yellow histograms), after the DIS and diffractive selections. The variables z_{vtx}, R_{CTD}, θ_e and γ_h (upper part), and $E - p_z$, E_{had}, y_{JB} and $p_{T,h}/p_{T,e}$ (lower part) are shown.*

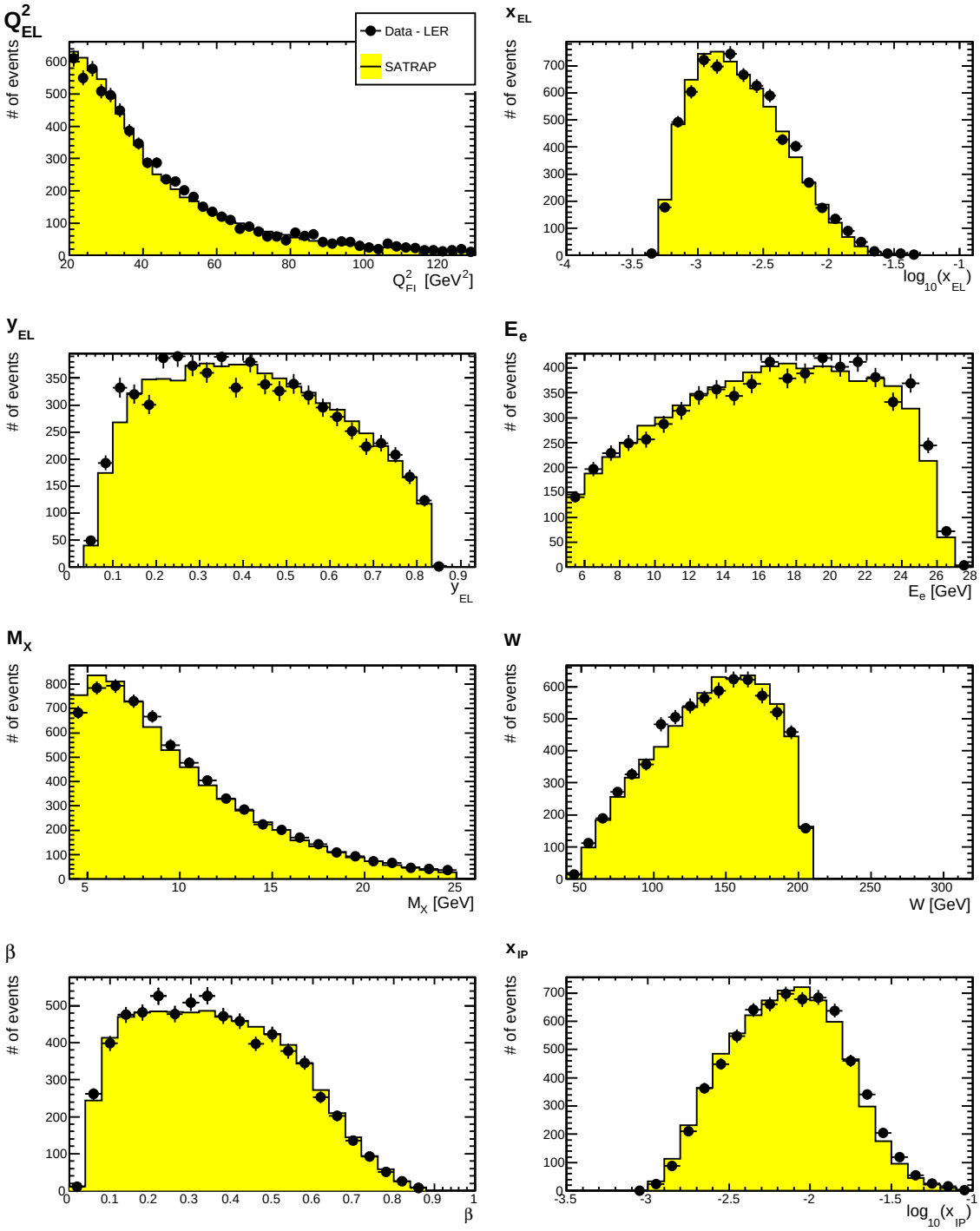

Figure 5.13: *Comparison between the LER data set (black dots) ant the* SATRAP *diffractive MC (yellow histograms), after the DIS and diffractive selections. The variables Q^2_{EL}, x_{EL}, y_{EL} and E'_e (upper part), and M_X, W, β and $x_{I\!P}$ (lower part) are shown.*

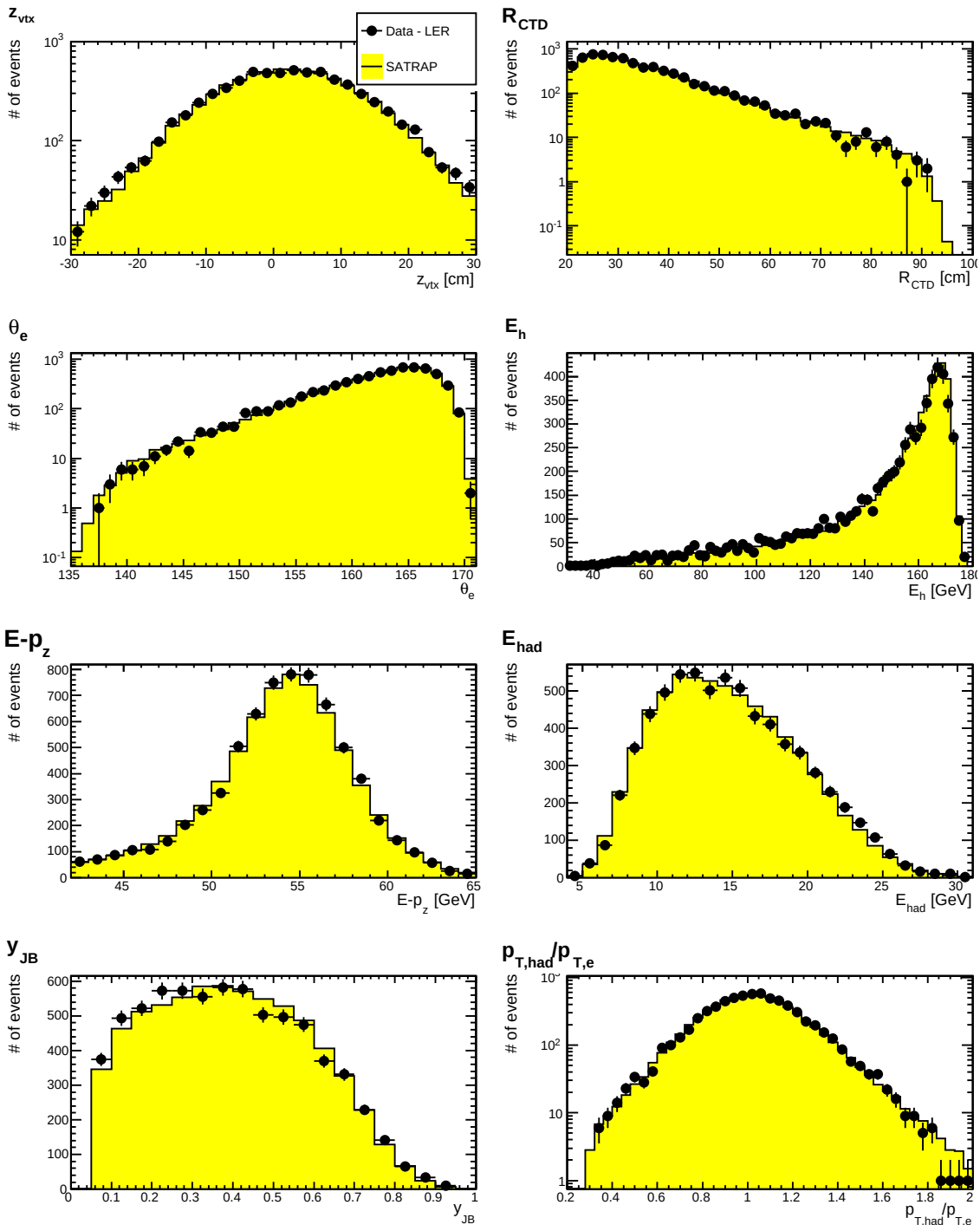

Figure 5.14: *Comparison between the LER data set (black dots) ant the* SATRAP *diffractive MC (yellow histograms), after the DIS and diffractive selections. The variables z_{vtx}, R_{CTD}, θ_e and γ_h (upper part), and $E - p_z$, E_{had}, y_{JB} and $p_{T,h}/p_{T,e}$ (lower part) are shown.*

5.4.6 Background Discussion

As already mentioned, no background sources were observed to affect the final data. Why this happens is further discussed in Sect. 5.4.6.1. The contribution of double diffractive events (DD) is expected to affect the diffractive sample after the η_{MAX} selection (see Sect. 3.4). Such effect is discussed in Sect. 5.4.6.2. Some background induced by the machine or by detector effects could still bias the data distributions and is further investigated (see Sect. 5.5).

5.4.6.1 The Photoproduction Background

PHP represents a relevant contribution in the inclusive DIS sample, especially in the high y region. The strong suppression observed in the diffractive sample (see Fig. 5.10) can be explained by the fact that diffractive events are relatively clean, low-multiplicity events, allowing high efficiency of the electron finder. However, diffractive photoproduction events simulated with Pythia are soft events, while for the kinematic region considered by this analysis some hard PHP events could pass the diffractive selection. Therefore, a sample of hard diffractive PHP events was generated with Rapgap (see Sect. 5.2.4) and compared to the HER data after the full event selection, once normalised to the luminosity of the data sample, as shown in Fig. 5.15. The figure shows that also the hard diffractive component of PHP is completely rejected by the diffractive selection.

The absence of PHP events in the data sample allowed to lower the threshold on the scattered electron energy to 5 GeV. It was decided not to relax the angle selection, which would have allowed to reach lower Q^2 values, since the track requirement based on the UVF tool played a crucial role in the PHP rejection and loosening that selection would imply gaining a relevant amount of PHP background.

5.4.6.2 The Double Dissociative Background

The diffractive samples selected with the Large Rapidity Gap method suffer from the presence of double dissociative events (DD). These are events which pass the η_{MAX} selection because the low-mass proton dissociative system is narrow enough to escape inside the beam hole without any interaction with the ZEUS detector, as in the case of single diffractive events. DD background only affects the normalisation of the diffractive cross section, without modifying the shape, as predicted by proton-vertex factorisation (see Sect. 1.3.4.1). To correct for the DD background contribution from the present analysis, the resulting cross section was normalised to the HERA combined cross section from Proton Spectrometer data (see Sect. 4.3.5).

It is important to notice that the amount of DD background is expected to be different between the HER and LER samples: due to the different proton beam energies ($E_p^{HER} = 920$ GeV and $E_p^{LER} = 460$ GeV) the boost in the forward direction of the proton dissociative system is different: thus the HER system is more boosted than the LER one and has a higher probability

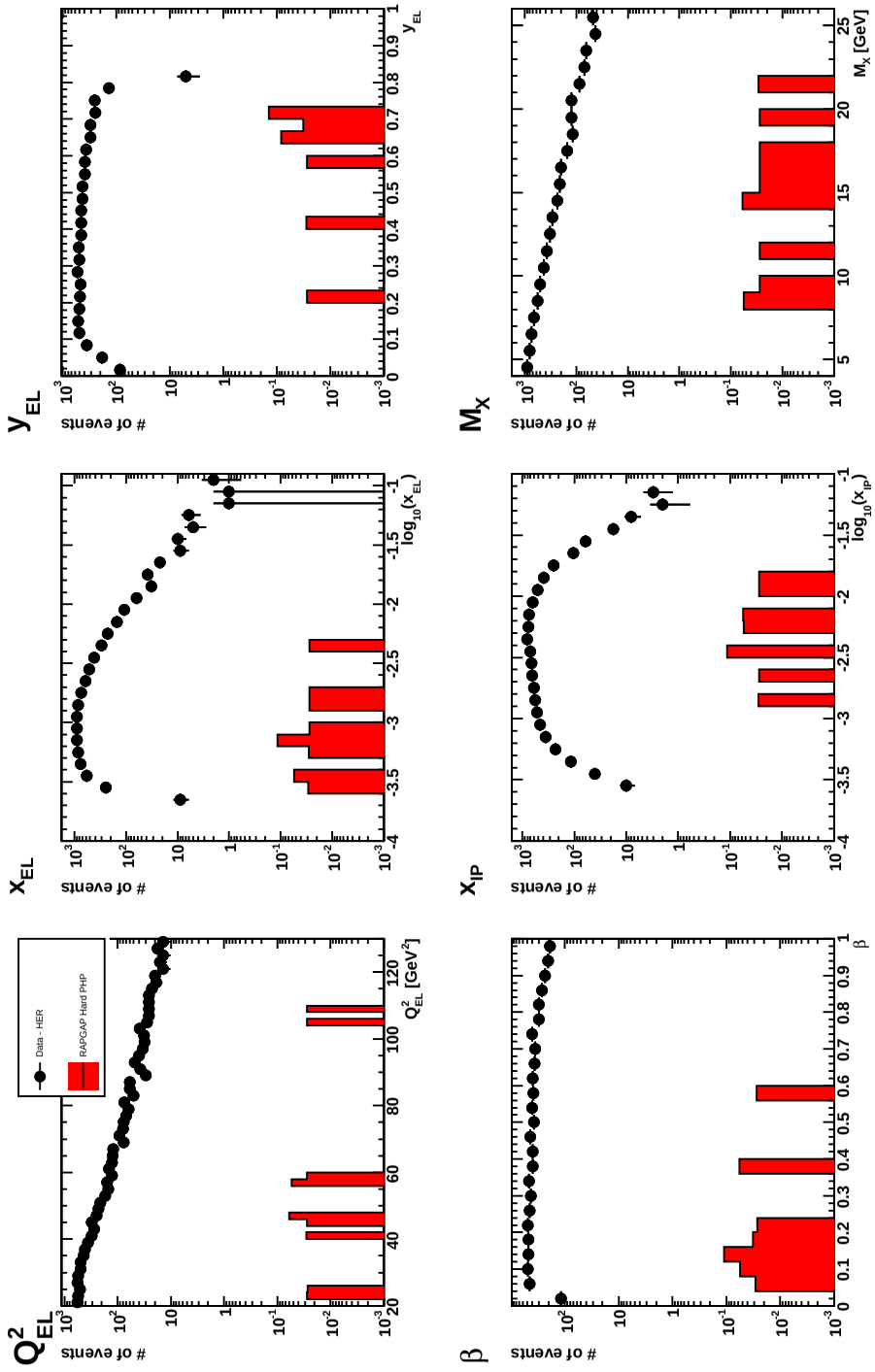

Figure 5.15: *Comparison between HER data set (black dots) and the* RAPGAP *hard diffractive PHP sample (red histograms). The DIS variables Q^2_{EL}, x_{EL} and y_{EL}, and the diffractive variables β , $x_{I\!P}$ and M_X are shown.*

to enter the forward beam pipe without interacting with the ZEUS detector. Therefore, the DD background contribution is expected to be higher in the HER rather than in the LER data sample (see Sect. 5.6.3).

5.5 Detector Studies

Several studies were performed to understand if any residual background induced by the machine or by detector effects could affect the present analysis. The energy flow distributions were carefully investigated to check if the Monte Carlo properly reproduces the data; the huge amount of non-vertex tracks observed in some diffractive events was examined; and the trigger efficiency was studied. All the checks presented here are based on the HER sample, statistically more powerful compared to the LER one.

As a general rule, red points/histograms represent data, while black ones are MC.

5.5.1 Energy Flow Studies

The energy flow was carefully studied in the diffractive samples. Several comparisons between data and MC distributions were performed, as possible discrepancies could be due to noise, to some not considered background or to a wrong hadronisation modelling in the simulation, and could introduce a bias in the measurement of the diffractive cross section.

5.5.1.1 Energy Flow and W

The Energy Flow Objects (see Sect. 5.3.4) used to reconstruct the hadronic final state were investigated in different regions of W, the invariant mass of the photon-proton system. For low x values, as it is the case of this analysis, W is related to the inelasticity of the event by the relation $W^2 \sim sy$ (using Eq. (5.13) and $Q^2 = sxy$). For low values of the inelasticity, and hence of W, γ_h is small and the hadronic final state X mostly populates the forward part of the detector, while as y increases, and so does W, the system X moves backward, towards the rear part of the detector. Therefore, W also gives information about the topology of the event.

Figure 5.16 shows the number of ZUFOs[5] per event, their mean energy, E_{ZUFO}, and the resulting invariant mass, M_X, as a function of θ_{ZUFO}, the polar angle of the object inside the detector, for five different W regions ($50 < W < 300$ GeV, $\Delta W = 50$ GeV). The invariant mass distributions are also shown. Some discrepancies are observed between the data and the SATRAP MC in the low W bins ($W < 100$ GeV), concentrating in the forward region of the detector ($\theta_{ZUFO} \lesssim 1$). However, the agreement is good in the high-W, and consequently high-y region,

[5]It is useful to remember that Energy Flow Objects, introduced in Sect. 5.3.4 are commonly indicated as ZUFOs within the ZEUS nomenclature.

with the exception of some remaining small disagreement for $\theta_{ZUFO} \sim 0.7$, corresponding to the crack region between the BCAL and the FCAL.

5.5.1.2 Energy in the Calorimeter

The energy distributions of the ZUFOs in different regions of the calorimeter (FCAL, BCAL, RCAL) were investigated as a function of the η_{MAX} of the event both for data and MC, as shown in Fig. 5.17. Some differences in the mean energy per event were observed in the high η_{MAX} region, for all the calorimeter sections. Data exhibit higher energies in the FCAL and BCAL regions, and lower in the RCAL, compared to the MC. However, the noise level in data (E_{ZUFO} 0.2 GeV) when the corresponding CAL component was not fired ($\eta_{MAX} < 1.1$ for FCAL, $\eta_{MAX} < -0.9$ for BCAL) is well reproduced by the MC. To understand if this effect could bias the mass reconstruction, the M_X of the event was studied as a function of η_{MAX} and γ_h and no particular discrepancies are observed, meaning that the small E_{ZUFO} discrepancies are well balanced by the $\vec{p}_{ZUFO}$ components, once the invariant mass is reconstructed (see Fig. 5.18).

The crack region between the BCAL and the FCAL, corresponding to $\eta \sim 1.0 - 1.1$, is a delicate region, where both the event simulation and the event reconstruction can fail. In Fig. 5.19 some relevant distributions are shown, such as the ZUFO energy, E_{ZUFO}, its CAL component and the electromagnetic CAL fraction, the type of ZUFO, TUFO[6], the number of cells forming each ZUFO island, and the invariant mass M_X reconstructed in the crack region. In all the distributions the MC is in reasonable agreement with the data, which allows to considered the crack region safe.

5.5.1.3 Energy Flow and η_{MAX}

The η_{MAX} variable is an important quantity for this analysis, since it determines the selection of the diffractive sample. The same quantities already studied for the crack region were investigated for the ZUFO which defines the η_{MAX} of the event, as shown in Fig. 5.20. The agreement between data and MC is good and the η_{MAX} reconstruction looks reliable.

[6]The type of ZUFOs are encoded as follow: TUFO ~ 1 is a track ZUFO, TUFO between 10 and 22 is a track+island ZUFO, TUFO ~ 30 is an island ZUFO (for informations on the ZUFO reconstruction algorithm, see Sect. 5.3.4).

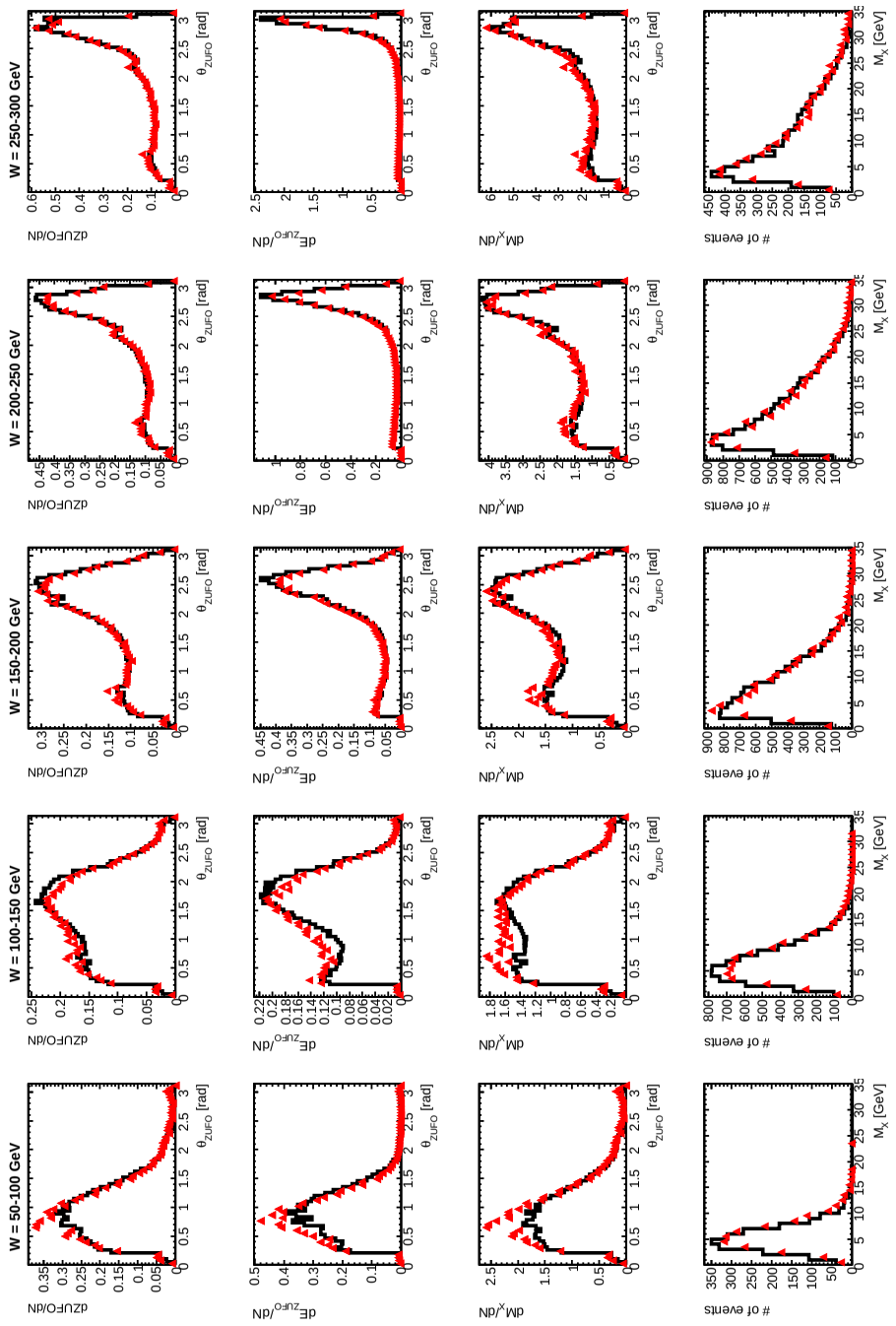

Figure 5.16: *Comparison between HER data (red triangles) and* SATRAP *MC (black histograms) for the number of ZUFOs per event, their mean energy, E_{ZUFO}, and the resulting invariant mass, M_X, as a function of θ_{ZUFO}, the polar angle of the object, and the M_X distributions in different bins of W, from $W = 50$ GeV to $W = 300$ GeV ($\Delta W = 50$ GeV).*

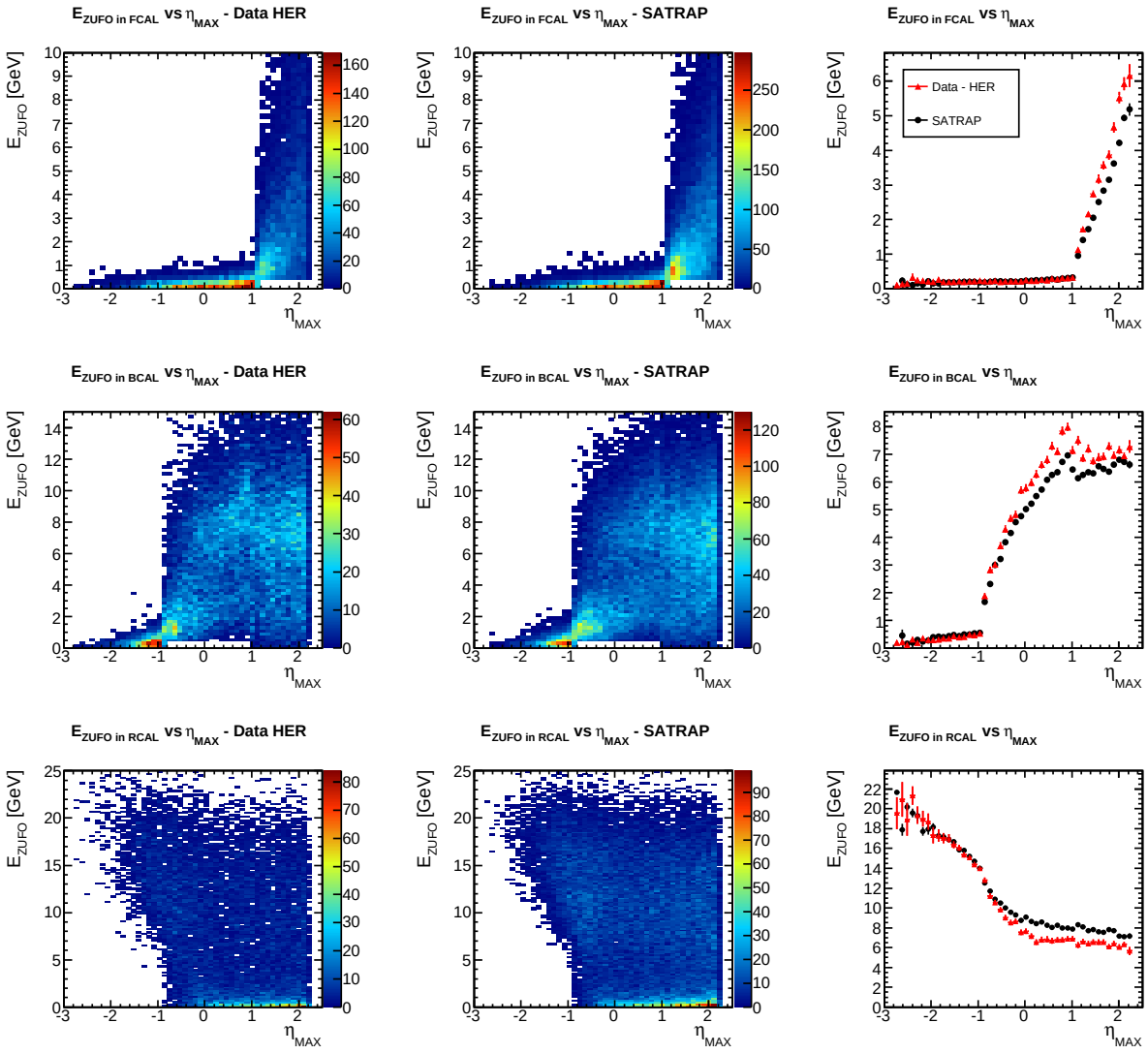

Figure 5.17: *Scatter plot of the ZUFO energy, E_{ZUFO}, as a function of η_{MAX} for HER data (left) and MC (centre), and the profile plot of the two distributions (right), for the FCAL (up), BCAL (medium) and RCAL (low) components. Red triangles are data and black dots MC.*

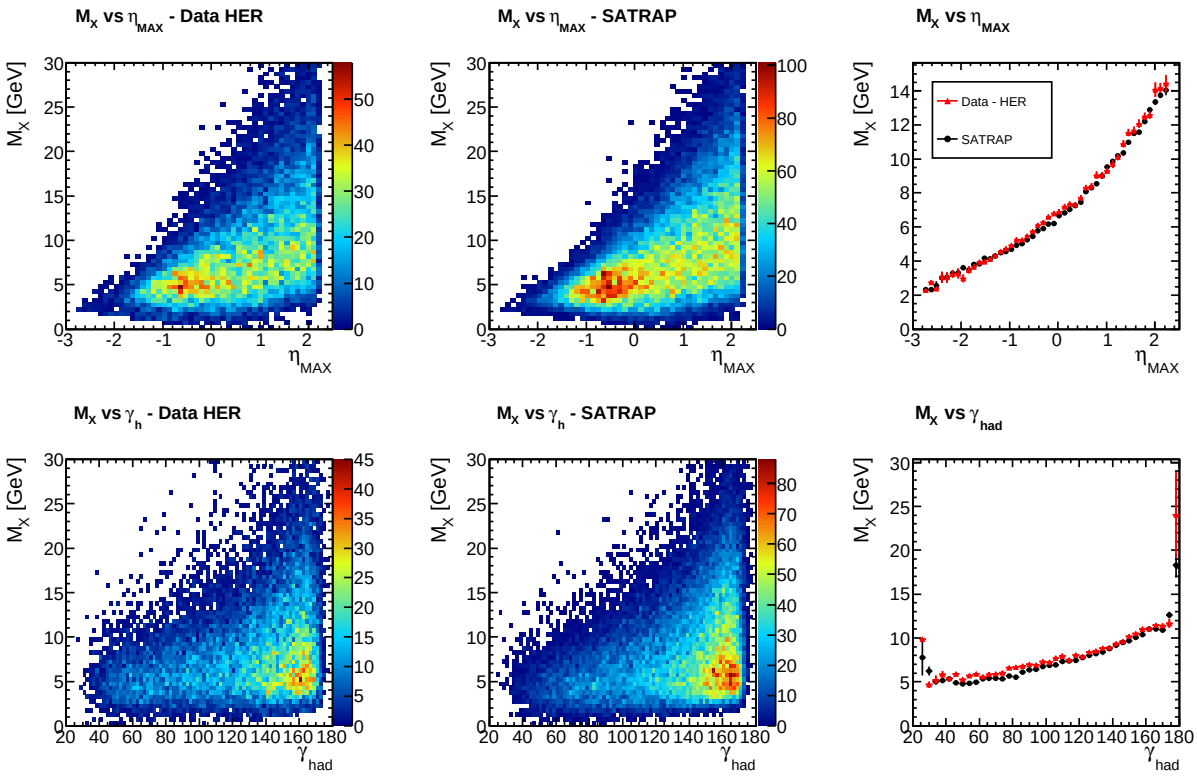

Figure 5.18: *Scatter plot of the invariant mass of the X system, M_X, as a function of η_{MAX} (up) and γ_h (low) for HER data (left) and MC (centre), and the profile plot of the two distributions (right). Red triangles are data and black dots MC.*

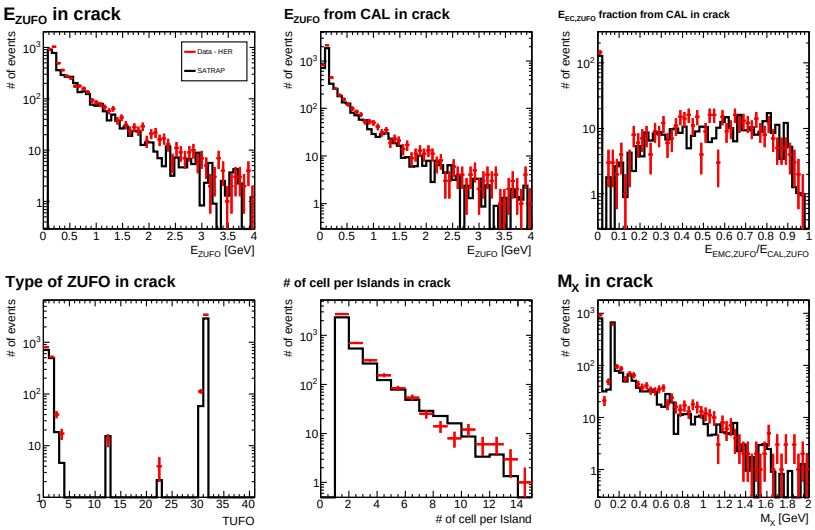

Figure 5.19: *Comparison between HER data (red points) and the* SATRAP *MC simulation (black histograms) for some variables related to the ZUFOs in the crack between RCAL and FCAL: the ZUFO energy, E_{ZUFO}, also decoupled in its CAL component and the electromagnetic CAL fraction, the type of ZUFO, TUFO, the number of cells that composed each ZUFO island, and the invariant mass M_X reconstructed in the crack region.*

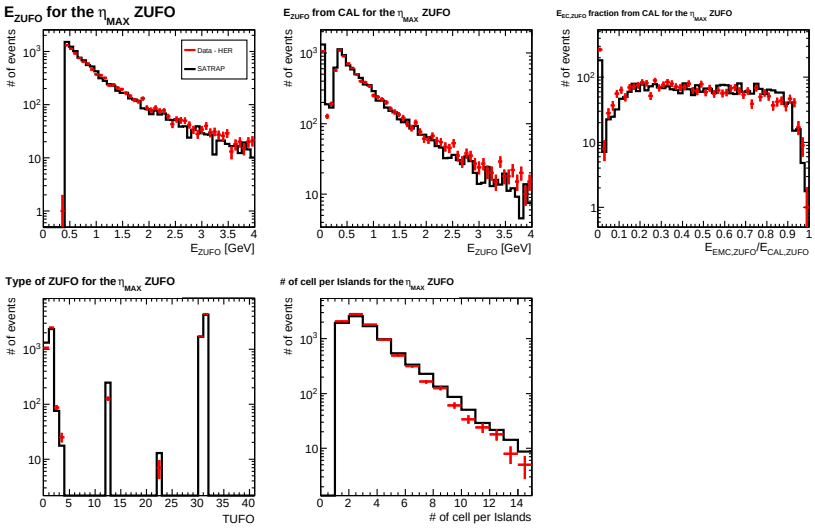

Figure 5.20: *Comparison between HER data (red points) and the* SATRAP *MC simulation (black histograms) for some variables related to the η_{MAX} ZUFO: the ZUFO energy, E_{ZUFO}, also decoupled in its CAL component and the electromagnetic CAL fraction, the type of ZUFO, TUFO, and the number of cells that composed each ZUFO island.*

5.5.1.4 Energy Flow and Event Topology

Studies were made of the topology of diffractive events as reconstructed either from ZUFOs or with primary-vertex tracks. The maximum difference in rapidity between two particles inside the detector, excluding the scattered electron, was investigated. The variable $\Delta\eta_{MAX}$ was built as the maximum gap in rapidity between the particles of the hadronic final state X, where particles were defined either by using vertex tracks or ZUFOs. $\Delta\eta_{MAX}$ distributions, as well as correlations between $\Delta\eta_{MAX}$ from tracks and from ZUFOs are shown in Fig. 5.21. There is good agreement between data and MC.

Events with $\Delta\eta_{MAX}^{ZUFOs} - \Delta\eta_{MAX}^{tracks} > 1$ were further investigated, as this region could be only populated by ZUFOs originated from neutral particles or noisy cells, making the gap reconstructed from ZUFOs much smaller than the gap from tracks. The two objects forming the $\Delta\eta_{MAX}$, the forward ZUFO and the backward ZUFO (from $\Delta\eta_{MAX} = \eta_{forward} - \eta_{backward}$), were studied. Figure 5.22 shows some distributions for these particular ZUFOs. Studies were repeated for FCAL, BCAL and crack region separately. The MC always reproduced the data satisfactorily.

In conclusion, the event topology of data is well reproduced by MC.

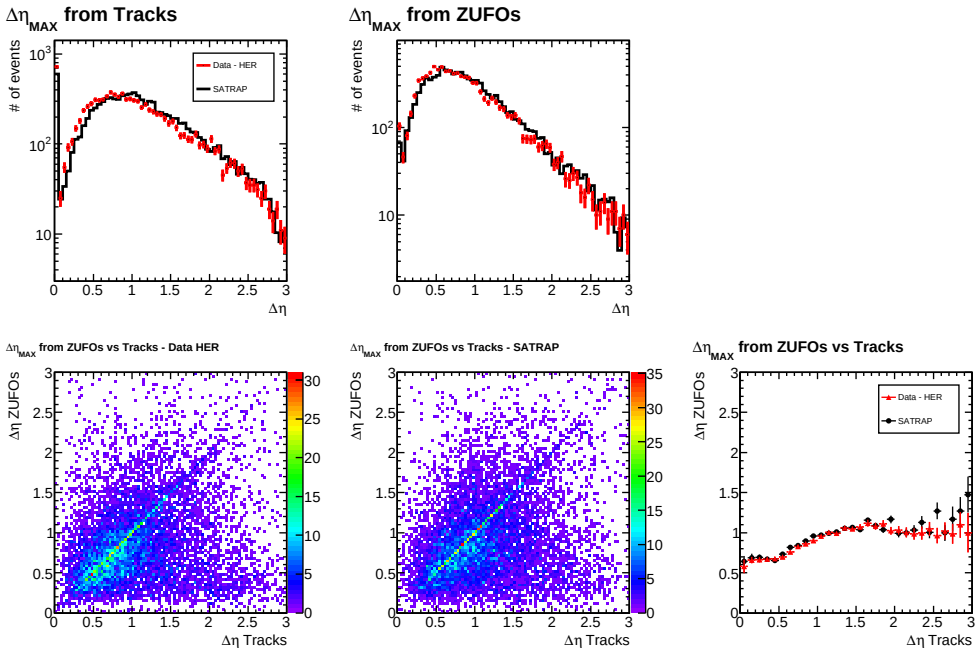

Figure 5.21: *Comparison between HER data (red points) and the* SATRAP *MC simulation (black histograms/points) for $\Delta\eta_{MAX}$ variables. Upper part show $\Delta\eta_{MAX}^{tracks}$ (left) and $\Delta\eta_{MAX}^{ZUFOs}$ (centre); the lower part a scatter plot o $\Delta\eta_{MAX}^{ZUFOs}$ vs $\Delta\eta_{MAX}^{tracks}$ for data (left) and MC (centre) and their profile plot (right).*

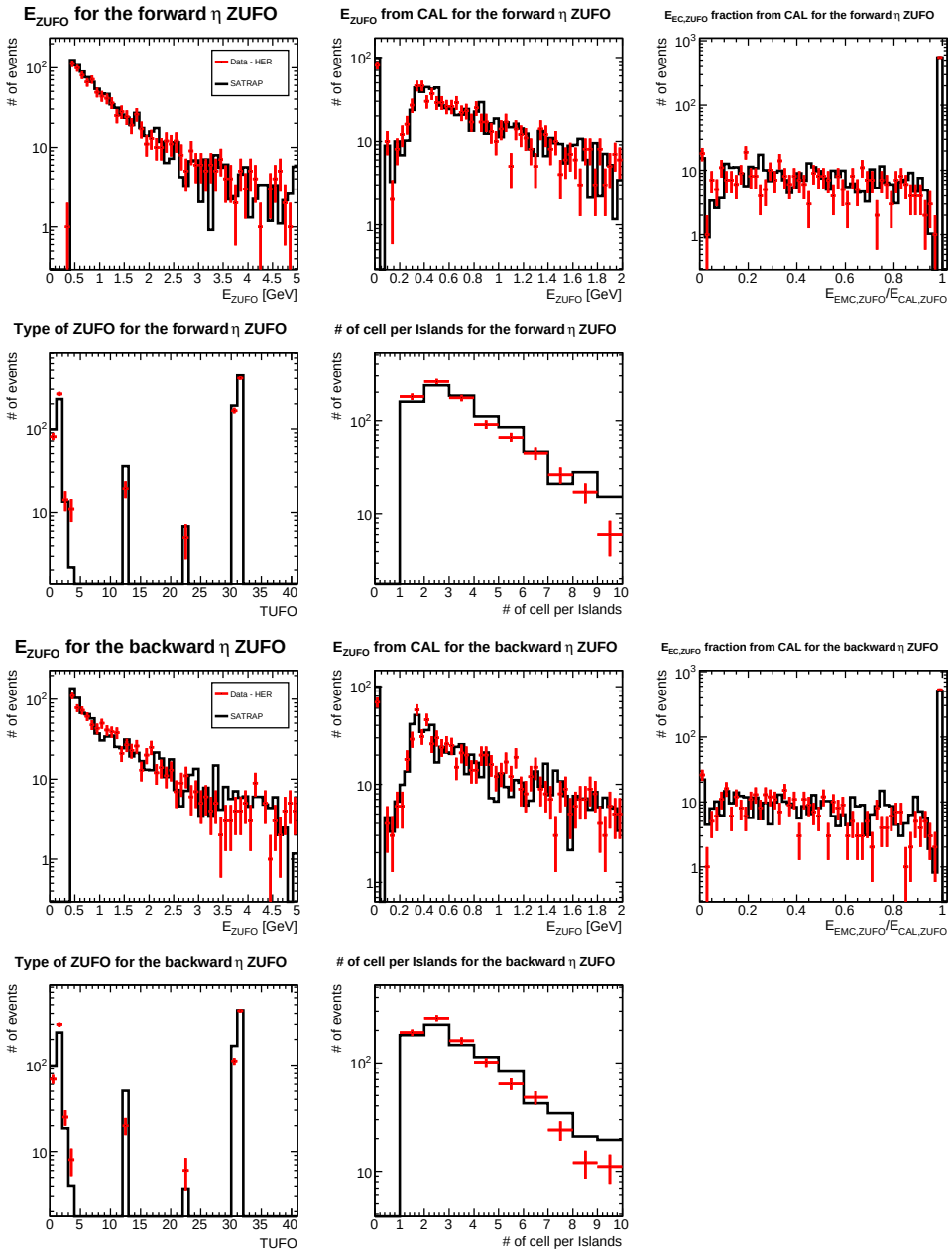

Figure 5.22: *Comparison between HER data (red points) and the* SATRAP *MC simulation (black histograms) for some variables related to the forward (upper plot) and backward (lower plot) ZUFO that set $\Delta\eta_{MAX}$: the ZUFO energy, E_{ZUFO}, also decoupled in its CAL component and the electromagnetic CAL fraction, the type of ZUFO, TUFO, and the number of cells that composed each ZUFO island.*

5.5.2 Non-Vertex Track Studies

After the HERA luminosity upgrade, a relevant amount of tracks not connected to the primary vertex was observed in the ZEUS events. Figure 5.23 shows, as an example, an event with more than 40 tracks not fitted to the primary vertex, passing the full selection of this analysis. Non-vertex tracks could hit the calorimeter and produce an energy deposit. If those calorimeter cells were identified as neutral particles, they could fake the reconstruction of kinematic variables.

A comparison between data and MC for some track variables as the impact parameter (IP), the distance of closest approach of the track to the primary vertex (DCA) and its z component (z_{DCA}) are shown in Fig. 5.24, both for vertex tracks and non-vertex tracks. For vertex tracks the distributions show good agreement between data and MC, while discrepancies are visible in case of non-vertex tracks. For data, non-vertex tracks reached very high values of DCA and they could also originate very far from the interaction point, as shown from the z_{DCA} distribution.

Non-vertex tracks with large values of DCA were further investigated. Figure 5.25 shows the number of non-vertex tracks with DCA > 10 cm per event and the difference between data and MC is evident. It was decided to reject events with more than 10 tracks with DCA > 10 cm and to correct the integrated luminosity of the data and MC samples accordingly. In Table 5.2 the percentage of events rejected by this selection is shown for data and MC, both for the HER

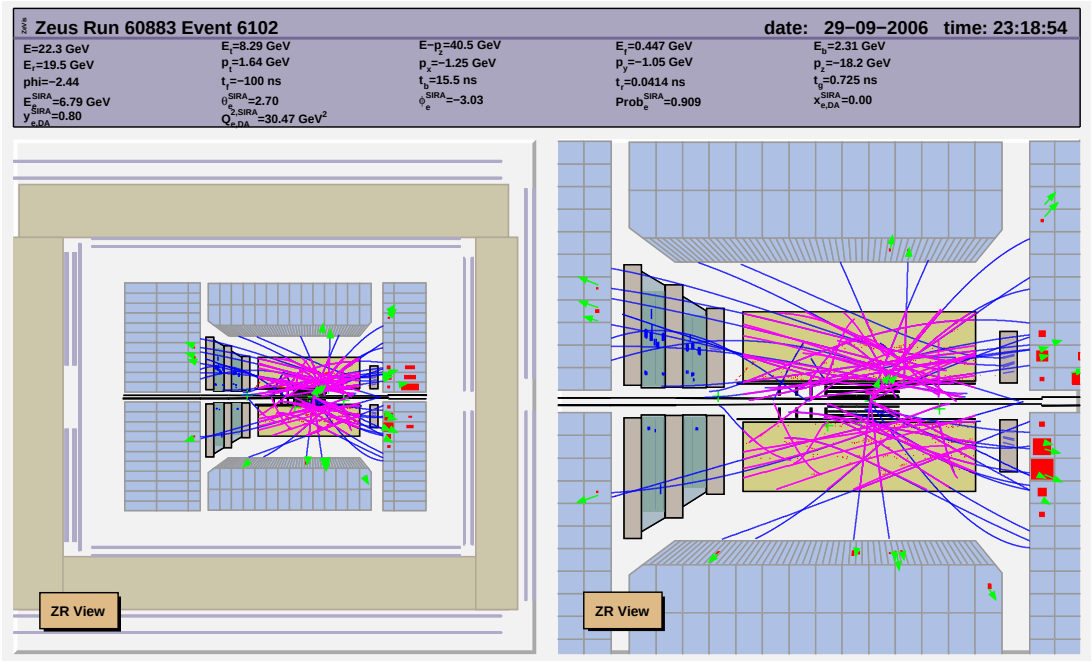

Figure 5.23: *A diffractive DIS event with more than 40 tracks not from the primary vertex, as seen in the ZEUS detector. The ZR view of the event (left) and its zoom (rigth) are shown.*

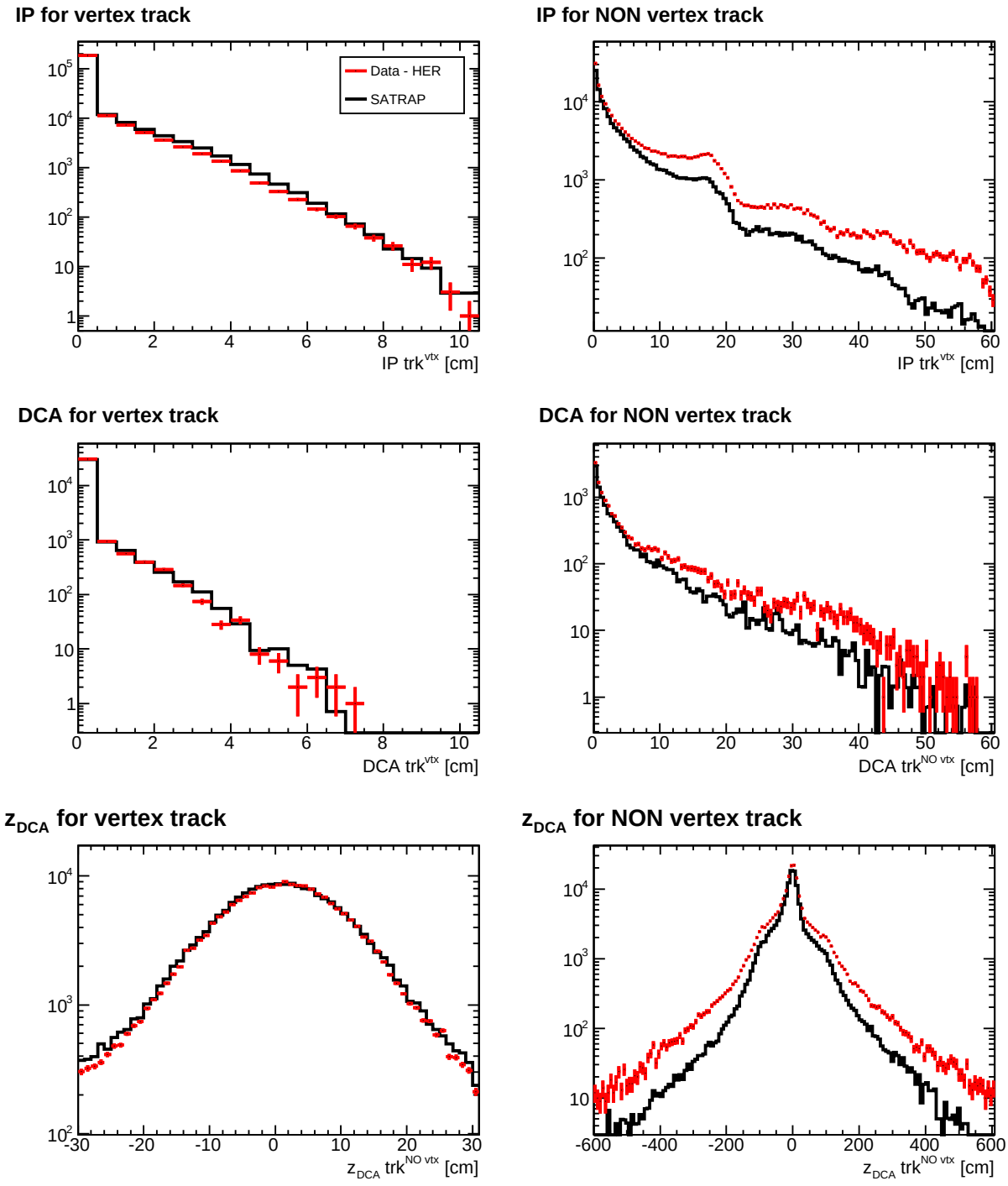

Figure 5.24: *Comparison between HER data (red points) set and the* SATRAP *MC simulation (black histograms) for some variables related to vertex (left) and non-vertex (right) tracks: the interaction point (up), the distance of closest approach (middle) and its z component (low) relative to the primary vertex of the event.*

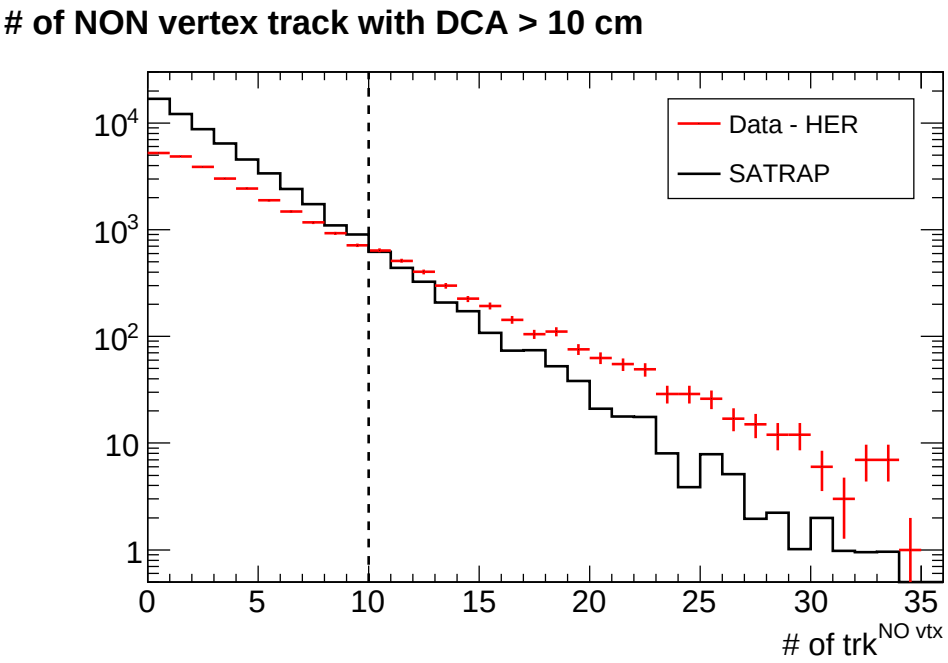

Figure 5.25: *Distributions of non-vertex tracks per events with DCA* $>$ 10 *cm. Red points are HER data and the black histogram* SATRAP *MC.*

and LER samples.

However, prior to appling the selection, checks were made on the dependence of the reconstructed mass on the number of non-vertex tracks with DCA $>$ 10 cm, as shown in Fig. 5.26. The distribution of the mass M_X of the event shows a mild dependence on the number of non-vertex tracks with good agreement between data and MC. The value of the generated mass is also shown superimposed to data and MC and the agreement is very good.

	HER	LER
Data	9.99	10.21
SATRAP	2.90	2.78

Table 5.2: *Percentage of events rejected from the cut on the number of non-vertex tracks with DCA* $>$ 10 *cm. The vertical dashed line shows the analysis cut (see Sect. 5.4.3.2).*

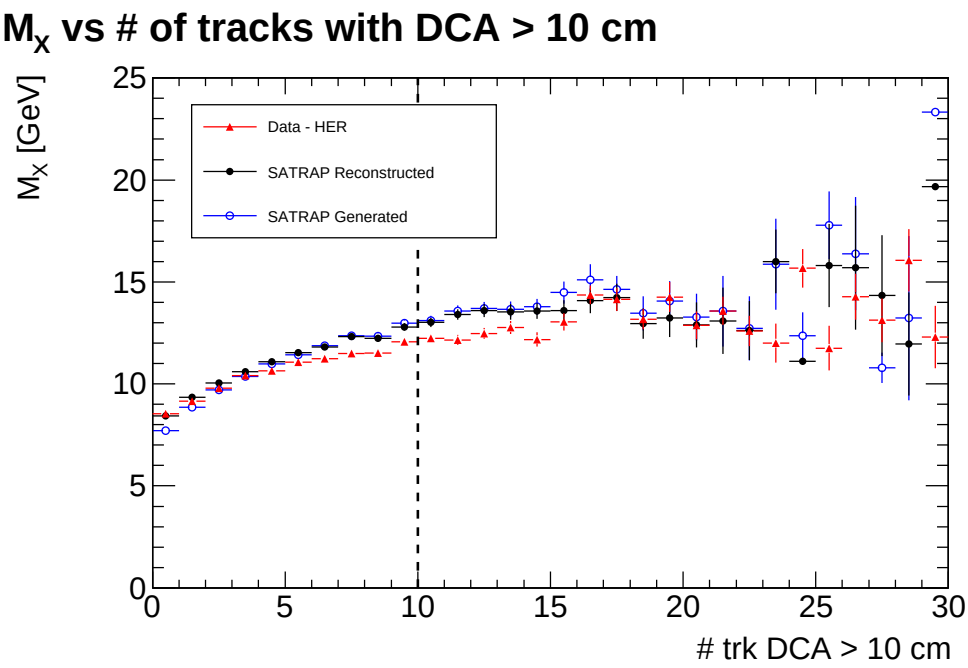

Figure 5.26: *Profile plot of the mass of the event as a function of the number of non-vertex tracks per events with DCA* > 10 *cm. Red triangles are HER data, black dots are MC reconstructed and blue open dots the MC generated values. The vertical dashed line shows the analysis cut (see Sect. 5.4.3.2).*

5.5.3 Efficiency Studies

5.5.3.1 Trigger Efficiency

The trigger selection was applied online to the data, prior to their record on tape (see Sect. 2.2.9), while Monte Carlo events passed through the trigger simulation (see Sect. 5.2.5). A disagreement between data and MC trigger efficiencies could introduce a bias on the measurements and therefore was carefully checked.

The trigger efficiency was studied by selecting a sample with a combination of FLT slots independent of FLT30 to which the offline selection was applied. From all the selected events, N_{all}, the events with the FLT30 slot fired, N_{FLT30}, were estimated. The efficiency was obtained as the ratio:

$$\mathrm{eff}_{\mathrm{FLT30}} = \frac{N_{FLT30}}{N_{all}} \ . \tag{5.27}$$

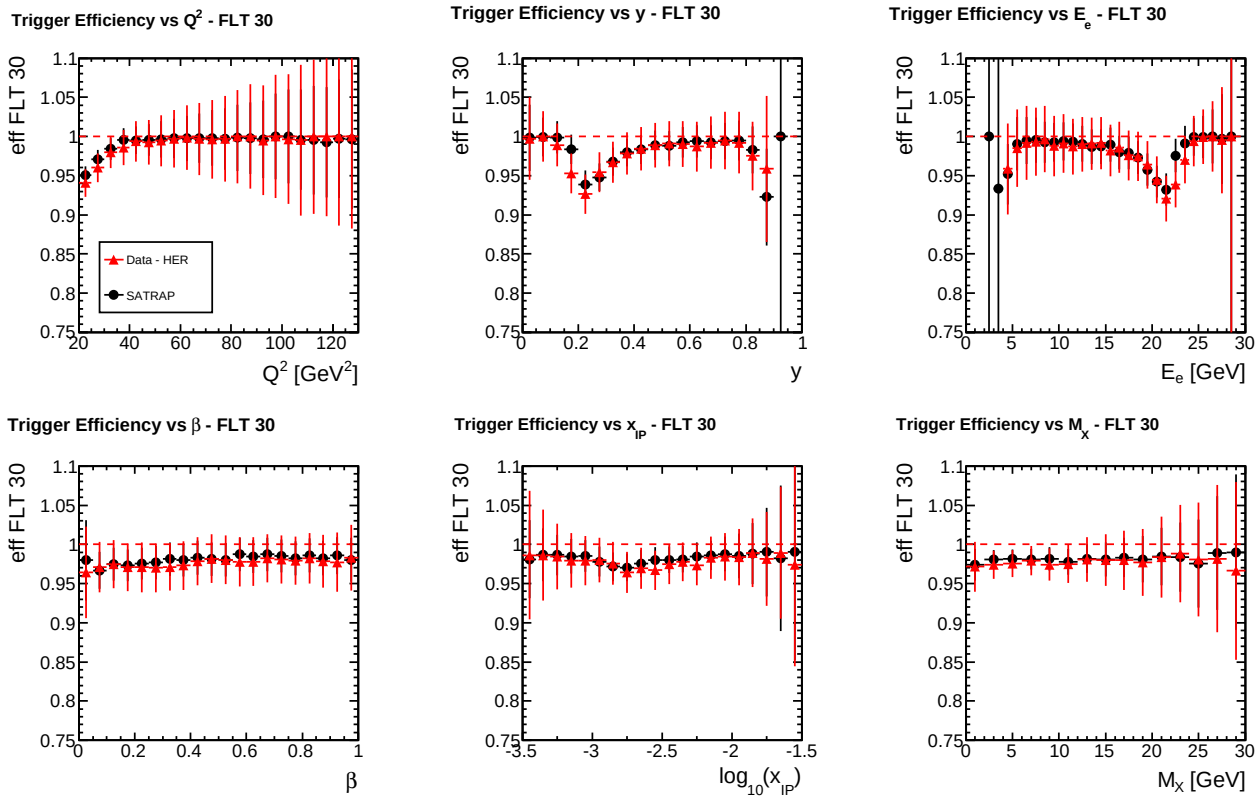

Figure 5.27: *Comparison between HER data (red triangles) set and* SATRAP *MC (black dots) for the FLT30 trigger efficiency as a function of the DIS variables Q^2_{EL}, y_{EL} and E'_e, and the diffractive variables β , $x_{I\!P}$ and M_X.*

Figure 5.27 shows the trigger efficiencies of data and MC as a function of the main DIS and diffractive kinematic variables. The efficiencies are ~ 1 in most of the phase space, however a dip appears in the region $E'_e \sim 22$ GeV. From a further investigation (see Fig. 5.28, upper plot) it emerged that the drop in efficiency was due to a trigger inefficiency in the first inner ring of the RCAL. It disappears upon rejecting all the events with $E < 5$ GeV in the RCAL first inner ring. However, this is a severe cut that rejects a considerable amount of events, $\sim 20\%$. In order to keep all the events, a simple reweighting factor was applied to the HER MC to correct for this effect. The reweighting function is given by:

$$\begin{aligned} f(E'_e) &= 1.304 - (0.015 \times E'_e) \text{ for } 20.0 < E'_e < 22.5\ GeV\ , \\ &= 0.620 + (0.015 \times E'_e) \text{ for } 22.5 < E'_e < 25.0\ GeV\ , \end{aligned} \tag{5.28}$$

with all energies in GeV. After the reweighting the trigger efficiency as a function of M_X was checked, as shown in Fig. 5.28 (lower plot), and no differences were observed for data and MC, except in the region $M_X > 25$ GeV, where the MC efficiency was slightly lower than data.

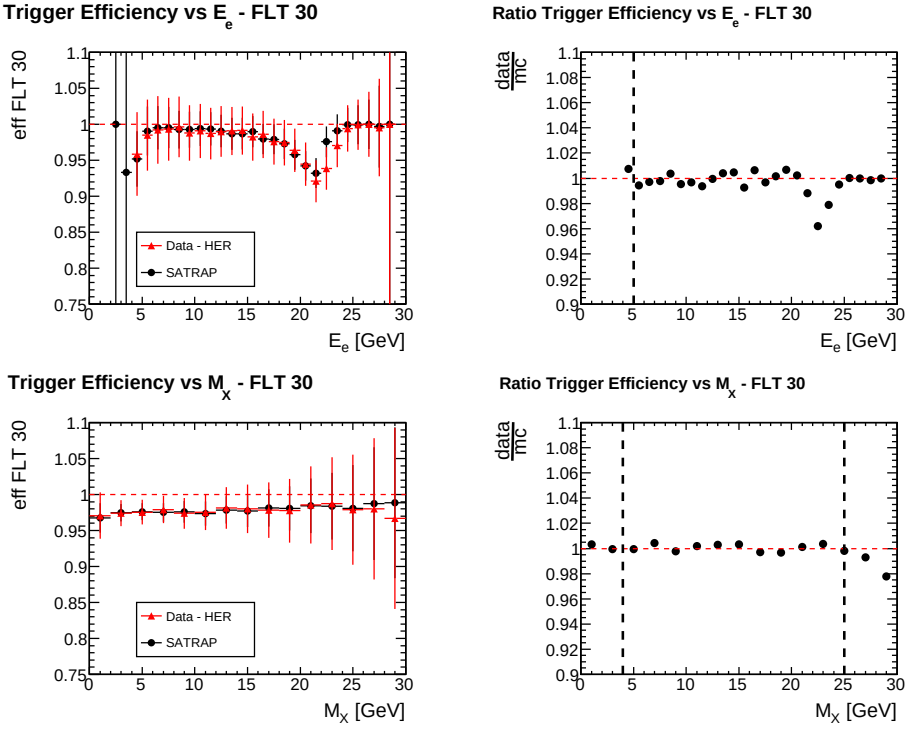

Figure 5.28: *Detailed comparison between HER data and* SATRAP *MC FLT30 trigger efficiency as a function of E'_e (left) and their ratio (right) before the correction (upper plot). Same ditributions are shown as a function of M_X after the reweighting was applied (lower plot). Red triangles represent data, black dots MC. The vertical dashed lines show the analysis cuts (see Sect. 5.4.3).*

5.5.3.2 Vertex Efficiency

All the events without a reconstructed vertex were rejected (see Sect. 5.4.3). However, this requirement could introduce a bias for diffractive analyses, as diffractive events have a lower multiplicity compared to the inclusive ones and the tracking algorithm could fail to find a vertex in the event.

The vertex efficiency was studied as the ratio of the event yield with a reconstructed vertex divided by the total event yield, as a function of γ_h for different regions of M_X, as shown in Fig. 5.29. The results show that the vertex reconstruction algorithm had an extremely high efficiency (~ 1) along most of the phase space and only for very low values of M_X ($M_X < 6$ GeV) were observed some inefficiencies. Moreover, the efficiency of the data is well reproduced by the MC.

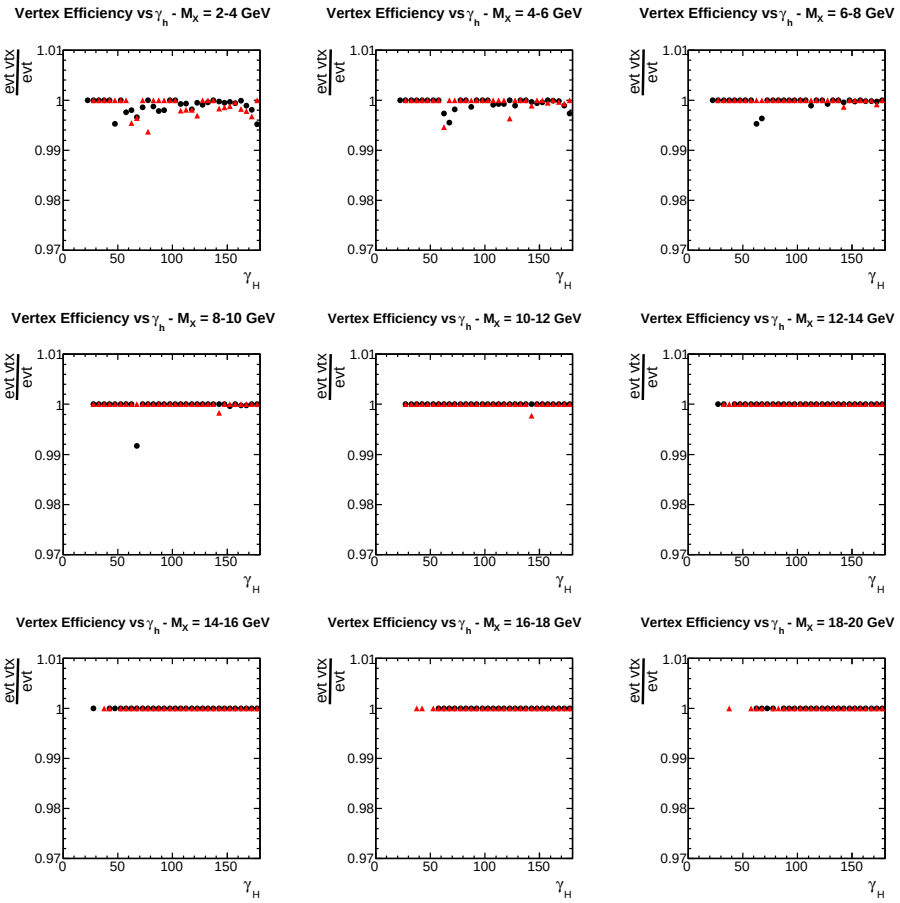

Figure 5.29: *Vertex efficiency for HER data (red triangles) and* Satrap MC *(black dots) as a function of γ_h in bin of M_X, from $M_X = 2$ GeV to $M_X = 20$ GeV ($\Delta M_X = 2$ GeV).*

5.6 Results

5.6.1 Bin Selection

The inclusive diffractive DIS ep reduced cross section $\sigma_r^{D(3)}$, introduced in Sect. 1.3.3, can be described in terms of the kinematic variables Q^2, β and $x_{I\!P}$. A binning scheme dependent on these variables was studied. The size of each bin was decided according to the statistical precision of the data and the resolution of the kinematic variables. In Fig. 5.30 the binning scheme adopted for the present analysis is shown superimposed to the HER data sample, after the complete event selection described in Sect. 5.4.

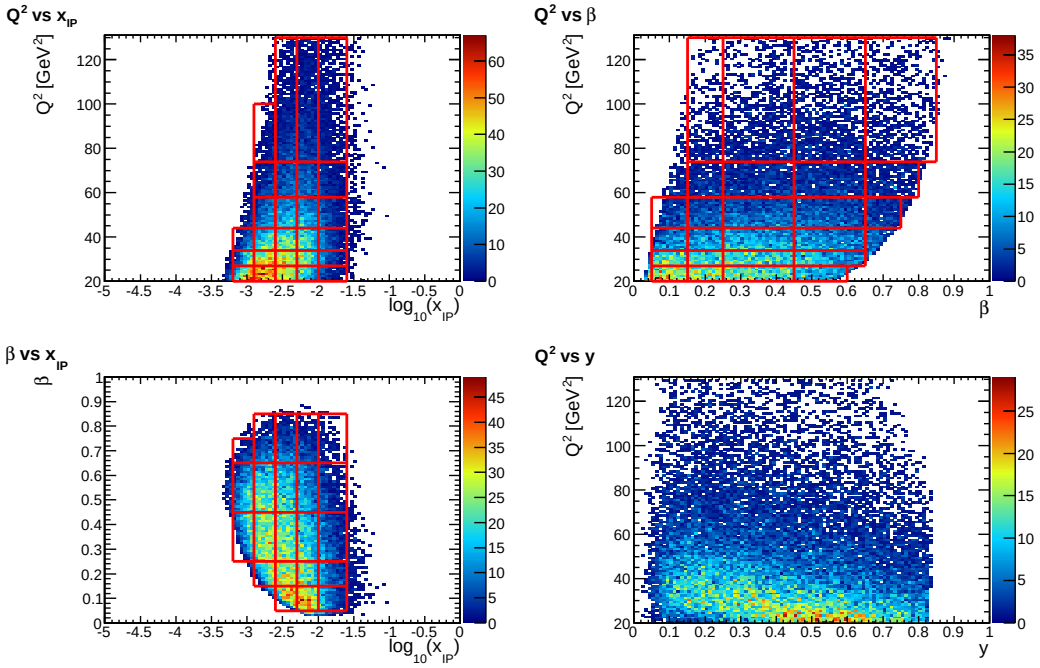

Figure 5.30: *The binning scheme adopted for the present analysis is shown as a function of Q^2, β and $x_{I\!P}$, superimposed to the selected HER data sample. The kinematic coverage of the present data in the (Q^2,y) plane is also shown.*

5.6.1.1 Resolution of the Kinematic Variables

The finite resolution of the ZEUS detector causes a smearing of the kinematic variables reconstruction and consequently migration across the bins. To reduce this effect the bin size must be larger than the resolution.

In Fig. 5.31 the Q^2, β and $x_{I\!P}$ resolutions are shown for the HER sample. The Q^2 variable

has a very high resolution in the whole region considered; β and $x_{I\!P}$ resolutions are poorer, but still smaller than the bin size.

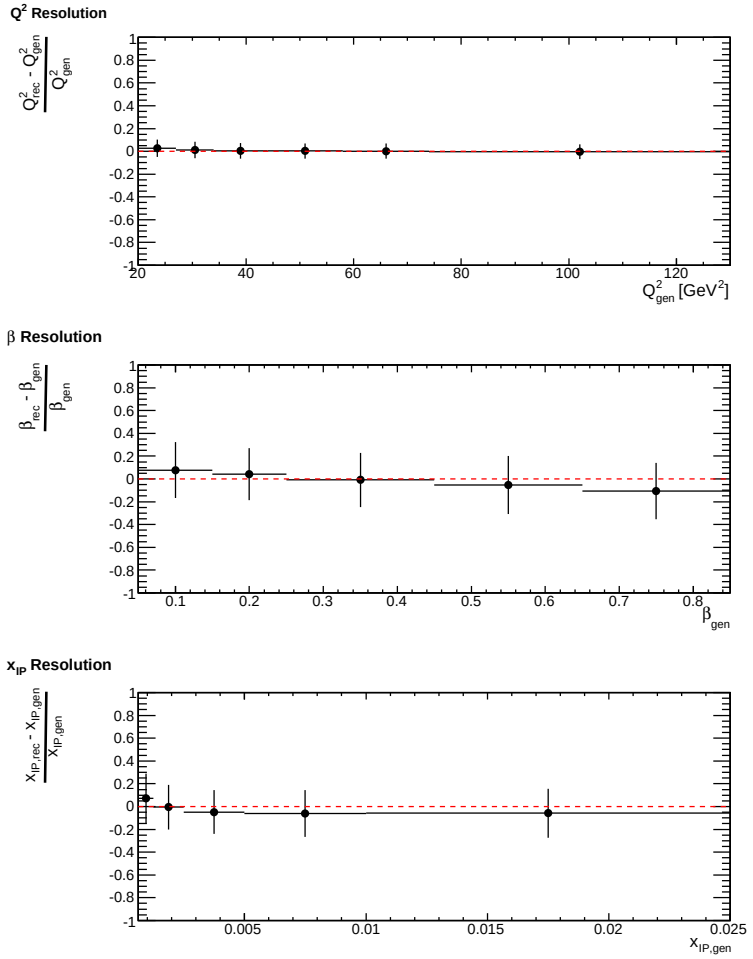

Figure 5.31: *The Q^2 (up), β (middle) and $x_{I\!P}$ (low) resolutions are shown in the binning scheme adopted for the analysis, as a function of generated values.*

5.6.1.2 Acceptance and Purity

For each bin i, the acceptance, A_i, and the purity, P_i, were defined as:

$$A_i = \frac{N_i^{rec}}{N_i^{gen}} \ , \tag{5.29}$$

$$P_i = \frac{N_i^{gen\&rec}}{N_i^{gen}} \ , \tag{5.30}$$

where N_i^{rec} is the number of reconstructed MC events passing all the selection cuts measured in the i-th bin, N_i^{gen} is the number of generated events in the i-th bin, and $N_i^{gen\&rec}$ represents the number of events which are measured and generated in the same bin i. The acceptance reflects the effect of the trigger and the offline selection, of the detector geometry and efficiency, and of the reconstruction efficiency on the measured number of events. Due to bin-by-bin migration effects, the value of the acceptance can be larger than 100%. The purity is an estimate of the migration from adjacent bins to and from the measured one. A high purity value for a bin means small migration into or from that bin.

Geometrical and Diffractive Acceptance and Purity In order to choose the bins of the present analysis the acceptance was factorised into two terms: the acceptance depending on Q^2, sensitive to geometrical effects related to the electron reconstruction, and the acceptance in (β, $x_{I\!P}$), sensitive to the identification and reconstruction of the diffractive system.

The Q^2 acceptance was evaluated from the DIS sample, prior to apply the diffractive selection and it is only sensitive to the reconstruction and selection of the scattered DIS electron. It is mainly affected by the geometry cut (see Sect. 5.4.3.1 and Fig. 5.9) which rejected regions where the scattered electron could hit the calorimeter. Due to the tight geometrical selection the Q^2 acceptance lies between 20% and 60%; however, the Q^2 dependence of the cross section is well known by the MC generator and the detector effects on Q^2 can be precisely corrected.

The (β, $x_{I\!P}$) acceptance was extracted once the DIS selection was applied to both the generated and reconstructed samples, and therefore it is directly influenced by the diffractive selection, and by the resolution effects along the bins. Bins with (β, $x_{I\!P}$) acceptance $> 70\%$ were used for the cross section extraction; bins with (β, $x_{I\!P}$) acceptance between 50 and 70% were accepted under the condition that the contribution of the systematic uncertainties (see Sect. 5.6.2.3) on the measured cross section was below 10%; bins with (β, $x_{I\!P}$) acceptance $< 50\%$ were rejected.

In Fig. 5.32 the Q^2 and (β, $x_{I\!P}$) acceptance and purity are shown for the HER and LER samples.

Bin Acceptance and Purity Once the bins were selected, the acceptance and purity were studied in the (β, Q^2, $x_{I\!P}$) bins used for the cross section extraction. In Figs. from 5.33 to 5.36 the bin-by-bin acceptance and purity are shown, for the HER and LER samples, respectively. The bin acceptance is given by the convolution of the Q^2 and (β, $x_{I\!P}$) acceptances. For $Q^2 \geq 38$ GeV^2, the acceptance was $\sim$ 40%. All the bins had a moderate purity, $\sim$ 40%, that was considered satisfactory for the kinematic region covered by the analysis.

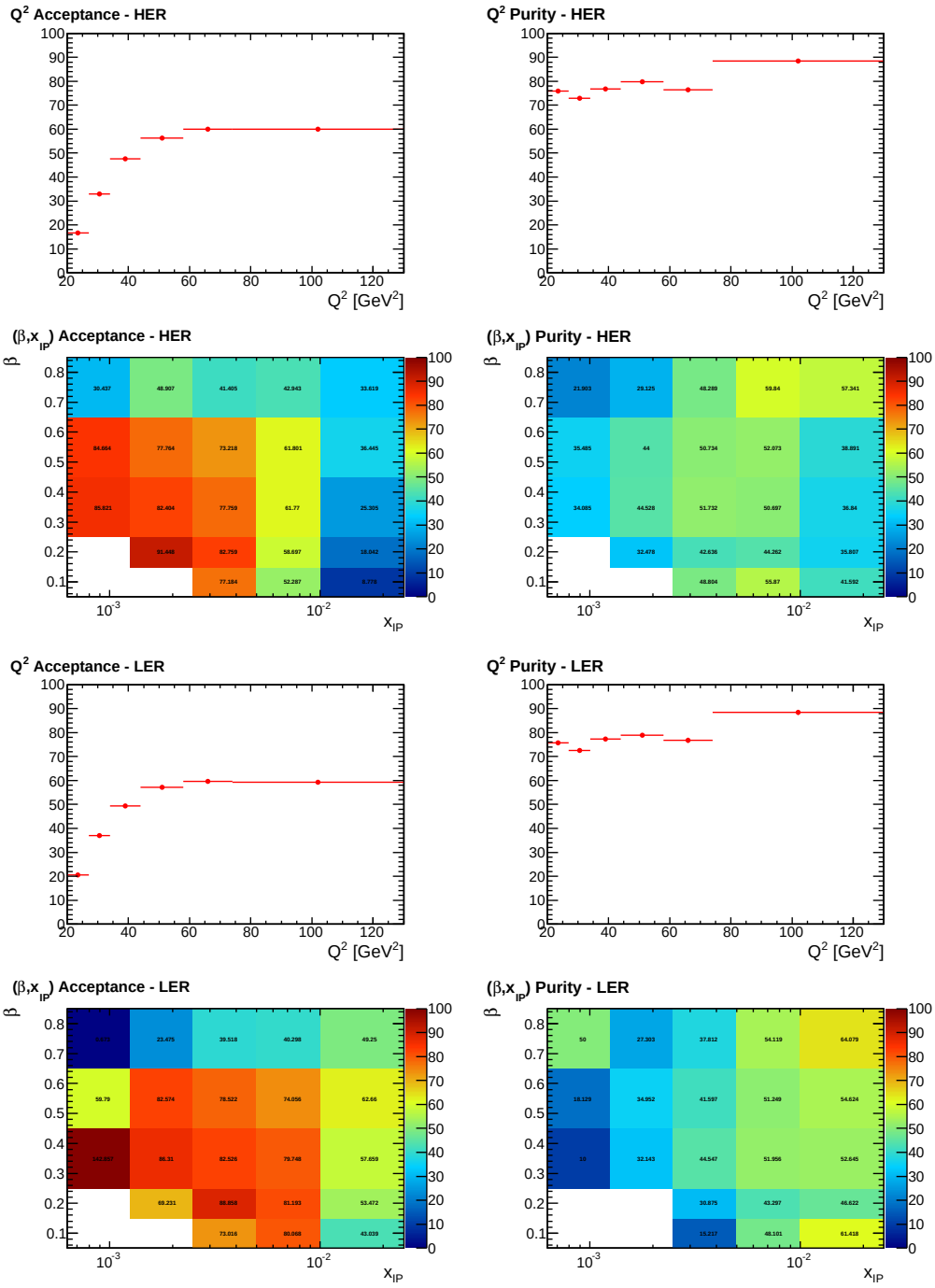

Figure 5.32: *The Q^2 and (β, $x_{I\!P}$) acceptance (left) and purity (right) for the HER (up) and LER (down) samples are shown.*

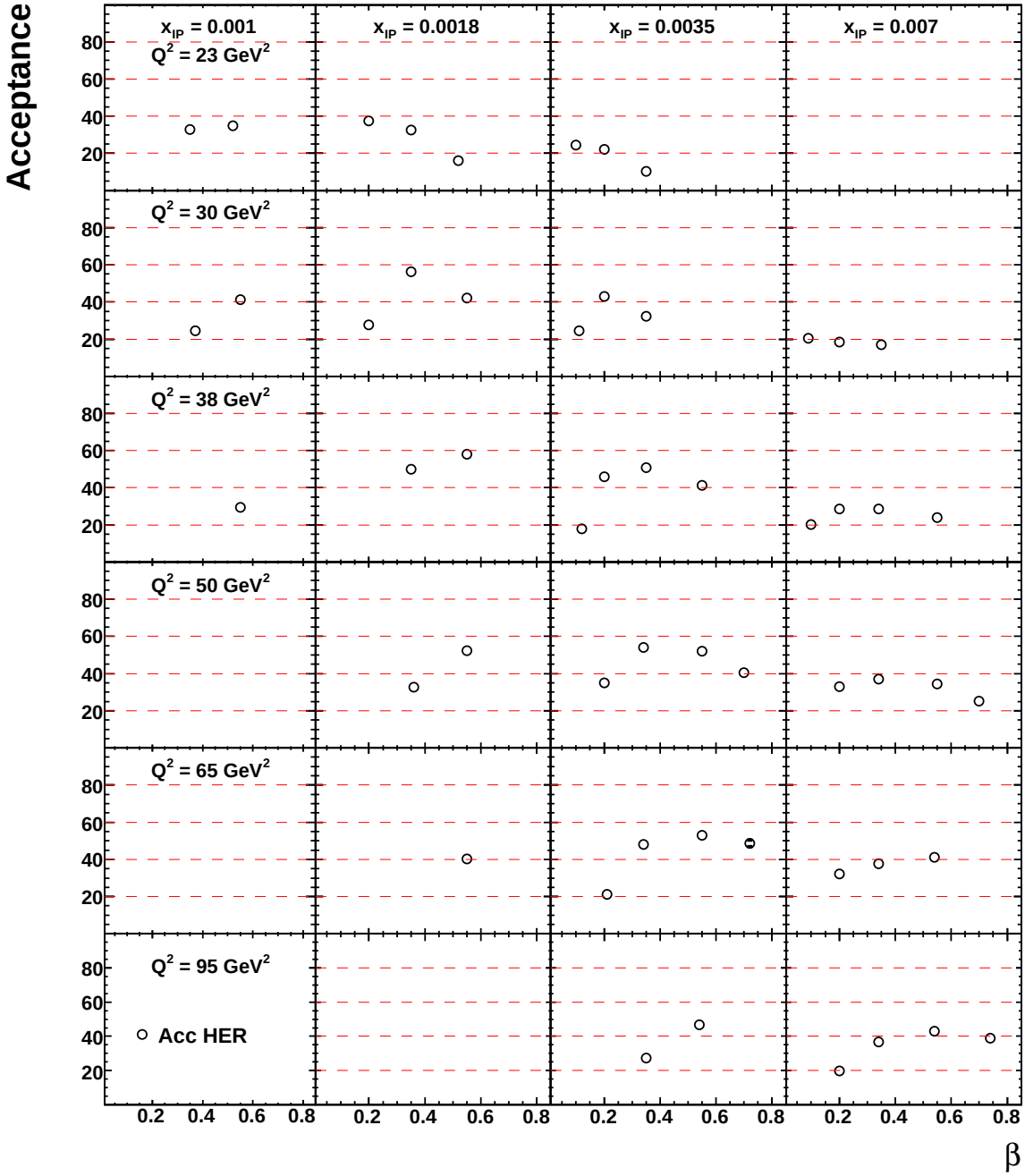

Figure 5.33: *The (β, Q^2, $x_{I\!P}$) acceptance of the HER sample is shown in bins of Q^2 and $x_{I\!P}$ as a function of β.*

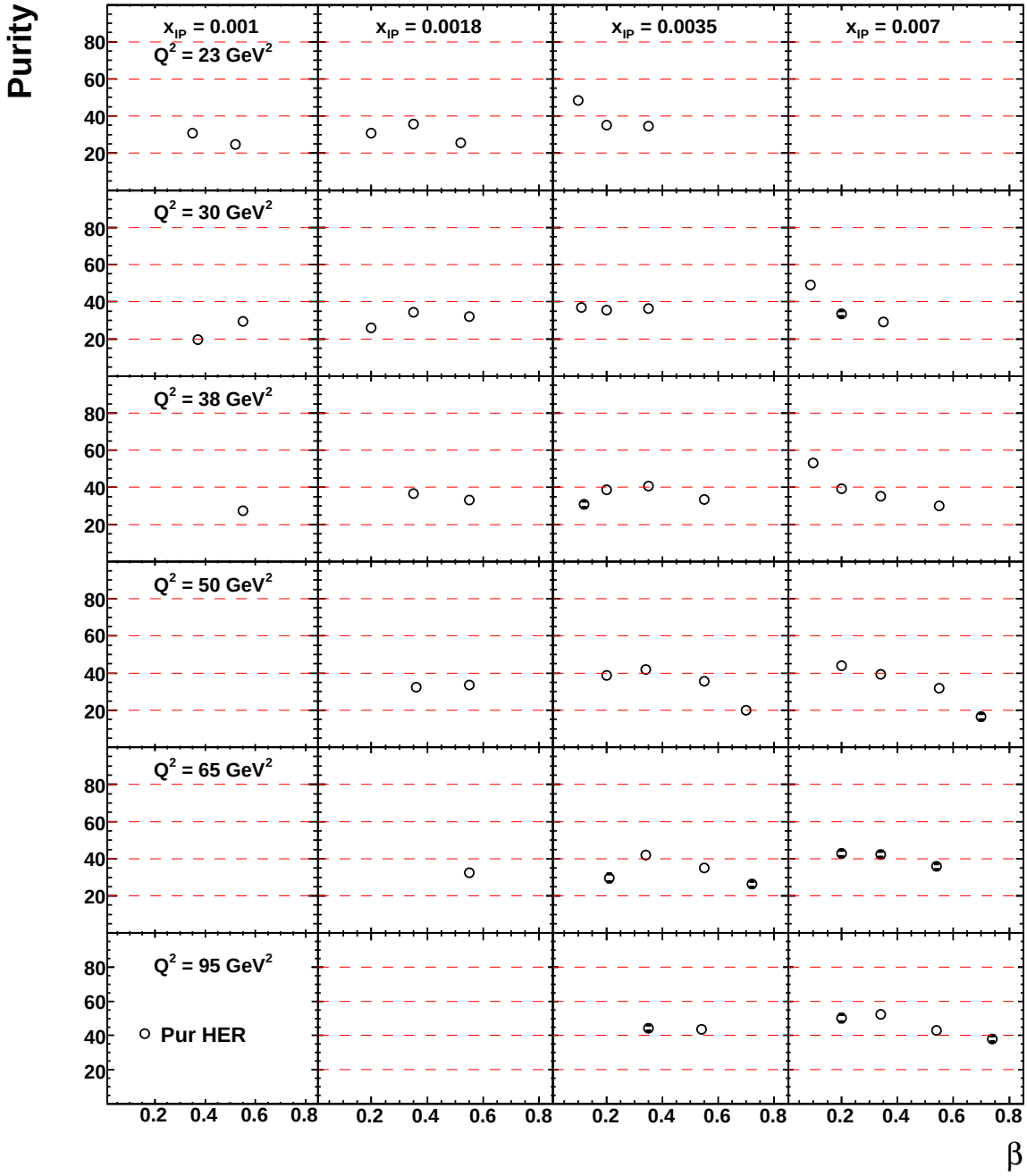

Figure 5.34: *The (β, Q^2, $x_{I\!P}$) purity of the HER sample is shown in bins of Q^2 and $x_{I\!P}$ as a function of β.*

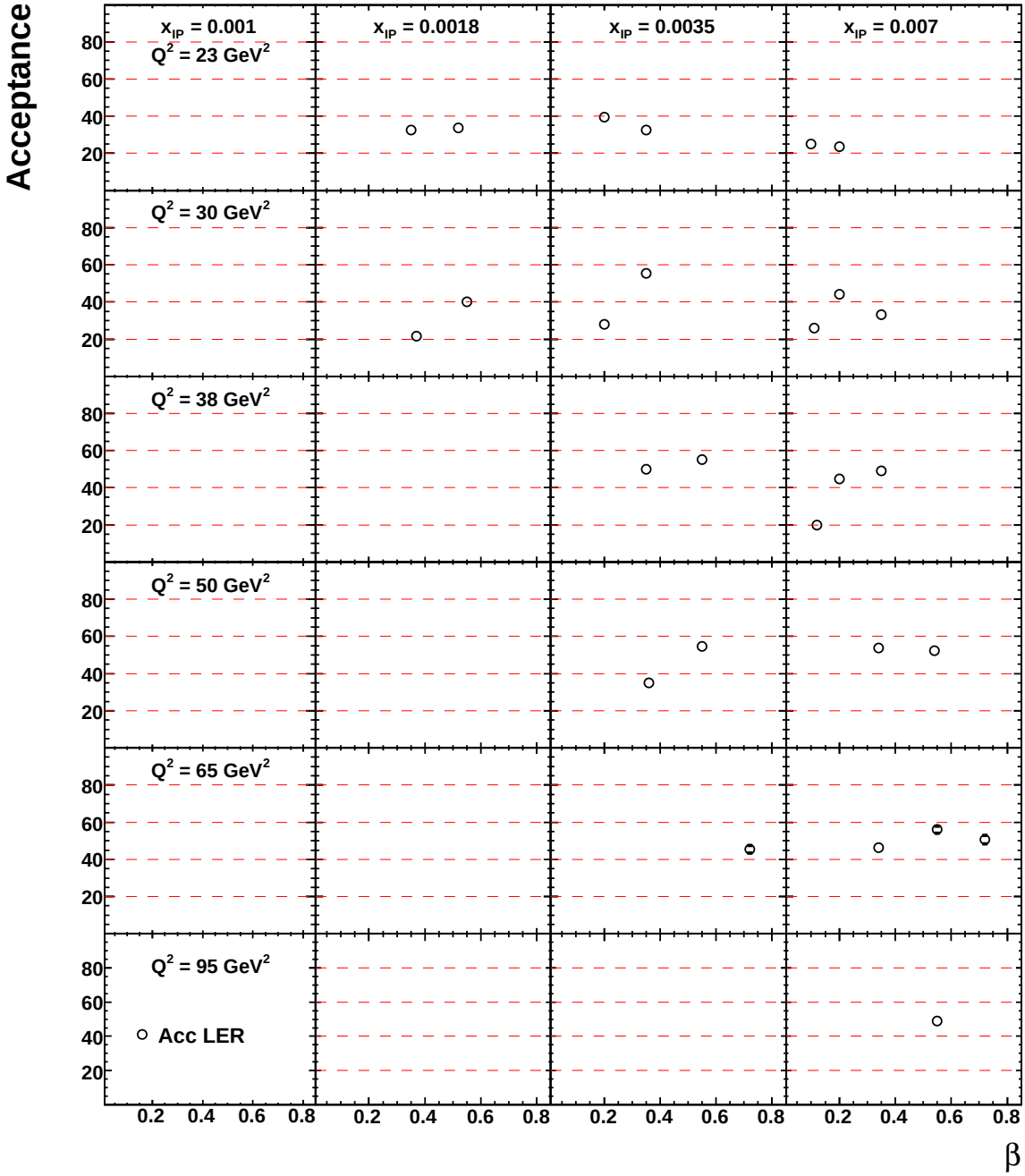

Figure 5.35: *The (β, Q^2, $x_{I\!P}$) acceptance of the LER sample is shown in bins of Q^2 and $x_{I\!P}$ as a function of β.*

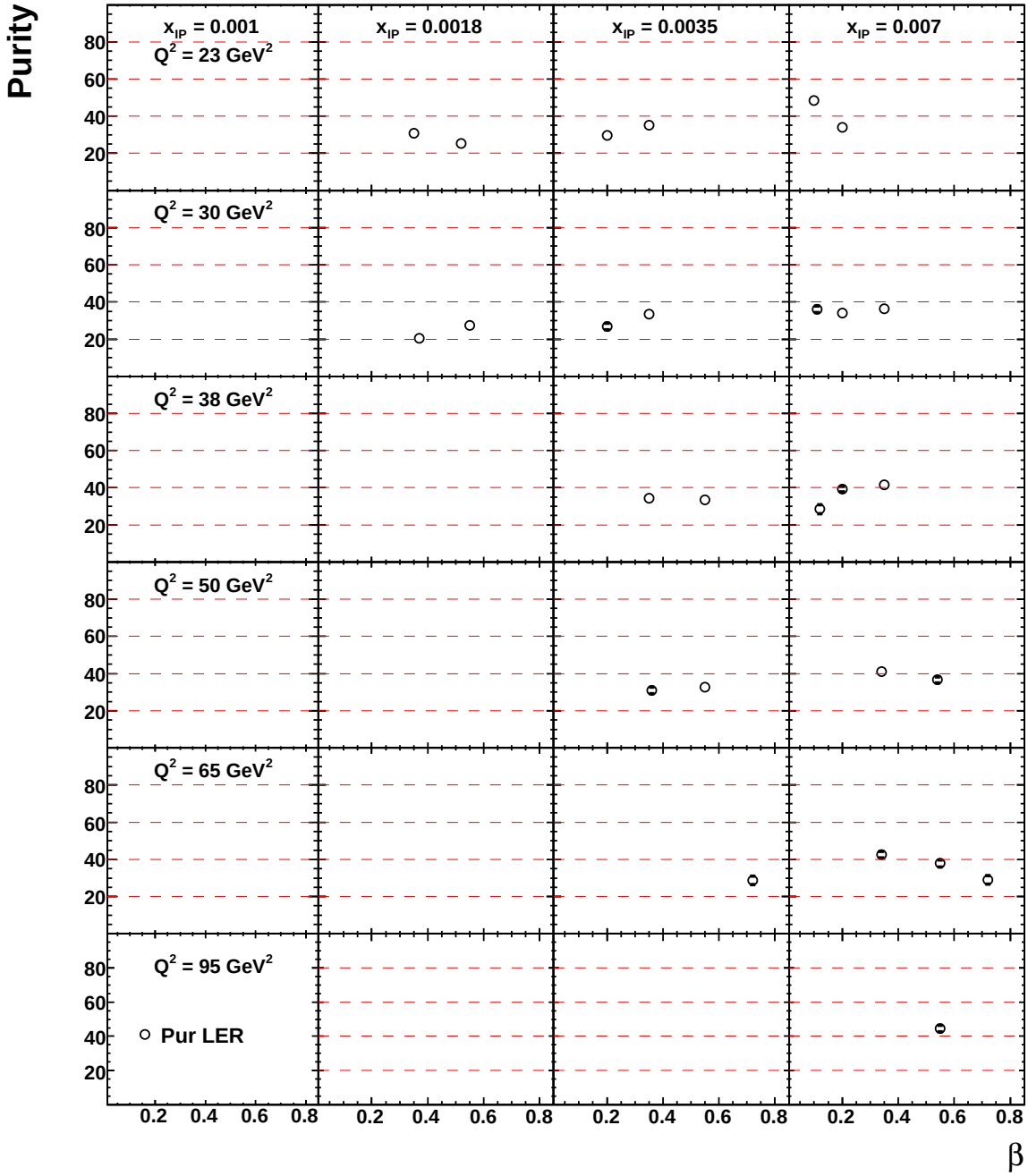

Figure 5.36: *The (β, Q^2, $x_{I\!P}$) purity of the LER sample is shown in bins of Q^2 and $x_{I\!P}$ as a function of β.*

5.6.2 Cross Section and Uncertainties

5.6.2.1 Cross Section Extraction

The diffractive reduced cross section in a given (β, Q^2, $x_{I\!P}$) bin was extracted from the ratio of data and MC cross sections, multiplied by the theoretical diffractive reduced cross section used in the SATRAP MC generator:

$$\sigma_r^{D(3)}(\beta, Q^2, x_{I\!P}) = \frac{\sigma_{data}}{\sigma_{MC}} \tilde{\sigma}_r^{D(3)}(\beta, Q^2, x_{I\!P}) \ . \tag{5.31}$$

For each bin, the data (MC) cross section was calculated as the sum (sum of weights) of all the reconstructed events in that bin divided by the integrated luminosity of the sample:

$$\frac{\sigma_{data}}{\sigma_{MC}} = \frac{N_{data}/\mathcal{L}_{data}}{N_{MC,rec}/\mathcal{L}_{MC}} \ . \tag{5.32}$$

The MC diffractive reduced cross section $\tilde{\sigma}_r^{D(3)}(\beta, Q^2, x_{I\!P})$ was calculated at the Born level, with the SATRAP MC predictions at the (β, Q^2, $x_{I\!P}$) bin value. The generator values were multiplied by the weighting factors defined in Sect. 5.4.4 (see Eqs. (5.22-(5.26)) calculated at the (β, Q^2, $x_{I\!P}$) point at which the cross section is extracted.

5.6.2.2 Statistical Uncertainties

The statistical uncertainty of the cross section depends on the number of events in data, N_{data}, and the weighted number of the event in the MC, $N_{MC,rec}$. Since most of the bins have a large number of events (> 50), the Gaussian approximation could be used to calculate the statistical errors for data and MC.
The statistical uncertainty for data, ΔN_{data}, is given by:

$$\Delta N_{data} = \sqrt{N_{data}} \ . \tag{5.33}$$

Since $N_{MC,rec}$ was calculated as the sum of all the weights of the events in the bin:

$$N_{MC,rec} = \sum_{ev} w_{MC,ev} \ , \tag{5.34}$$

the statistical uncertainty for the MC, ΔN_{MC}, was obtained as:

$$\Delta N_{MC} = \sqrt{\sum_{ev} (w_{MC,ev})^2} \ . \tag{5.35}$$

From the above formulas, $\Delta\sigma_{data} = \Delta N_{data}/\mathcal{L}_{data}$ and $\Delta\sigma_{MC} = \Delta N_{MC}/\mathcal{L}_{MC}$, and the statistical uncertainty on the cross section, $\Delta\sigma$, can be calculated as:

$$\Delta\sigma = \sqrt{\frac{1}{(\sigma_{MC})^2}(\Delta\sigma_{data})^2 + \frac{(\sigma_{data})^2}{(\sigma_{MC})^4}(\Delta\sigma_{MC})^2} \ . \tag{5.36}$$

Due to the high statistics of the MC samples used for the cross section extraction (see Sect. 5.2), the contribution of the term related to $\Delta\sigma_{MC}$ is negligible.

5.6.2.3 Systematic Uncertainties

The systematic uncertainties give information on the stability of the result and on the bias potentially introduced by the measurement procedure. Many aspects of the event reconstruction related to the detector resolution, such as the energy scale and the detector alignment, cannot be known with infinite precision. Moreover, a bad description of the data distributions by the MC simulation could wrongly reproduce the event migration across the kinematic region and bias the cross section extraction. These effects are taken into account by varying some critical parameters in the analysis and studying the impact of these changes on the measured cross section.

The systematic checks carried out are described below:

Electromagnetic energy scale (see Fig. 5.37)

The energy of the scattered electron in the MC was multiplied and divided by:

$$factor = max(1.01, 1.02 - (E'_e - 5)/10 \times 0.01) \ ,$$

which varies from 2% at $E'_e = 5$ GeV to 1% for $E_e > 15$ GeV. This systematic check mostly influenced the reconstruction of the DIS kinematic variables and the M_X reconstruction. The resulting variation of the cross section is $< 5\%$ for most of the points.

Hadronic energy scale (see Fig. 5.38)

The energy of the hadronic system in the MC was varied by $\pm 2\%$. This systematic check acted mostly on the η_{MAX} reconstruction and partially on the M_X and $E - p_z$ reconstruction.

The resulting effect on the cross section is always below 5%.

Electron position (see Figs. 5.39 and 5.40)

To check the detector alignment, the x_e and y_e positions of the scattered electron were varied by ± 2 mm, separately, in the MC. This variation directly reflected on the θ_e reconstruction and therefore on the DIS kinematic variables.

The average effect on the cross section is $\sim 2\%$ for both variations.

MC reweighting (see Fig. 5.41)

The MC reweighting functions applied on the generated variables (see Sect. 5.4.4) were varied. The power of the $f(W_{gen})$ factor was varied by ± 0.1, while the power of the $f(\beta_{gen})$ factor was varied by ± 0.05.

The average effect on the cross section is $\sim 2\%$ for both variations.

Threshold on the number of non-vertex tracks with DCA > 10 cm variation (see Fig. 5.44)
The cut for the non-vertex track requirement (see Sect. 5.5.2) was varied by ± 2 both in data and MC.
The average effect on the cross section is always below 5%.

M_X **reconstruction method variation** (see Fig. 5.44)
Since the M_X variable was reconstructed through the electron information (see Sect. 5.3.6) in the nominal case, as a cross check the measurement was also performed with M_X reconstructed from the hadronic final state information.

Only bins with systematic uncertainty $< 15\%$ were considered in the cross section extraction.

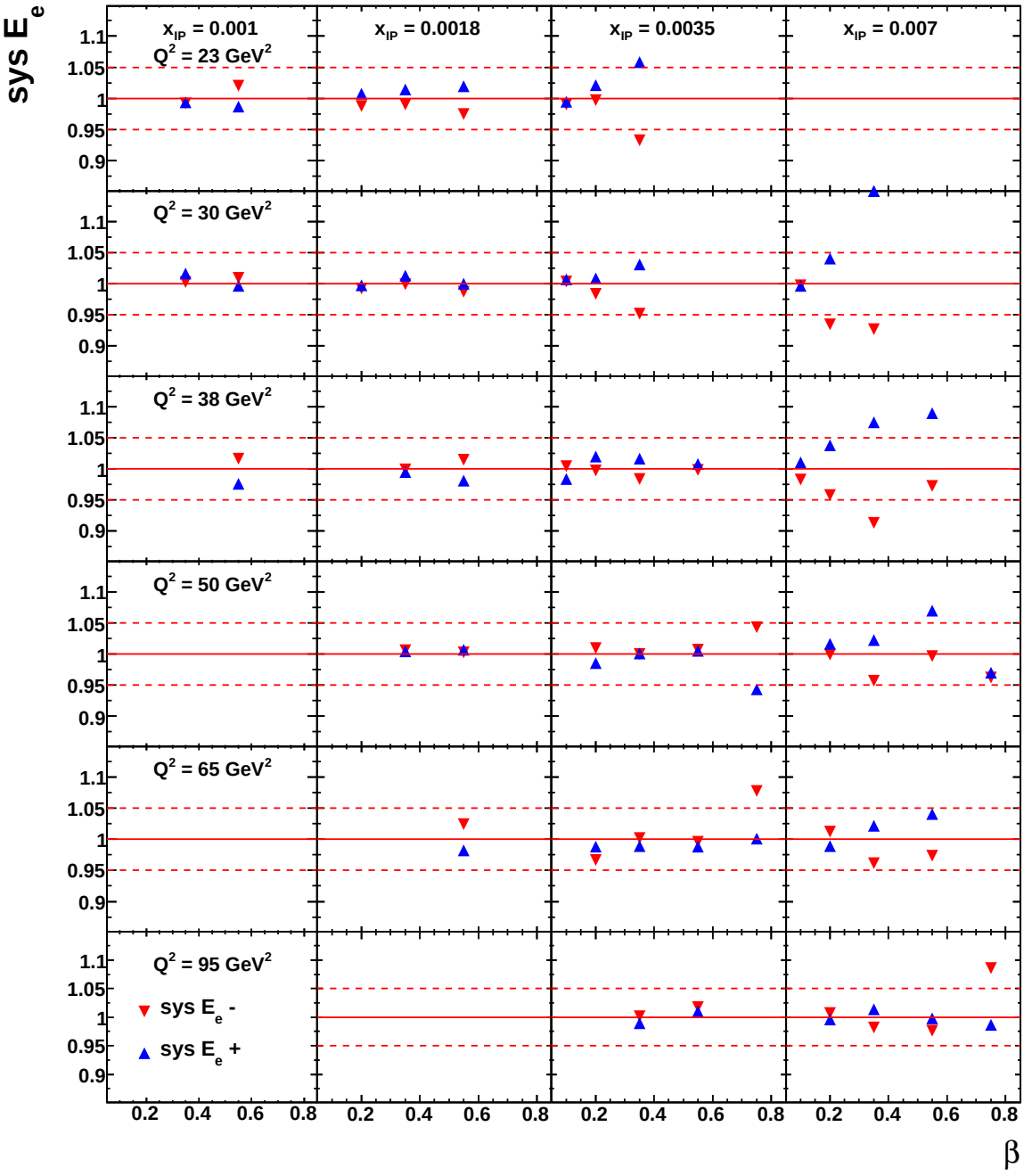

Figure 5.37: *The relative systematic uncertainty on the HER cross section introduced by the electromagnetic energy scale variation in bins of Q^2 and $x_{I\!P}$ as a function of β. Blue upward triagles are the result of the positive variation, red downward triangles of the negative variation.*

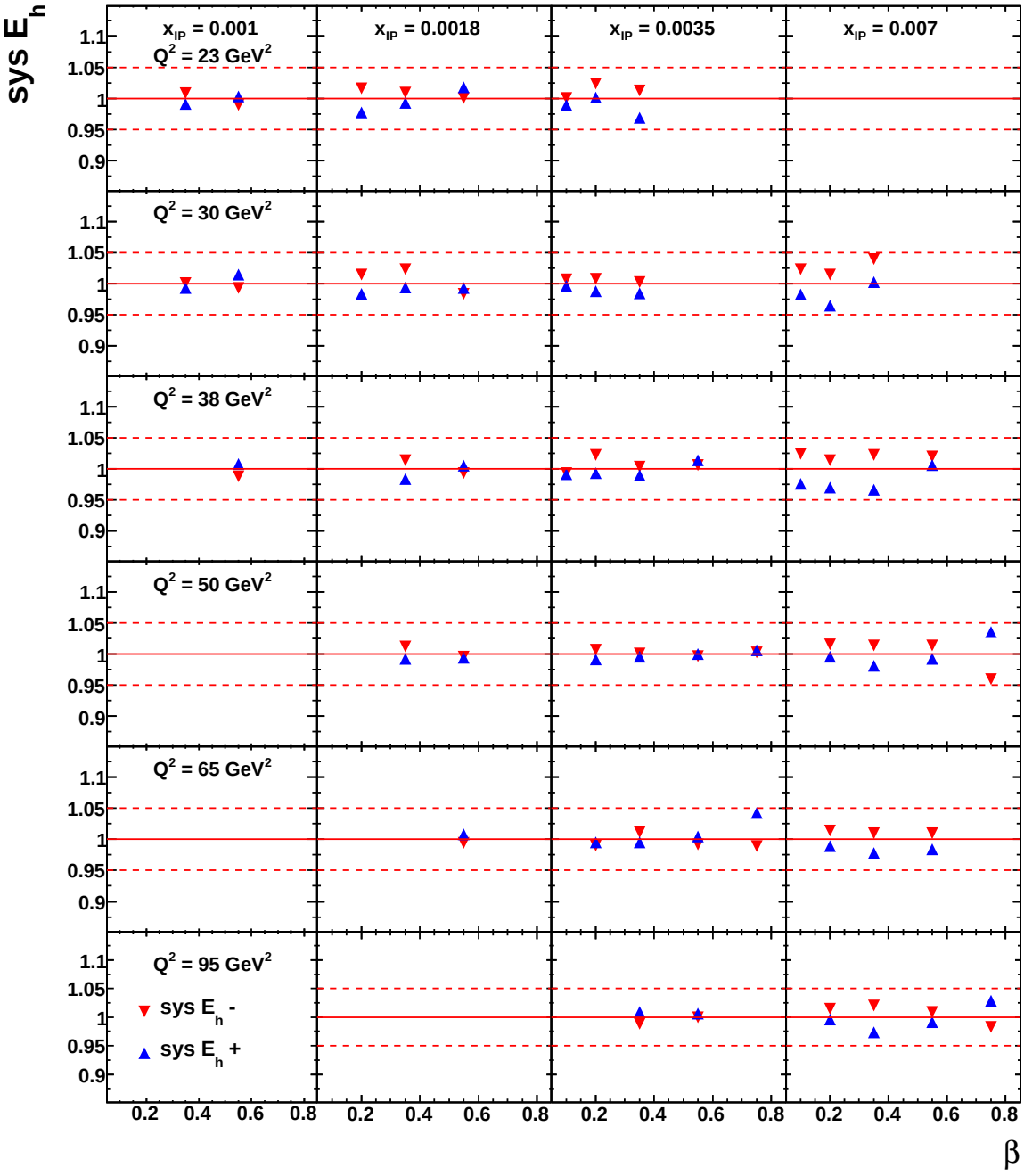

Figure 5.38: *The relative systematic uncertainty on the HER cross section introduced by the hadronic energy scale variation in bins of Q^2 and $x_{I\!P}$ as a function of β. Blue upward triagles are the result of the positive variation, red downward triangles of the negative variation.*

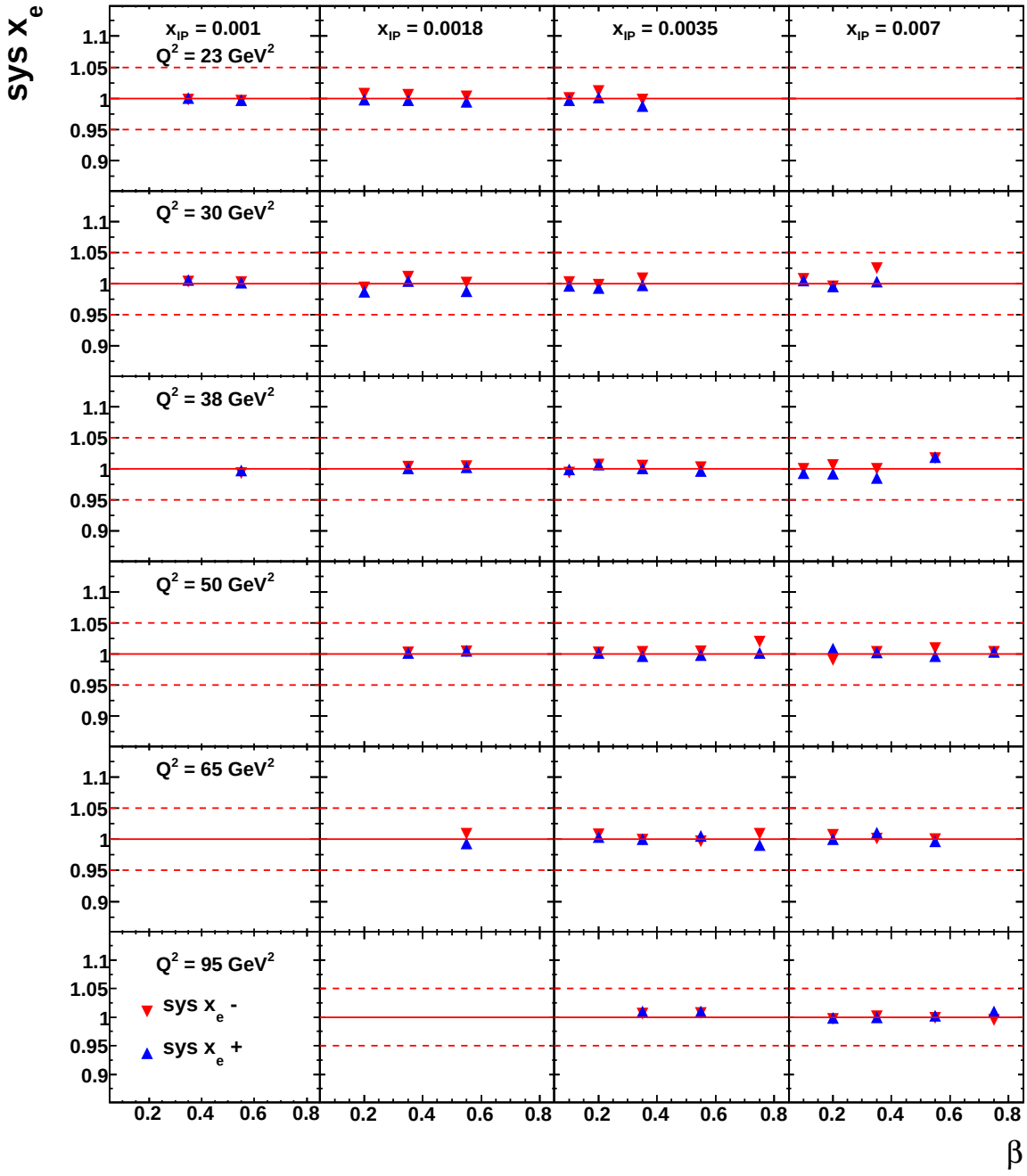

Figure 5.39: *The relative systematic uncertainty on the HER cross section introduced by the x_e scattered electron position variation in bins of Q^2 and $x_{I\!P}$ as a function of β. Blue upward triagles are the result of the positive variation, red downward triangles of the negative variation.*

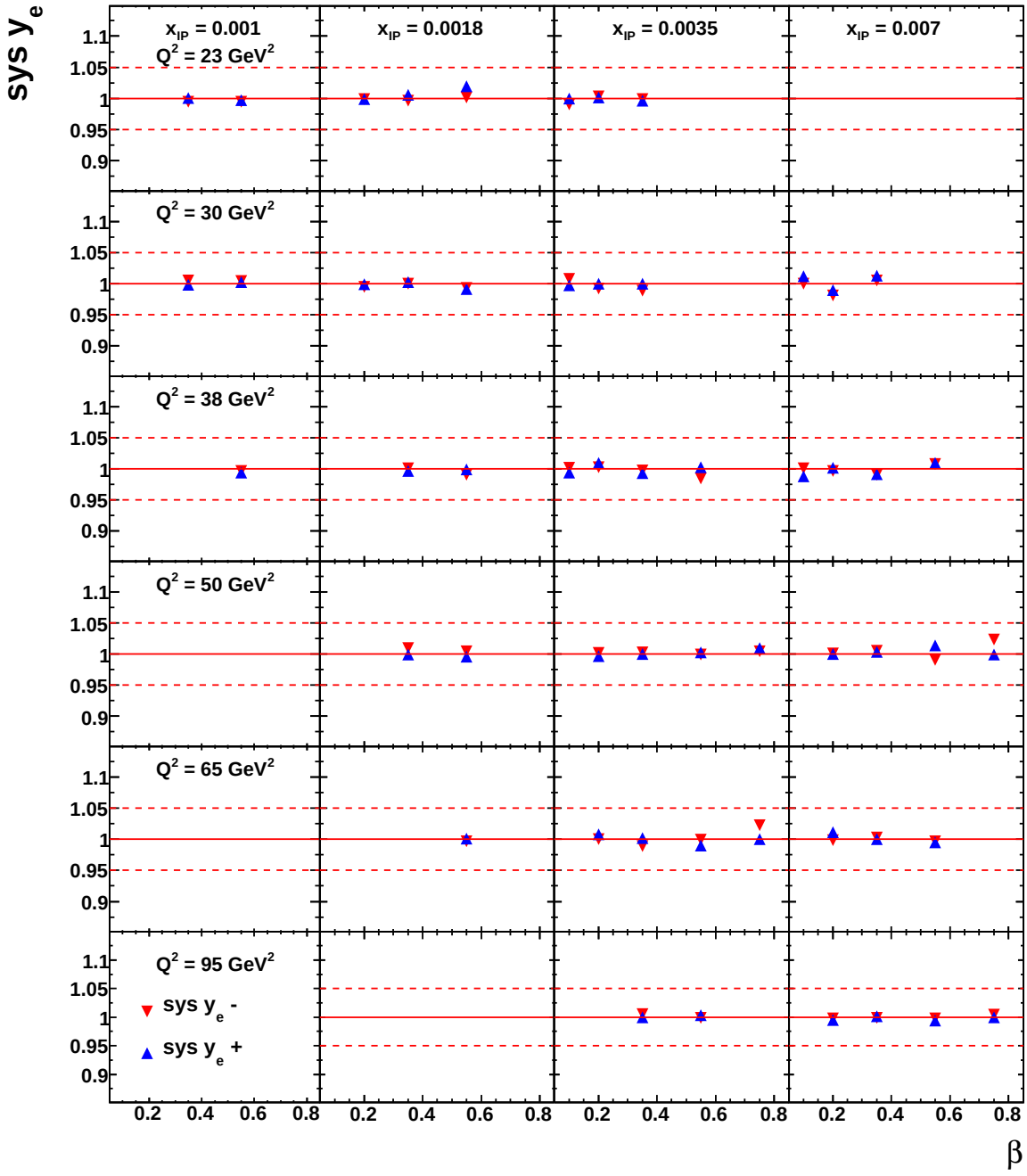

Figure 5.40: *The relative systematic uncertainty on the HER cross section introduced by the y_e scattered electron position variation in bins of Q^2 and $x_{I\!P}$ as a function of β. Blue upward triagles are the result of the positive variation, red downward triangles of the negative variation.*

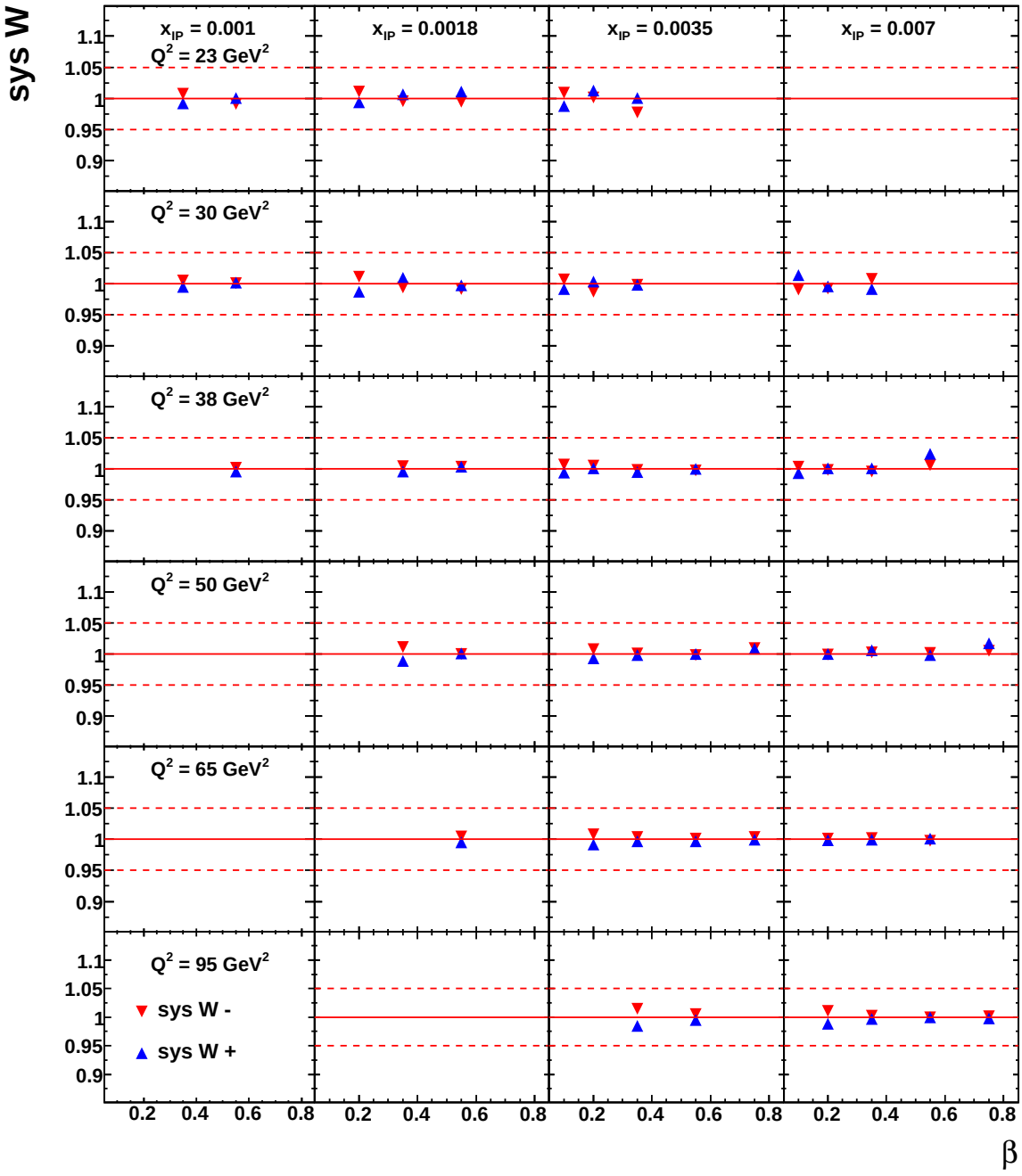

Figure 5.41: *The relative systematic uncertainty on the HER cross section introduced by the W reweighting variation in bins of Q^2 and $x_{I\!P}$ as a function of β. Blue upward triagles are the result of the positive variation, red downward triangles of the negative variation.*

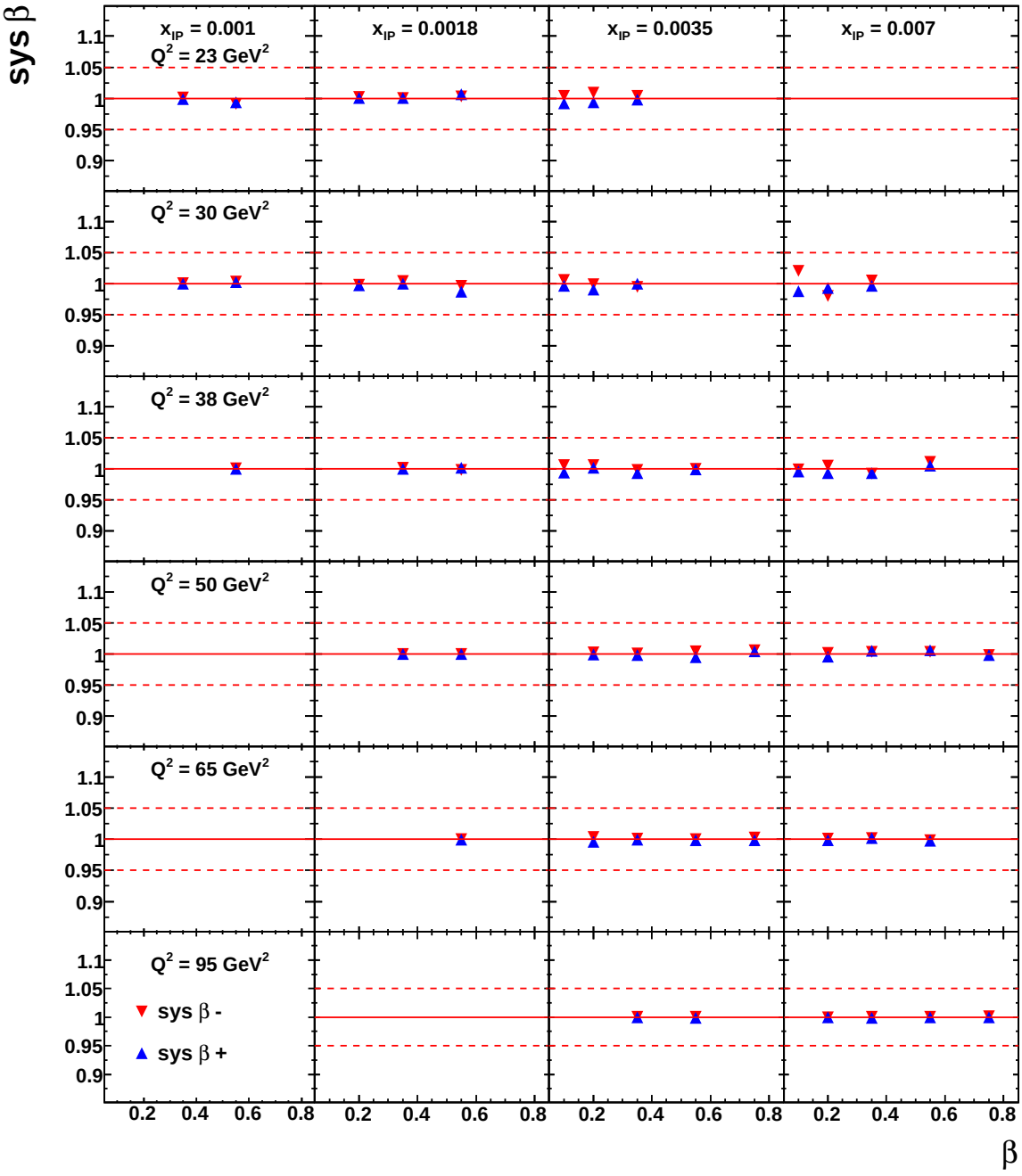

Figure 5.42: *The relative systematic uncertainty on the HER cross section introduced by the β reweighting variation in bins of Q^2 and $x_{I\!P}$ as a function of β. Blue upward triagles are the result of the positive variation, red downward triangles of the negative variation.*

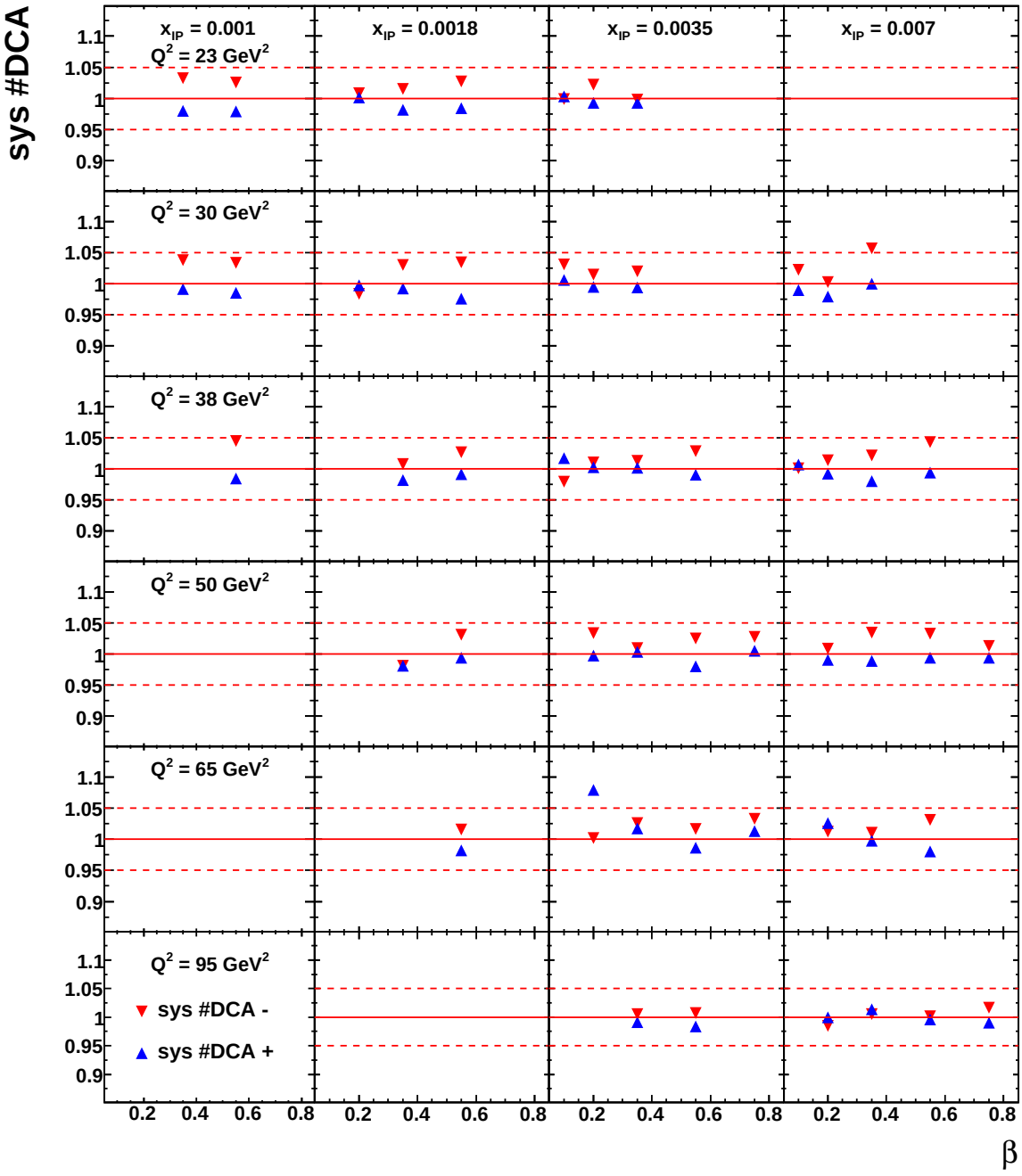

Figure 5.43: *The relative systematic uncertainty on the HER cross section introduced by the threshold on non-vertex tracks variation in bins of Q^2 and $x_{I\!P}$ as a function of β. Blue upward triagles are the result of the positive variation, red downward triangles of the negative variation.*

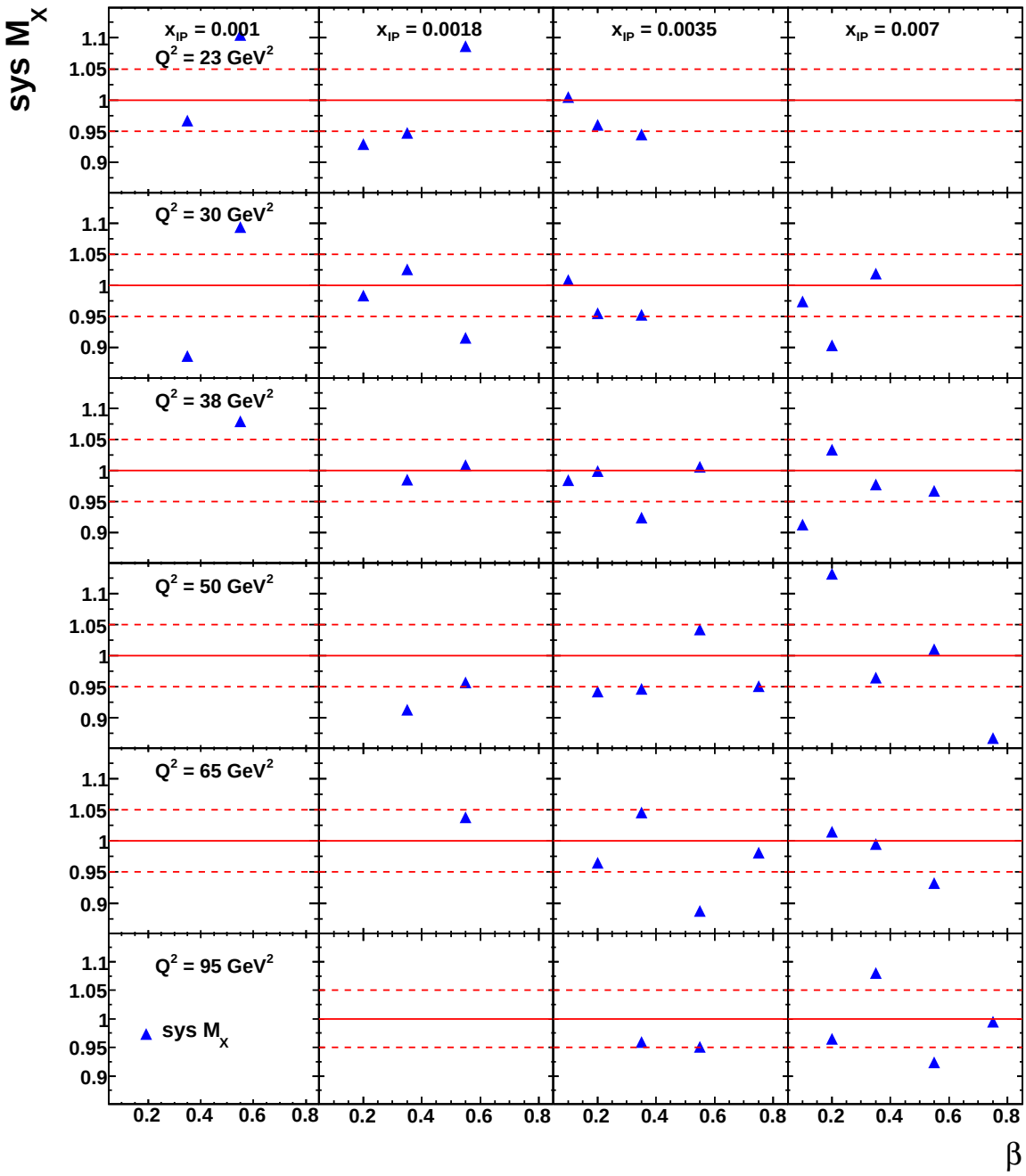

Figure 5.44: *The relative systematic uncertainty on the HER cross section introduced by the M_X reconstruction method variation in bins of Q^2 and $x_{I\!P}$ as a function of β.*

5.6.3 Diffractive DIS Cross Section Measurement

The inclusive diffractive DIS reduced cross section was extracted both for the HER and LER samples at centre-of-mass energies $\sqrt{s} = 318$ GeV and $\sqrt{s} = 225$ GeV, respectively. Results are presented in Fig. 5.45 at fixed Q^2 and $x_{I\!P}$, as a function of β. The 3-dimensional diffractive reduced cross section is given by (Eq. (1.39)):

$$\sigma_r^{D(3)}(\beta, Q^2, x_{I\!P}) = F_2^{D(3)}(\beta, Q^2, x_{I\!P}) - \frac{y^2}{Y_+} F_L^{D(3)}(\beta, Q^2, x_{I\!P}) \ ,$$

where $Y_+ = (1 + (1 - y)^2)$. Therefore, the F_L^D contribution becomes relevant only in the region $y > 0.5$. From the relations $Q^2 = sxy$ and $x = \beta \mathrm{x}_{I\!P}$, for a single data set (i.e. at constant s) at fixed Q^2 and $x_{I\!P}$, high y values are reached at low β points. Moreover, for each measured bin, at fixed (β, Q^2, $x_{I\!P}$), due to the different centre-of-mass energies between the HER and LER samples, $y_{LER} = 2y_{HER}$ (this directly follows from $E_{p,HER} = 2E_{p,LER}$).

As discussed in Sect. 5.4.6.2, due to the different double dissociative contribution, the LER results were normalised to the HER points in a region where the F_L^D contribution is negligible, namely for $y_{LER} < 0.5$. The LER sample was normalised to the HER data using the factor 1.084 ± 0.029.

To correct the measured cross sections for the contribution of the proton dissociative events the measurements were normalised to the region where the proton remains intact by using the information from the combined Proton Spectrometer results extracted in the extended t-range ($|t| < 1$ GeV^2), presented in Sect. 4.3.5. The difference in normalisation between the combined and the HER samples was estimated with a global fit to the data for $Q^2 > 8$ GeV^2 and $y < 0.5$. The contribution of proton dissociation backgound in the present data was found to be 0.59 ± 0.01. This correction factor was applied both to the HER and LER cross sections, once the LER results were normalised to the HER ones.

In Fig. 5.45 the HER and LER cross sections are shown as a function of β, at fixed values of Q^2 and $x_{I\!P}$. The error bars include the contribution of the statistical and systematic uncertainties, added in quadrature. For the present measurement 54 and 27 data points were extracted for the HER and LER samples, respectively, in the kinematic range $20 < Q^2 < 130$ GeV^2, $0.05 < \beta < 0.85$ and $0.00063 < x_{I\!P} < 0.01$. The y value of the measured points varies between 0.1 and 0.82, and extends the kinematic coverage towards high values with respect to previous ZEUS diffractive measurements [50–53], where the cross section was extracted for $y \lesssim 0.55$. As already mentioned, small values of β correspond to high-y values, where a decrease of the reduced cross section is expected due to the F_L^D constribution. However, once properly normalised, the HER and LER results are in good agreement also in the high-y region, suggesting that the present samples are only marginally sensitive to F_L^D, as discussed in Sect. 5.6.3.1.

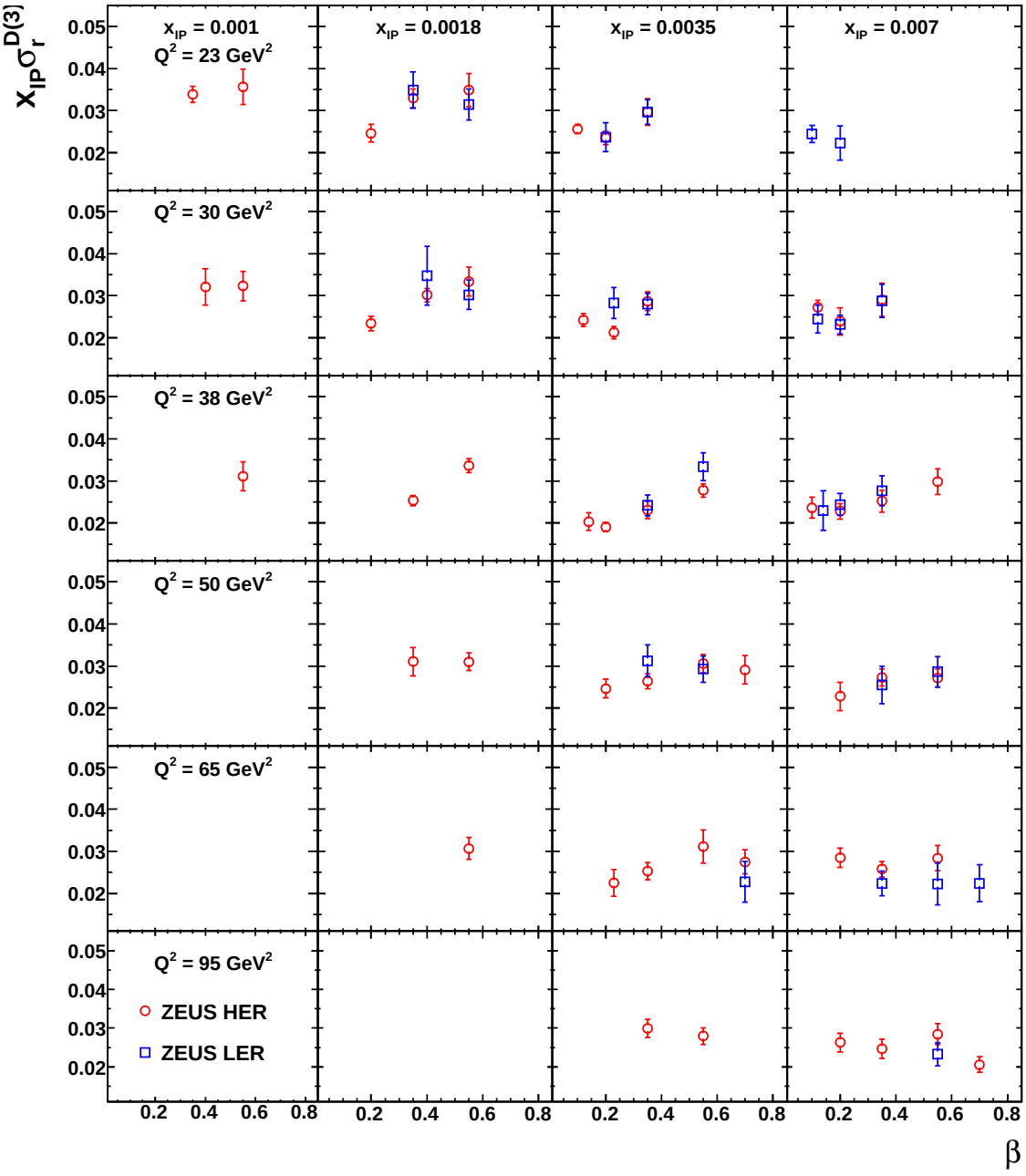

Figure 5.45: *The HER (red circles) and LER (blue squares) cross sections in bins of Q^2 and $x_{I\!P}$ as a function of β. The error bars include the contribution of the statistical and systematic uncertainties, added in quadrature.*

5.6.3.1 Comparison with Previous Measurements

In Fig. 5.46 results from the last published ZEUS measurement based on the M_X method [53] (see Sect. 3.3) are shown superimposed to the HER and LER cross sections. To fit with the binning scheme of the present analysis, the M_X data were interpolated in Q^2 and $x_{I\!P}$ according to the BEWK parametrisation [53]. The M_X data were multiplied by the factor 0.75 to subtract the proton dissociation background. This factor is the result of the scaling of the M_X data to the ZEUS LPS measurement (see Sect. 4.3.1), quoted as 0.83 ± 0.04 [51], times the renormalisation to the combined Proton Spectrometer results in the extended t-range (see Sect. 4.3.5), found to be 0.90 ± 0.02 from a fit to the data. From the figure it is visible that the present analysis is optimised for the high-y region. In the low-β/high-y region the statistics of the M_X measurement becomes poor and in the lowest β bins only results from the present HER and LER data sets are available. On the other hand all the M_X values are accessible with the M_X method (see Sect. 3.3), including $M_X < 4$ GeV, rejected for the present measurement, which from Eq. (1.35) corresponds to the high-β region. In the overlap region, corresponding to medium-β/medium-y values, good agreement between the two analyses is observed. The present data thus enlarge significantly the kinematic coverage of previous ZEUS measurements.

In Fig. 5.47 the HER and LER cross sections are presented in the same binning as that of the last ZEUS LRG published results from 2000 data [51]. Results are shown as a function of $x_{I\!P}$ for fixed Q^2 and β values. None of the points were corrected for the proton-dissociation backgound for the present plot. Good agreement in shape is observed in most of the phase space, with some exception in the high-$x_{I\!P}$ region. The difference in normalisation is a consequence of the different geometric coverage of the ZEUS detector in the 2000 and 2006/07 data taking period (in the latter the Forward Plug Calorimeter was dismantled, see Sect. 2.2.8). This reflects in a larger amount of double dissociative events in the present analysis, resulting in a $16 \pm 1\%$ difference in normalisation between the LRG 2000 and the 2006/07 HER data sets.

5.6.3.2 Comparison with Predictions

Figures 5.48 and 5.49 show the comparison between the present results and the prediction from the ZEUS DPDF SJ [59] and H1 Fit B [48] parametrisations, respectively. The normalisation factors are taken from [59], and further multiplied by 0.90 (see Sect. 5.6.3.1) to compare the predictions to the present data. The contribution of F_L^D becomes visible in the high-y region, where the value of the HER and LER reduced cross sections deviate from the pure F_2^D contribution. Due to the very small effect of F_L^D and the limited statistical precision of the present measurement it is difficult to observe a deviation of the data from the F_2^D predictions.

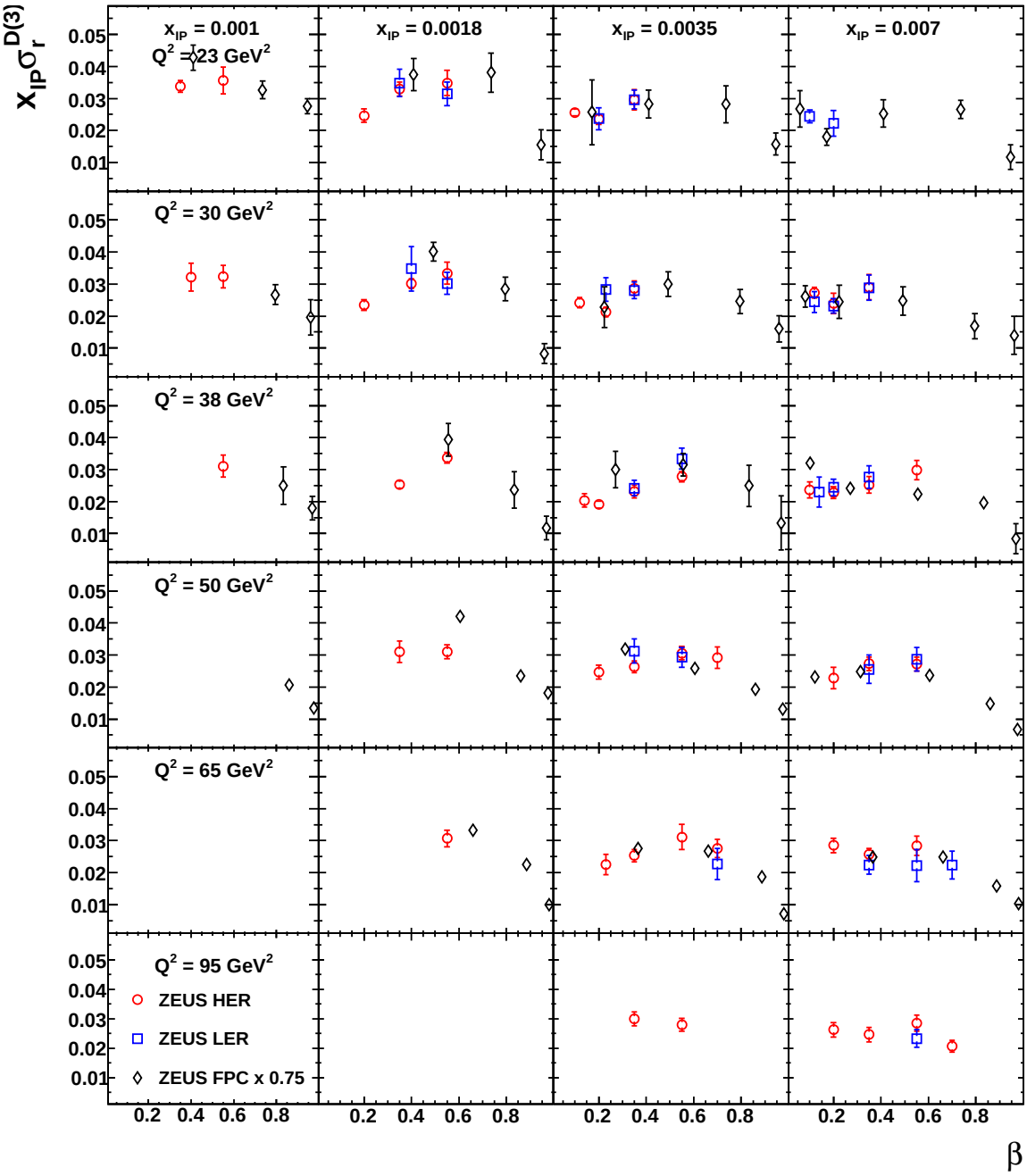

Figure 5.46: *The HER (red dots) and LER (blue squares) cross sections compared to ZEUS M_X measurements from 2000 data [53] (black diamonds), in bins of Q^2 and $x_{I\!P}$ as a function of β. The error bars include the contribution of the statistical and systematic uncertainties, added in quadrature.*

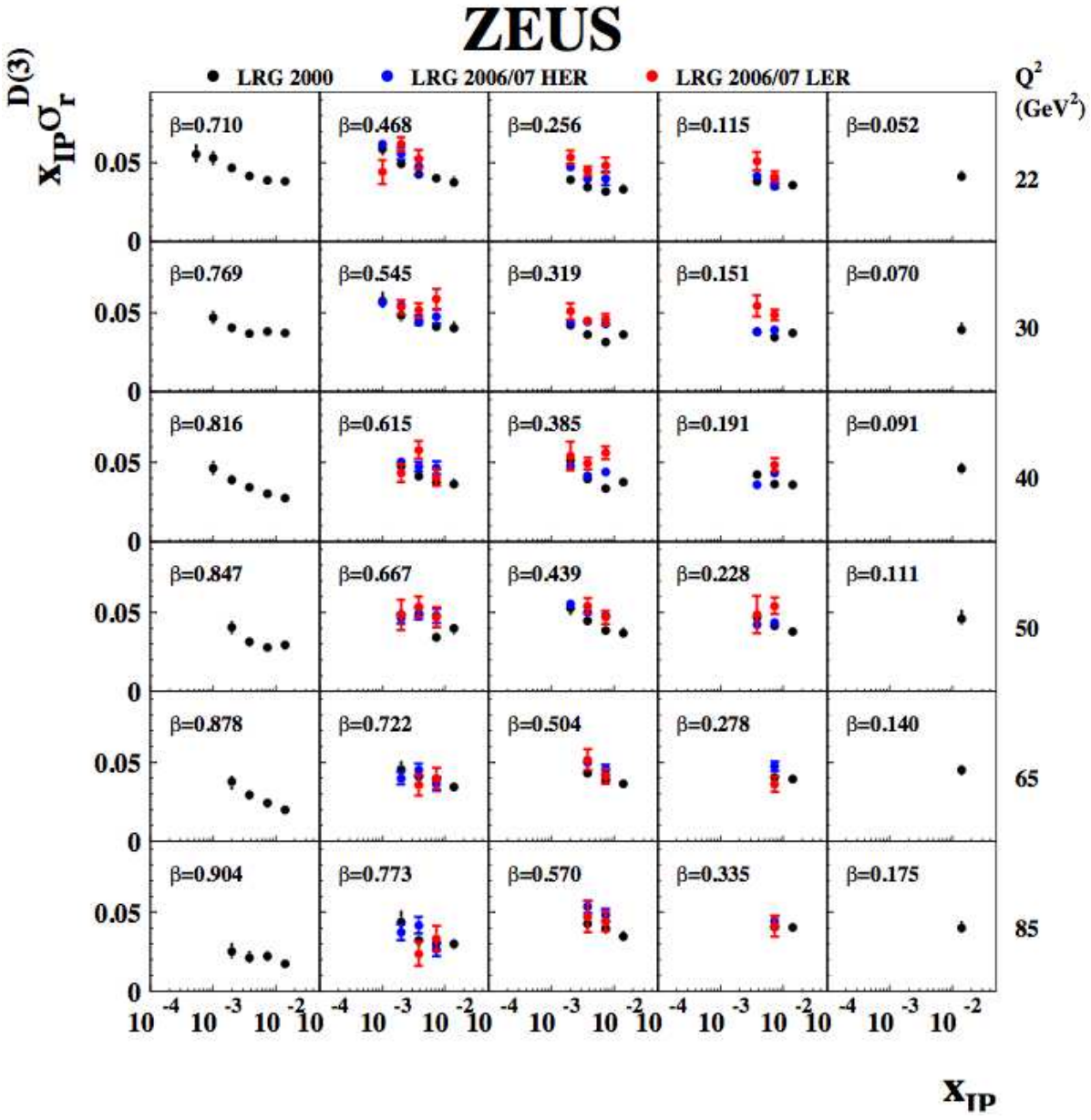

Figure 5.47: *The HER (blue points) and LER (red points) cross sections compared to ZEUS LRG measurements from 2000 data [51] in the same bins of the published analysis, at fixed Q^2 and β as a function of $x_{I\!P}$. The error bars include the contribution of the statistical and systematic uncertainties, added in quadrature.*

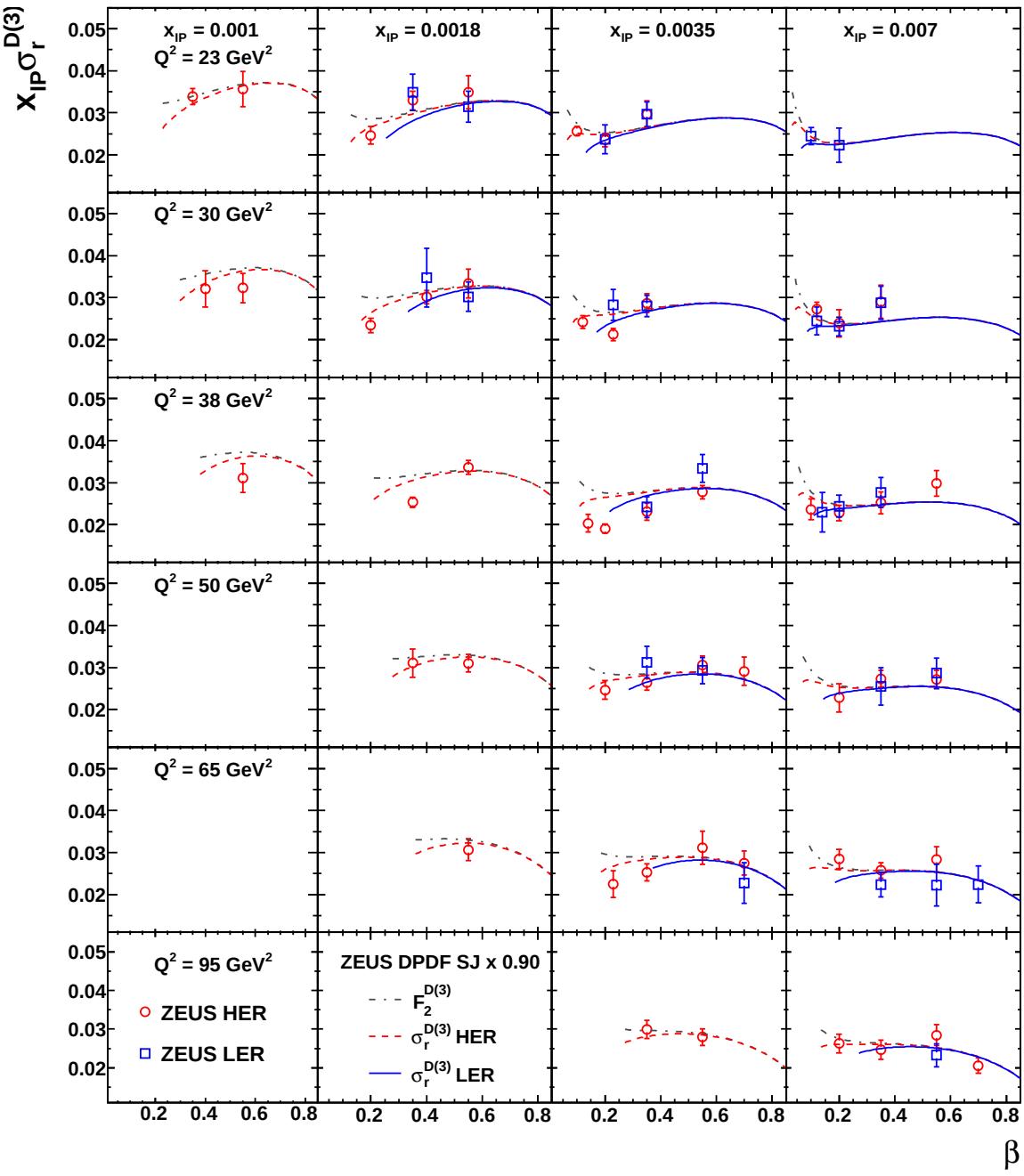

Figure 5.48: *The HER (red dots) and LER (blue squares) cross sections in bins of Q^2 and $x_{I\!P}$ as a function of βcompared to ZEUS DPDF SJ predictions [59]. Grey dotted-dashed lines represent F_2^D, red dashed lines $\sigma_{r,HER}^{D(3)}$ and blue lines $\sigma_{r,LER}^{D(3)}$. The error bars include the contribution of the statistical and systematic uncertainties, added in quadrature.*

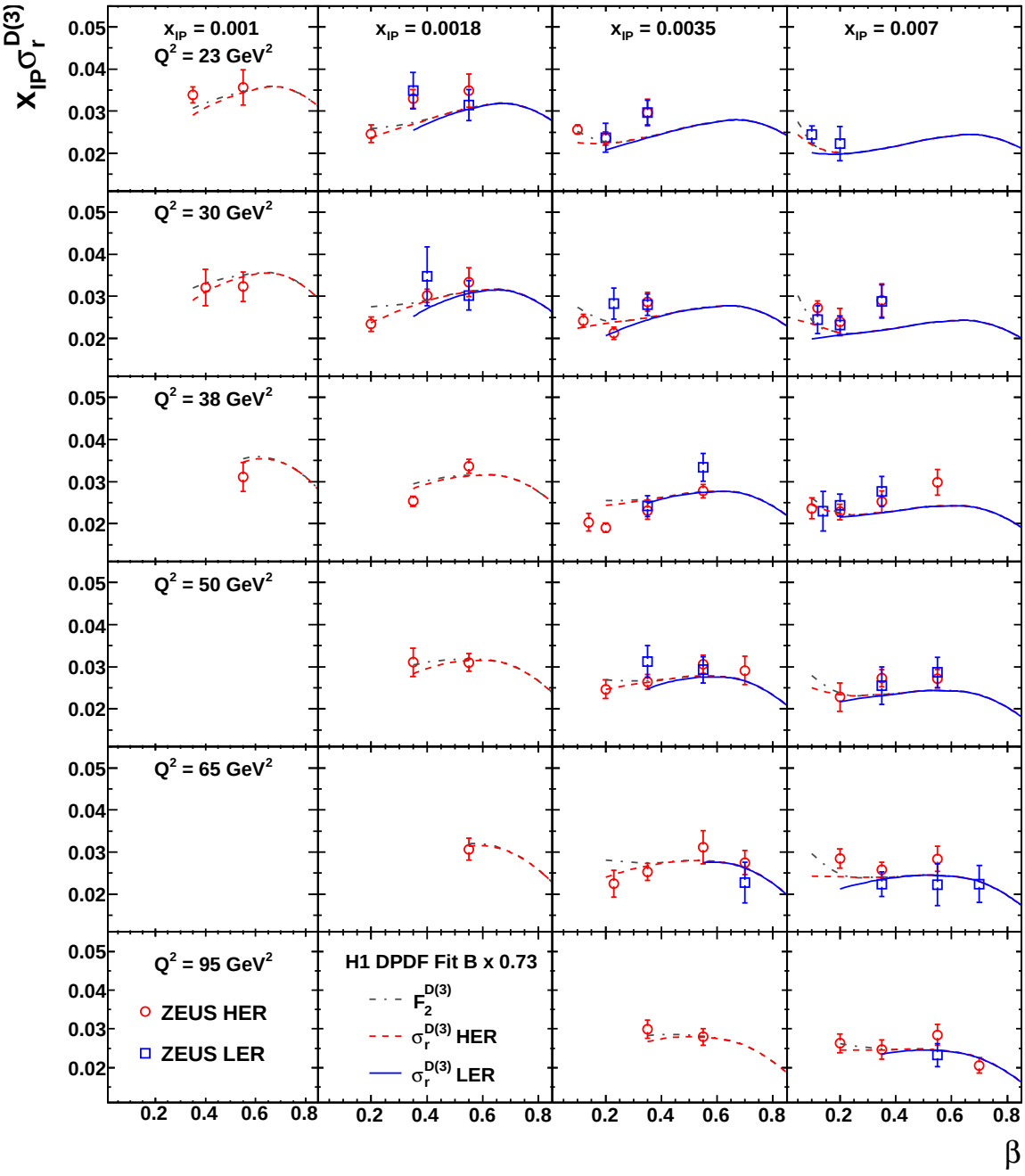

Figure 5.49: *The HER (red dots) and LER (blue squares) cross sections in bins of Q^2 and $x_{I\!P}$ as a function of βcompared to H1 Fit B predictions [48]. Grey dotted-dashed lines represent F_2^D, red dashed lines $\sigma_{r,HER}^{D(3)}$ and blue lines $\sigma_{r,LER}^{D(3)}$. The error bars include the contribution of the statistical and systematic uncertainties, added in quadrature.*

Chapter 6

Summary

The main focus of my work has been the analysis of diffractive deep-inelastic scattering events, $ep \to eXp$, collected with the ZEUS experiment at the HERA ep collider. I have also contributed extensively to the calibration of the electromagnetic calorimeter of the CMS experiment at CERN.

The ZEUS data analysis I carried out culminated in two main results:

1. The cross sections for inclusive diffraction measured by the H1 and ZEUS Collaborations were combined, providing a model-independent check of the data consistency and a cross calibration between the two experiments, and resulting in single data sets with improved accuracy and precision with respect to the original measurements. Two sets of combined results are available:

   (a) The cross sections from the proton-spectrometer data, both in the t range common to FPS and LPS [1] ($0.09 < |t| < 0.55$ GeV^2) and in the extended t-range $|t| < 1$ GeV^2. The combined result extends the kinematic coverage with respect to the original H1 and ZEUS measurements; the resulting cross sections cover the region $2.5 \leq Q^2 \leq 200$ GeV^2, $0.0018 \leq \beta \leq 0.816$ and $0.0003 \leq x_{I\!P} \leq 0.09$. Thanks to the cross calibration between the two experiments, the combined measurement exhibits an average improvement in accuracy and precision of about 20% with respect to the original H1 data, statistically more powerful. The combined results in the extended t-range fix the absolute normalisation of the inclusive diffractive ep reduced cross section. The combined measurement in the common t-range is about to be published in Physics Letters B.

   (b) The cross sections with the large rapidity gap signature. The kinematic range in this case is $2.5 \leq Q^2 \leq 1600$ GeV^2, $0.0017 \leq \beta \leq 0.8$ and $0.0003 \leq x_{I\!P} \leq 0.03$, for $M_X > 4$ GeV. The combined measurement is driven by the ZEUS results, statistically

more powerful, and shows an average 17% improvement in accuracy and precision with respect to the input ZEUS data.

2. The inclusive diffractive reduced cross section $\sigma_r^{D(3)}$ was measured with data collected by the ZEUS experiment in the years 2006/07, at two different centre-of-mass energies, 318 and 225 GeV. The diffractive data were selected with the large rapidity gap method, and cover the kinematic region $20 < Q^2 < 130$ GeV^2, $0.05 < \beta < 0.85$ and $0.00063 < x_{I\!P} < 0.01$. The y value of the measured points varies between 0.1 and 0.82, and extends the kinematic coverage towards high-y values with respect to previous H1 and ZEUS diffractive measurements, where the cross section was extracted for $y \lesssim 0.55$.

Appendix A

Intercalibration of the CMS Electromagnetic Calorimeter with the Azimuthal Symmetry Method

This Section describes first in-situ calibration results achieved by exploiting the azimuthal symmetry method with up to 250 nb^{-1} collected by the CMS detector at LHC at centre-of-mass energy of $\sqrt{s} = 7$ TeV, during the first months of operation in 2009/2010 [2]. The last two paragraphs are devoted to the calibration work performed in 2010 and 2011.

A.1 The CMS Electromagnetic Calorimeter

The electromagnetic calorimeter (ECAL) of the Compact Muon Solenoid (CMS) experiment consists of a barrel section (EB) and two endcaps (EE). The EB contains 61 200 lead tungstate crystals arranged in 170 $\eta-$rings of 360 $PbWO_4$ crystals each (one crystal covers 1 degree in ϕ). It is subdivided into 36 supermodules, each containing 1 700 crystals, and provides coverage in pseudorapidity up to $|\eta| < 1.5$. The two ECAL Endcap subsystems consist of four half-disks named Dees, each containing 3 662 crystals. The EE provides a coverage of $1.5 < |\eta| < 3.0$. The scintillation light is detected by avalanche photodiodes (APDs) in the EB and vacuum phototriodes (VPTs) in the EE. An extended description of the CMS ECAL is provided in [122]. The general performance and commissioning of the ECAL with the first 7 TeV data are described in [123]. A detailed description of the CMS experiment can be found in [124].

The ECAL energy resolution has been measured in test beams to be [124]:

$$\frac{\sigma(\text{E})}{\text{E}} = \frac{2.8\%}{\sqrt{\text{E(GeV)}}} \oplus \frac{12\%}{\text{E(GeV)}} \oplus 0.3\%\,, \tag{A.1}$$

where the three contributions correspond to the stochastic, noise, and constant terms, respectively. This result was obtained in the absence of magnetic field, with almost no inert material in front of the calorimeter and with the beam aligned on the centre of the crystals.

The high resolution of the ECAL is particularly important for a discovery of the Higgs boson in the decay channel $H \to \gamma\gamma$.

A.2 The CMS ECAL Calibration Strategy

The signals from the ECAL channels are first shaped and then amplified with multiple gains before subsequent digitization by a multiple channel ADC. Signals are digitized by the ADC every 25 ns and in standard operation the signal from an event is read out as a series of 10 samples. The amplitude of the signal is reconstructed to form uncalibrated *RecHits* using a linear combination of these samples: $A = \sum_i w_i \cdot S_i$, where S_i is the sample value in ADC counts and w_i is a weight. Calibrated RecHits are obtained from the uncalibrated RecHits by applying the energy scale, which is the ADC to GeV conversion factor, and the inter-calibration constant of the corresponding channel.

The ECAL was pre-calibrated before installation with laboratory measurements of the crystal light yield and the photo-detector gain (all EB and EE channels), with test beam electrons (9 EB supermodules and about 500 EE crystals) and with cosmic ray muons (all EB channels). After installation in the LHC, circulating beams were stopped in collimators 150 m away from CMS in September 2008 and November 2009. The resulting *beam dump* events have been used to improve the pre-calibration precision in the EE and most recently in the EB, providing an independent inter-calibration precision of 1.6% across the full pseudorapidity range covered by the barrel. The final calibration is made *in-situ* at the LHC using collision data.

The estimated particle energy, obtained from the ECAL, can be expressed as:

$$E = F \cdot \sum_{cluster\ crystals} G(GeV/ADC) \cdot c_i \cdot A_i \tag{A.2}$$

where the sum is over the crystals in a *cluster*[1]. The quantities A_i are the reconstructed amplitudes in ADC counts (the uncalibrated RecHit), c_i are the inter-calibration constants while G is the ECAL energy scale. The factor F is defined as an additional energy correction which depends on the type of particle, its energy and pseudorapidity and in particular takes into account shower leakage and bremsstrahlung losses for electrons [125].

[1] An electromagnetic shower involves more than one channel: typically more than 90% of the energy of a 35 GeV electron or photon is contained in a 5×5 matrix of crystals. Thus, hits need to be clustered in order to associate the energy deposits to the particles impinging on the calorimeter. Profiting from the test beam experience, two specific algorithm have been developed, one for EB and one for EE. The algorithms are optimized for the different geometries of EB and EE and take into account the spread of energy in the ϕ direction due to the propagation of electrons and photons through the material in front of the calorimeter in the 3.8 T magnetic field, which produces bremsstrahlung photons and photon conversions, respectively.

For the in-situ calibration, the following strategies have been implemented:

- ϕ-symmetry, which provides a fast inter-calibration exploiting invariance around the beam axis of energy flow in minimum bias events [126]. This method inter-calibrated crystals at the same pseudorapidity, so that other methods are needed to inter-calibrate regions at different pseudorapidity.
- π^0 and η calibration, which uses the photon pairs from $\pi^0(\eta) \to \gamma\gamma$ candidates [127]. At the startup, this method was also used to investigate the ECAL energy scale.

A.3 Calibration with the ϕ-Symmetry Method

A.3.1 The Method

The ϕ-symmetry method is based on the expectation that for a large sample of minimum-bias events the total deposited transverse energy (E_T) should be the same for all crystals in a ring at fixed pseudorapidity. Inter-calibration in ϕ is performed by comparing the total transverse energy (ΣE_T) deposited in one crystal with the mean of the total ΣE_T collected by crystals at the same absolute value of η. Therefore, for each ring in ϕ, the average of the 360 inter-calibration constants c_i is equal to unity by construction. The average calibration of each η ring then relies on the pre-calibrations. In the EB, crystals are arranged in 85 pairs of rings symmetric in pseudorapidity with 360 crystals along ϕ in each ring.

In the determination of the transverse energy sum, only deposits with energies between a lower and an upper limit were considered. The former was applied to remove the noise contribution and was derived by studying the noise spectrum in randomly triggered events. The latter was applied to avoid a possible bias from very high E_T deposits (e.g. from electrons originating from W or Z decays). The lower threshold, in the EB, had a fixed value in energy of 250 MeV, corresponding to about 6.25 σ of the energy equivalent noise. The corresponding lower E_T cut was therefore 250 MeV/cosh(η). In the EE, channels are arranged so that VPTs with lower gain are located at higher pseudorapidity. Therefore, the equivalent noise distribution varies with pseudorapidity and the lower threshold was parametrized accordingly. The upper E_T threshold was set to be 1 GeV above the lower limit in both the EB and the EE.

Because the transverse energy sum was obtained from a truncated E_T distribution, a given fractional change in the E_T sum did not correspond to the same fractional change in the value of the inter-calibration constant. Therefore, a correction to the obtained inter-calibration coefficient was applied, as described in [126].

A.3.2 ϕ-Symmetry Online Calibration Stream

The trigger of the CMS experiment is designed to accept high E_T events and reject minimum bias events. Therefore, the standard physics triggers do not provide a sufficiently high data-

taking rate to apply the azimuthal symmetry method. For this reason, a special trigger path was deployed to feed a special, small-size calibration stream. The trigger is seeded by a set of minimum bias L1 triggers. At least one energy deposit in the EB above 150 MeV or at least one energy deposit in the EE above 650 MeV are further requested. If these criteria are met, all ECAL energy deposits above these thresholds are saved to the calibration stream and all other event data are dropped.

A.3.3 Effect of Azimuthal Detector Non-Uniformity

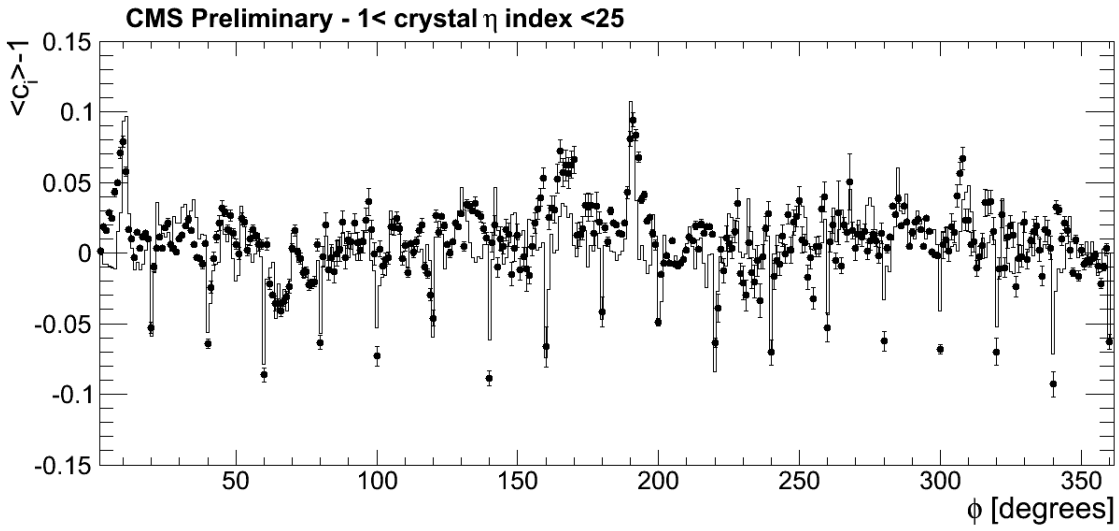

Figure A.1: *Average difference from unity of the inter-calibration constants derived with the ϕ symmetry method for data (solid circles) and simulation (histogram) in the crystal η index range [1, 25]. In the absence of the systematics effects described in the text, a flat distribution with statistical fluctuations around zero is expected.*

The ϕ-symmetry of the detector is not perfect for two reasons: the ECAL geometry itself is not uniform in azimuth and the material budget between the calorimeter and the interaction point is not perfectly homogeneous. The asymmetry in the ECAL geometry affects the method in the following way. In the EB, at the boundary between each supermodule, due to the inter-module gap and the 3^o tilt with respect to the interaction point direction, particles can hit crystals on the side face as well as the front, as explained in [126]. Therefore, such crystals receive more hits and the method assigns a lower inter-calibration constant. The inhomogeneity of the material budget, on the other hand, results in an inhomogeneous particle flux impinging on the calorimeter. ECAL areas with more material in front of them have higher inter-calibration constants in this method.

These effects were found to vary with pseudorapidity and to be forward-backward asymmetric. They were studied as follows. The average of the inter-calibration constants derived from ϕ-symmetry was calculated, as a function of ϕ, for each module of the calorimeter, separately for the forward and for the backward region. In the absence of asymmetries, a flat distribution within statistical fluctuations would be expected. Instead, as shown in Fig. A.1, several features were observed. The lower values observed at $\phi = 20^o$, 40^o, 60^o, etc. are due to the inter-module boundaries as explained above. Some of them do not fully agree with Monte Carlo. This discrepancy is probably associated with an under estimation of some of the gaps due to a geometry displacement of supermodules with respect to the ideal positions implemented in the simulation. The two peaks at 10^o and 190^o, corresponding to the horizontal plane, reflect the presence of the rails and associated sliding pads used to support the silicon tracker. Other deviations from a flat distribution can be ascribed to inhomogeneities in the silicon tracker material, and are reproduced by the simulation. A data-driven correction for the effect of inter-module gaps and silicon tracker rails was introduced.

A.3.4 Supermodule Relative Scale

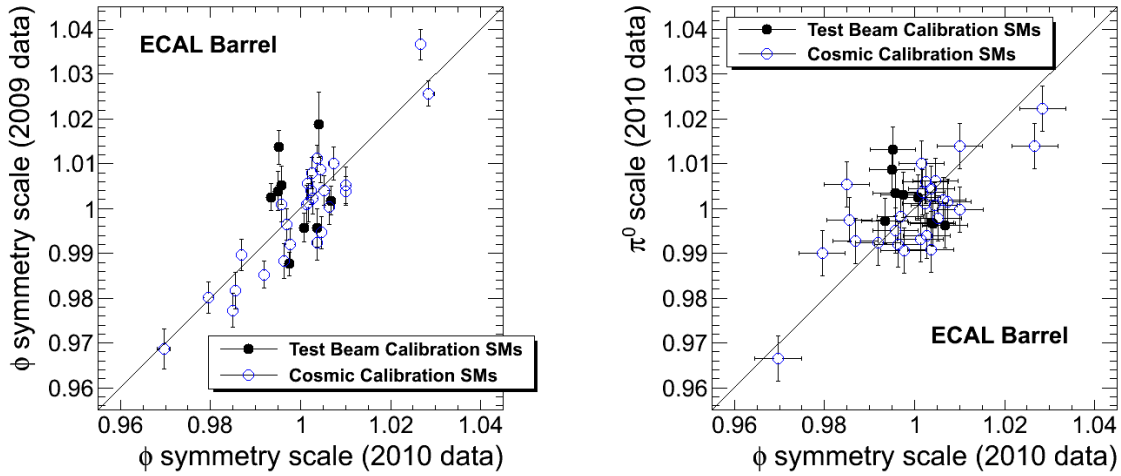

Figure A.2: *Comparison of relative supermodule scale with ϕ-symmetry method between $\sqrt{s}$ = 900 GeV (2009) and $\sqrt{s}$ = 7 TeV (2010) data. Only statistical errors are shown. The systematic uncertainty of the method was estimated to be $\pm$0.5%(left). Comparison between the supermodule scales derived with the ϕ-symmetry and π^0 method (right).*

In order to extract the relative supermodule scale in the EB the inter-calibration constants were derived from a data sample with an integrated luminosity of 8.8 nb^{-1}, corresponding to about $1.6{\cdot}10^8$ minimum bias events. For each of the 36 supermodules the distribution of the

1 700 constants was studied. The mean of the Gaussian fit to this distribution was defined as the SM scale. To estimate the systematic error, the distribution of the relative scale was derived for those supermodules which were calibrated at the test beam, with a precision several times better than expected from the method with the considered data. The width of this distribution, about 0.5%, is the convolution of the precision of the test beam inter-calibration and the ϕ-symmetry inter-calibration, and poses therefore an upper limit to the systematic error of the method. In Fig. A.2 (*left*), the comparison of the SM scale derived from 2009 data (~ 0.01 nb^{-1} at $\sqrt{s} = 900$ GeV) and 2010 data ($\sqrt{s} = 7$ TeV) is shown.

An independent set of supermodule scales was derived from a sample of π^0 decays [127]. The set of 36 constants is compared with the supermodule scales from the ϕ-symmetry method in Fig. A.2 (*right*).

A.3.5 Crystal-by-Crystal Calibration

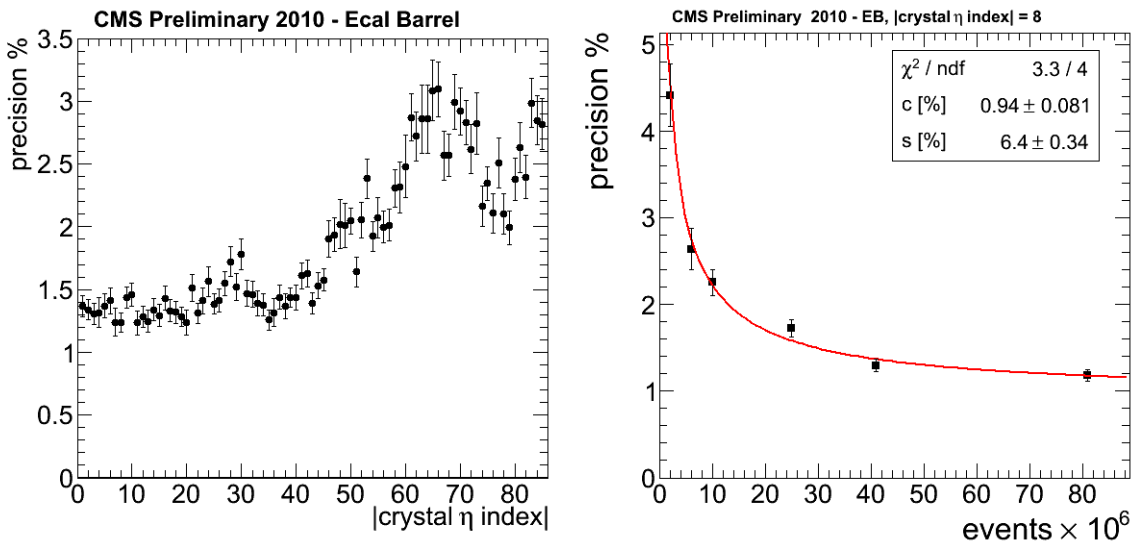

Figure A.3: *Precision of the inter-calibration constants derived with the ϕ-symmetry method as a function of ring index in EB (left). Precision as a function of the number of events for the rings at | crystal η index | = 8 (right).*

The ϕ-symmetry inter-calibration procedure was applied on the first $1.6{\cdot}10^8$ minimum-bias events collected in 2010 and inter-calibration constants c_i were derived for all crystals in the EB. To estimate the precision of the set of constants, the distribution of the c_i for each ring of constant η was studied. The width of the distribution reflects the convolution of the precision of the pre-calibration with the precision of the method. For the nine test-beam calibrated supermodules, the expected pre-calibration precision was about 0.5%, several times better

than that expected from the ϕ-symmetry method. Therefore, the width of distribution of the c_i limited to those supermodules gave an upper bound of the inter-calibration precision achieved with the ϕ-symmetry method. The width of the c_i distribution was estimated by performing a Gaussian fit and extracting the sigma. Figure A.3 (*left*) shows the estimated precision as a function of ring index as black solid circles. Figure A.3 (*right*) shows the inter-calibration precision as a function of the number of events for $\eta-$ring 8. The measured distribution is fitted with a function $\sqrt{c^2 + s^2/N}$. The fitted value of c (the constant term) suggests that the systematic limit of the method is nearly reached with 150M of events.

A.4 In-Situ Inter-Calibration from 2010 Data

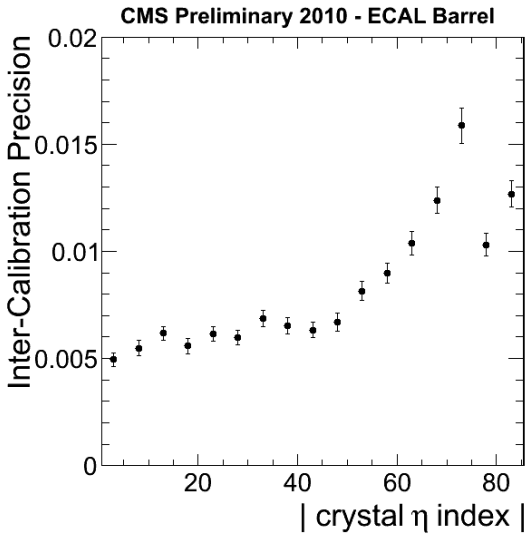

Figure A.4: *Precision of combined inter-calibration constants (beam dump, π^0 and ϕ-symmetry) as a function of crystal pseudorapidity.*

The crystal-by-crystal inter-calibration constants using the first 250 nb^{-1} collected with the CMS detector in 2010 at a centre of mass energy of 7 TeV were derived as the average of ϕ-symmetry, π^0/η and beam dump results, weighted by their error. The precision of the combined inter-calibration is shown in Fig. A.4 as a function of crystal pseudorapidity. The assumed 0.5% test beam precision is not negligible with respect to the combination precision and therefore subtracted in quadrature. For the central barrel (|crystal η index| $\leq$ 45) the combined inter-calibration precision was found to be 0.6%.

The entire statistics collected in 2010 was then used to calibrate all the crystals in EB and EE. The achieved precision at the end of 2010 was estimated to be 0.5% at $|\eta| < 1$; $\sim$ 1% at

$1 < |\eta| < 1.45$ and $\sim 2\%$ in EE by comparing results of different inter-calibration methods. The precision in EB was close to the asymptotic limit.

A.5 The ϕ-Symmetry Calibration with 2011 Data

The ϕ-symmetry method gave a valuable contribution to the calibration of the Electromagnetic Calorimeter of CMS also during the 2011 data taking period, combined with π^0 and η results. While the precision of the method is dominated by the systematic limit due to the inhomogeneity of the tracker material ($\sim 1.5\%$ in central EB, as shown in Fig. A.3 poor with respect to other methods), the statistical precision could reach few per mill level in short time ($\sim$ 1 week). Moreover, the ϕ symmetry provided a high granularity inter-calibration.

During the LHC cycles, the ECAL response varies depending on irradiation conditions, which modify the transparency of the $PbWO_4$ crystals. This effect takes place on a time scale of hours and can cause transparency changes of a few percent during LHC fills/interfill periods, depending on the instantaneous and integrated luminosity, therefore it became particularly important with the increase of the luminosity delivered by the LHC machine in 2011. To maintain the ECAL design performance, continuous corrections to the single channel response must be delivered with a precision better than 0.5%. The changes in crystal transparency are monitored at 40 min intervals by means of laser light injected into each crystal through optical fibers [128]. A detailed calibration procedure of the monitoring system itself is needed, as imperfection of the monitoring system could give rise to residual inaccuracies of the ECAL response. Within this context, the ϕ-symmetry method gave a valuable contribution as monitoring tool. In the ratio of the inter-calibration constants extracted from different sets of data, the largest part of the systematic errors cancels out and the residual distribution spread is the result of the statistical error convoluted with the instability of the crystals. The relative precision obtained comparing two sets of inter-calibration constants from 200M of events is of the order of 0.5%, evaluated with 2010 data, when the effects due to the loss in transparency were negligible. Therefore, the ϕ-symmetry method was deeply exploited as a monitoring tool to detect and correct regions with problematic calibration values and to make fine-grained checks on the transparency corrections obtained from the ECAL laser system.

Due to its fast and high-granularity calibration power, the ϕ-symmetry was a fundamental tool for the inter-calibration of the CMS Electromagnetic Calorimeter in 2011 and still maintains an important role in 2012 calibration plans.

Bibliography

[1] H1 and ZEUS Coll., F.D. Aaron *et al.*, H1prelim-11-111, ZEUSprelim11-011 (2011).

[2] CMS Coll., *Electromagnetic calorimeter calibration with 7 TeV data*, CMS PAS **EGM-10-003** (2010).

[3] W.H.K. Panofsky, *Proceedings of the 14th International Conference on High Energy Physics*, J. Prentki and J. Steinberger (ed.), Vienna (1968).

[4] W. Albrecht *et al.*, contributed paper to *Proc. of the 4th Int. Symp. on Electron and Photon Interaction*, Liverpool (1969) and DESY Report 69/46 (1969) unpublished.

[5] J.D. Bjorken, Phys. Rev. **179**, 1547 (1969).

[6] R.P. Feynman, Phys. Rev. Lett. **23**, 1415 (1969).

[7] C.G. Callan and D.J. Gross, Phys. Rev. Lett. **22**, 156 (1969).

[8] M. Gell-Mann and Y. Ne'eman, *The Eightfold Way*, Benjamin, New York (1964).

[9] G. Zweig, CERN preprints **8182/TH 401** and **8182/TH 412** (1964).

[10] T. Eichten *et al.*, Phys. Lett. **B 46**, 243 (1973).

[11] G. 't Hooft and M. Veltman, Nucl. Phys. **B 44**, 189 (1972).

[12] H1 Coll., S. Aid *et al.*, Nucl. Phys. **B 470**, 3 (1996);
H1 Coll., C. Adloff *et al.*, Eur. Phys. J. **C 13**, 609 (2000);
H1 Coll., C. Adloff *et al.*, Eur. Phys. J. **C 19**, 269 (2001);
H1 Coll., C. Adloff *et al.*, Eur. Phys. J. **C 30**, 1 (2003);
H1 Coll., F.D. Aaron *et al.*, Eur. Phys. J. **C 63**, 625 (2009);
H1 Coll., F.D. Aaron *et al.*, Eur. Phys. J. **C 64**, 561 (2009).

[13] ZEUS Coll., M. Derrick *et al.*, Z. Phys. **C 72**, 399 (1996);
ZEUS Coll., J. Breitweg *et al.*, Phys. Lett. **B 407**, 432 (1997);
ZEUS Coll., J. Breitweg *et al.*, Eur. Phys. J. **C 7**, 609 (1999);

ZEUS Coll., J. Breitweg *et al.*, Phys. Lett. **B 487**, 53 (2000);
ZEUS Coll., S. Chekanov *et al.*, Eur. Phys. J. **C 21**, 443 (2001);
ZEUS Coll., S. Chekanov *et al.*, Eur. Phys. J. **C 28**, 175 (2003);
ZEUS Coll., S. Chekanov *et al.*, Phys. Rev. **D 70**, 052001 (2004).

[14] H1 and ZEUS Coll., F.D. Aaron *et al.*, JHEP **01**, 109 (2010).

[15] F. Halzen and A.D. Martin, *Quarks & Leptons*, J. Wiley and Sons (1984).

[16] V.N. Gribov and L.N. Lipatov, Sov. J. Nucl. Phys. **15**, 438 (1972);
Yu.L. Dokshitzer, Sov. Phys. JETP **46**, 641 (1977);
G. Altarelli and G. Parisi, Nucl. Phys. **B 126**, 298 (1977).

[17] E.A. Kuraev, L.N. Lipatov and V.S. Fadin, Sov. Phys. JETP **45**, 199 (1977);
Y.Y. Balitsky and L.N. Lipatov, Sov. J. Nucl. Phys. **28**, 22 (1978).

[18] L.V. Gribov, E.M. Levin and M.G. Ryskin, Phys. Rep. **100**, 1 (1983).

[19] P.D.B. Collins, *An Introduction to Regge Theory and High Energy Physics*,
Cambrige University Press, (1977).

[20] J.C. Collins, D.E. Soper and G. Sterman, *Perturbative Quantum Chromodynamics*, A.H. Mueller, World Scientific (1989).

[21] R.K. Ellis, W.J. Stirling and B.R. Webber, *QCD and Collider Physics*, Cambridge Monographs on Particle Physics, Nuclear Physics and Cosmology, Vol. **8**, Cambridge University Press, 1996.

[22] G. Altarelli and G. Martinelli, Phys. Lett.**B 76**, 89 (1978).

[23] R. Devenish and A. Cooper-Sarkar, *Deep Inelastic Scattering*, Oxford (2004).

[24] H1 Coll., F.D. Aaron *et al.*, Phys. Lett. **B 665**, 139 (2008);
H1 Coll., F.D. Aaron *et al.*, Eur. Phys. J. **C 71**, 1579 (2011).

[25] ZEUS Coll,. S. Chekanov *et al.*, Phys. Lett. **B 682**, 8 (2009).

[26] H1 and ZEUS Coll., F.D. Aaron *et al.*, H1-prelim-10-043, ZEUS-prel-10-001.

[27] M.L.Good and W.D.Walker, Phys. Rev. **120** (1960) 1957.

[28] G. Alberi and G. Goggi, Phys. Rep. **74**, 1 (1981);
K. Goulianos, Phys. Rep. **101**, 169 (1983).

[29] T. Regge, Nuovo Cimento **14**, 951 (1959);
T. Regge, Nuovo Cimento **18**, 947 (1960).

[30] V. Barone and E. Predazzi, *High-Energy Particle Diffraction*, Springer, Heidelberg (2002).

[31] C.F. Chew and S.C. Frautschi, Phis. Rev. Lett. **8**, 41 (1962).

[32] Particle Data Group, K. Nakamura *et al.*, J. Phys. **G 37**, 075021 (2010).

[33] V.N. Gribov, Sov. Phys. JETP **14**, 478 (1962).

[34] A. Donnachie and P.V. Landshoff, Nucl. Phys. **B 244**, 322 (1984);
A. Donnachie and P.V. Landshoff, Phys. Lett. **B 296**, 227 (1992).

[35] J.R. Cudell, K. Kang and S.K. Kim, Phys. Lett. **B 395**, 311 (1997).

[36] F.E. Low, Phys. Rev. **D 12**, 163 (1975).

[37] S. Nussinov, Phys. Rev. Lett. **34**, 1286 (1975);
S. Nussinov, Phys. Rev. **D 14**, 246 (1976).

[38] E.A. Kuraev, L.N. Lipatov and V.S. Fadin, Sov. Phys. JETP **44**, 443 (1976);
E.A. Kuraev, L.N. Lipatov and V.S. Fadin, Sov. Phys. JETP **45**, 199 (1977).

[39] I.I. Balitisky and L.N. Lipatov, Sov. J. Nucl. Phys. **28**, 822 (1978).

[40] G. Ingelman and P.E. Schlein, Phys. Lett. **B 152**, 256 (1985).

[41] UA8 Coll., R. Bonino *et al.*, Phys. Lett. **B 211**, 239 (1988);
UA8 Coll., A. Brandt *et al.*, Phys. Lett. **B 297**, 417 (1992);
UA8 Coll., A. Brandt *et al.*, Phys. Lett. **B 421**, 395 (1998).

[42] ZEUS Coll., M. Derrick *et al.*, Phys. Lett. **B 315**, 481 (1993).

[43] H1 Coll., T. Ahmed *et al.*, Nucl. Phys., **B 429**, 477 (1994).

[44] H. Abramowicz, L. Frankfurt and M. Strikman, Surveys High Energy Phys. **11**, 51 (1997).

[45] H1 Coll., A. Atkas *et al.*, Eur. Phys. J. **C 48**, 749 (2006).

[46] H1 Coll., F.D. Aaron *et al.*, Eur. Phys. J. **C 71**, 1578 (2011).

[47] H1 Coll., F.D. Aaron *et al.*, H1prelim-10-014 (2010).

[48] H1 Coll., A. Atkas *et al.*, Eur. Phys. **C 48**, 715 (2006).

[49] H1 Coll., F.D. Aaron *et al.*, H1prelim-10-011 (2010).

[50] ZEUS Coll., S. Chekanov *et al.*, Eur. Phys. J. **C 38**, 43 (2004).

[51] ZEUS Coll., S. Chekanov *et al.*, Nucl. Phys. **B 816**, 1 (2009).

[52] ZEUS Coll., S. Chekanov *et al.*, Nucl. Phys. **B 713**, 3 (2005).

[53] ZEUS Coll., S. Chekanov *et al.*, Nucl. Phys. **B 800**, 1 (2008).

[54] H1 Coll., F.D. Aaron et al., DESY-11-084, submitted to Eur. Phys. J. **C** (2011) [arXiv:**hep-ex/1107.3420**].

[55] C. Marquet, Phys. Rev. **D 76**, 094017 (2007) [arXiv:**hep-ph/0706.2682**].

[56] J.C. Collins, Phys. Rev. **D 57**, 3051 (1998) [Erratum - *ibid.* **D 61** 019902 (2000)] [arXiv:**hep-ph/9709499**].

[57] L. Trentadue and G. Veneziano, Phys. Lett. **B 323**, 201 (1994);
A. Berera and D.E. Soper, Phys. Rev. **D 53**, 6162 (1996).

[58] J.D. Bjorken, Phys. Rev. **D 47**, 101 (1993);
E. Gotsman, E. Levin and U. Maor, Phys. Lett. **B 390**, 199 (1993).

[59] ZEUS Coll., S. Chekanov *et al.*, Nucl. Physics **B 831**, 1 (2010).

[60] ZEUS Coll., S. Chekanov *et al.*, Eur. Phys. J. **C 52**, 813 (2007).

[61] N.N. Nikolaev and B.G. Zakharov, Z. Phys. **C 53**, 331 (1992).

[62] J. Bartels, J. Ellis, H. Kowalski and M. Wüsthoff, Eur. Phys. J. **C 7**, 443 (1999).

[63] S.J. Brodsky *et al.*, Phys. Rev. **D 50**, 3134 (1994).

[64] K.J. Golec-Biernat and M. Wüsthoff, Phys. Rev. **D 59** 014017 (1998) [arXiv:**hep-ph/9807513**];
K.J. Golec-Biernat and M. Wüsthoff, Phys. Rev. **D 60** 114023 (1999) [arXiv:**hep-ph/9903358**].

[65] *HERA: A Proposal for a large electron-proton colliding beam facility at DESY*, DESY-HERA-81-10, Hamburg (1981).

[66] ZEUS Coll., U. Holm (ed.), *The ZEUS Detector*, Status Report (unpublished), DESY (1993), available on `http://www-zeus.desy.de/bluebook/bluebook.html` .

[67] H1 Coll., I. Abt *et al.*, Nucl. Instrum. Meth. **A 386**, 310 (1997);
H1 Coll., I. Abt *et al.*, Nucl. Instrum. Meth. **A 386**, 348 (1997).

[68] *The HERA Luminosity Upgrade*, DESY-HERA-98-05, Ed. U. Schneekloth (1998).

[69] U. Klein, `http://www-zeus.desy.de/physics/lumi/` .

[70] ZEUS Coll., *The ZEUS detector, Status Report 1993*, U. Holm ed. (1993).

[71] A. Polini *et al.*, Nucl. Instr. and Meth. **A 581**, 656 (2007) [**arXiv:0708.3011v1**].

[72] L.A.T. Bauerdick *et al.*, Nucl. Instr. and Meth. **A 501**, 340 (2003) [**arXiv:hep-ex/0212037v1**].

[73] B. Foster *et al.*, Nucl. Instr. and Meth. **A 338**, 254 (1994).

[74] R. Hall-Wilton *et al.*, *The CTD Tracking Resolution*, Internal ZEUS-Note **99-024** (1999).

[75] E. Maddox, *Study of heavy quark production at HERA using the ZEUS microvertex detector*, Ph.D. Thesis, NIKEF (2004).

[76] ZEUS Calorimeter Group, A. Andersen *et al.*, Nucl. Instr. and Meth. **A 309**, 101 (1991).

[77] M. Derrick *et al.*, Nucl. Instr. and Meth. **A 309**, 77 (1991).

[78] A. Caldwell *et al.*, Nucl. Instr. and Meth. **A 321**, 356 (1992).

[79] A. Bernstein *et al.*, Nucl. Instr. and Meth. **A 336**, 23 (1993).

[80] A. Bamberger *et al.*, Nucl. Instr. and Meth. **A 401**, 63 (1997).

[81] A. Dwurazny *et al.*, Nucl. Instr. and Meth. **A 277**, 176 (1989).

[82] J. Andruszkow *et al.*, Acta Phys. Polon. **B 32**, 2025 (2001).

[83] M. Helbich *et al.*, *The Spectrometer System for Measuring ZEUS Luminosity at HERA*, Internal ZEUS-Note **06-002** (2006).

[84] ZEUS Coll., M. Derrick *et al.*, Z. Phys. **C 73**, 253 (1997).

[85] ZEUS Coll., A. Bamberger *et al.*, Nucl. Inst. Meth. **A 450**, 235 (2000).

[86] W.H. Smith, K. Tokushuku and L. Wiggers, *Proc. Computing in High-Energy Physics (CHEP), Annency, France 1992*, C. Verkeck and W. Wojcik (eds.), p.222, Geneva, Switzerland (1992).
Also in pre-print DESY-92-150B.

[87] ZEUS Coll., J. Breitweg *et al.*, Eur. Phys. J. **C 1**, 81 (1998).

[88] H1 Coll., T. Ahmed *et al.*, Nucl. Phys. **B 435**, 3 (1995).

[89] P. Newman and M. Ruspa, contributed paper to *HERA and the LHC - 2nd workshop on the implications of HERA for LHC physics*, H. Jung and A. De Roeck, Hamburg-Geneva (2006-2008) [arXiv:**hep-ex/0903.2957**].

[90] S. Glazov, AIP Conf. Proc. **792**, 237 (2005).

[91] H1 Coll., F.D. Aaron *et al.*, Eur. Phys. J. **C 63**, 625 (2009) [arXiv:**hep-ex/0904.0929**].

[92] V. Sola, in *Proceedings of the PANIC 2011 Conference* to be published in AIP Conference Proceedings, G. Stephans and F. Taylor, MIT, Cambridge, USA (2011).

[93] V. Sola, in *Proceedings of IFAE 2011*, to be published in Nuovo Cimento C - Colloquia on Physics (2011).

[94] P. Kaur, *Neutral Current Cross-Section Measurement at low Q^2 and high-y with ZEUS detector at HERA*, Ph.D. Thesis, Panjab University, Chandigarh (2011).

[95] H. Kowalski, *Proceedings of the Workshop on New Trends in HERA Physics*, G. Grindhammer, B.A. Kniehl and G. Kramer (eds.), Rinberg, June 1999, 361 (1999); H. Kowalski and M. Wüsthoff, *Satrap Model for Diffractive DIS Processes*, prepared for 8th International Workshop on Deep Inelastic Scattering and QCD (DIS 2000), Liverpool, England (2000).

[96] H. Spiesberg, HERACLES *and* DJANGOH*: event generation for ep Interactions at HERA including Radiative Processes* (2005), available on `http://wwwthep.physik.uni-mainz.de/~hspiesb/djangoh/djangoh.html` .

[97] T. Sjöstrand, Comp. Phys. Comm. **82**, 74 (1994).

[98] Torbjorn Sjostrand (Lund University), Stephen Mrenna (Fermilab), Peter Skands (Fermilab)

T. Sjöstrand, S. Mrenna and P. Skands, PYTHIA *6.4: Physics and Manual* (2006) [arXiv:**hep-ph/063175**].

[99] H. Jung, Comp. Phys. Comm. **86**, 147 (1995);
H. Jung, *The RAPGAP Monte Carlo for Deep Inelastic Scattering, version 3.1*, DESY Hamburg, 2005, available on `http://www.desy.de/~jung/rapgap/` .

[100] A. Kwiatkowski, H. Spiesberg and H.J. Möhring, Comp. Phys. Comm. **69**, 155 (1992). Also available in *Proc. Workshop Physics at HERA*, eds. W. Buchmüller and G. Ingelman, DESY, Hamburg (1991);
H. Spiesberg, *An Event Generator for ep Interactions at HERA Including Radiative Processes (Version 4.6)*, 1996, available on `http://www.desy.de/~hspiesb/heracles.html` .

[101] L. Lönnblad, Comp. Phys. Comm. **71**, 15 (1992).

[102] B. Andersson *et al.*, Phys. Rep. **97**, 31 (1983).

[103] CTEQ Coll., H.L. Lai *et al.*, Eur. Phys. J. **C 12**, 375 (2000).

[104] *Amadeus - ZEUS Interface to Monte Carlo Generators*, available at `http://www-zeus.desy.de/ZEUS_ONLY/analysis/Amadeus/index.html` .

[105] R. Brun *et al.*, GEANT3, Technical Report CERN-DD/EE/84-1, CERN, 1987.

[106] E. de Wolf *et al.*, ZGANA, *ZEUS trigger simulation library*, 1981.

[107] *Funnel - The ZEUS Monte Carlo Production Facility*, available at `http://www-zeus.desy.de/components/funnel/TOP.html` .

[108] B. Straub, *Introduction to ORANGE*, available at `http://www-zeus.desy.de/lectures/` .

[109] PAW, *Physics Analysis Workstation*, documentation available on `http://wwwasd.web.cern.ch/wwwasd/paw/` .

[110] ROOT, *An Object-Oriented Data Analysis Framework*, documentation available on `http://root.cern.ch/` .

[111] G.F. Hartner *et al.*, *VCTRAK (3.07/04): Offline Output Information*, Internal ZEUS-Note **97-064** (1997);
G.F. Hartner, *VCTRAK Briefing: Program and Math*, Internal ZEUS-Note **98-058** (1998).

[112] R. Frühwirth, Nucl. Instr. Meth. **A 262**, 444 (1987).

[113] H. Abramowicz, A. Caldwell and R. Sinkus, Nucl. Instr. Meth. **A 365**, 508 (1995).

[114] S. Bentvelsen, J. Engelen and P. Kooijman, *Proc. Workshop on Physiscs at HERA*, W. Buchmüller and G. Ingelman (eds.), Vol. 1, p. 23, Hamburg, Germany, DESY, 1992.

[115] N. Tuning, *Proton Structure Function at HERA*, Ph.D. Thesis, University of Amsterdam (2001).

[116] S. Shimizu, *Measurement of the Proton Longitudinal Structure Function F_L at HERA*, Ph.D. Thesis, KEK and Department of Physiscs, University of Tokyo (2009).

[117] Y. Ri, *Measurement of neutral current deep inelastic ep scattering cross section with longitudinally polarized electrons with ZEUS at HERA*, Ph.D. Thesis, Tokyo Metropolitan University (2009).

[118] G.M. Briskin, *Diffractive Dissociation in Deep Inelastic Scattering*, Ph.D. Thesis, University of Tel Aviv, Report DESY-THESIS-1998-036 (1998).

[119] N. Tuning, *ZUFOs: Hadronic final state reconstruction with calorimeter, tracking and backsplash correction*, Internal ZEUS-Note **01-021** (2001).

[120] F. Jaquet and A. Blondel, *Proc. the Study of an ep Facility for Europe*, U. Amaldi (ed.), p. 391, (1979).
Also in preprint DESY 79-48.

[121] ZEUS Coll., S. Chekanov *et al.*, Phys. Lett. **B 545**, 244 (2002).

[122] CMS Coll., JINST **5** T03010 (2010), doi:10.1088/1748-0221/5/03/T03010.

[123] CMS Coll., *Electromagnetic calorimeter commissioning and first results with 7 TeV data*, CMS NOTE **2010/012** (2010).

[124] CMS Coll., R. Adolphi *et al.*, JINST **0803** (2008) S08004, doi:10.1088/1748-0221/3/08/S08004.

[125] CMS Coll., *CMS technical design report, volume I: Detector Performance and Software* CERN/LHC **2006-001** (2006).

[126] D. Futyan and C. Seez, *Intercalibration of ECAL crystals in ϕ Using Symmetry of Energy Deposition*, CMS NOTE **2002/031** (2002).

[127] V. Litvin, *Inter-calibration of the CMS barrel electromagnetic calorimeter using $\pi^0 \to \gamma\gamma$ decays*, CMS CR **2007/069** (2007).

[128] M. Anfreville *et al.*, Nucl. Instrum. Meth. **A 594**, 292 (2008).

Aknowledgements

Al termine di questi tre anni incredibili e indimenticabili sono molte le persone che vorrei ringraziare per avermi aiutato, sostenuto e incoraggiato e per aver contribuito alla mia crescita personale e professionale. A tutti rivolgo un sentito e sincero grazie.

Il primo grazie va indubbiamente a Marta e Michele, la causa e le guide di questo lavoro. Grazie a Michele per l'esempio e la costanza che mi ha trasmesso. Grazie a Marta per la presenza e la perseveranza, per gli insegnamenti di fisica e per la fiducia che mi ha sempre dimostrato, e grazie anche per le feste a sorpresa. Un grazie speciale va a Ada per i suoi saggi e preziosi consigli, per non avermi mai lasciato sola nel momento del bisogno e per tutti i caffè quando era il momento di fare sul serio.

Grazie a tutto il gruppo di CMS Torino che in questi anni mi ha accompagnato nel mio percorso accademico e sostenuto nella mia attività di giovane fisica. In particolare grazie al gruppo ECAL per i momenti indelebili trascorsi insieme: grazie a Nadia per il suo esempio e la sua energia, a Margherita per la sua presenza e l'allegria, a Stefano per gli insegnamenti e i momenti nerd, a Nicolò per la sua esperienza, a Matteo per aver condiviso la vita 'ginevrina', e a Roberta per le cene e le risate.

This thesis is the result of a wonderful work within the ZEUS Collaboration, and I'm very grateful to everyone who helped and guided me through this experience. I would like to thank all the coordinators of the SFEX and H1ZEUS groups and the ZEUS management that followed and supported the developing of my analyses: O. Behnke, B. Reisert, A. Geiser, I. Abt, T. Haas, A. Levy and all the others. Many thanks to E. Gallo, who shared with me her great experience and the pleasure of an inclusive diffractive measurement. I received a special guidance and an unvaluable human support from H. Abramowicz and A. Levy, I will always be grateful to them and I will bring Tel Aviv in my heart forever and ever.
Many thanks also to the members of the H1 Collaboration that made possible the combination of the HERA diffractive results: M. Kapishin, R. Polifka, K. Krueger, K. Daum, C. Diaconu and P. Newman.

Grazie al nocciolo duro della famiglia italiana ad Amburgo e in particolare a Monica e Andrea per un memorabile battesimo allo spritz.

Many thanks to the CMS Collaboration and in particular to the ECAL group for the chance

they gave me to enjoy the data-taking time and the detector-maintenance experience.

Grazie davvero ai compagni fisici che, sparsi per Torino, per l'Italia o per il mondo, sanno sempre essere un punto fisso e un valido supporto per ogni evenienza, in particolare nelle feste. Più nel dettaglio vorrei ringraziare il sempre verde Adriano, fratello Sola, la rock star Lava, lo scanzonato Bjünd, Arianna la giramondo, Marcello, Jack, Mauro e Mary*. Un grazie anche a chi ha continuato, imperterrito, a dar colore a un edificio grigio, come hanno saputo fare il Pennaz, Carla e Elisa.

Un grazie speciale va alla squadra del Real Calcio Femminile per i momenti di allegria, leggerezza e spensieratezza che ho trascorso in compagnia delle ragazze tutte. Cercando di non dimenticarne nessuna ringrazio: il capitano Nonna Gabry, Ilaria, Silvietta, Melinda, Monichina, Mony, Micky, Claudia, Crock, Mamy Giò, Chiara, Valentina, Roma Netta Gargano, Bianca, Eliana Belli Capelli, Gaia, Patty, Stuzzy, Gino, Carmine, Giancky e Paolo. Per mantenere fede a una promessa fatta un grazie personalizzato a TurboDrammis, per quella famosa traversa-palo che non mi ha mai dedicato.

Un grazie da urlo lo dedico al GT tutto, per le sudate, le sciate, le risate e per tutte le bravate fatte in questo ultimo, indimenticabile, anno insieme. In particolare vorrei ringraziare Lucky, il nostro mitico capitano, Isa, la mia fedele compagna di scuffiate, Fabio&Fabio e Speeder, e la nostra indimenticabile pista deserta nel tramonto monginevrino, Nicolas Vedo Largo, che è il più psycopazzo di tutti, Diego Deza Huete e un po' anche il suo amico sfigato con gli occhiali, ManuGamba e Gigia, Manu&Leo, con la loro immancabile ventata d'allegria, la pulce coi codini Giulia, Guido, le sorelle Pasca, Cina, Javier, e ultimo, ma non per caso, il molestissimo Livio.

Grazie agli amici di una vita, a chi c'è sempre stato, a chi è tornato e a chi non si è mai tirato indietro.

Grazie Alessandra, il mio saggio e fidato Kaqo, perché nonostante gli anni, gli impegni e la vita, stare accanto a te è sempre come tornare a casa dopo tanto tempo.

Grazie Stella, per tutte le risate, le follie, le vacanze, la neve morbida, il surf, il vento tra i capelli, la tua presenza costante, ma soprattutto grazie per la tua fiducia incondizionata, sempre e comunque.

Un grazie a Luisa, la mia fan n.1, perché nonostante ciò non contribuisca ad accrescere la mia autostima, la sua presenza pacata nella mia vita è un'abitudine a cui non voglio rinunciare.

Grazie Eleonora, per le nostre serate con tanto di risate, per quel puzzle ancora a metà e per la nostra amicizia che non sa finire.

Grazie di cuore Roberta, per questi tre anni, per ogni giorno e per ogni singolo secondo. Ho imparato a sognare!

E sempre ultimi ma mai meno importanti, ringrazio la mia famiglia, per la forza, la fiducia, il sostegno e il divertimento che non mi fanno mai mancare. Grazie Mamma, Papà, Veronica e Simone, perché insieme ce la spassiamo sempre alla grande. Grazie alle nonne, agli zii&zie, ai cugini&cugine, perché è bello sapere di avere qualcuno su cui poter sempre contare.